

# UC Irvine

## UC Irvine Electronic Theses and Dissertations

### Title

Structural, chemical, and electronic properties of epitaxially-fused quantum dot superlattices

### Permalink

<https://escholarship.org/uc/item/4df4w4zc>

### Author

Abelson, Alexander

### Publication Date

2021

### Copyright Information

This work is made available under the terms of a Creative Commons Attribution-NonCommercial License, available at <https://creativecommons.org/licenses/by-nc/4.0/>

Peer reviewed|Thesis/dissertation

UNIVERSITY OF CALIFORNIA,  
IRVINE

Structural, chemical, and electronic properties of epitaxially-fused quantum dot superlattices

DISSERTATION

submitted in partial satisfaction of the requirements  
for the degree of

DOCTOR OF PHILOSOPHY

in Materials Science and Engineering

by

Alexander David Abelson

Dissertation Committee:  
Professor Matt Law, Chair  
Associate Professor Allon Hochbaum  
Associate Professor Shane Ardo

2021

Structural, chemical, and electronic properties of epitaxially-fused quantum dot superlattices

© 2021 Alex Abelson

## DEDICATION

This work is dedicated to my family. To my parents: I hope that this work and what it represents gives you a sense of pride, because I got here through you. To my brothers, for keeping me honest and true, and never a dull moment. To my grandfather, Arnold, for instilling in me a love of science and the value of truth. To my grandmother, Irene, for sharing with me your values, love, and spirit of toughness. To my grandmother, Joan, for your love and good humor, reminding me it is always a good time to laugh. To the memory of my late grandfather, Bob, for your unrivaled optimism, no matter the circumstance. And to my aunts and uncles that have supported me, questioned me, and made me laugh.

And to my loyal dog, Jango: you are a very good boy.

## TABLE OF CONTENTS

LIST OF FIGURES .....	VII
LIST OF TABLES.....	XII
ACKNOWLEDGEMENTS.....	XIII
VITA.....	XIV
ABSTRACT.....	XV
CHAPTER 1 INTRODUCTION AND BACKGROUND .....	1
1.1 . Quantum Dots .....	2
<i>1.1.1 . A Brief History</i> .....	3
<i>1.1.2 . Anatomy of Quantum Dots</i> .....	4
<i>1.1.3 . Electronic Structure of Quantum Dots</i> .....	5
<i>1.1.4 . Optical Properties of Quantum Dots</i> .....	6
1.2 . PbSe: From Bulk to the Nanoscale .....	9
<i>1.2.1 . Crystal Structure</i> .....	9
<i>1.2.2 . Electronic Structure</i> .....	10
<i>1.2.3 . Carrier Multiplication</i> .....	13
1.3 . Quantum Dot Synthesis .....	14
<i>1.3.1 . PbSe Quantum Dot Synthesis</i> .....	16
1.4 . Quantum Dot Self-Assembly .....	19
<i>1.4.1 . Quantum Dot Superlattices</i> .....	20
<i>1.4.2 . Quantum Dot Film Fabrication</i> .....	22
1.5 . Quantum Dot Surface Chemistry .....	23

1.5.1 . <i>PbSe Quantum Dot Surface Chemistry</i> .....	24
1.5.2 . <i>Ligand Exchange</i> .....	26
1.5.3 . <i>Relation Between Surface Chemistry and QD Doping</i> .....	27
1.5.4 . <i>Matrix Engineering with Atomic Layer Deposition</i> .....	28
1.6 . Charge Transport in QD Solids.....	29
1.6.1 . <i>Hopping Transport</i> .....	29
1.6.2 . <i>Band-like Charge Transport</i> .....	32
1.6.3 . <i>Mini-band Transport</i> .....	34
1.7 . Epitaxially-fused Quantum Dot Superlattices .....	36
1.7.1 . <i>Oriented Attachment</i> .....	37
1.7.2 . <i>Structural Analysis of epi-SLs</i> .....	38
1.7.3 . <i>Electronic Properties of Epi-SLs</i> .....	40
1.8 . Overview of Work .....	42
CHAPTER 2 EPITAXIALLY-FUSED QUANTUM DOT SUPERLATTICES .....	45
2.1 . Quantum Dot Building Blocks.....	47
2.2 . Superlattice Synthesis and Surface Chemistry .....	54
2.3 . Structure Analysis .....	63
2.4 . Collective Topo-epitaxy.....	77
2.5 . Effects of Atomic Layer Deposition.....	84
2.6 . Conclusions.....	91
2.7 . Methods.....	93
2.7.1 . <i>PbSe QD Synthesis</i> .....	93
2.7.2 . <i>Epi-SL film fabrication</i> .....	93

2.7.3 . <i>Basic optical and chemical characterization</i> .....	94
2.7.4 . <i>Small-angle X-ray scattering</i> .....	94
2.7.5 . <i>Oleate coverage in FTIR experiments</i> .....	95
2.7.6 . <i>Isotope labelling experiments</i> .....	95
2.7.7 . <i>Determination of surface oleate coverage</i> .....	96
2.7.8 . <i>Inductively coupled plasma mass spectrometry</i> .....	96
2.7.9 . <i>GISAXS fitting refinement</i> .....	99
2.7.10 . <i>Transmission electron microscopy</i> .....	100
2.7.11 . <i>Electrical measurements</i> .....	100
 CHAPTER 3 PHOTOINITIATED EPI-SL FORMATION .....	 101
3.1 . Epi-SL Formation with Brønsted Bases .....	103
3.2 . Photo-initiated Epi-SLs.....	108
3.3 . Proposed Mechanism of Ligand Exchange.....	113
3.4 . Conclusion .....	115
3.5 . Methods.....	116
3.5.1 . <i>Film fabrication and basic characterization.</i> .....	116
3.5.2 . <i>Analysis of FTIR spectra</i> .....	117
3.5.3 . <i>Image analysis</i> .....	117
3.5.4 . <i>pK<sub>b</sub> of amines</i> .....	120
 CHAPTER 4 SINGLE-GRAIN EPI-SL ELECTRONICS .....	 121
4.1 . Single-grain Field-effect Transistors .....	121
4.2 . Variable-temperature FET Measurements .....	131
4.3 . Conclusion .....	137

4.4 . Methods.....	137
4.4.1 . <i>Epi-SL device fabrication</i> .....	137
4.4.2 . <i>Process design criteria</i> .....	138
4.4.3 . <i>Device fabrication recipe</i> .....	139
4.4.4 . <i>Photolithography</i> .....	144
4.4.5 . <i>Thermal evaporation of metals</i> .....	145
4.4.6 . <i>Atomic layer deposition of alumina</i> .....	146
4.4.7 . <i>Electron beam lithography</i> .....	146
4.4.8 . <i>Electrical properties of ALD alumina</i> .....	149
4.4.9 . <i>Alumina wet etch</i> .....	150
4.4.10 . <i>Quantum dot synthesis and purification</i> .....	153
4.4.11 . <i>Bias-stress effect</i> .....	153
CHAPTER 5 CONCLUSION.....	155
5.1 . Summary.....	155
5.2 . Outlook .....	156
REFERENCES .....	158



## LIST OF FIGURES

Figure 1.1. Photoluminescence from quantum dot suspensions. ....	2
Figure 1.2. Spectral range of different QDs.....	7
Figure 1.3. Structure of PbSe.....	10
Figure 1.4. Band diagram of bulk PbSe.....	11
Figure 1.5. Optical spectra of PbSe QDs.....	12
Figure 1.6. Schematic of LaMer growth model.....	15
Figure 1.7. Schematic of a hot-injection QD synthesis. ....	17
Figure 1.8. Proposed mechanism of PbSe monomer formation. ....	18
Figure 1.9. Carrier mobility in PbSe QD solids with different ligands. ....	31
Figure 1.10. Temperature-dependent mobility of disordered HgTe QD films.....	33
Figure 1.11. 2D epitaxially-fused PbSe QD superlattices. ....	37
Figure 2.1. HAADF-STEM single-particle reconstruction of PbSe QDs.....	48
Figure 2.2. Size analysis of PbSe QDs. ....	49
Figure 2.3. <sup>1</sup> H NMR spectrum of a PbSe QD suspension. ....	51
Figure 2.4. Estimate of facet-specific oleate surface coverage of PbSe QDs.....	53

Figure 2.5. Fabrication and ligand chemistry of epitaxially-fused PbSe quantum dot superlattices (epi-SLs). .....	56
Figure 2.6. Impact of alternative secondary treatments on the epi-SLs.....	58
Figure 2.7. FTIR spectra of SL films made with deuterated ethylene glycol (HOCD <sub>2</sub> CD <sub>2</sub> OH, EG- <i>d</i> <sub>4</sub> ) and deuterated ethylenediamine (H <sub>2</sub> NCD <sub>2</sub> CD <sub>2</sub> NH <sub>2</sub> , EDA- <i>d</i> <sub>4</sub> ). .....	59
Figure 2.8. X-ray photoelectron spectra of SL films. ....	61
Figure 2.9. Process map for determining the complete unit cell of QD superlattices. ....	64
Figure 2.10. Structure of the oleate-capped QD SL films. ....	65
Figure 2.11. Representative SEM images of oleate-capped SLs. ....	66
Figure 2.12. SL unit cell description relation. ....	66
Figure 2.13. Models of the oleate-capped SL surfaces. ....	67
Figure 2.14. Structure of the epi-SL films. ....	69
Figure 2.15. Representative SEM images of epi-SLs. ....	70
Figure 2.16. Correlated imaging and diffraction of a twinned (100) <sub>SL</sub> -oriented epi-SL grain. ....	70
Figure 2.17. TEM images of 3D epi-SLs showing QD fusion along the <100> <sub>AL</sub> directions.....	72
Figure 2.18. TEM images of 2D oleate-capped SL and epi-SLs showing QD fusion along the <100> <sub>AL</sub> directions.....	73

Figure 2.19. Representative wide-angle $\theta$ - $2\theta$ XRD patterns of oleate-capped and epi-SL films.	74
Figure 2.20. The epi-SL tomogram and QD positions.....	75
Figure 2.21. The phase transition pathway. ....	78
Figure 2.22. Impact of QD cleaning cycles on oleate coverage and the size of the rhombohedral distortion of the oleate-capped SLs.....	80
Figure 2.23. $\{100\}_{AL}$ facet overlap as a function of lattice angle $\alpha$ for oleate-capped SLs with rhombohedrally-distorted bcc unit cells.....	82
Figure 2.24. Molecular dynamics simulation on the deformability of polar PbSe QDs.....	83
Figure 2.25. Wide-angle $\theta$ - $2\theta$ XRD patterns of an epi-SL showing no change in QD size after ALD infilling.....	85
Figure 2.26. Effect of ALD alumina infilling on the epi-SL structure. ....	85
Figure 2.27. Effect of ALD alumina infilling on the epi-SL chemical, optical, and electronic properties.....	86
Figure 2.28. Model of the ALD-infilled epi-SL sample shown in Figure 2.27a-b. ....	87
Figure 2.29. Epi-SL field-effect transistor results. ....	88
Figure 2.30. SEM image analysis used to constrain the GISAXS fits of the SL unit cell.....	99
Figure 3.1. Amine-triggered conversion of oleate-capped PbSe QD SLs to epi-SLs.....	104
Figure 3.2. Hydroxide-triggered conversion of oleate-capped SLs to epi-SLs. ....	105

Figure 3.3. Structural analysis of SLs treated with amines and TBAOH. ....	106
Figure 3.4. Structural and optical characterization of the photobase generator (E)-1-piperidino-3-(2-hydroxyphenyl)-2-propen-1-one (WPBG-027).....	110
Figure 3.5. Characterization of epi-SLs made using a photobase generator. ....	111
Figure 3.6. Structural analysis of photobase epi-SL film controls. ....	113
Figure 3.7. Proposed chemical pathways for epi-SL formation. ....	114
Figure 3.8. Method for quantifying oleate removal from QD SL films using FTIR. ....	117
Figure 3.9 Semi-automated superlattice image analysis.....	118
Figure 3.10. $pK_b$ values of amines in water and ethylene glycol.....	120
Figure 4.1. Single-grain epi-SL field-effect transistors. ....	123
Figure 4.2. Single-grain field-effect transistor electronic properties.....	124
Figure 4.3. Impact of annealing on the doping profile of ALD-infilled PbSe QD films.....	126
Figure 4.4. Temperature-dependent mobility of single-grain epi-SL field-effect transistors.....	131
Figure 4.5. Variable-temperature transfer curves and mobility single-grain transistor.....	133
Figure 4.6. Gate-induced state-filling of a single-grain epi-SL field-effect transistor. ....	134
Figure 4.7. Variable-temperature mobility of a single-grain field-effect transistor between 14 to 250 K.....	136

Figure 4.8. Schematic of single-grain epi-SL field-effect transistor. ....	138
Figure 4.9. Epi-SL device chips following Step 5. ....	139
Figure 4.10. Epi-SL device chips following Step 6. ....	140
Figure 4.11. Epi-SL device chips following Step 11. ....	141
Figure 4.12. Epi-SL device chips following Step 13. ....	141
Figure 4.13. Epi-SL device chips following Step 16. ....	142
Figure 4.14. Epi-SL device chips following Step 18. ....	143
Figure 4.15. Completed epi-SL device chip. ....	143
Figure 4.16. Overview of single-grain device photomask and associated die patterns. ....	145
Figure 4.17. Steps for drawing coarse electrodes in Design CAD Express 16. ....	149
Figure 4.18. Electrical resistivity of ALD alumina thin films deposited at 60 °C as a function of film thickness. ....	150
Figure 4.19. Etch rate of alumina using X-ray reflectivity. ....	151
Figure 4.20. Evaluating the etch rate of ALD alumina deposited on a QD thin film. ....	152
Figure 4.21. Impact of the bias-stress effect on charge mobility calculations. ....	154

## LIST OF TABLES

Table 1. Summary of PbSe QD size and shape. ....	54
Table 2. Surface elemental composition of the SL films as determined from XPS data.....	62
Table 3. Results of Scherrer XRD crystallite size analysis. ....	74
Table 4. Statistics from structural analysis of an epi-SL tomogram.....	76
Table 5. NMR quantification of oleate ligand coverage.....	81
Table 6. Linear field-effect mobilities for the epi-SL FETs. ....	89
Table 7. ICP-MS results for Pb removal by prolonged in-situ ligand treatments.....	97
Table 8. ICP-MS results for Pb and Se removal by normal in-situ ligand treatments.....	98
Table 9. Structural parameters of SL films treated using various amines. ....	108
Table 10. Structural parameters of SL films treated using tetrabutylammonium hydroxide (TBAOH).....	108
Table 11. NMR peak analysis of W-027 photobase molecule.....	110
Table 12. Summary of electronic and structural properties of epi-SL single-grain devices.....	128

## ACKNOWLEDGEMENTS

I am deeply appreciative of my advisor and committee chair, Professor Matt Law, for teaching me how to be a scientist—it was never easy, but it was often fun. I have immeasurable respect for Matt and his breadth and depth of knowledge, attention to detail, unwavering patience, and unflinching commitment to getting at the truth.

I would like to thank my committee members, Professor Shane Ardo and Professor Allon Hochbaum for your support and guidance over the past 5 years, whether it was in the classroom or in the hallway.

I would like to thank the many graduate students and post-docs with whom I had the opportunity to work: Sam Keene, Trenton Salk, Nima Farhi, Darren Neo, Christian Engelbrekt, Juliette Micone, Zhongyue Luan, Kan Fu, Yash Gargasya, Andy Yang, and Ian Sequeira. And to the undergraduates: Glen Junor, Avo Pisikyan, Amanda Shack, Dalton DeDianous, and Robert Capp.

A special thanks to Caroline Qian, who worked fearlessly and tirelessly with me on the quantum dot project. I think we made a pretty good team, and I am very appreciative of your teamwork over the years.

I would like to thank all of my collaborators over the years, in particular Clark Travaglini, Mahmut Kavrik, Xinxing Peng, Yu Wang, Scott Ueda, Xiaolei Chu, and Chenhui Zhu. Together we accomplished a great deal. I would like to acknowledge the staff of the Irvine Materials Research Institute for all your assistance over the years, including Jian-Guo Zheng, Ich Tran, Toshihiro Aoki, Qiyin Lin, Li Xing, and Mingjie Xu.

## VITA

- 9) Hansen, C., Unruh, D., Alba, M., Qian, C., Abelson, A., *et al.* Hierarchical carrier transport simulator for defected nanoparticle solids. *Scientific Reports* (2021).
- 8) Chu, X., Heidari, H., Abelson, A., *et al.* Structural characterization of a polycrystalline epitaxially-fused colloidal quantum dot superlattice by electron tomography. *Journal of Materials Chemistry A*. (2020).
- 7) Ueda, S.T., Kwak, I., Abelson, A., *et al.* Electronic passivation of PbSe quantum dot solids by trimethylaluminum vapor dosing. *Applied Surface Science*. (2020).
- 6) Abelson, A., Qian, C., Salk, T., Luan, Z., Fu, K., Zheng, J-G., Wardini, J. L. & Law, M. Collective topo-epitaxy in the self-assembly of a 3D quantum dot superlattice. *Nature Materials*. (2020).
- 5) Luan, Z., Salk, T., Abelson, A., *et al.* Reversible aggregation of covalently cross-linked gold nanocrystals by linker oxidation. *Journal of Physical Chemistry C*. (2019).
- 4) Geremew, A., Qian, C., Abelson, A., *et al.* Low-Frequency Electronic Noise in Superlattice and Random-Packed Thin Films of Colloidal Quantum Dots. *Nanoscale*. (2019).
- 3) Wang, Y. Peng, X., Abelson, A., *et al.* Dynamic deformability of individual PbSe nanocrystals during superlattice phase transitions. *Science Advances*. (2019).
- 2) Wang, Y., Peng, X., Abelson A., *et al.* In situ TEM observation of neck formation during oriented attachment of PbSe nanocrystals. *Nano Research*. (2019).
- 1) Peng, X., Abelson, A., *et al.* In situ TEM study of the degradation of PbSe nanocrystals in air. *Chemistry of Materials*. (2018).



## ABSTRACT

Quantum dots (QDs) are semiconductor nanocrystals with optical and electronic properties that can be manipulated through subtle changes to their size, shape, and composition. This remarkable tunability—coupled with their ease of manufacturing and low cost—makes them promising building blocks for emerging and next-generation semiconductor, optoelectronics, and energy conversion devices. QDs are already proving their utility and commercial viability in modern television displays, which use QDs to expand their color gamut beyond that of traditional technologies. However, many impactful applications (*e.g.*, solar cells, cameras, machine vision, quantum information systems, illumination systems) of QD thin films are precluded by their poor charge transport properties. This thesis is broadly focused on improving charge transport in QD thin films. Towards achieving this goal, we focused on the development and characterization of an epitaxially-fused QD superlattice (epi-SL), which is a periodic assembly of QDs in which the constituent QDs are crystallographically aligned and epitaxially connected to form a porous single-crystal. Epi-SLs are exciting because of their predicted ability to combine the electronic and optical tunability of individual QDs with the efficient charge transport of bulk semiconductors through the emergence of collective, delocalized electronic states.

This thesis details the conversion of colloidal QDs into electronic devices composed of individual epi-SL grains, establishing foundational insight into key aspects of epi-SL synthesis, chemistry, structure, and electronic behavior. The first chapter provides a broad introduction to QDs and QD-based devices. In the second chapter, multi-modal structural analysis reveals how colloidal PbSe QDs assemble into a 3-D epi-SL. The structural metamorphosis occurs with the

help of a critical intermediate parent superlattice (SL) phase, which converts into the epi-SL through an impressive choreography of QD translation and rotation. Chemical analysis of parent and epi-SL phases reveals the underlying chemical processes that initiate the SL phase transformation. In the third chapter, these insights are leveraged to make epi-SLs using UV light (rather than injection of a chemical) to trigger the SL phase transformation. The final chapter of this work contains a demonstration of, for the first time, single-grain epi-SL field-effect transistors. Individual epi-SL grains are deterministically integrated into optoelectronic devices of arbitrary geometry and architecture (although here we focus on field-effect transistors) by way of a novel nanofabrication process. Single-grain epi-SL transistors show hole mobilities approaching  $10 \text{ cm}^2/\text{Vs}$ , which represents a  $\sim 10\text{x}$  improvement in charge carrier mobility over previously reported PbX QD solids. Variable-temperature transistor measurements reveal several interesting electronic phenomena that warrant future study.

# CHAPTER 1

## INTRODUCTION AND BACKGROUND

Integration of semiconductors into next-generation commercial optoelectronics is limited by their hard-to-tune band gaps, high manufacturing costs, and appreciable processing challenges. Each compound (*e.g.*, Si, GaAs, HgCdTe) is a world unto itself, requiring unique processing facilities and material-specific expertise. High-performance, versatile, low-cost, and easily manufactured semiconductors with tunable band gaps are a holy grail of materials science.

Quantum dots (QDs) are semiconductor nanocrystals that feature size-tunable band gaps, low processing costs, and scalable synthesis. QD band gaps are readily tuned during synthesis, making them useful building blocks for semiconductor materials-by-design, and for integration into thin films and optoelectronic devices. By virtue of their band gap tunability and sharp color resolution, QDs have found success as phosphors in modern television displays. The ubiquity of QDs within the display market attests to their viability in real-world applications. However, widespread use of QDs beyond photoemission applications is limited by inefficient hopping transport characteristic of traditional random-packed QD assemblies. The work in this thesis aims to dramatically improve charge transport in QD solids through the formation of spatially-ordered QD assemblies that exhibit delocalization of electronic wavefunctions and formation of bulk-like electronic bands (“mini-bands”).

To these ends, we focus on a remarkable and emerging class of materials called epitaxially-fused superlattices (epi-SLs). Epi-SLs are thin films comprised of monocrystalline QDs that are epitaxially connected (*i.e.*, the atomic lattices of each QD are aligned and attached to one-another)

to form a porous single-crystal. Epi-SLs are predicted to combine the size-tunable photophysics of QDs with the high-performance electronic properties of bulk semiconductors. Intimate and atomically precise inter-QD epitaxy is expected to result in the strong and homogeneous electronic coupling needed for mini-band formation, improved charge transport, and attainment of holy grail status. Realization of mini-band transport in epi-SLs has thus far been hampered by the presence of structural and chemical defects that conspire to suppress miniband formation.

This chapter provides a broad overview of concepts relevant to the formation and study of epitaxially-fused superlattices.

### *1.1. Quantum Dots*



Figure 1.1. Photoluminescence from quantum dot suspensions. Each vial contains a solution of colloidal quantum dots, increasing in size from left to right. (Figure adapted from Antipoff, 2012. CC BY-SA 3.0. Wikimedia Commons).

QDs are semiconductor nanocrystals with size-tunable band gaps, meaning they can absorb or emit light at wavelengths determined by their size. Figure 1.1 shows photoluminescence from QD suspensions in which the constituent QDs are composed of the same crystalline material, but have

different average diameters. The simple relationship between QD size and band gap has motivated interest in their use as building blocks for novel, solution-processable semiconductor materials.

### *1.1.1. A Brief History*

In 1982, A. I. Ekimov and A.A. Onushchenko reported on the first observation of size-dependent exciton absorption energies in 0-dimensional semiconductor islands (*i.e.*, QDs) embedded in a metal oxide matrix.<sup>1,2</sup> In 1988, the first *colloidal* CdSe QD synthesis was reported<sup>3</sup>, followed in 1993 by the first colloidal CdSe QD synthesis using the “hot-injection” method (discussed later in the text).<sup>4</sup> These two CdSe synthesis papers are remarkable because they demonstrated bottom-up fabrication of 0-dimensional nanostructures—rather than the top-down approach of Ekimov and Onushchenko—enabling all the versatility, accessibility, and cost-savings of solution processing over traditional semiconductor processing.

The use of QDs as building blocks rather than isolated entities soon followed (in 1995) with the first demonstration of QD superlattice (SL) self-assembly.<sup>5</sup> This work showed that nearly monodisperse QDs could assemble into 3D super crystals that mimicked structural aspects of atomic solids. These QD SLs were electrically insulating due to the long, insulating QD capping ligands QD that enabled their self-assembly. Another major milestone was the fabrication of electronically coupled QD solids, through which an electrical current could pass.<sup>6,7</sup> Since then, a multitude of QD compositions, sizes and shapes have been prepared and assembled into novel, interesting, and useful QD solids, including QD-based photovoltaic devices.<sup>8</sup> Reported in 2011, metal oxide infilling of QD films (*via* atomic layer deposition) to produce a QD/metal oxide composite represented a completely bottom-up reproduction of Ekimov’s embedded-QD structures.<sup>9</sup>

### 1.1.2. Anatomy of Quantum Dots

QDs are clusters of atoms typically spanning 1–20 nm in all directions. They are often made of II-VI, III-V, or IV-VI semiconductors and can exhibit optical band gaps that range from the far infrared to deep ultraviolet. Monocrystalline (as opposed to polycrystalline) QDs are routinely synthesized. Due to their high surface area and the need for colloidal and charge stabilization, colloidal QDs are capped with ligands. Because the surface area to volume scales as  $1/r$  (where  $r$  is the QD radius) surface atoms make up a significant portion of atoms within the QD. Thus, the surface composition has a massive impact on all properties relevant to QD-based optoelectronic devices. Furthermore, QD stoichiometries are sometimes ill-defined and depend heavily on the synthesis, ligand capping, solvent, and other chemical interactions.

QD shape is dynamic and *a priori* adopts the lowest surface energy configuration.<sup>10</sup> The Wulff construction is the primary approach for describing the shape of a nanoparticle or QD. Control of QD shape can be exerted during synthesis<sup>11,12</sup> or *via* post-hoc chemical treatments.<sup>13</sup> A wide variety of simple and complex shapes have been realized through rational control of precursor reactivity and facet-dependent growth rates.<sup>14</sup>

Added functionality and complexity are attainable through heterostructured QDs.<sup>15</sup> The most common example is the core-shell structure in which differing core and shell materials work synergistically to tune carrier dynamics or some other property of the QD. Some core-shell QDs are optimized to suppress non-radiative recombination and increase photoluminescence quantum yield. In this scenario, the core provides the band gap for radiative recombination of excitons and the shell removes deleterious mid gap states (induced by surface defects and/or ligands) that quench photoluminescence.<sup>16</sup>

### 1.1.3. Electronic Structure of Quantum Dots

The relation between QD size and band gap originates from the quantum confinement effect. Quantum confinement occurs when the QD size is smaller than the exciton Bohr radius, a material property that depends on the QD's electron and hole effective masses and dielectric properties. One consequence of quantum confinement is the discretization of allowed electronic states, akin to those derived for a simple "particle-in-a-box" model. In this way, QDs have electronic structures more like atoms and molecules than bulk semiconductors. The position and spacing of electronic states, and behavior of carriers within the allowed electronic states, depend on structural aspects of the QD besides size, including compositional and interface effects. The energies of quantized states that comprise the electronic structure of a spherical QD are expressed as:

$$E_{n,L} = \frac{\hbar^2 \phi_{n,L}^2}{2m_{e,h} R^2}, \quad (1.1)$$

where  $\phi_{n,L}$  is the  $n^{\text{th}}$  root of the spherical Bessel function of the  $L^{\text{th}}$  order,  $m_{e,h}$  is the effective mass of the electron or hole (for conduction or valence states, respectively),  $R$  is the QD radius, and  $\hbar$  is Planck's constant. The band gap energy  $E_g$  of a spherical QD can be approximated as:

$$E_g = E_{g,0} + \frac{\hbar^2 \pi^2}{2m_{eh} R^2} - \frac{1.8e^2}{\epsilon R}, \quad (1.2)$$

where  $E_{g,0}$  is the bulk band gap,  $m_{eh}$  is the reduced effective mass of electrons and holes. The second term arises from boundary conditions applied by the spherical potential well (*i.e.*, the QD). The third term arises from Coulombic attraction between the electron-hole pair (exciton) and is modulated by the high frequency dielectric constant  $\epsilon_\infty$ . Equations (1.1) and (1.2) reveal that an increase in QD radius  $R$  will reduce the spacing of quantized states and eventually result in a band

gap equal to that of the bulk semiconductor. The above picture is somewhat simplified, and perturbations to the positions and degeneracy of the quantized states depend on interband coupling, crystal field effects, QD shape asymmetry effects, crystal strain and electron-hole exchange effects.<sup>17</sup> For a more comprehensive discussion of the electronic structure of QDs, the reader is referred to Ref. 18.

#### *1.1.4. Optical Properties of Quantum Dots*

QDs exhibit optical band gaps that depend on their composition and size (Figure 1.2), which motivates their use in photoemission applications such as solid state lighting,<sup>19</sup> television displays,<sup>20</sup> security inks,<sup>21</sup> continuous wave lasers,<sup>22</sup> luminescent solar concentrators,<sup>23</sup> medical and biological imaging,<sup>24</sup> single photon emitters,<sup>25</sup> and light-emitting diodes.<sup>26</sup> The emission and absorption properties of QDs are relevant for QD-based device engineering and as diagnostic tools for a variety of QD properties.



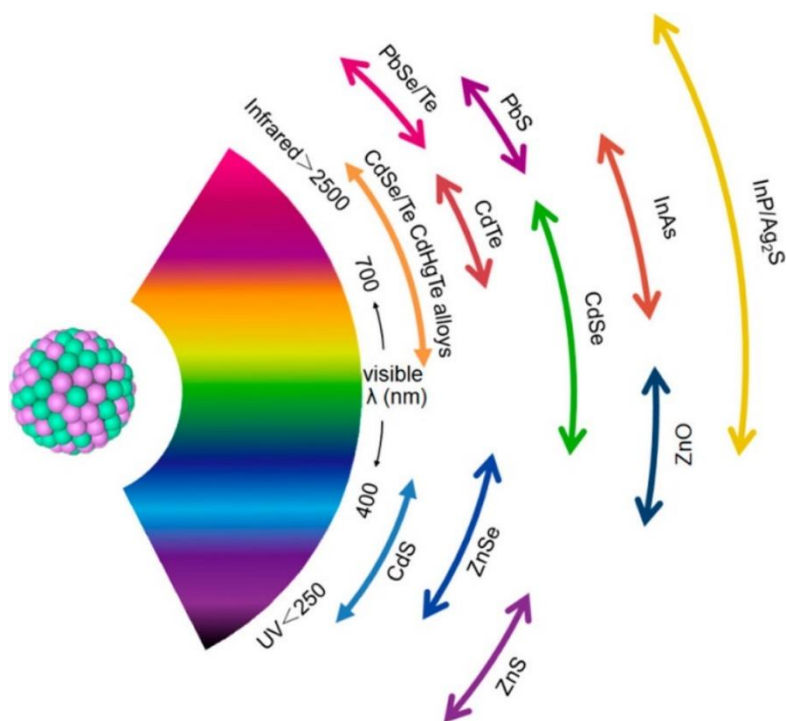


Figure 1.2. Spectral range of different QDs. The range covered by a particular QD composition is tuned with the QD diameter. PbSe QDs inhabit the region from >2500 nm to ~1240 nm. (Reprinted with permission from Ref. <sup>27</sup>. Copyright 2018 American Chemical Society.)

Time- and frequency-dependent photoemission properties provide insight into QD electronic structure and defect states.<sup>28</sup> Photoluminescence quantum yield (PLQY) is an important metric of a fluorophore's efficiency and utility. Ultra-high PLQY (>99%) has been reported in a variety of surface passivated and core-shell QDs.<sup>29</sup> Non-unity PLQY is caused by non-radiative recombination and Auger recombination. QDs can also exhibit intermittent photoluminescence (known as "blinking") that fluctuates with a time scale of seconds and precludes their use in applications requiring steady photoemission. Blinking has been attributed to 1) intermittently populated surface traps that quench hot or band edge carriers through nonradiative recombination; 2) intermittent QD charging (formation of trion) that leads to enhanced Auger recombination.<sup>30,31</sup> Blinking can be suppressed and PLQY can be increased by eliminating surface traps through QD shelling and ligand selection. Photoemission linewidth is another critically important QD metric

and depends on QD inhomogeneity (size, shape) as well as electron-phonon interactions and other thermal effects.<sup>32</sup>

Understanding and control of QD optical absorption properties are important for their practical application and diagnostic purposes. The propagation of light through a QD film/device can be exactly modeled using the complex dielectric response of the film(s).<sup>33</sup> QD shape, size, composition, ligation, and the dielectric properties of the surrounding medium dictate the frequency-dependent absorption spectrum of a QD.<sup>34</sup> Maxwell-Garnett effective medium theory can be used to accurately model the absorption of a dilute solution of QDs.<sup>34</sup> This approach has been used to generate empirical relationships between the concentration and optical absorbance of a “dilute” QD suspension.<sup>35,36</sup> The situation for QD thin films is more complex due to heterogeneity in the dielectric environment surrounding each QD. An appropriate framework for describing the dielectric response of a QD film depends on the local environment of the QDs (*e.g.*, ligand-capped or ligand-free) and the degree of electronic coupling between QDs.<sup>37</sup> Effects like crystal strain can also modulate QD oscillator strengths.<sup>22</sup> Several groups have used spectroscopic ellipsometry to evaluate the dielectric function of QD thin films for device engineering.<sup>33,37,38</sup> Bawendi *et al.* measured the dielectric constant of QD thin films using AC-capacitance measurements<sup>39</sup>, finding an increasing dielectric constant with QD volume fraction and poor agreement with a structure-based effective-medium theory. Poor agreement was attributed to a size-dependent dielectric constant of the individual QDs, which is thought to originate from surface induced effects. There is no unifying *structure-based* model for the dielectric function of a QD thin film, likely due to several important unknowns about their internal structure. While monolayers can be assessed unambiguously, it is more difficult to obtain insight into the internal structure of 3D QD assemblies.<sup>40</sup>

The optical properties of QDs are sensitive to their composition, size, shape, local environment, and interfacial effects; this sensitivity offers tunability but necessitates fine processing control to make QD ensembles with a well-defined optical response.

## ***1.2. PbSe: From Bulk to the Nanoscale***

### *1.2.1. Crystal Structure*

PbSe is a crystalline semiconductor that adopts the cubic rocksalt structure ( $a = 6.12 \text{ \AA}$ ). Figure 1.3 shows the PbSe unit cell (Figure 1.3a) and coordination polyhedra of Se (Figure 1.3b). Se adopts an FCC lattice, with Pb forming an FCC sub-lattice offset by  $(a/2, 0, 0)$ . Each element is octahedrally coordinated by the other. Figure 1.3 shows the edge-sharing Se coordination octahedra. PbSe QDs are circumscribed by  $\{100\}$ ,  $\{110\}$  and  $\{111\}$  facets. Single layer slices of these planes are shown in Figure 1.3c-e. The  $\{100\}$  and  $\{110\}$  facets are stoichiometric, whereas  $\{111\}$  consist of alternating planes of Se and Pb (Figure 1.3f).

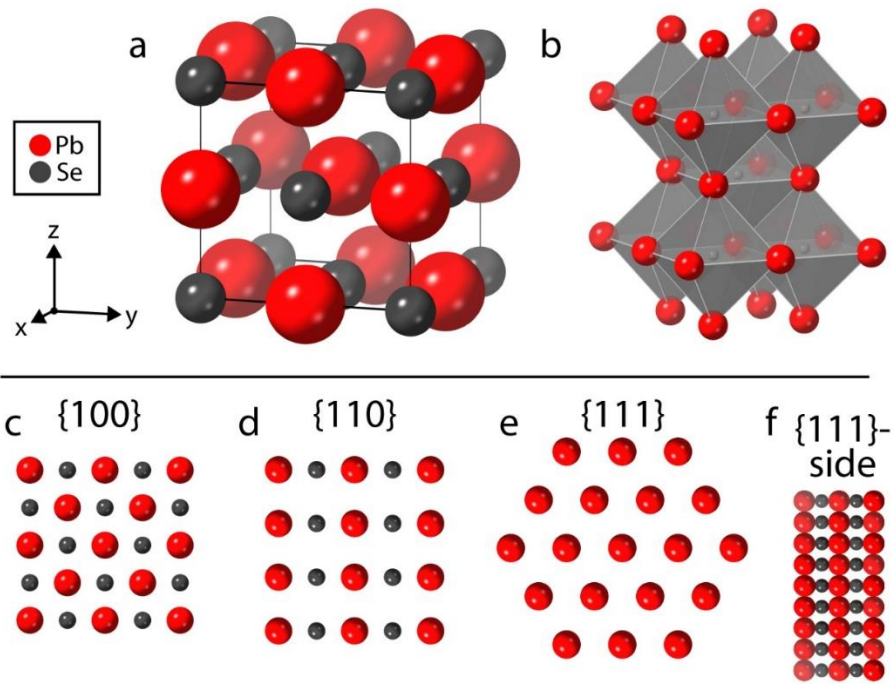


Figure 1.3. Structure of PbSe. a) Complete unit cell of rock salt PbSe, b) Polyhedral depiction showing the six-fold octahedral coordination of Pb to Se, c) Stoichiometric  $\{100\}$  surface of PbSe, d) Stoichiometric  $\{110\}$  surface of PbSe, e)  $\{111\}$  surface of PbSe which consists of alternating layers of Pb and Se atoms, e) Side-view of the  $\{111\}$  surface of PbSe, highlighting the alternating layers of Pb and Se.

### 1.2.2. Electronic Structure

Pb is an  $s^2p^2$  column-IV element, yet it behaves like a pseudo-divalent  $p^2$  atom because of the high atomic number of Pb leading to localization of the valence 6s orbital.<sup>41</sup> Thus, PbSe (along with PbS and PbTe) are considered quasi-II-VI semiconductors. Figure 1.4 shows the calculated band diagram of bulk PbSe, with valence band maxima annotated by red circles. The band gaps of Pb-chalcogenides are direct and occur at the L-point of the Brillouin zone, whereas traditional II-VI semiconductors have theirs at the  $\Gamma$ -point. This distinction leads to important differences in the electronic properties and photophysics of Pb-chalcogenides and II-VI compounds (*e.g.*, CdSe, ZnSe), such as differences in state degeneracy of the VBM and CBM.

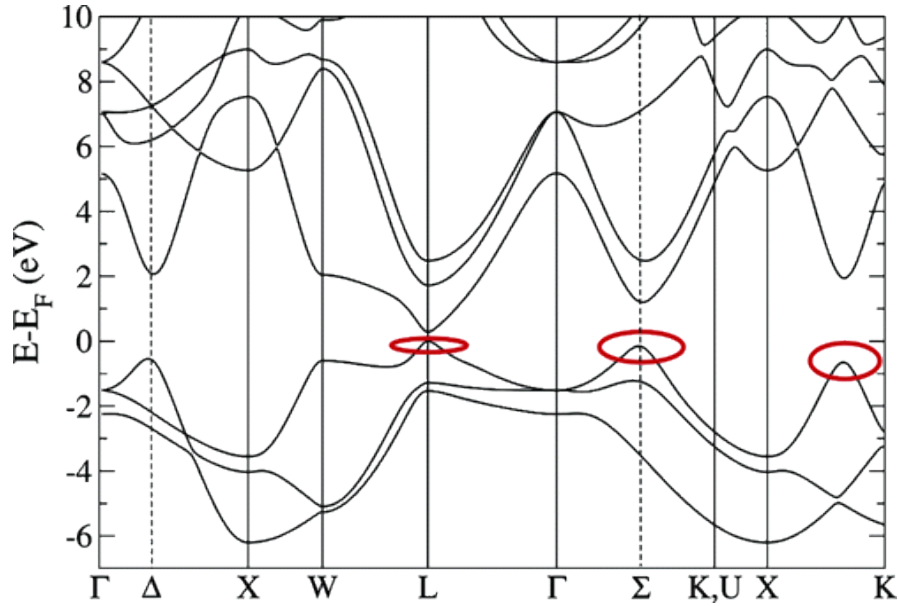


Figure 1.4. Band diagram of bulk PbSe. Calculated by the empirical pseudopotential method. The bulk band gap occurs at the L-point as is annotated in the graph. Reprinted with permission from Ref. 41. Copyright 2006 American Chemical Society.

PbSe has small electron and hole effective masses ( $< 0.1m_0$ ) and a static dielectric constant  $\epsilon_r$  of  $\sim 250$  (high frequency dielectric constant  $\epsilon_\infty = 23$ ). Together, these lead to a Bohr exciton radius of  $\sim 46$  nm, as given by:

$$a_0 = \frac{\epsilon_r \epsilon_0 \hbar^2}{e^2 \mu} \quad (1.3)$$

A large exciton radius leads to strong quantum confinement at synthetically accessible QD sizes, a sparse density of states, and band gap tunability from 0.28 eV up to  $\sim 1.1$  eV (see Equation (1.2)). PbSe QDs are therefore an excellent material platform for investigating QDs in the strong-confinement limit. The relationship between optical band gap and QD size varies roughly with  $1/d$  and was determined empirically by Moreels *et al.*<sup>36</sup>

$$E_0(d) = 0.278 + \frac{1}{0.016d^2 + 0.209d + 0.45} \quad (1.4)$$

They also determined the molar extinction coefficient at 3.1 eV, which is far enough above the band gap that the absorptivity is size independent:

$$\epsilon_{3.1eV} = (0.0277 \pm 0.005)d^3 [cm^{-1}\mu M^{-1}] \quad (1.5)$$

These two formulae are often used to spectroscopically determine the average QD size and molar concentration of a PbSe QD suspension.

Colloidal PbSe QDs often suffer from poor PLQY, which decreases with increasing QD size.<sup>42–44</sup> Sub-3 nm oleate-capped PbSe QDs can exhibit >50% PLQY, whereas larger QDs are often closer to 1%. This trend has been attributed to a dependence on the QD band gap, which leads to differences in non-radiative relaxation into trap states and ligand vibrational modes.<sup>43</sup> Surface chemistry also plays a pivotal role and will be discussed more later in the text.<sup>28,45,46</sup>

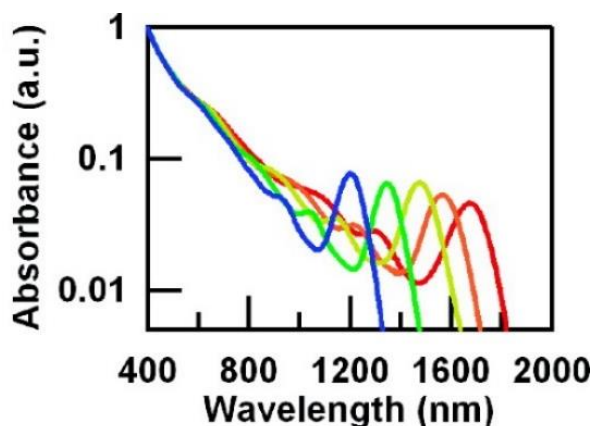


Figure 1.5. Optical spectra of PbSe QDs. Different colors represent different average QD sizes. Reprinted with permission from Ref 36. Copyright 2007 American Chemical Society.

Figure 1.5 shows a series of absorption spectra from suspensions of PbSe QDs. The first low-energy peak is the  $1S_h-1S_e$  transition, the second is the  $1P_h-1P_e$  transition, and the third is the  $1D_h-$

1D<sub>e</sub>.<sup>41,47,48</sup> At high enough energy, the manifold of electronic states becomes semi-continuous and the spectrum becomes bulk-like.

After a QD absorbs a photon of some energy, excited electrons and holes undergo a variety of relaxation pathways. Quantum confinement in QDs enhances carrier-carrier interactions and leads to transition (relaxation) rates that differ from their bulk counterpart. One exciting and useful difference in PbSe QDs is the prominence of carrier multiplication (CM).

### *1.2.3. Carrier Multiplication*

PbSe QDs show promise for boosting photovoltaic power conversion efficiencies through CM, which is the generation of multiple electron-hole pairs from a single high energy photon.<sup>49</sup> Generation of two excitons from a single photon of energy twice that of the band gap enables a theoretical solar cell efficiency of 42%, compared to 33% for a traditional single-junction semiconductor PV.<sup>50</sup> For solar cells that exploit CM, the ideal band gap is reduced from 1.34 eV to 0.7 eV, which is nearly ideal for PbSe QDs.<sup>51</sup> The photon energy onset for CM is lower in QDs than bulk semiconductors due to relaxed momentum conservation constraints in dispersion-less (*i.e.*, no E vs k relation) QDs and occurs at  $\sim 3E_g$  in PbSe.<sup>49</sup> The cooling rates and pathways of hot-carriers and multi-excitons ultimately determine the efficiency of CM and *free* multiple carrier generation in PbSe QDs and have been studied in detail.<sup>33,51–54</sup>

PbSe has a unique electronic structure that enables strong quantum confinement in experimentally accessible QD sizes. Enhanced CM efficiency in PbSe QDs theoretically boosts photovoltaic efficiency above the Shockley-Queisser limit.

### 1.3. Quantum Dot Synthesis

QDs are typically synthesized in non-aqueous, high boiling point solvents at temperatures between 100 to 350 °C. The synthetic protocols are designed to exploit thermodynamic and kinetic aspects of particle nucleation and growth in order to produce monodisperse and colloidally stable particles. There are two primary solution-phase QD synthetic approaches: the “hot-injection method” and the “heat up method”. Both methods can be approximately described by the LaMer particle growth model (see Figure 1.6) developed in 1950.<sup>55,56</sup> Key to this particle growth model is the temporal separation of particle nucleation and growth steps. The basic concept is as follows: the concentration of monomers (molecular building blocks of the QD) in a solution is increased until the solution becomes supersaturated and a “burst of nucleation” occurs, followed by sub-supersaturation conditions that allow dynamic growth of the freshly produced QD nuclei. In zone 1 of the LaMer model, the monomer concentration increases, eventually reaching a supersaturation limit where crystal embryos consisting of  $n$  monomers homogeneously nucleate (*i.e.*, precipitate). The free monomer concentration is thus reduced below the supersaturation point, and nucleation is quenched. In zone 3, monomers join with the previously nucleated  $n$ -mers (heterogeneous growth) to form larger colloids, until eventually the monomer concentration approaches equilibrium. In 1990s, the pioneering work of LaMer and Dinegar inspired development of a hot-injection CdSe QD synthesis protocol by Murray, Norris and Bawendi.<sup>4</sup> The concept of “burst nucleation” was applied by rapidly mixing metal and chalcogenide precursors such that the Cd and Se monomer concentrations increased above the supersaturation threshold, resulting in homogeneous nucleation, then heterogeneous growth of CdSe nanocrystals. This basic approach has been adopted and modified for synthesis of several compound semiconductor QDs (and nanocrystals, more generally).



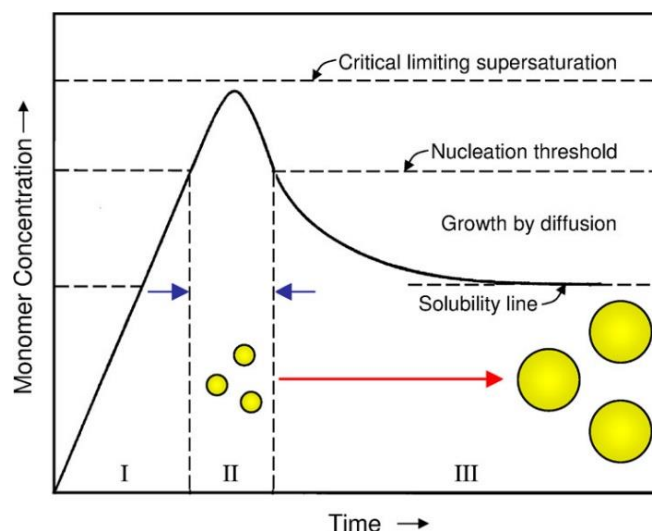


Figure 1.6. Schematic of LaMer growth model. Reprinted with permission from Ref <sup>56</sup>. Copyright 2013 American Chemical Society.

Supersaturation of the reaction solution results in precipitation of crystal nuclei. For any set of reaction conditions, there is some critical nuclei size above which the crystal embryo can begin to grow and below which the nuclei will dissolve back into monomers. This size-dependent solubility is described by the Thomson-Gibbs relation and arises because of curvature-induced surface tension.<sup>57</sup> The critical nucleus radius  $r_c$  is the radius at which the surface free energy equals that of the crystal volume free energy, and can be expressed as:

$$r_c = -\frac{2\gamma}{\Delta G_v} = \frac{2\gamma V_m}{RT \ln(S)}, \quad (1.6)$$

where  $\gamma$  is the surface energy per unit area of the QD,  $\Delta G_v$  is the change in free energy required to form a unit volume of the QD crystal from monomers,  $V_m$  is the molar volume of the QD crystal, and  $S$  is the ratio of monomer concentration to the saturation concentration. The hot-injection method works by quickly and significantly increasing  $S$ , thereby lowering the critical nuclei radius

needed to sustain particle growth. The growth rate of a QD, including monomer diffusion, reaction rate kinetics and Thomson-Gibbs dissolution effects is expressed:

$$\frac{dr}{dt} = V_m D C_b \left( \frac{S(t) - e^{\frac{2\gamma V_m}{rRT}}}{r + \frac{D}{k} e^{\alpha \frac{2\gamma V_m}{rRT}}} \right) \quad (1.7)$$

where  $S(t) = \frac{C_\infty}{C_b}$  is the supersaturation of monomers in solution,  $k$  is the rate constant for precipitation in the limit  $r \rightarrow \infty$ , and  $\alpha$  is a transfer coefficient for precipitation. A comprehensive derivation can be found in Ref. 58. Ref 59 provides useful insights into the impact of each variable in Equation (1.7) on the overall particle growth rate and resultant polydispersity.

### 1.3.1. PbSe Quantum Dot Synthesis

In 2001, the initial synthesis of colloidal PbSe QDs was reported by Murray *et al.*<sup>60</sup> They used a hot-injection approach that starts with the formation of a solution of lead oleate, using lead acetate and oleic acid as precursors. The formation of lead oleate occurs at temperatures  $> 60$  °C via coordination to Pb by two oleate molecules. This reaction results in the formation of acetic acid as a byproduct. Oleic acid—a commonly used carboxylate binding ligand—enables good solubility in non-polar solvents and prevents QD aggregation. With the lead oleate solution at elevated temperature (180 °C), they injected technical grade (90%) n-trioctylphosphine selenide (TOPSe) to first nucleate, then grow the oleate-capped PbSe QDs. A schematic depicting modern hot-injection syntheses of PbSe QDs is shown in Figure 1.7.

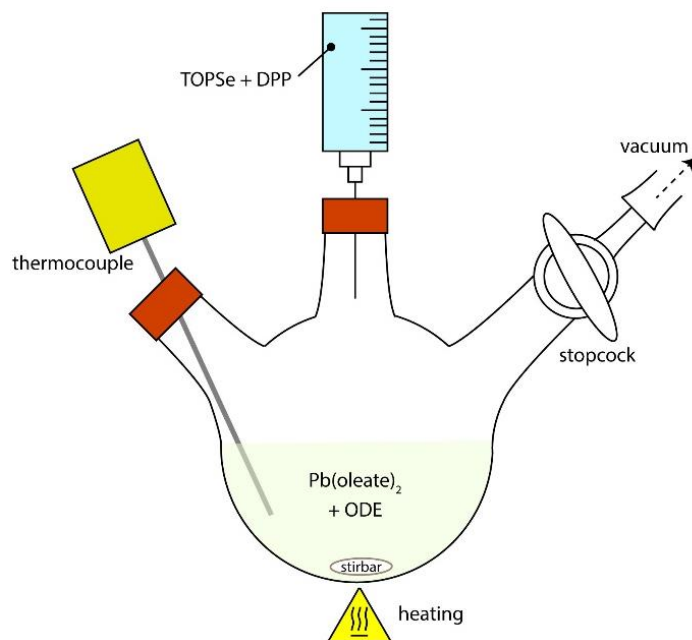


Figure 1.7. Schematic of a hot-injection QD synthesis. A solution of  $\text{Pb(oleate)}_2$  in 1-octadecene (ODE) is formed via heating under dynamic vacuum. The solution temperature is measured via thermocouple and heated using a heating mantle. A solution of TOPSe and DPP is injected at 180 °C to initiate growth of PbSe QDs.

Several important insights and modifications have been made since this initial synthesis protocol, but major elements remain in use today. Some modern syntheses use PbO instead of Pb acetate—leading to the formation of water rather than acetic acid as a reaction byproduct—as residual acetic acid was found to disturb QD growth.<sup>61</sup> More environmentally benign reaction solvents such as 1-octadecene have replaced ethers.

Two major efforts revealed several unexpected and important insights about the mechanism by which precursors convert into QD nuclei. TOPSe was originally thought to react directly with  $\text{Pb(oleate)}_2$  to form the PbSe monomeric unit, as is the case in CdSe synthesis. However, it was shown that pure TOPSe, when mixed with  $\text{Pb(oleate)}_2$  at typical reaction temperature, fails to nucleate QDs.<sup>62</sup> Secondary phosphines—a known impurity in technical grade TOP—were shown to be essential for nucleation of PbSe QDs. Thus, the addition of sub-stoichiometric amounts of

secondary phosphines was implemented to increase QD yields and improve batch-to-batch reproducibility that was lacking as a result of variations in TOP impurities. The general reaction scheme for PbSe QD nucleation is presented in Figure 1.8.

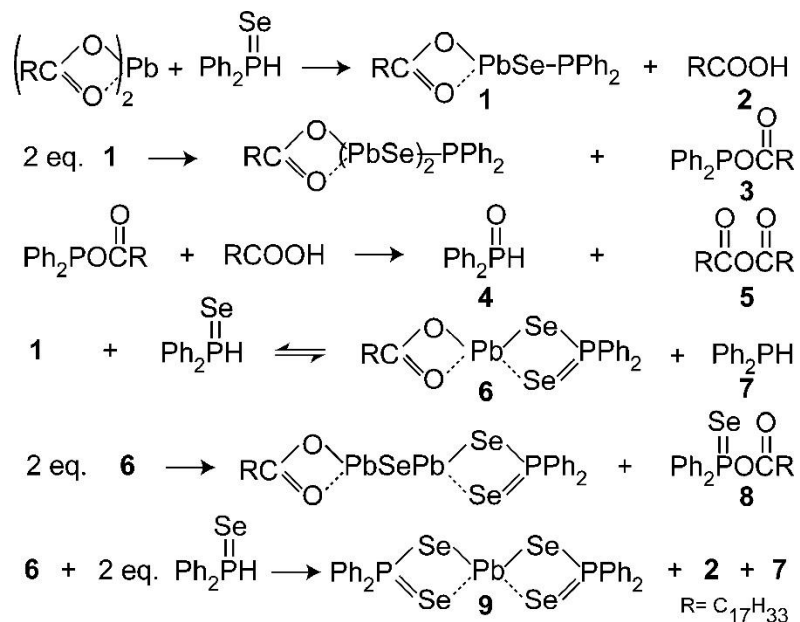


Figure 1.8. Proposed mechanism of PbSe monomer formation. Beginning with complexation of diphenylphosphine selenide and lead oleate, eventually resulting in PbSe monomer formation. (Reprinted with permission from Ref 10. Copyright 2010 American Chemical Society.)

The critical role of diphenylphosphine selenide (DPPSe) is to displace oleate from Pb(oleate)<sub>2</sub>, thereby forming an initial PbSe unit (1 in Figure 1.8). DPP is not consumed in this reaction scheme and will once again convert into DPPSe by reacting with the large excess of TOPSe. It is important to note that these experiments were done below 200 °C and that different mechanisms may be operative at higher temperatures. For example, TOPSe was found to thermally decompose at 250 °C, generating reactive H<sub>2</sub>Se, another potential Se source for monomer nucleation.<sup>63</sup> It is not clear whether this can occur at the temperatures used in most PbSe syntheses (<210 °C). The exact PbSe monomer species (as it is described in LaMer-type growth) is still not clear.<sup>64</sup>

Several limitations of the hot-injection approach prohibit simple scale-up, including reagent mixing times, reaction cooling times, impracticality of the required injection solution volume, and batch-to-batch reproducibility. Reaction flask underpressure,<sup>65</sup> increased precursor concentrations,<sup>66</sup> novel precursors,<sup>67</sup> and more sophisticated injection methods have been explored as means of improving the quality of large-scale hot-injection syntheses.

The “heat-up method” circumvents kinetic limitations of the hot-injection approach and offers a scalable and controllable route for the synthesis of large, uniform batches of QDs. In this approach, heat is used to drive the formation of monomers until supersaturation and QD nucleation occurs. Because supersaturation, nucleation, and growth are driven by chemical reactivity of precursors rather than simple mixing of reagents, the selection of precursors is critical. Owens *et al.* developed a library of selenourea precursors with tailored reactivities to generate monodisperse PbSe QDs of various sizes using the heat-up method.<sup>68</sup> An excellent review of heat-up synthesis can be found in Ref. 69. There are several examples of PbSe QD synthesis using the heat-up method.<sup>64,68</sup> Cation exchange synthesis have garnered interest in recent years as a means of producing PbSe QDs with novel heterostructures, air-stability, and the ability to exploit advantages of other QD syntheses.<sup>70–</sup>

72

The hot-injection protocol used for making PbSe QDs has not changed significantly since its development. In the intervening years, researchers have developed mechanistic insights and clarified the role of various reagents used in the synthesis.

#### ***1.4. Quantum Dot Self-Assembly***

QD solids (*e.g.*, 2D and 3D QD assemblies) are the foundation of QD-based solid-state optoelectronic devices and are formed during colloidal destabilization of QDs induced by solvent

evaporation, ligand stripping/exchange, or anti-solvent mixing. Through controlled destabilization of low polydispersity QDs, ordered QD superlattice (SL) structures can be formed. We first discuss the mechanics of QD self-assembly: namely, free energy constraints that dictate the morphology of a QD solid, followed by some kinetic aspects of self-assembly.

#### *1.4.1. Quantum Dot Superlattices*

The structure of a QD SL is determined by a complex interplay of QD size, shape, ligand coverage, solvent effects, and deposition methodology. QDs do not behave solely as prototypical hard or soft objects, but instead exist at some intermediate point determined by details of the QD/ligand structure. Thus, QD SLs inhabit a rich phase space.<sup>73</sup> We start first with a conceptual understanding of self-assembly of prototypical hard spheres and polyhedra, then incorporate effects from ligands.

Non-interacting hard spheres and polyhedra adopt close-packed structures that maximize their volumetric density. Spheres adopt fcc and hcp lattices, which have the highest volume filling fraction (0.74). The impetus for close packing arises from entropic driving forces. As the density of a solution of spheres slowly increases (for instance, through solvent evaporation) there is a critical density at which the translational and rotational entropy of each sphere is increased—at the cost of configurational entropy—by maximizing the volume available to each sphere.<sup>74</sup> Thus, at a certain density, the free energy of the system splits, resulting in a lower energy ordered state and higher energy disordered state.

However, QDs are not *truly* spherical and instead adopt an energy minimizing Wulff polyhedron.<sup>75</sup> Maximum entropy SL structures have been determined for many types of hard polyhedra.<sup>76</sup> Orientational alignment of hard polyhedra (particularly those with large, flat facets)

emerges as a result of entropy maximization and directional entropy forces.<sup>76-78</sup> In other words, there is an entropy-induced pseudo-force that directs orientational registry of neighboring QDs. Thus, the effective QD shape provides a design template for specific QD SL structures.

QDs have ligand coronas that may account for a substantial portion of their overall volume. Thus, QDs do not behave as ideal hard polyhedra, leading to adoption of non-close packed structures.<sup>79</sup> This deviation from close-packing has been rationalized on the basis of SL internal area minimization. In this case, internal area refers to the overall surface area of the Wigner-Seitz (W-S) cell (*i.e.*, Voronoi decomposition) of each lattice site within the SL. The W-S cell is the fundamental domain occupied by a QD and is constructed from points in space that are closer to a particular lattice point than to any other. The more spherical the W-S cell, the lower the internal surface area and the more uniformly ligands can fill the interstitial space.<sup>79</sup> The bcc structure has a more spherical Voronoi cell than the fcc structure. Thus, the bcc structure is entropically favorable for packing of soft spheres. As the ratio of ligand length to QD radius increases, QD assembly is dictated to an increasing extent by ligand-ligand interactions rather than the hard cores.<sup>80</sup> Additional deviations from a hard-sphere model include ligand-ligand and QD-QD van der Waals interactions, facet-dependent ligand coverage, and solvent-ligand interactions.<sup>73,81</sup>

The use of small ligands (*e.g.*, SCN<sup>-</sup>) rather than sterically bulky ligands leads to glassy (*i.e.*, order-free) QD solids upon destabilization because attractive van der Waals attractive forces between QD cores dominate, leading to premature QD aggregation. In other words, QDs with short ligands “stick” to one another and therefore cannot sample enough sites to achieve the entropically favored SL structure. To achieve weak pairwise attraction, even in the limit of low solvent concentration (high QD concentration), long, sterically bulky ligands are nearly a requirement.

#### 1.4.2. Quantum Dot Film Fabrication

While there are numerous approaches for QD film formation, dip-, spin-, and drop-casting are most common. Layer-by-layer dip-coating results in densely packed amorphous QD films, but requires a ligand exchange between sequential QD depositions to insolubilize the QDs.<sup>8</sup> Spin-coating of oleate-capped QDs produces films with good short-range order and tunable thickness. Ligand exchange of spin-cast films with short ligands leads to significant nanoscale tearing and amorphization. SL unit cell volume contraction that occurs upon ligand exchange cannot be accommodated by the solid substrate, which provides a significant friction force that prevents smooth QD motion. In contrast to the rapid solvent evaporation and substrate-induced pinning typical of dip- and spin-coating processes, drop-casting onto a liquid surface (such as ethylene glycol) and using long solvent evaporation times results in highly ordered oleate-capped superlattice films. The spatial order of these films is better than spin-cast films because of longer solvent evaporation times and weaker QD/solvent-substrate interactions that disrupt self-assembly. An exciting and useful aspect of this liquid-interfacial assembly is the ability to perform an *in-situ* ligand exchange.<sup>82</sup>

**This *in-situ* approach is vital for preparation of epitaxially-fused superlattices.** Injection of a chemical trigger or ligand into the liquid sub-phase leads to intercalation and the exchange/removal of ligands bound to the QD surface. Most importantly, the liquid surface accommodates SL volume contraction and therefore the formation of closely-packed or epi-SLs without significant cracking or amorphization. The formation pathway and chemical evolution of QD SL films fabricated on a liquid surface are a primary focus of this work.



In the limit of slow solvent removal, QDs will adopt their energy-minimized structure, which varies depending on QD shape, ligation, and solvent. Self-assembly and ligand exchange on a liquid surface is the premier approach for fabrication high-quality epi-SLs.

### ***1.5. Quantum Dot Surface Chemistry***

QDs have a large surface area to volume ratio and so their interfaces play a dramatic role in shaping their optical, chemical, and electronic properties. Variable surface termination (*i.e.*, faceting), dynamic surface reconstruction, and highly tunable ligand chemistry lead to differences in doping, electronic state energies, charge carrier dynamics, solvent solubility, and self-assembly phenomena.<sup>1</sup> Particle facets have facet-specific surface energies, stoichiometries, growth/dissolution rates, binding affinities for ligands, and localized electronic states. These facet-specific properties can be exploited to grow anisotropic particles with exotic shapes,<sup>11,12</sup> control oriented attachment between QDs,<sup>83</sup> tune ligand coverage density,<sup>75</sup> and alter carrier dynamics.<sup>84</sup> The reconstruction and atomic-scale details of QD surfaces can also lead to changes in QD optical and electronic properties, although insights into these effects are relatively limited.

Besides QD composition and shape, ligand chemistry (or surface termination, more broadly) is the most significant determinant of the behavior of QD solids. Ligand chemistry can be programmed during QD synthesis and altered thereafter via “ligand exchange”. A ligand has two primary regions: the head group, which binds to the QD surface, and the tail group, which interacts with the solvent or other ligands on adjacent particles. The head group can be ionic (*i.e.* a carboxylate anion) or neutral with lone pairs of electrons available for bonding to metal ions on the QD surface. Using the terminology of Green’s bonding classification method, these are X-type and L-type ligands, respectively. In both cases, electron-deficient metal ions at the QD surface

bind with nucleophilic ligand head groups.<sup>85</sup> To maintain charge neutrality, QDs with X-type ligands (anions) are typically metal-rich (excess cations), whereas L-type ligands lead to more stoichiometric QDs. The use of a third type of “Z-type” neutral ligand—for example, a metal cation bound to halide or chalcogenide anions—has been demonstrated in a variety of QD systems. Small, adventitious anions such as OH<sup>-</sup> or Cl<sup>-</sup> have been observed on QD surfaces and may result from byproducts formed during QD synthesis or environmental/solvent contaminants.<sup>86</sup> The head group has been shown to affect QD energy levels and charge carrier dynamics, such as photoluminescence quantum yield.<sup>45</sup> The tail group often determines the solubility and stability of QD colloids in solution. Commonly used ligands include oleylamine and oleic acid, which offer solubility in nonpolar solvents. Long-chain hydrocarbon ligands such as oleic acid interact through weak Van der Waals interactions and are sterically bulky, both of which serve to prevent QD agglomeration.

### *1.5.1. PbSe Quantum Dot Surface Chemistry*

The ligand composition of as-synthesized oleate-capped PbSe QDs (*via* the Murray method or a slight modification<sup>60</sup>) has been characterized in detail using nuclear magnetic resonance (NMR) and infrared spectroscopy, among other techniques (see review article, Ref 85). Oleic acid is the primary native ligand and binds as oleate (RCOO<sup>-</sup>) to surface Pb.<sup>75,87</sup> Oleate is anionic and therefore necessitates a Pb-rich surface to preserve overall charge neutrality. The amount of oleate on the surface has been quantified<sup>87</sup>, the distribution across different facets has been calculated<sup>75</sup> using density functional theory, and different binding modes have been identified.<sup>13</sup> The binding affinity of oleate to different PbSe facets increases as  $E_{\{100\}} < E_{\{110\}} < E_{\{111\}}$ , a trend that has important implications for facet-dependent ligand coverage, QD shape, QD surface reactivity, and QD-QD oriented attachment.<sup>75</sup> The facet-dependent binding strength of oleate decreases with

increasing coverage due to steric repulsion effects, leading to sub-maximal oleate packing densities (based on the density of allowable surface Pb). For example, PbSe {111} facets have a Pb area density of  $6.16 \text{ nm}^{-2}$ , which is higher than the maximum lateral density of  $4.0\text{-}4.6 \text{ nm}^{-2}$  for pure, semi-crystalline oleic acid.<sup>88</sup> Thus, one would expect dangling bonds and other surface sites that are highly reactive but inaccessible to complete passivation by oleate.

Co-adsorbates passivate these hard-to-reach surface sites and can have a significant impact on the photophysics and chemical reactivity of PbSe QDs. Yet, their identity and relative abundance are challenging to quantify. Synthesis reactants/byproducts, ambient contaminants (*e.g.*, water or oxygen), and halides have been found to co-adsorb with oleate on PbSe QDs. Selenium bound *n*-trioctylphosphine and diphenylphosphine—both reactants in modern PbSe QD syntheses—have been observed *via* NMR and were shown to impact PbSe QD photophysics.<sup>46</sup> It has been suggested that small adventitious anions such as  $\text{OH}^-$  co-adsorb to the surface to provide QD charge neutrality, however they are challenging to observe and quantify.<sup>86</sup> Perhaps the most serious and omnipresent co-adsorbate on PbSe QDs is oxygen. The optical properties of oleate-capped PbSe QDs are immediately affected upon exposure to air, yet reversible if the air exposure is brief.<sup>89</sup> This reversibility is attributed to physisorption of  $\text{O}_2$ . Longer air exposure generates numerous surface oxidation products, eventually resulting in destruction of the PbSe QD.<sup>89</sup> Several ligand co-passivation strategies have been used to increase ligand coverage, prevent oxidation, and bind surface sites inaccessible to bulky oleate. Halides in particular have shown utility in binding and chemically stabilizing the QD surface, leading to enhanced air stability, improved photoemission and charge transport behavior.<sup>64,88,90–92</sup>

Chemicals used during purification can also influence QD surface chemistry.<sup>93</sup> QDs are typically separated from reaction byproducts through sequential rounds of precipitation and resuspension

using a solvent/anti-solvent mixture. For example, ethanol can be added to an octadecene-based QD reaction mixture to precipitate the QDs, allowing the solvent and reaction byproducts to be separated. Combinations of hexane and ethanol/methanol are commonly used in further purification steps. However, the Hens group found that alcohols can protonate and strip oleate from the QD surface, thereby reducing the colloidal stability of the particles and quenching PL.<sup>94</sup> Stripping of oleate also impacts QD self-assembly. Despite alcohols being extremely weak acids, the large excess used to precipitate the QDs—in combination with metastable QD surfaces and a subset of weakly bound oleate molecules—enable exchange of oleate for the alcohol. The use of acetonitrile as the anti-solvent eliminates oleate stripping.<sup>94</sup>

### 1.5.2. Ligand Exchange

It is often useful to replace the oleate ligands with new ligands that have different functionality. The new ligands can modify charge carrier properties of a QD or QD ensemble, including relaxation dynamics, doping, and charge transport.<sup>95</sup> Here we focus primarily on ligand exchange intended to decrease inter-QD distances as a means of increasing electronic coupling (more on this later).

Ligand exchange can either be performed on QDs in suspension<sup>96-99</sup> or after a QD film is cast on solid substrate (termed “solid-state exchange”). A modification of the latter approach involves ligand exchange of a floating QD film on a liquid surface. This technique is referred to as *in-situ* exchange.

Solution-phase ligand exchange is *a priori* more homogenous and complete than solid-state exchange but has the tendency to colloiddally de-stabilize the QDs, resulting in aggregation. QDs

exchanged with a variety of short, inorganic ligands<sup>97</sup> and functionalized cinnamate ligands<sup>96</sup> are two examples of solution-phase Pb(S,Se) QD ligand exchange.

Solid state ligand exchange is the most used approach and can be applied on films deposited by layer-by-layer dip coating, spin coating, drop casting and doctor-blading. Thick films can be generated by sequential rounds of deposition and exchange, with each ligand exchange step insolubilizing the QDs to their native solvent (*e.g.*, octane).

*In-situ* exchange is the least common approach and is used in the work described here.<sup>82</sup> A dried, floating QD film can be chemically modified (*i.e.*, ligand exchanged) through introduction of additives into the sub-phase upon which the film sits. This ligand can penetrate the floating film and proceed to exchange with the native oleate ligands. Details of film wetting, ligand diffusion through the QD film, and the QD film/sub-phase interface are not well understood. Some recent work from the Hanrath group discusses dynamics of PbSe QD self-assembly at the liquid interface.<sup>100</sup>

### 1.5.3. Relation Between Surface Chemistry and QD Doping

QD surface composition is a significant determinant of QD doping. Stoichiometric control of PbSe QDs can lead to quantitative shifts in majority carrier concentration and type.<sup>101</sup> Excess Pb and Se generate electron-rich and hole-rich free carrier populations, respectively.<sup>102,103</sup> This observation can be mapped onto early studies of Pb- and Se-rich bulk PbSe films.<sup>104</sup> Treatment of PbSe QDs with halides (Cl, Br, I) leads to n-type doping.<sup>105</sup> Hydrazine leads to n-type doping, whereas other amines lead to mixed p- and n-type doping.<sup>106,107</sup> Oxygen exposure leads to unipolar p-type behavior and high conductivity.<sup>9</sup> Thiols and thiocyanate lead primarily to p-type conductivity, which has been rationalized in the context of increasing the surface anion

(chalcogenide) concentration. Several papers have demonstrated that ligand dipoles lead to shifts in PbS QD band positions of up to  $\sim 2$  eV.<sup>96,108</sup> In general, the doping effect of a certain ligand is determined empirically, although some universal frameworks have been developed.<sup>101</sup>

#### 1.5.4. Matrix Engineering with Atomic Layer Deposition

QD solids are porous and often metastable. Law *et al.* first demonstrated atomic layer deposition (ALD) as an effective method for stabilizing and “solidifying” QD solids.<sup>9</sup> ALD is a layer-by-layer chemical vapor deposition technique uniquely suited to uniformly coating high aspect ratio, nanoscale structures and nanoscopic void spaces in 3D solids.<sup>109</sup> Wide band gap metal oxides such as alumina ( $\text{Al}_2\text{O}_3$ ) and zinc oxide are examples of commonly used ALD materials. Low-temperature ALD processing is achievable using reactive precursors such as trimethyl aluminum, making the process amenable to thermally unstable QDs.<sup>110</sup> Researchers have extended the concept of gas-phase ALD to *colloidal*-ALD, which relies on solution phase chemistry to grow protective shells around QDs.<sup>111,112</sup>

ALD infilling and overcoating prevents oxidation of QD solids and enhances their photothermal stability.<sup>113</sup> Pb-chalcogenide QDs are highly sensitive to oxidation and can sinter at temperatures less than 100 °C. ALD infilling with alumina enables short and long term environmental/thermal stability.

ALD infilling impacts charge transport, photophysics and optical properties of QDs.<sup>51,114,115</sup> For one, ALD can alter QD surface chemistry, which in turn leads to changes in the density, energy, and dynamics of surface charge traps.<sup>51,114,116</sup> Infilling with ALD also changes the dielectric environment of the QDs. This can lead to changes in the charging energy of QDs and doping efficiency of surface dopants.<sup>117</sup> Changing the dielectric constant of the pore network is expected

to impact the effective dielectric constant of the QD film as well as the oscillator strengths of QD optical transitions.<sup>34</sup>

QD surface chemistry is a major determinant of carrier dynamics, transport, and doping.

### ***1.6. Charge Transport in QD Solids***

The use of QD active layers in photovoltaics, photodetectors, LEDs, and other optoelectronic devices requires efficient charge transport.<sup>95</sup> QDs capped with long aliphatic ligands like oleate generate insulating films with low carrier mobilities and so ligand removal or exchange with short ligands is needed to electronically couple QDs and form conductive QD solids.

There are three primary types of charge transport possible in QD solids. Hopping transport—the most common QD charge transport mechanism—dominates in the limit of relatively weak inter-QD coupling and a high degree of energetic disorder.<sup>118</sup> Delocalized (*i.e.*, metallic) transport is a more efficient charge transport mechanism and dominates in disordered QD solids with strong inter-QD coupling and relatively low energetic disorder.<sup>119,120</sup> Finally, mini-band transport, which is predicted to emerge in QD SLs with strong inter-QD coupling and exceptionally low energetic disorder.<sup>121–123</sup> Mini-band transport has not yet been experimentally demonstrated in colloidal QD solids.

#### ***1.6.1. Hopping Transport***

Phonon-assisted tunneling is a sequential electron tunneling process between unequal energy states, such as those of  $1S_e$  states in neighboring QDs of slightly different size. Charge transport in the phonon-assisted tunneling regime is commonly described using the Miller-Abrahams (M-

A) expression for the hopping rate  $\Gamma_{ij}$  between discrete electronic states of neighboring QDs  $i$  and  $j$ :<sup>118,124</sup>

$$\Gamma_{ij} = \Gamma_0 \exp(-\beta d) \begin{cases} \exp\left(-\frac{E_j - E_i}{kT}\right) & (E_j > E_i) \\ 1 & (E_j \leq E_i) \end{cases} \quad (1.8)$$

$\Gamma_0$  is an attempt frequency,  $d$  is the width of the tunneling barrier, and  $E_j$  and  $E_i$  are the energies of the initial and final states, respectively.  $\beta = 2\sqrt{2mV_B/\hbar^2}$  and represents the attenuation of the wavefunction across a tunneling barrier of height  $V_B$  with a local effective mass  $m$ . The second exponential term is included when the final state is of higher energy because this transition is thermally activated and therefore slower than an energetically downhill transition. Relevant material properties of the QD (such as Bohr radii of electrons and holes) are included in the  $\Gamma_0$  pre-factor. Some have incorporated a  $T^{-1}$  dependence when calculating mobility, because Einstein's diffusion equation contains such a term (in 3D):<sup>125</sup>

$$\mu = \frac{ed^2}{6\Gamma kT} \quad (1.9)$$

Here we can see that the carrier mobility is directly proportional to the electron hopping rate. In the limit of insufficient thermal energy for charge hopping between QDs with different site energies, variable-range hopping (VRH) dominates. VRH is a process whereby charges tunnel between non-neighboring QDs that have more similar site energies (*i.e.*, where  $E_j - E_i < kT$ ).<sup>126</sup>

One limitation of the simple M-A model is that it does not incorporate a “reorganization energy” that is explicitly included in the Marcus model of polaronic hopping.<sup>125,127,128</sup> In the context of carrier hopping, reorganization energy refers to an energy penalty induced by electron-phonon



coupling during an electron tunneling event. One significant difference between the Miller-Abrahams and polaronic hopping models is the difference in temperature dependence. In the polaronic hopping picture it is possible for the mobility to *decrease* as the temperature increases.<sup>128</sup>

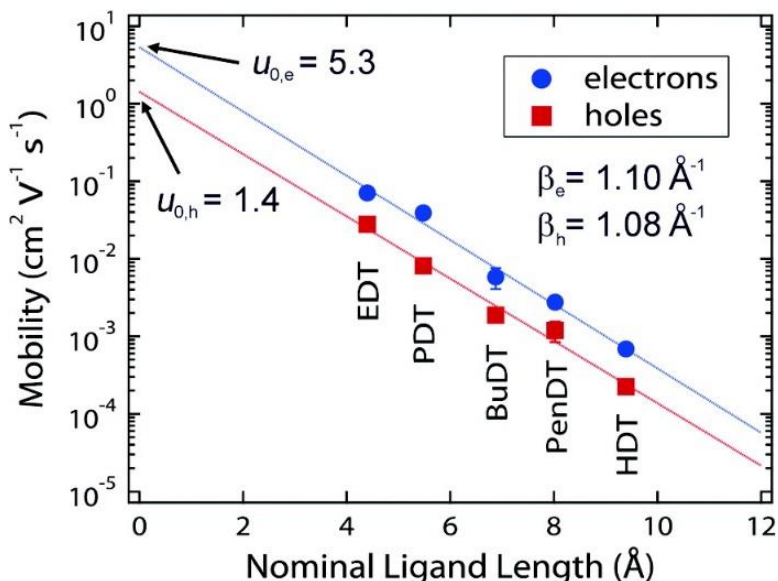


Figure 1.9. Carrier mobility in PbSe QD solids with different ligands. Dependence on ligand length of electron and hole mobilities in PbSe QD thin films treated with bidentate alkythiol ligands. Reprinted with permission From Ref 118. Copyright 2010 American Chemical Society.

Figure 1.9 presents seminal work by Law *et al.* which shows that room-temperature electron mobility in films of alkanedithiol-capped PbSe QDs is inversely proportional to the ligand length, in excellent agreement with Equation (1.8).<sup>118</sup> These results highlight that the M-A model can effectively capture the behavior of QD solids in the “weak coupling limit” where hopping transport dominates. To further increase mobilities (beyond 5 cm²/Vs) in PbSe QD films,  $d$  was further decreased by using S<sup>2-</sup>, and HS<sup>-</sup> as ligands.<sup>114,129</sup> Decreasing  $\beta$  is another approach used to increase carrier mobilities in QD solids, and has been achieved using molecules with conjugated pi bond systems coupled to head groups that can bind to surface Pb.<sup>130–132</sup>

While transport in weakly-coupled QD films is well captured by nearest-neighbor or variable-range hopping models (within the Miller Abrahams framework), there is serious debate about transport mechanisms in films with mobilities greater than  $1 \text{ cm}^2/\text{Vs}$ .<sup>125</sup> Recently, electron mobilities of  $\sim 24 \text{ cm}^2/\text{Vs}$  have been reported in 2D PbSe epi-SLs.<sup>133</sup>

### 1.6.2. Band-like Charge Transport

First, some clarity on the definition of “band-like transport”, a term that has been used widely in QD literature. Phenomenologically, band-like transport refers to delocalization of carriers (*i.e.*, metallic charge transport) across multiple QDs. However, the term “band-like transport” has been used primarily to describe the observation of electron or hole mobility that decreases with increasing temperature ( $\delta\mu/\delta T < 0$ ). While this temperature-dependence has been taken as a signature of carrier delocalization, there are other possible explanations (such as the previously-discussed polaronic hopping model). We further distinguish here between “band-like” transport and “mini-band” transport, where the latter requires periodicity in the QD lattice (*i.e.*, a superlattice) to generate a band dispersion. For clarity, I will use the term “band-like transport” for transport that has decreasing mobility with increasing temperature. The term “delocalization” is used to discuss the phenomenon of carrier delocalization across multiple QDs. Several relevant perspectives discussing delocalized transport in QD solids are available in the literature.<sup>95,125,134,135</sup>

There is a growing body of literature in which the authors have demonstrated band-like transport in QD solids (*i.e.*,  $\delta\mu/\delta T < 0$ ),<sup>119,120,136–138</sup> but skepticism persists over whether this is truly due to carrier delocalization.<sup>119,120,125,127</sup> There are several alternative explanations for this observation, including polaronic hopping,<sup>127</sup> changes in QD packing with temperature,<sup>139</sup> or interfacial effects.<sup>137</sup> Researchers also cite a mobility beyond the hopping limit as proof of carrier

delocalization.<sup>95</sup> However, there is weak consensus on that upper limit.<sup>119</sup> Another consideration for systems exhibiting band-like transport is whether the QD structure is so perturbed (for example, through annealing) that the film is closer to a bulk semiconductor rather than a QD solid. It is therefore unclear how one might provide conclusive evidence for carrier delocalization in QD solids, although it has been done for 1-D epitaxial superlattices.<sup>140–142</sup>

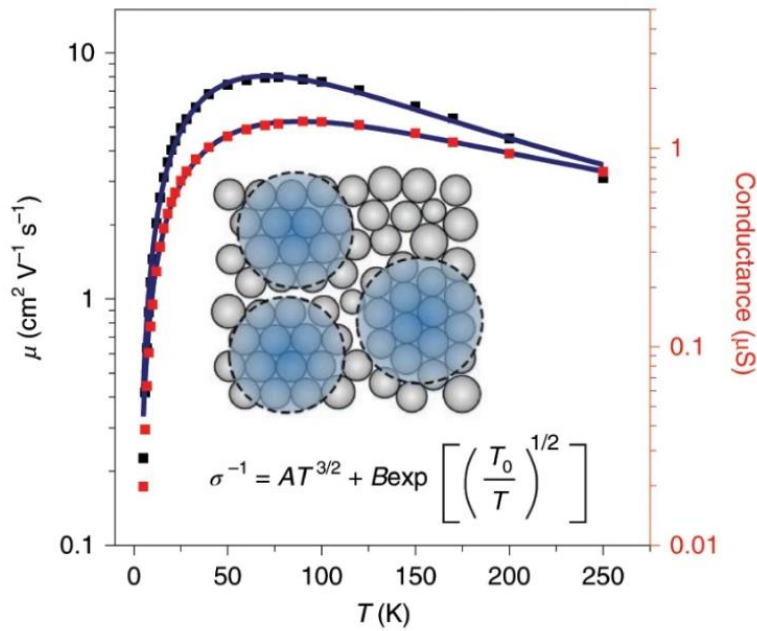


Figure 1.10. Temperature-dependent mobility of disordered HgTe QD films. These data were fitted with a mixed hopping and diffusive (band-like) transport model. Reprinted with permission from Springer Nature, Nature Materials. Ref 119, Copyright 2020.

We now turn to a recent report of band-like transport *and* carrier delocalization in QD solids by the groups of Guyot-Sionnest and Talapin. This paper provides insight into contemporary understanding of charge transport in highly-coupled, random-packed QD thin films.<sup>119</sup> Figure 1.10 shows temperature-dependent mobilities extracted from FET measurements of HgTe QD films. Of note is the mobility approaching 10 cm<sup>2</sup>/Vs and the region with  $\delta\mu/\delta T < 0$ . The inset in Figure 1.10 is a schematic diagram of their proposed transport model. This model consists of

delocalization of carriers within small clusters of QDs, with hopping in between those clusters. To correctly fit the mobility data, they invoked a heterogeneous conductor model with components of delocalized ( $\sigma^{-1} \propto AT^{3/2}$ ) and Efros-Shklovskii VRH ( $\sigma^{-1} \propto B \exp \left[ \left( \frac{T_0}{T} \right)^{\frac{1}{2}} \right]$ ) transport. The former term originates from the classic model of impurity scattering in bulk semiconductors.

Others have explored an insulator-to-metal transition (IMT) through controlled doping and sintering of ZnO and Si nanocrystals.<sup>135,143</sup> These authors predict that an IMT occurs at  $n_c \rho \cong 0.3$  in films of touching (*i.e.*, connected) nanocrystals with facet overlap area of  $\rho$  and free carrier concentration  $n_c$ . The authors show a close approach to the IMT, but are apparently unable to dope the films to a sufficient degree to cross the threshold. The fact that these films require extremely high doping densities renders them less-than-useful for most applications requiring light absorption by the nanocrystal or QD layer.

At the present time there is no definitive understanding of charge transport in relatively high mobility ( $\mu > 1 \text{ cm}^2/\text{Vs}$ ) QD solids. The picture is even less clear when discussing the emergence of mini-band transport.

### 1.6.3. Mini-band Transport

Mini-band transport is a form of delocalized charge transport occurring in dispersive bands that are formed through strong electronic coupling and spatial ordering of constituent elements of a 1-3D periodic potential (in this case, QDs). Arrangement of QDs into a 3D lattice results in a periodically varying potential that acts on conduction electrons and holes to create a Brillouin zone and miniature energy bands (*i.e.*, mini-bands) that are superimposed on the electronic states of the individual QDs.<sup>122,144</sup> Theorists have shown that minibands can form in ideal QD SLs composed

of a variety of semiconductor QDs, including PbSe.<sup>121,123,145–147</sup> The mini-band energy width can be approximated using a tight-binding model and is directly proportional to the strength of electronic coupling between QDs. As the mini-band width increases, the curvature necessarily increases, which leads to a decrease in the effective mass of charge carriers:

$$m_{QDSL}^* = \frac{\hbar^2}{\left(\frac{d^2E}{dk^2}\right)} \quad (1.10)$$

The mobility of carriers in a QD SL miniband is inversely proportional to their effective mass:

$$\mu = \frac{e\tau}{m_{QDSL}^*}, \quad (1.11)$$

where  $\tau$  is the mean-free scattering time and  $e$  is the fundamental charge constant. Thus, the emergence of mini-bands in strongly coupled QD SLs is expected to significantly boost carrier mobilities up to and above  $100 \text{ cm}^2/\text{Vs}$ .<sup>99,100,123</sup>

Balandin *et al.* and Green *et al.* calculated the band structures of InAs and Si QD SLs, demonstrating the effects of dot size, interdot distances, barrier height, and dielectric effective mass on band structure.<sup>121,145</sup> This simple theoretical model serves as a starting point for investigating the electronic structure of QD SLs. Green and Balandin showed that smaller interdot distances and barrier heights led to wider band dispersions with more curvature, smaller effective masses, and higher mobility.

Signatures of mini-band transport such as Bloch oscillations<sup>140–142</sup> and negative differential conductivity<sup>149,150</sup> have been observed in QD superlattices grown *via* molecular beam epitaxy. QD SLs made from *colloidal* QDs have not yet demonstrated unambiguous mini-band transport.<sup>146</sup>

Energetic disorder that localizes carriers (*i.e.*, reduces their mean-free scattering times) and leads to inhomogeneity in the QD SL energy landscape appear to prevent miniband formation.<sup>147</sup>

PbSe QDs are perhaps the best candidate (among common QDs) for making QD SLs that exhibit mini-band transport.<sup>147</sup> From a practical standpoint, there are synthetic methods for making low-polydispersity PbSe QD suspensions which are stable and well understood. From a materials standpoint, their degenerate 1S state, large exciton Bohr radius, and low bulk effective mass (see Section 1.1.4) are expected to generate very large miniband widths and high mobilities.<sup>147</sup> To our knowledge, however, there are no reports of band-like transport in PbSe QD films (superlattice or otherwise). Epitaxially-fused QD SLs composed of PbSe QDs show promise for mini-band transport because they combine excellent spatial order with strong electronic coupling necessary for mini-band formation.

### ***1.7. Epitaxially-fused Quantum Dot Superlattices***

Epitaxially-fused superlattices (epi-SLs) are spatially ordered QD films with atomically coherent bridges that connect neighboring QDs. They can be either 2D (one QD thick) or multi-layered. Epi-SLs are typically assembled on a liquid surface (*e.g.*, ethylene glycol) in a two-step process. First, a parent SL is formed on the liquid surface through controlled evaporation of a carrier solvent. QDs in this parent SL have a ligand capping layer (such as oleate) that facilitates self-assembly and prevents premature QD fusion. Next, a trigger (usually a chemical, but sometimes heat) is introduced to the system that causes desorption or exchange of oleate. By removing oleate, the QDs can interact more strongly, leading to a decrease in the inter-QD distance, rotational alignment of the QDs, and eventually epitaxial fusion.

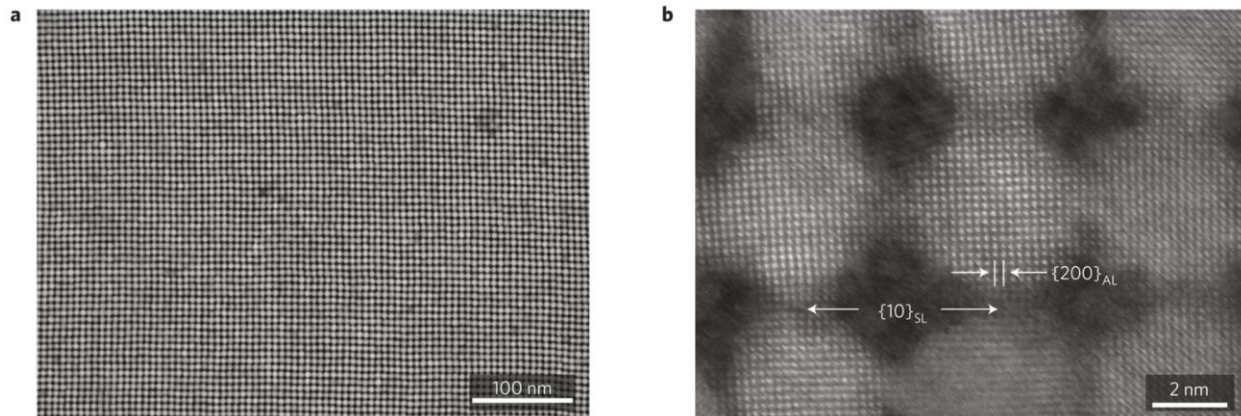


Figure 1.11. 2D epitaxially-fused PbSe QD superlattices. a,b) Annular dark-field scanning transmission electron microscopy shows superlattice structure (a) and atomic structure (b). Reprinted with permission from Springer Nature, Nature Materials. From Ref 146. Copyright 2016.

Epi-SLs are commonly formed from oleate-capped PbSe QDs. Figure 1.11 shows transmission electron microscope of 2D PbSe QD epi-SLs from the Hanrath group that were among the first reported.<sup>i</sup> Previously (in 2013), the Van Maekelbergh group demonstrated the assembly of PbSe QDs into 2D sheets with honeycomb and square symmetry.<sup>152</sup> Inspiration for epi-SLs comes from the concept of oriented attachment, which describes the attachment of two discrete crystallites that are oriented in such a way to form a single crystallite that is free of crystal defects.<sup>83,153</sup> To better understand the formation and properties of epi-SLs, we start with a brief discussion of oriented attachment.

### 1.7.1. Oriented Attachment

Oriented attachment describes a crystal growth mechanism whereby crystallites coalesce to form larger crystals. In the moments leading up to crystallite attachment, short-range forces cause alignment of the crystal lattices, resulting in formation of a new, defect-free crystal. This work was

<sup>i</sup> Surprisingly, the first report of PbSe QD synthesis appears to show (Figure 1, Ref 151) unintentional formation of an epi-SL, which to my knowledge has not been noted in any publication.

pioneered by Banfield and De Yoreo (among others) in the late 1990s and is an area of active research.<sup>83,154–156</sup>

Initial insight into oriented attachment of PbSe QDs was provided by Murray *et al.* in 2005.<sup>157</sup> Their method differs significantly from the one described in this thesis, but their results are illuminating. They prepared PbSe nanowires with a variety of morphologies by altering reaction conditions of the hot-injection synthesis. They found that all nanowires spontaneously grow along  $\langle 100 \rangle$ , which was attributed to dipole moments induced by non-equivalent {111} facet termination (Pb or Se). Assuming a binarized Pb or Se termination of {111}, they calculated the dipole moment for all permutations of {111} faceting, with the restriction that the overall QD stoichiometry is held at 1:1. While it is now established that PbSe QDs capped with oleate are non-stoichiometric, some truth may still apply to Murray's dipole argument.<sup>36</sup> They also showed that pairwise attachment of two QDs is likely the rate-limiting step, as only monomers or long nanowires were observed ex-situ.

In 2013, the Hanrath group showed that small 1 or 2D assemblies of “confined-but-connected” PbSe QDs could be formed through careful ligand deprotection of oleate-capped QDs deposited on a solid substrate. It was noted that the degree of epitaxial fusion (epi-fusion) was dictated by the type and concentration of ligand/reagent to which they exposed the QDs. This work was the precursor (no pun intended) for their 2016 Nature Materials report (see Figure 1.11).

### 1.7.2. Structural Analysis of epi-SLs

The structure and assembly of epi-SLs has been studied using a variety of X-ray scattering/diffraction and electron imaging techniques.<sup>40,146,158–170</sup> Most of the work has focused on 2D epi-SLs, in part because the synthesis and analysis of 3D epi-SLs is more technically



challenging. The most common epi-SL consists of PbSe QDs arranged in a distorted cubic lattice with epitaxial fusion along {100} crystal facets.

Some researchers have investigated epi-SL assembly using *in-situ* methods. Van Maekelbergh and coworkers performed in-situ X-ray scattering experiments that showed the gradual conversion of an oleate-capped SL into the epi-SL.<sup>164</sup> They found that as the QD carrier solvent (toluene) evaporates, QDs assemble into a hexagonal 2D SL rotator phase. As this hexagonal phase sits on a subphase liquid (ethylene glycol), ligands desorb and the QDs begin to align, their spacing decreases, the SL symmetry converts from hexagonal to square, and eventually the QDs fuse together. Schreiber *et al.* also investigated the assembly of epi-SLs using X-ray scattering methods.<sup>168</sup>

Several techniques have been used to evaluate the SL structure of epi-SLs—in particular, researchers have focused on understanding and quantifying various forms of structural disorder. Understanding structural disorder in epi-SLs is important because disorder obstructs mini-band formation. Hanrath and coworkers analyzed the connectivity and neck width of 2D epi-SLs, finding an average neck width of 2.9 nm (using ~6.5 nm PbSe QDs) and a standard deviation of 0.68 nm, which is approximately 1 unit cell of PbSe. Neck width is an important determinant of coupling strength in these systems. Therefore, it follows that variation in neck width leads to spatial variations in coupling strength and results in more energetic disorder within the system.<sup>123,135,146,171</sup> The propagation of translational disorder in 2D and 3D epi-SLs has been evaluated using a paracrystal framework.<sup>158</sup> In particular, researchers found that missing bonds between neighboring QDs leads to significant translational SL disorder. These findings show that all forms of structural disorder are inter-related: misalignment of QDs leads to loss of connectivity (necking), which in turn leads to propagating translational disorder.

Rotational misalignment of QDs within the epi-SL generates atomic lattice defects (dislocations) and has been studied using electron microscopy and X-ray diffraction.<sup>133,159,172</sup> These insights have prompted discussion of design principles for making more perfect epi-SLs.<sup>173</sup> Edge or screw dislocations<sup>174,175</sup> can act as scattering centers for charge carriers and so eliminating them should improve charge transport properties. To eliminate these QD rotational misalignments and dislocations, researchers have begun exploring thermal annealing treatments, although there are ongoing concerns about over-sintering of the QDs.<sup>160,172</sup> It seems that gentle heating can indeed anneal out various structural imperfections within 2D epi-SLs.

Another critical aspect of epi-SL assembly is the role of the chemical trigger. Most groups rely upon amines (particularly, ethylenediamine) injected into the subphase to initiate conversion from the parent SL to the epi-SL, although others have used mild heating to achieve similar results.<sup>167</sup> Researchers have produced basic insight into the relationship between the chemical trigger and structural properties (such as neck width and SL unit cell) of the epi-SL.<sup>40,133,152,176</sup> Some have used post-hoc treatments of the epi-SL to try and modify neck widths/distributions.<sup>177</sup>

Some of the work in this thesis focuses on aspects of epi-SL formation and structural disorder (translational and rotational) in the epi-SL. Whereas other groups focus primarily on 2D epi-SLs, we have chosen to work with 3D films because they offer greater potential for integration in optoelectronic devices. We have published four papers on the assembly and structure of epi-SLs or “confined-but-connected” QD solids.<sup>169,170,178,179</sup> Much of this work is described in this thesis.

### *1.7.3. Electronic Properties of Epi-SLs*

Strong electronic coupling in highly-uniform epi-SLs is predicted to generate high carrier mobilities through mini-band transport<sup>122,146,180</sup> and the emergence of exotic electronic structures

including topological states and Dirac cones.<sup>123</sup> The electronic coupling between epitaxially connected QDs is expected to be much higher than QDs with ligands between them, as one would predict using a tight-binding model. One outstanding question is whether strong enough coupling can be produced while retaining the tunable band gap of the QD building blocks.

Researchers have studied various aspects of charge transport in epi-SLs. Non-contact AC measurements of charge transport in highly-fused epi-SLs showed electron mobilities up to 260  $\text{cm}^2/\text{Vs}$ , although DC transport measurements showed mobilities of  $\sim 13 \text{ cm}^2/\text{Vs}$ .<sup>181</sup> The disparity in these mobility values arises from the distance that carriers travel during the time of the measurement—for AC measurements the carriers only sample a few nanometers, whereas for DC measurements the carriers must transit a  $\sim 1 \mu\text{m}$  long film. Researchers commonly study charge transport using gated (either solid dielectric or electrolytic gating) DC measurements, such as field-effect transistors (FETs). Seminal work by the Hanrath group used variable-temperature FET measurements to show that carrier transport through 2D epi-SLs (see Figure 1.11) occurs through hopping, rather than mini-band transport.<sup>146</sup> They used band structure calculations to evaluate the impact of several sources of structural disorder, including neck width variation and QD size disorder. These calculations showed that improved structural order is a pre-requisite for mini-band formation. More recent FET measurements on 2D epi-SLs with electrolytic gating show carrier mobilities as high as 18 and 24  $\text{cm}^2/\text{Vs}$ , a remarkable number that is difficult to attribute to hopping conduction (see Section 1.6).<sup>133,182</sup> The mechanism of charge transport in these systems is an active area of research, and efforts to understand carrier mobility as a function of state-filling are underway.<sup>119</sup>

Understanding the dielectric properties of epi-SLs is also of interest for next-generation epi-SL-based optoelectronic. The dielectric constant of epitaxially-fused SLs has been calculated and

shows deviation (towards the dielectric constant of the QD) from Maxwell-Garnet theory when the center-to-center distance of QDs is less than the nominal QD diameter.<sup>171</sup> This should increase absorptivity of the epi-SL, making thinner films viable for solar absorbing devices. Highly-fused epi-SLs have been shown to exhibit optical features reminiscent of 2D PbSe sheets.<sup>165</sup> State-filling measurements have been performed using electrolytic gating—these measurements give insight into the electronic structure and occupation of states within the epi-SL.<sup>119,182</sup>

Ultimately, the question for researchers to answer is whether epi-SLs can exhibit high carrier mobilities and reasonably low carrier densities while preserving the optical band gap of the constituent QDs. The work in this thesis is aimed at helping to answer this question. Strong coupling and excellent spatial order in epi-SLs should lead to mini-band formation, delocalized charge transport, and carrier mobilities as high as  $100 \text{ cm}^2/\text{Vs}$ , a 10-100-fold increase over current state-of-the-art QD films. At their best, epitaxially-fused superlattices represent a platform for inexpensive “materials-by-design” with readily tunable band gap energies and high-performance charge transport. While the tunability is already attainable, significant improvements in charge transport remain elusive. There are several practical challenges to fabricating high quality epi-SLs that exhibit mini-bands and highly efficient charge transport.

### ***1.8. Overview of Work***

The work in this thesis focuses on the study and development of epi-SLs, with an overarching goal of achieving enhanced charge transport through the emergence of mini-bands. We reasoned that a thorough understanding of epi-SL structuro-chemical formation (starting from individual colloidal QDs) should enable us to make epi-SLs with a sufficient degree of structural and chemical perfection to exhibit mini-band transport.

We answer several important questions about epi-SLs. We show that high-quality 3D epi-SLs are synthetically accessible, and provide unprecedented insight into their three dimensional structures. Through these studies, we discover the full transformation pathway from colloidal QDs to 3D films of epitaxially-fused QDs. We also elucidate how the QD surface composition changes throughout this process, and the chemical mechanisms that drive structural transformations. We use these structuro-chemical insights to solve a practical synthetic challenge, and design a new methodology for epi-SL fabrication. Finally, we make electronic devices from individual epi-SL grains and provide basic results from variable-temperature electronic measurements. While there are tantalizing signatures of delocalized carrier transport, it is difficult to say whether that is the dominant charge transport mechanism in state-of-the-art epi-SLs.

The following chapter describes key structural and chemical changes that occur during epi-SL formation. We demonstrate the synthesis of 3D epi-SLs with controlled thickness, then use a powerful combination of analytical techniques to determine the surface chemistry and structure of the epi-SL. We use these insights to determine the complete structural and chemical epi-SL formation pathway. Electronic and optical studies show that these nascent 3D epi-SLs are highly doped but have reasonable charge transport properties.

In Chapter 3 we demonstrate the concept and realization of light-initiated epi-SLs formation. In this schema, UV light activates photoreactive chemicals which proceed to trigger epi-SL formation. Our findings should enable more sophisticated epi-SL fabrication and patterning methods, easier scale-up, and higher quality films.

Chapter 4 focuses on the study of intrinsic charge transport phenomena in epi-SLs. We introduce a novel microfabrication process that allows for deterministic integration of individual epi-SL

grains into micron-scale transistors or other optoelectronic devices. Variable-temperature field-effect transistor measurements show that charge transport occurs through a process that, while difficult to rationalize using a thermally-activated hopping model, is not conclusively attributable to mini-band transport.

## CHAPTER 2

### EPITAXIALLY-FUSED QUANTUM DOT SUPERLATTICES

A grand challenge in mesoscience is to achieve the delocalization of electronic wavefunctions and formation of bulk-like electronic bands (“mini-bands”) in assemblies of nanoscale building blocks. Colloidal semiconductor quantum dots (QDs) are well-defined, novel, and versatile building blocks whose interactions in self-assembled solids are highly tunable, making QD solids an exciting playground for mesoscale science.<sup>73</sup> Theoretical calculations predict that mini-band formation in highly-ordered, highly-coupled QD superlattices (crystals of QDs) can boost charge carrier mobility and diffusion length,<sup>121,122,146,147</sup> which might enable a new class of designer QD solids that combines bulk-like electronic performance with the unique photophysics and solution processability of colloidal QDs. However, the relatively high energetic and spatial disorder of all colloidal QD solids studied to date has inhibited the emergence of new collective mesoscale behavior, resulting instead in weakly-coupled QD films with unremarkable properties.<sup>95,114,125,146,181</sup>

Several groups have recently pioneered the fabrication of highly-ordered PbX (X = S, Se) QD superlattices in which the QDs are epitaxially interconnected to form porous single crystals.<sup>152,176</sup> Typically made by self-assembly on a liquid surface,<sup>82,183</sup> these “confined-but-connected” epitaxially-fused QD SLs (epi-SLs) feature exceptional coupling and spatial order and are promising systems for mini-band formation. Most reports have focused on 2D epi-SLs (QD monolayers) due to their anticipated exotic band structures and relatively simple fabrication and characterization.<sup>40,100,133,146,159,160,163–165,167,172,176,181,184</sup> 3D epi-SLs have received much less

attention.<sup>158,163,176,185</sup> Transport measurements of 2D epi-SLs show that multiple sources of disorder (such as variations in the number, width, and atomic perfection of epitaxial connections) prevent significant carrier delocalization despite strong inter-QD coupling.<sup>133,146,181,182</sup> To provide a basis for rationally improving the spatial and energetic order of epi-SLs, it is essential to establish the mechanism(s) by which epi-SLs form. Researchers have studied the formation of 2D epi-SLs by in situ X-ray scattering<sup>163,164</sup> and presented a conceptual formation mechanism for 3D epi-SLs,<sup>163</sup> but a basic structuro-chemical understanding of the phase transition is far from complete, particularly for 3D films.

Here, we establish the formation mechanism of a 3D PbSe QD epi-SL based on a thorough understanding of the structures of the parent and product phases. We show that the epi-SL forms from a rhombohedrally-distorted body-centered cubic unit cell in which each QD is surrounded by six nearest neighbors rotationally aligned with cofacial {100} facets. The phase transition occurs by nearly-pure translational motion of the QDs ( $10^\circ$  rotation), followed by epitaxial fusion of their {100} facets in three dimensions. This phase transition combines collective 3D epitaxy with atomic topotaxy, meaning that the atomic lattices of the two SLs have a specific 3D crystallographic relationship.<sup>186</sup> Formation of the epi-SL is a collective topotactic transformation of an entire ensemble of crystals ( $10^3$ - $10^5$  QDs per SL grain).

This content in this chapter encompasses two years of study on the synthesis and characterization of 3D epi-SLs. The ultimate goal of this work was to make epi-SLs with sufficient structural order to elicit mini-band formation. Towards achieving this goal, we performed myriad experiments across several technical disciplines to understand how epi-SLs are formed, and the variables that control their structure, surface chemistry, and optoelectronic behavior. Further studies on electronic properties of epi-SLs are provided in subsequent chapters. The work here is—by its



nature—interdisciplinary, drawing on aspects of synthetic, physical, and surface chemistry, materials science, solid-state physics, electronics, thermodynamics, and fluid dynamics.

We begin by describing the composition, shape, and ligand coverage of the quantum dot building blocks used to make epi-SLs. Next, we present the QD self-assembly process and various structural and chemical aspects of the parent SL phase (a SL precursor to the epi-SL). We determine the SL unit cells for the parent and epi-SL structures. The chemical mechanism that facilitates epi-SL formation is discussed and placed into context with previous studies. Next, we detail the complete SL unit cells of parent and epi-SL phases, determined using a dual-space approach. We discuss the impact of ligand coverage and QD faceting on the parent SL and epi-SL structures. From the complete SL unit cells, we deduce the epi-SL transformation pathway and determine that it is the first known example of collective topo-epitaxy. The effects of alumina infilling of the epi-SL using atomic layer deposition on optical and electronic properties are then presented and discussed. We finish by summarizing our findings and highlighting possibilities for future work.

### ***2.1. Quantum Dot Building Blocks***

PbSe quantum dots (QDs) were used as building blocks for the superlattices studied in this work. To better understand self-assembly and ensemble properties of these superlattices, we first investigated the size, shape, and surface composition of PbSe QDs. Oleate-capped colloidal PbSe QDs have a ~20 year history, so their properties—and methods for characterizing them—are relatively well understood.<sup>60</sup>

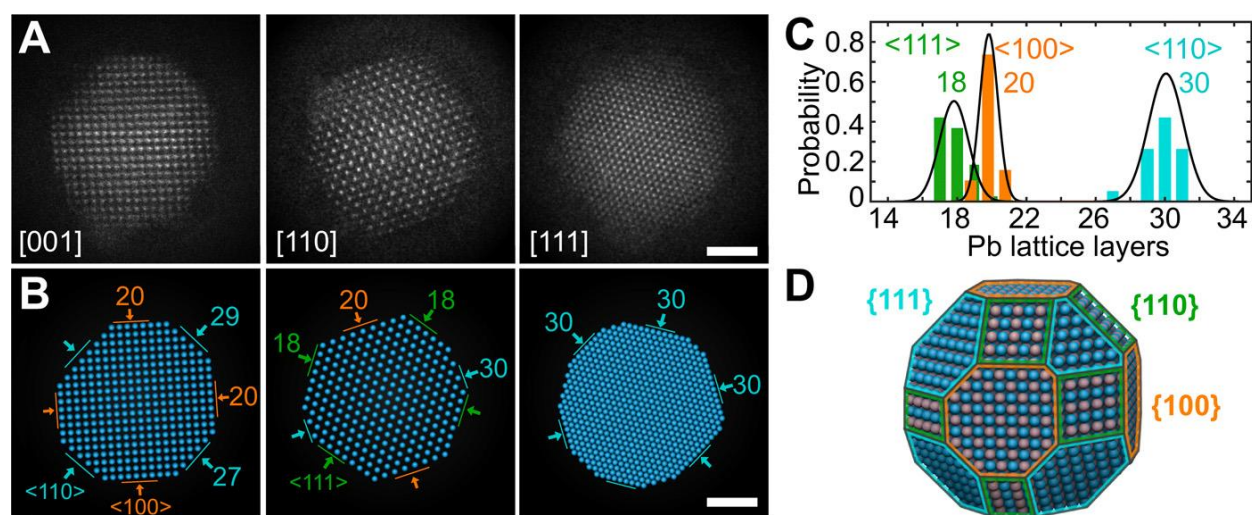


Figure 2.1. HAADF-STEM single-particle reconstruction of PbSe QDs. a) HAADF-STEM images of three different nanocrystals before oriented attachment. Zone axes are labeled. b) Corresponding atomic models of the three nanocrystals. Labels indicate the number of Pb layers along the  $\langle 100 \rangle$  (orange),  $\langle 110 \rangle$  (blue), and  $\langle 111 \rangle$  (green) directions. c) Histograms of the number of Pb layers along these three directions as obtained from analysis of 32 nanocrystals. d) Reconstructed 3D model of the average nanocrystal. Blue spheres, Pb; pink spheres, Se. Facets are labeled. Scale bars are 2 nm. From Reference 178. Reprinted with permission from AAAS. A complete description of the methods are provided in that paper.

We investigated both the inorganic PbSe core as well as the organic capping layer. The inorganic core (*e.g.*, Pb and Se) was evaluated using electron microscopy, X-ray scattering, and optical measurements. From these measurements we determined the size, shape, stoichiometry, and faceting of the as-made QDs, all of which influence the structural, optical, and electronic properties of the resultant superlattices. Next, we analyzed the organic capping layer to quantify the number of oleate ligands on the surface, and to look for co-adsorbates or other impurities.

The shape and surface structure (*i.e.*, faceting) of oleate-capped PbSe QDs was determined using high-angle annular dark-field scanning transmission electron microscopy (HAADF-STEM).<sup>ii</sup> Through analysis of 32 HAADF-STEM images, Wang *et al.* produced a single-particle

<sup>ii</sup> This work was performed in collaboration with the Zheng group at Lawrence Berkeley National Laboratory and is discussed more thoroughly in Ref 178.

reconstruction which represents an averaged, atomic-scale model of our PbSe QDs.<sup>178</sup> Figure 2.1a shows representative QD images aligned along different zone axes. The QDs are nearly spherical and uniform in size. Atomic models of the images shown in Figure 2.1b reveal the QD surface faceting. These imaging data were compiled to produce a single-particle reconstruction (Figure 2.1d) which represents the average QD shape: nonuniform truncated cuboctahedra with six {100}, twelve {110}, and eight {111} facets (accounting for 33%, 27%, and 40%, respectively, of the total QD surface area of 145 nm<sup>2</sup>).

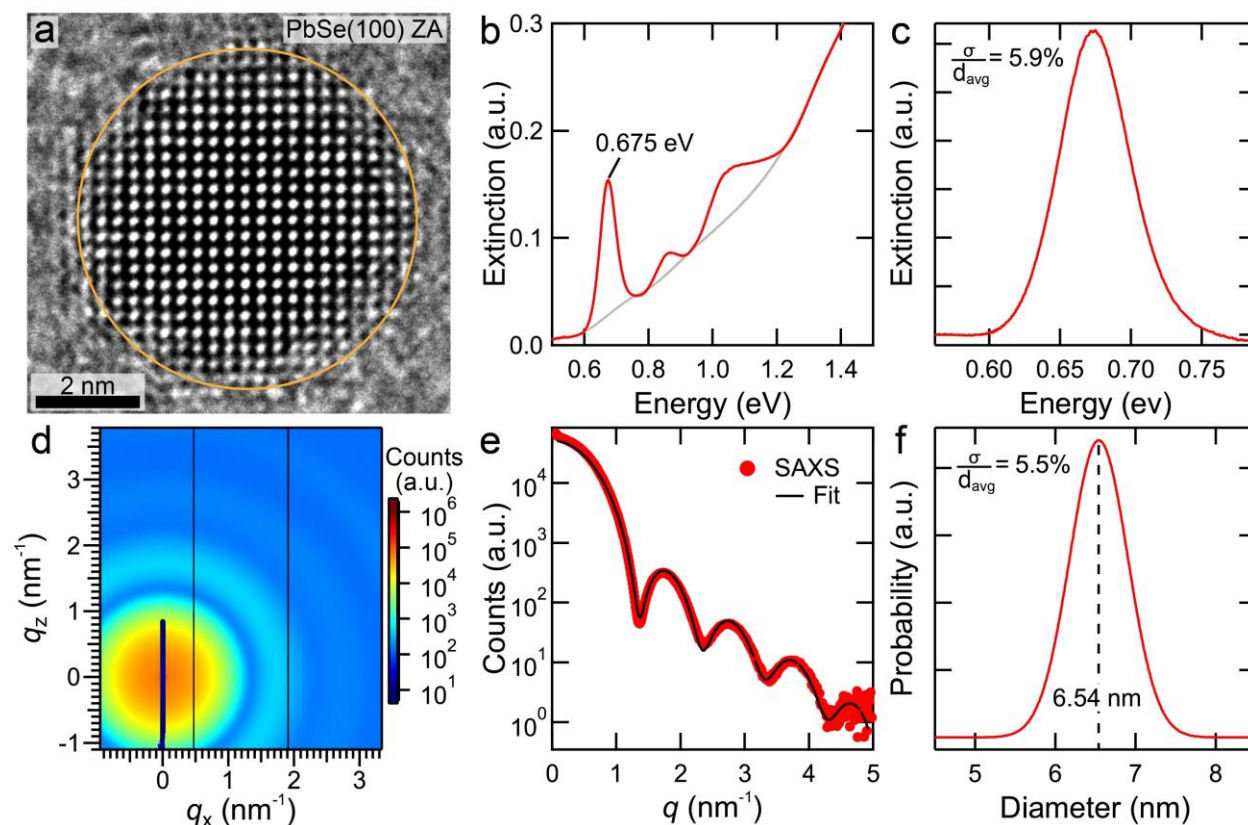


Figure 2.2. Size analysis of PbSe QDs. a) High-resolution TEM image of a single PbSe QD aligned to the (100)AL zone axis (ZA). A circle with a diameter of 6.5 nm provides a visual aid. The scale bar is 2 nm. b) Optical extinction spectrum of the QDs dispersed in tetrachloroethylene (TCE). The first exciton absorption ( $1S_h-1S_e$ ) peak energy is 0.675 eV. The grey trace is a spline baseline fit. c) Estimate of the first exciton peak width after baseline subtraction. The ratio of the standard deviation of the diameter distribution over the average QD diameter ( $\sigma/d_{\text{avg}}$ ) provides an estimate of the size polydispersity as calculated using the empirical relationship of Moreels *et al.*<sup>36</sup> d) 2D transmission small-angle X-ray scattering (SAXS) pattern of the QDs dispersed in octane. e) Azimuthally-integrated SAXS data with overlaid model fit. f) QD size

distribution extracted from SAXS data using a spherical form factor and Gaussian size distribution.<sup>187,188</sup>  $\sigma/d_{\text{avg}}$  is an estimate of the size polydispersity from the SAXS data. From Ref 169.

UV-vis spectroscopy and X-ray scattering experiments were performed to complement the single-particle reconstruction model and better relate our experiments with previously published work. Methods for these measurements are described in Sections 2.7.3 and 2.7.4. Whereas high-resolution TEM experiments are time-intensive and incorporate only several tens of QDs in the analysis, SAXS and optical measurements are fast ensemble measurements of  $\gg 10^{13}$  QDs. An average QD diameter of  $6.58 \pm 0.39$  nm was extracted from UV-vis spectra (Figure 2.2b-c) using the empirical relationship established by Moreels *et al.*<sup>36</sup> Small-angle X-ray scattering patterns (Figure 2.2d) were collected, azimuthally integrated (Figure 2.2e), and fit to a normally-distributed spherical form factor scattering model (Figure 2.2f) with an average particle diameter of  $6.54 \pm 0.36$  nm. Results from the QD size and shape analysis are summarized in Table 1. Having firmly established the size and shape of our QDs, we turned to understanding their surface chemistry.

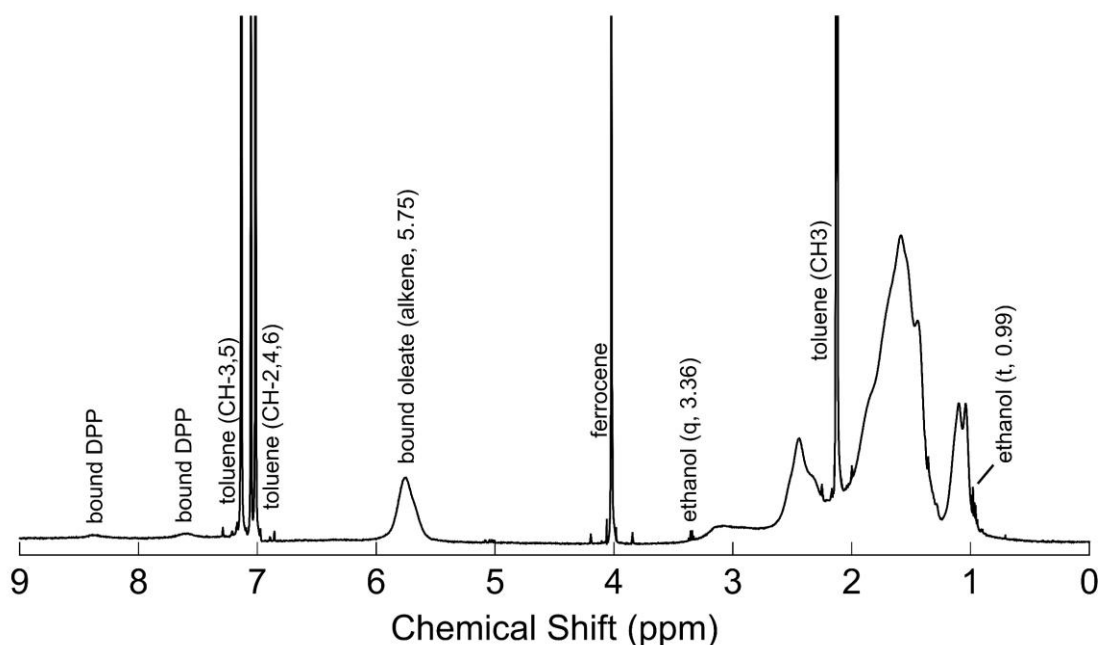


Figure 2.3.  $^1\text{H}$  NMR spectrum of a PbSe QD suspension. The QDs were dispersed in toluene- $d_8$ . The QDs were synthesized and washed according to Section 2.7.1. Ferrocene was added at a known concentration as an internal standard.

The composition, distribution, and binding strength of QD surface ligands strongly influence superlattice self-assembly, optoelectronic properties, and chemical reactivity.<sup>108,176,189</sup> We first quantified oleate coverage using a combination of nuclear magnetic resonance spectroscopy (NMR) and surface isotherm calculations. NMR is a useful tool for probing the composition and configuration (*e.g.*, bound *vs.* unbound) of organic ligands on QD surfaces<sup>190</sup> and has been previously used to quantify oleate coverage,<sup>36,191</sup> show that alcohols strip oleic acid and bind as alkoxides,<sup>94</sup> while amines can chelate and strip  $\text{Pb}(\text{OA})_2$ ,<sup>192</sup> and detect the presence of lead oleate clusters/oligomers in poorly-washed PbX QD samples.<sup>193</sup>

Quantitative NMR experiments reveal surface coverage of  $505 \pm 28$  oleate ligands per QD ( $3.48$  oleate/ $\text{nm}^2$ ). Figure 2.3 shows a representative NMR spectrum of oleate-capped PbSe QDs, notably with a broad peak at  $\sim 5.8$  ppm produced by the vinylic ( $\text{HC}=\text{HC}$ ) protons of oleate, which was

used for oleate quantification. The NMR resonances from surface-bound ligands are broadened due to their reduced rotation speeds (homogeneous broadening) and the variety of local chemical environments sampled by individual ligand molecules (heterogeneous broadening).<sup>194</sup> The two broad and weak peaks centered around ~8 ppm are assigned to adsorbed diphenylphosphine (DPP), a secondary dialkylphosphine used during synthesis to boost yield.<sup>195</sup> Peaks at 3.36 and 0.99 ppm come from ethanol, a solvent used during QD purification.

We next determined the facet-specific oleate distribution by combining the QD model derived from single-particle reconstruction, the oleate coverage determined using NMR, and a simple surface isotherm model. Figure 2.4 shows coverage-dependent oleate binding energy and adsorption isotherms for different PbSe crystal facets. Following the work of Bealing, *et al.* we calculated the binding energy ( $E_b$ ) of oleate ions using:<sup>196</sup>

$$E_b = A + B \cosh(C\Theta_{hkl}) \quad (2.1)$$

where  $\Theta_{hkl}$  is the oleate coverage on the  $\{hkl\}$  facet, and A, B, and C are empirical fitting parameters taken from Ref. 75. The calculation for  $\{100\}$  facets had an erroneous 2x multiplicative factor in the original work, which we have corrected and include as  $\{100\}_{\text{corrected}}$ . Figure 2.4a shows that, in terms of binding strength,  $E_b\{100\} < E_b\{110\} < E_b\{111\}$ . Using the calculated binding strengths, the oleate coverage ( $\Theta_{hkl}$ ) can be calculated using a Langmuir adsorption model:

$$\Theta_{hkl} = \frac{\frac{c}{c_o} \exp\left(\frac{E_b}{k_B T}\right)}{1 + \frac{c}{c_o} \exp\left(\frac{E_b}{k_B T}\right)} \quad (2.2)$$

where  $E_b$  is calculated using Eqn. (2.1),  $c$  is the ligand concentration,  $c_0$  is an arbitrary reference concentration,  $k_B$  is Boltzmann's constant, and  $T$  is temperature (set to 300 K). Figure 2.4b shows the isotherm of  $\Theta_{hkl}$  as a function of overall oleate concentration  $\left(\frac{c}{c_0}\right)$ .

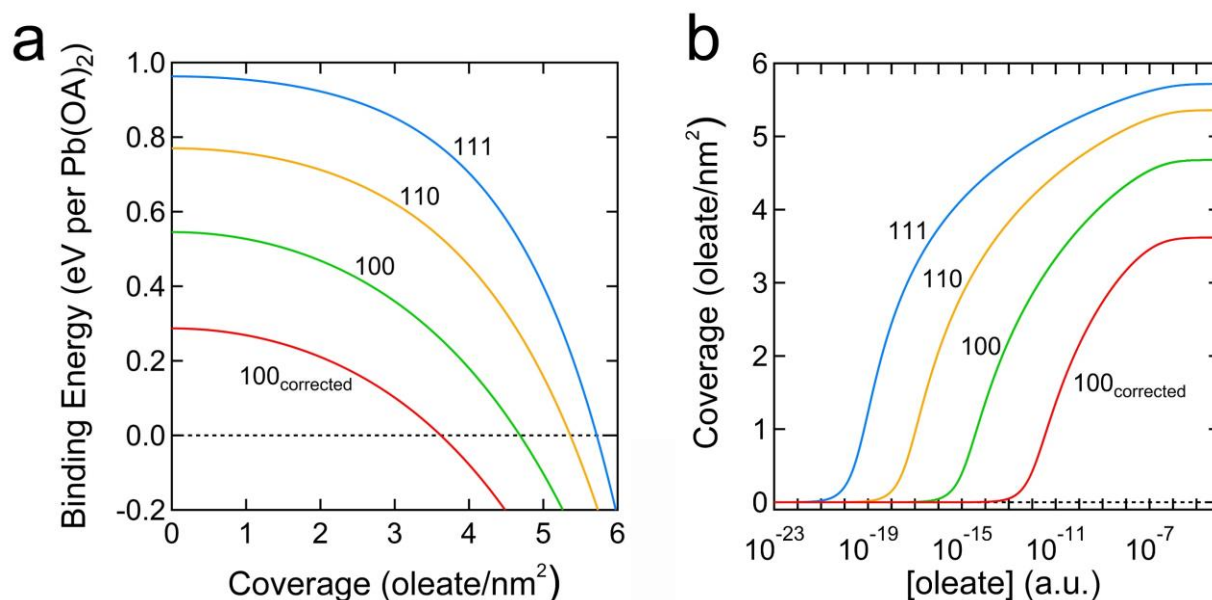


Figure 2.4. Estimate of facet-specific oleate surface coverage of PbSe QDs. a) Coverage-dependent binding energy of Pb(oleate)<sub>2</sub> ligands on the {111}, {110}, and {100} surfaces of PbSe. Results for the {111} and {100} surfaces are taken from Bealing *et al.*<sup>75</sup> Results for the {110} surface were calculated independently.<sup>196</sup> We find that the {100} results of Bealing *et al.* are in error by a factor of two. The corrected results are labeled “100corrected”. b) Isotherms for equilibrium coverage of oleate ligands on the three surfaces. The concentration axis is scaled by a reference concentration. From Ref 169.

According to the QD model shown in Figure 2.1 each QD has 210 Pb atoms at edges and corners. These are expected to have larger binding energies than any of the facets due to undercoordination of Pb by Se. If we assign one oleate to each of these edge/corner atoms, then we find the following oleate coverages for the three facets: 3.7 nm<sup>-2</sup> on {111}, 2.0 nm<sup>-2</sup> on {110}, and 0 nm<sup>-2</sup> on {100}. If we assume the opposite limit (zero oleate on edge/corner atoms), then we get coverages of 5.0 nm<sup>-2</sup> on {111}, 4.3 nm<sup>-2</sup> on {110}, and 1.0 nm<sup>-2</sup> on {100}. The actual coverage is likely somewhere in between these two limits, *i.e.*, 3.7-5.0 nm<sup>-2</sup> for {111}, 2.0-4.3 nm<sup>-2</sup> for {110}, and 0-1.0 nm<sup>-2</sup>

for {100}. These estimates use the  $100_{\text{corrected}}$  values for ligand binding to the {100} facets. We therefore believe that these QDs have patchy ligand coverage and nearly-bare {100} facets.

Based on the QD model and measured oleate loading, we can estimate the average molecular formula of our QDs. It is simplest to assume that each QD is charge neutral with charge balance achieved by a 2:1 ratio of oleate ( $\text{OA}^-$ ) to excess  $\text{Pb}^{2+}$  ions. This ratio implies that oleate is the only anionic ligand present in significant concentration (*e.g.*, no hydroxide ligands).<sup>86,197</sup> Given these assumptions, we find that the molecular formula of the average QD is  $\text{Pb}_{2737}\text{Se}_{2484}(\text{oleate})_{505}$ , which is equivalent to a QD mass of  $1.50 \times 10^{-18}$  g and a molecular weight of 905,535 g/mol. The Pb:Se ratio is 1.10. We note that evidence of surface-bound DPP in NMR data (see Figure 2.3) and a known affinity for ethanol<sup>94</sup> to bind surface-Pb as ethoxide suggests that we may slightly underestimate the Pb content of the QDs.

Table 1. Summary of PbSe QD size and shape.

Method	Direction	Planes	Diameter (nm)	Polydisp. (%)
	<111>	17.8	6.37	
HAADF-STEM	<100>	20	6.20	
	<110>	29.8	6.53	
SAXS	--	--	6.54	5.5
UV-Vis			6.58	5.9

## 2.2. Superlattice Synthesis and Surface Chemistry

We begin this section by introducing SL self-assembly, epi-SL formation, and the basic appearance of as-made and epi-SL films. We then answer several key questions about the ligand exchange process and resultant ligand content of epi-SLs. Using FTIR, XPS, and ICP-MS, we assess the organic and inorganic content of the oleate-capped, EDA-treated, and EDA/ $\text{PbI}_2$ -treated



SLs. These analyses are important because improved understanding of epi-SL formation chemistry should enable better control of epi-SL structural and chemical homogeneity, both of which strongly impact mini-band formation. Furthermore, knowing the ligand content of the SLs is important because surface chemistry usually dictates the electronic properties of QD films.<sup>95,108,198</sup>

Figure 2.5a shows the fabrication process used to make epi-SLs. First, oleate-capped QD SL films were formed by self-assembly from hexane suspension on the surface of liquid ethylene glycol (EG).<sup>82,183</sup> Controlled evaporation of the hexane results in polycrystalline SL films with a thickness of 50-80 nm and an average lateral grain size of ~500 nm (Figure 2.5b). Next, a solution of 1,2-ethylenediamine (EDA) is injected into the EG to trigger epitaxial fusion (epi-fusion) of the QDs across their {100} facets by removing oleate ligands and enabling direct QD-QD contact.<sup>146</sup> The ligand exchange and epi-fusion start at the bottom of the floating QD film and propagate upward to the top surface of the film. We believe that the polar ethylene glycol solution wicks into the film as oleate is replaced with glycoxide during the ligand exchange process (see below), ultimately yielding epi-SLs with uniform QD fusion and ligand coverage for films thin enough to avoid a significant exchange gradient (<250 nm). The epi-SLs are then stamp transferred to a solid substrate and immersed in a solution of PbI<sub>2</sub> with the goal of removing residual ligands and producing an all-inorganic SL with improved environmental stability and charge transport.<sup>88,199</sup>

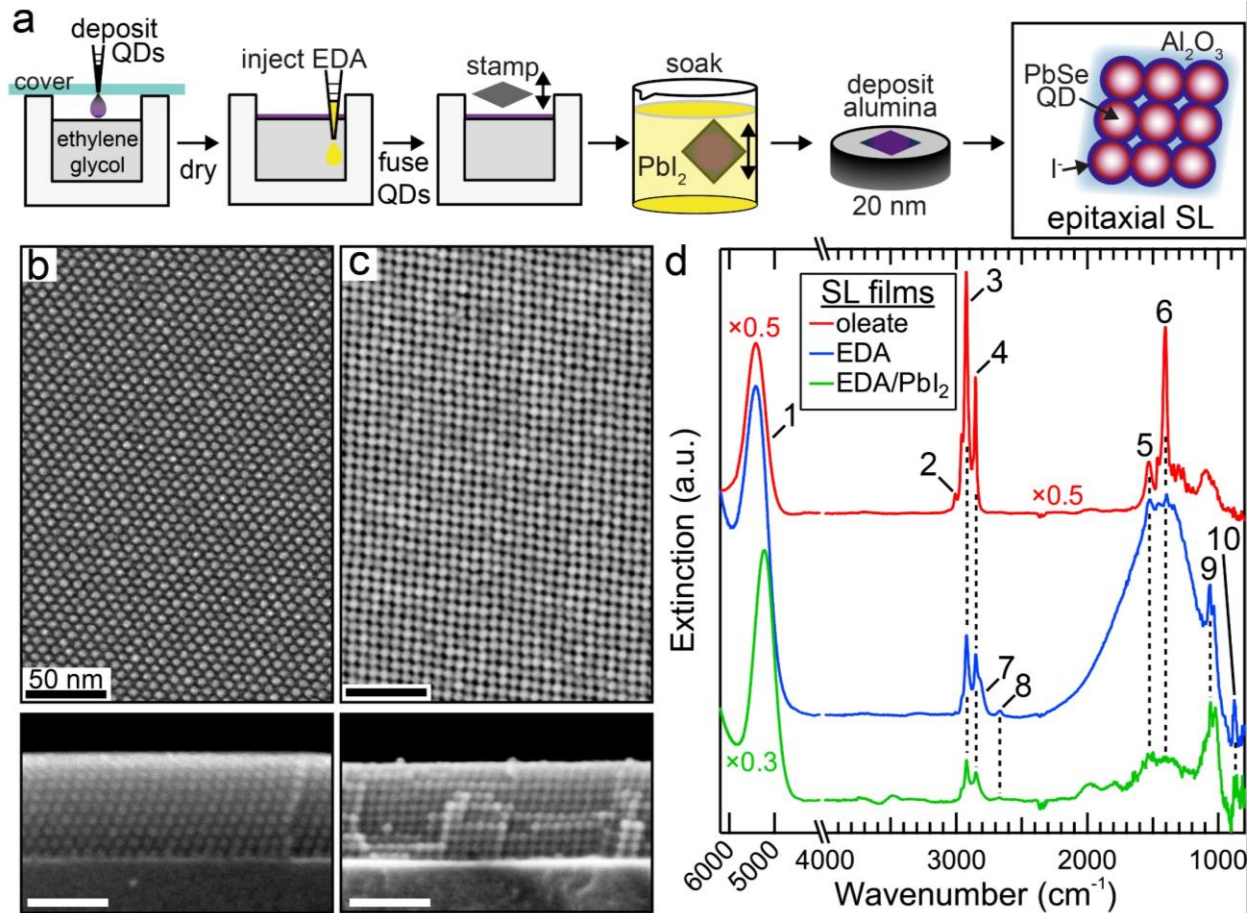


Figure 2.5. Fabrication and ligand chemistry of epitaxially-fused PbSe quantum dot superlattices (epi-SLs). a) Process flow for the fabrication of ALD-infilled PbSe QD epi-SLs. b) Plan-view and cross-sectional scanning electron microscopy (SEM) images of a typical oleate-capped SL film on a silicon substrate. The images show a (101)<sub>SL</sub>-oriented grain that is ten QDs thick. Scale bars are 50 nm. c) Corresponding SEM images of an epi-SL after EDA and PbI<sub>2</sub> treatment (no ALD). The images show a (100)<sub>SL</sub>-oriented grain, also ten QDs thick. Scale bars are 50 nm. d) FTIR spectra of an oleate-capped SL (red) and epi-SL before (blue) and after (green) the PbI<sub>2</sub> treatment. Labeled peaks are assigned as follows: peak 1 is the first exciton transition of the QDs, peaks 2-6 are adsorbed oleate (2:  $\nu(\text{HC}=\text{CH})$ , 3:  $\nu_{\text{as}}(\text{CH}_2)$ , 4:  $\nu_{\text{s}}(\text{CH}_2)$ , 5:  $\nu_{\text{as}}(\text{COO}^-)$ , 6:  $\nu_{\text{s}}(\text{COO}^-)$ ), and peaks 7-10 are adsorbed ethylene glycoxide (7:  $\nu_{\text{as}}(\text{CH}_2)$ , 8:  $\nu_{\text{s}}(\text{CH}_2)$ , 9:  $\nu(\text{CO})$  and  $\nu(\text{CC})$ , 10:  $\rho(\text{CH}_2 \text{ rocking})$ ). All films have the same number of QD layers and are 50-60 nm thick. Spectra are baseline corrected using a spline fit and offset. Note the break in the  $x$ -axis. The oleate-capped SL spectrum is scaled by  $\times 0.5$  and the exciton region of the PbI<sub>2</sub>-treated epi-SL is scaled by  $\times 0.3$ . From Ref 169. Reprinted with permission from Springer Nature Limited.

The resulting films are polycrystalline epi-SLs with an average lateral grain size of  $\sim 250$  nm and significant nanoscale cracking (Figure 2.5c). Finally, these epi-SLs are infilled and overcoated with amorphous alumina using low-temperature atomic layer deposition, which has been

previously shown to enhance the environmental stability and carrier mobilities of amorphous QD films.<sup>114</sup>

We evaluated the ligand composition of the oleate-capped and epi-SL films using Fourier-transform infrared spectroscopy (FTIR). Figure 2.5d shows FTIR spectra from oleate-capped, EDA-treated and EDA/PbI<sub>2</sub>-treated SL films. Each of the films contain a broad peak (peak 1) between 5000-6000 cm<sup>-1</sup> originating from the first excitonic transition of the PbSe QDs. Peaks 2-6 are attributed to oleate adsorbed to the surface of the QD and are assigned as: 2:  $\nu(\text{HC}=\text{CH})$ , 3:  $\nu_{\text{as}}(\text{CH}_2)$ , 4:  $\nu_{\text{s}}(\text{CH}_2)$ , 5:  $\nu_{\text{as}}(\text{COO}^-)$ , 6:  $\nu_{\text{s}}(\text{COO}^-)$ . The intensity of these peaks decreases in the EDA- and EDA/PbI<sub>2</sub>-treated films, indicating a loss of oleate after EDA and PbI<sub>2</sub> treatments. We find that the EDA treatment removes ~88% of the original oleate C-H signal intensity and the subsequent PbI<sub>2</sub> treatment results in a total oleate reduction (relative to the oleate-capped SL) of 94%. Efforts to eliminate oleate using other secondary ligand treatments (Figure 2.6) were unsuccessful and resulted in either amorphization of the epi-SL or incomplete oleate removal. FTIR shows that EDA treatment adds a large amount of adsorbed ethylene glycoxide to the epi-SL. We attribute peaks 7-10 to ethylene glycol bound to surface Pb, assigning them as: 7:  $\nu_{\text{as}}(\text{CH}_2)$ , 8:  $\nu_{\text{s}}(\text{CH}_2)$ , 9:  $\nu(\text{CO})$  and  $\nu(\text{CC})$ , 10:  $\rho(\text{CH}_2 \text{ rocking})$ .<sup>200-202</sup> FTIR experiments with deuterated EG and EDA confirm these peak assignments.

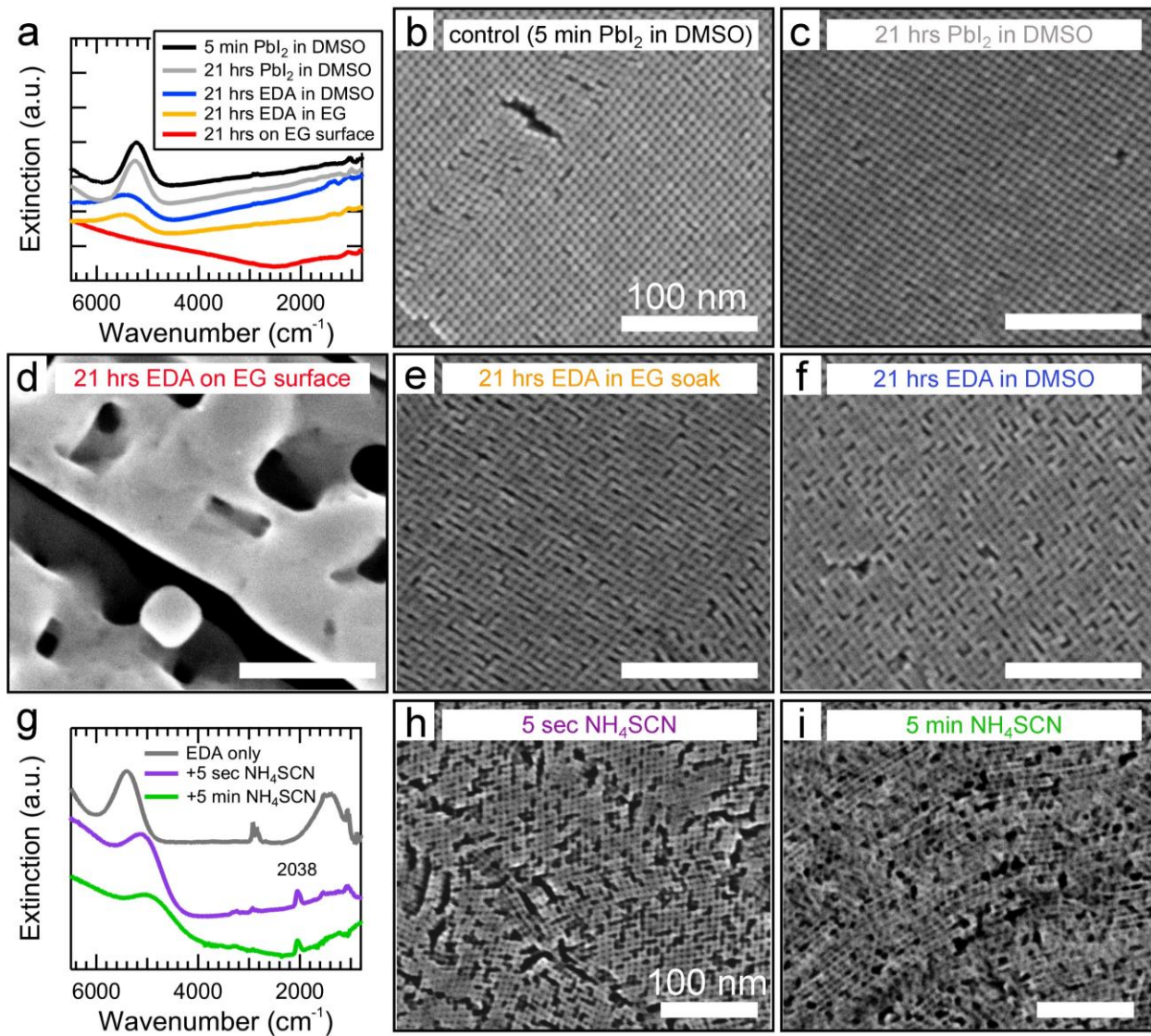


Figure 2.6. Impact of alternative secondary treatments on the epi-SLs. a) FTIR spectra of epi-SLs immersed for 5 minutes in 10 mM  $\text{PbI}_2$  in DMSO (the normal process; black trace), 21 hours in 105 mM  $\text{PbI}_2$  in DMSO (gray), 21 hours in 105 mM EDA in DMSO (blue), and 21 hours in 105 mM EDA in EG (orange), compared to a film left floating on the EG surface for 21 hours after EDA injection (total EDA concentration of 105 mM; red). b-f) Representative SEM images of these films. Prolonged  $\text{PbI}_2$  treatment results in negligible changes. However, prolonged EDA soaks in either DMSO or EG cause significant broadening of the first exciton peak due to excessive fusion of the QDs. Leaving the epi-SLs floating on the surface of EG after EDA injection results in complete coalescence and loss of the QDs. g) FTIR spectra of epi-SLs treated with ammonium thiocyanate (1 mM in acetonitrile) instead of  $\text{PbI}_2$  or additional EDA.  $\text{SCN}^-$  treatment results in the appearance of the CN stretching peak at  $2038\text{ cm}^{-1}$  from adsorbed  $\text{SCN}^-$ , loss of C-H stretching signal from oleate removal, and dramatic broadening of the first exciton peak due to progressively extreme QD fusion. h) SEM image of the film treated in  $\text{SCN}^-$  for five seconds, showing significant QD fusion. i) SEM image of the film treated in  $\text{SCN}^-$  for five minutes. The QD fusion is even more extensive, and the SL is largely destroyed. All scale bars are 100 nm. From Ref 169.

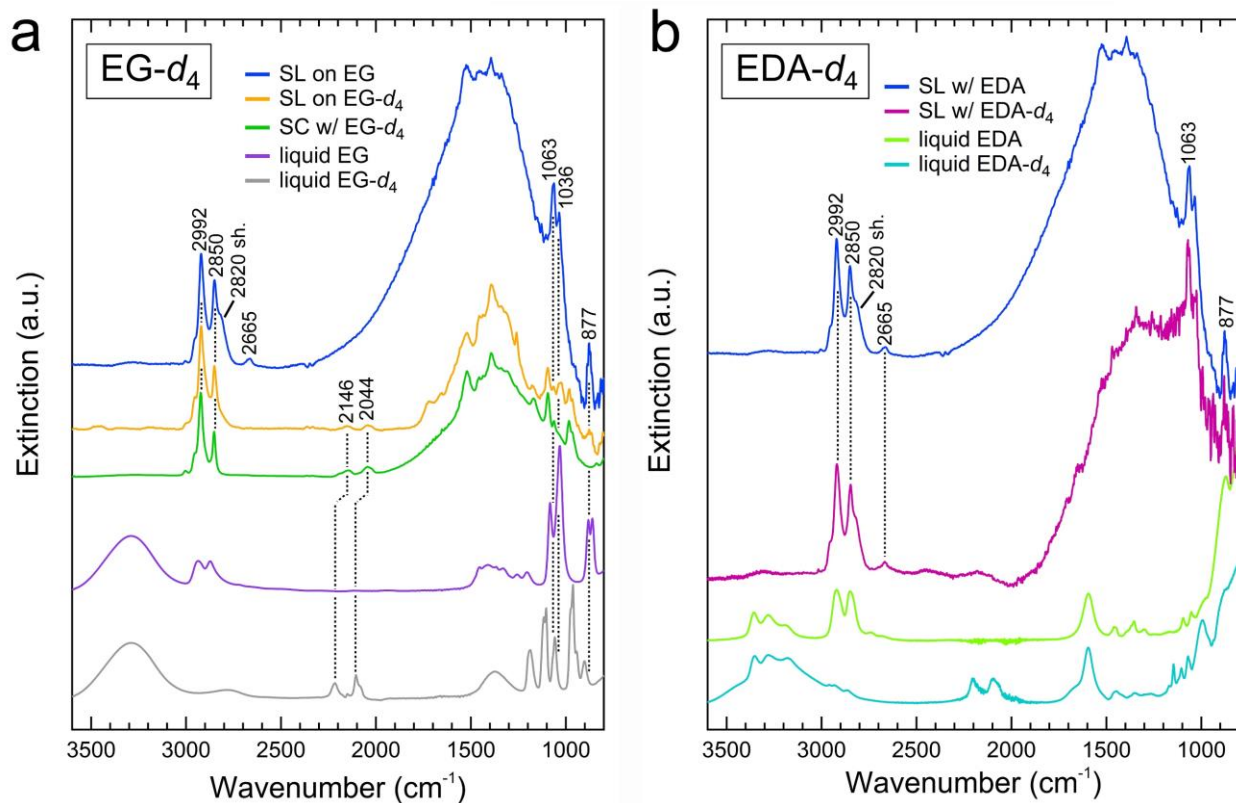


Figure 2.7. FTIR spectra of SL films made with deuterated ethylene glycol ( $\text{HOCD}_2\text{CD}_2\text{OH}$ ,  $\text{EG-}d_4$ ) and deuterated ethylenediamine ( $\text{H}_2\text{NCD}_2\text{CD}_2\text{NH}_2$ ,  $\text{EDA-}d_4$ ). a) Spectra of an EDA-treated epi-SL made on the surface of normal EG (blue), an EDA-treated epi-SL made on the surface of  $\text{EG-}d_4$  (orange), and a film made by five cycles of spin-casting and soaking in a solution of EDA in  $\text{EG-}d_4$  (using one minute soaks in 105 mM EDA, green). Attenuated total reflectance FTIR spectra of liquid EG (purple) and  $\text{EG-}d_4$  (gray) are shown for reference. We find strong evidence for adsorbed EG in all films. The peaks at 2820 and 2665  $\text{cm}^{-1}$  in the spectrum of the normal SL are assigned as the characteristic C-H stretching resonances of lead glycoxide (*i.e.*, ethylene glycoxide bound to Pb on the QD surface).<sup>200,201</sup> The C-O stretching and  $\text{CH}_2$  rocking modes of adsorbed EG are also evident (at 1030-1070  $\text{cm}^{-1}$  and 877  $\text{cm}^{-1}$ , respectively).<sup>202</sup> An absence of O-H stretching at  $\sim 3300$   $\text{cm}^{-1}$  suggests that the bound EG is doubly deprotonated and either bridging or chelating on the QD surface. The films made with  $\text{EG-}d_4$  rather than EG show loss of the C-H modes of adsorbed EG at 2820, 2665, and 877  $\text{cm}^{-1}$  and the appearance of C-D stretching modes at 2146 and 2044  $\text{cm}^{-1}$  associated with adsorbed  $\text{EG-}d_4$ . b) Spectra of epi-SLs prepared with EDA (blue) or  $\text{EDA-}d_4$  (purple) on the surface of normal EG. The  $\text{EDA-}d_4$  film was treated for  $\sim 10$  minutes rather than  $\sim 45$  seconds in order to achieve a comparable degree of oleate removal and epi-fusion (confirmed by SEM imaging). There are no significant differences between the two spectra, indicating negligible adsorption of EDA on these SLs. Attenuated total reflectance FTIR spectra of liquid EDA (light green) and  $\text{EDA-}d_4$  (light blue) are shown for reference. All films were prepared on double-side polished Si substrates. Dotted lines are guides to the eye. From Ref 169.

Figure 2.7 shows FTIR spectra of epi-SL films made with deuterated EG or EDA. Replacing EG with  $\text{EG-}d_4$  redshifts the  $\text{CH}_2$  peaks at 2820 (shoulder) and 2665  $\text{cm}^{-1}$  (peaks 7 and 8 in Figure

2.5d) to 2146 and 2044  $\text{cm}^{-1}$ , indicating that those peaks are from EG rather than EDA. The  $\text{CD}_2$  peaks ( $\sim 2200$  and  $2100 \text{ cm}^{-1}$ ) in liquid EG- $d_4$  are blue-shifted from the corresponding peaks in the film spectra, suggesting that the EG is likely bound to the QD surface rather than simply stuck within the porous SL film. An absence of O-H stretching at  $\sim 3300 \text{ cm}^{-1}$  indicates that the bound EG is doubly deprotonated and either bridging or chelating on the QD surface. In contrast to the impact of deuterated EG, spectra of films made with EDA and EDA- $d_4$  (Figure 2.7b) show no significant difference. From these isotope labelling experiments we conclude that there is significant EG adsorption and our peak assignments in Figure 2.5 are correct. FTIR experiments were next corroborated by X-ray photoelectron spectroscopy (XPS) measurements.

XPS spectra of EDA and EDA/ $\text{PbI}_2$  SL films (Figure 2.8 and Table 2) show no evidence for adsorbed EDA, in agreement with FTIR experiments. Coupled with an increase in Pb:Se, the presence of I on  $\text{PbI}_2$ -treated films indicates some direct addition of  $\text{PbI}_2$  to the QD surface. There is a large decrease in the carbon-to-oxygen ratio (C:O) upon EDA treatment due to desorption of carbon-rich oleate ( $\text{C}_{18}\text{H}_{33}\text{O}_2^-$ ) and adsorption of oxygen-rich glycoxide ( $\text{C}_2\text{H}_4\text{O}_2^{2-}$ ). This ratio approaches unity after treatment with  $\text{PbI}_2$ . We also see that the Pb:Se ratio is unchanged after EDA treatment.

We then looked with inductively coupled plasma mass spectrometry (ICP-MS) at the EG subphase to determine whether the EDA treatment used to trigger epi-SL formation strips Pb, Se, or both from the QD surface. Details of the ICP-MS experiments are provided in Section 2.7.8. In summary, we find that (i) removal of  $\text{Pb}(\text{OA})_x$  by EDA accounts for only a small fraction of the  $\sim 404$  oleate ligands removed per QD (80% of 505 ligands/QD) during the normal EDA treatment, (ii) no Se is removed from the QD surface, (iii) epitaxial fusion occurs despite the minimal loss of

surface Pb atoms, and (iv) extremely long exposures of the SL film to EDA in EG results in significant loss of Pb.

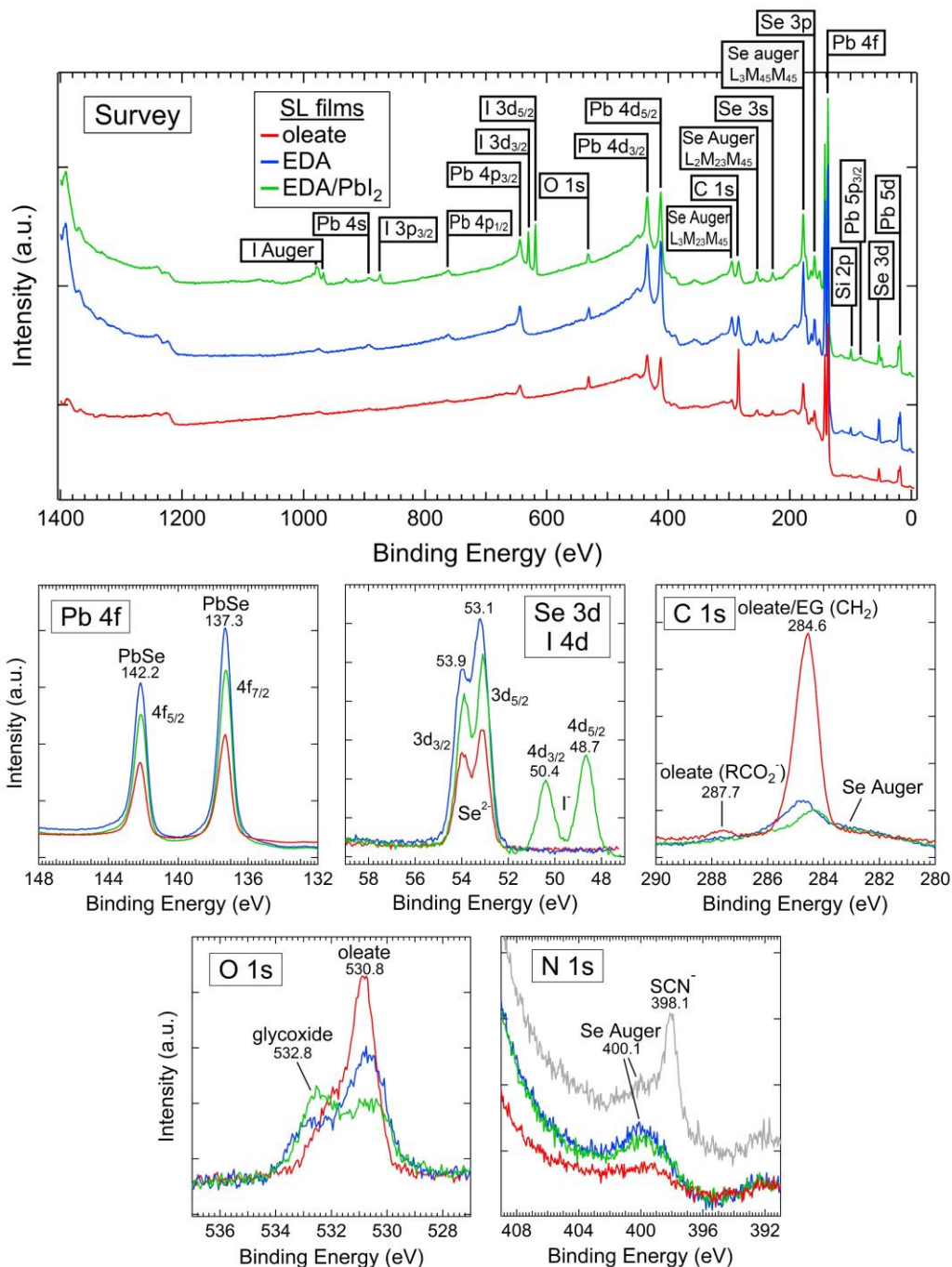


Figure 2.8. X-ray photoelectron spectra of SL films. Survey and high-resolution scans (Pb 4f, Se 3d, I 4d, C 1s, O 1s, and N 1s) of an oleate-capped SL (red) and epi-SLs before (blue) and after (green) the PbI<sub>2</sub> treatment. The oleate-capped SL spectrum was charge corrected to place the aliphatic carbon of oleate at 284.6 eV, while the other spectra were charge corrected to align the Pb 4f<sup>5/2</sup> peak of PbSe with that of the

oleate-capped SL spectrum at 137.3 eV. In addition to the presence of Pb, Se, C, and O in all three films, we observed a small amount of silicon in the epi-SLs (originating from the substrate) and a significant amount of iodine in the PbI<sub>2</sub>-treated SL. The Pb and Se spectra are consistent with Pb<sup>2+</sup> and Se<sup>2-</sup> of PbSe with no evidence of oxidation. Quantification of the XPS data shows that the atomic fractions of Pb and Se increase after the EDA treatment (see Table 2), consistent with removal of ~80% of the bulky oleate ligand shell as observed in FTIR spectra (Figure 2.5). The C 1s spectrum of the oleate-capped SL shows peaks arising from aliphatic and carboxylate carbon of oleate at 284.6 eV and 287.7 eV. Treatment with EDA greatly reduces the carbon content of the films (Table 2). Subsequent treatment with PbI<sub>2</sub> further decreases the carbon content and results in significant iodine signal, consistent with exchange of residual oleate and ethylene glycoxide by PbI<sub>2</sub>. The O 1s spectrum of the oleate-capped SL shows a main peak at 530.8 eV and a shoulder at 532.1 eV, assigned to different binding conformations of the carboxylate group of oleate. EDA treatment significantly reduces the oxygen content and produces a new peak at ~533 eV that we assign to adsorbed ethylene glycoxide. The oleate and glycoxide O 1s signal is further reduced after PbI<sub>2</sub> treatment (Table 2), in agreement with the FTIR data in the main text. The N 1s region is somewhat obscured by the broad Se L<sub>2</sub>M<sub>23</sub>M<sub>23</sub> Auger peak centered at 400.1 eV, but we observe no new peaks after EDA or PbI<sub>2</sub> treatment, consistent with our FTIR data showing no EDA adsorption to the SLs (Figure 2.7). As a positive control for nitrogen, we include the N 1s spectrum of a PbSe QD film prepared with SCN<sup>-</sup> ligand exchange (gray plot). A distinct N 1s peak is observed in this case. Si signal appears in the survey scans of the epi-SLs due to nanoscale cracking of the films that occurs during epi-fusion. Table 2 summarizes the surface elemental composition of the films as determined from the XPS data. From Ref 169.

Table 2. Surface elemental composition of the SL films as determined from XPS data.

SL film	Pb (%)	Se (%)	O (%)	C (%)	I (%)	Pb:Se	C:Se	O:Se	C:O
oleate	10.96	5.68	5.98	77.35	0	1.93	13.62	1.05	12.94
EDA	42.08	21.75	11.64	24.51	0	1.94	1.13	0.54	2.11
EDA/PbI <sub>2</sub>	44.45	21.52	12.88	14.14	6.99	2.07	0.66	0.60	1.10

We conclude that, under normal epi-SL synthesis conditions, EDA injection causes oleate loss without removing a significant amount of Pb. The conclusion that EDA does not form a Pb(oleate)<sub>2</sub> adduct and dissociate from the QD surface conflicts with previous reports.<sup>146,165</sup> We therefore offered an alternative hypothesis (discussed in more detail in Chapter 3) based on our findings: oleate removal occurs mainly by exchange of oleate with the relatively high concentration (~mM) of glycoxide ions produced by deprotonation of EG by EDA, a weak Brønsted base.



### 2.3. Structure Analysis

We determined the unit cells of both the oleate-capped and epi-fused SLs with an accuracy of  $\sim 1$  Å and  $\sim 1^\circ$  using a combination of synchrotron grazing-incidence small-angle X-ray scattering (GISAXS) of entire films and SEM and correlated TEM-based secondary electron imaging and electron diffraction of individual SL grains (see Sections 2.7.4 and 2.7.10 for methods). This dual-space approach is summarized in Figure 2.9 and was key to determining the complete SL unit cells and phase transformation pathway (from oleate-capped SL to epi-SL). Figure 2.10 shows the structural analysis results for oleate-capped SLs. Figure 2.11 contains representative SEM images of the oleate-capped SL. These films produce strong GISAXS spot patterns (Figure 2.10a) characteristic of highly-ordered polycrystalline thin-film SLs with a high degree of uniaxial (out-of-plane) crystallographic texture. The patterns were indexed to a body-centered unit cell with lattice parameters  $a \approx b \approx c = 9.8 \pm 0.2$  nm and  $\alpha \approx \beta \approx \gamma = 84.5 \pm 3^\circ$ . Although each individual film is triclinic, on average the oleate-capped SLs can be described with a rhombohedrally-distorted body-centered cubic (“distorted bcc”) conventional cell ( $a = 9.8$  nm,  $\alpha = 84.5^\circ$ ). The unit cell can also be described as a primitive triclinic cell with lattice parameters  $a \approx b \approx c = 8.2$  and  $\alpha \approx \beta \approx \gamma = 106.7^\circ$ . The structural relation between the two unit cell descriptions is shown in Figure 2.12. We chose the former description to better compare with previously-published QD SLs, but the latter makes for a more intuitive description of the epi-SL transformation process.<sup>189,203</sup> GISAXS shows that the films contain SL grains of two different in-plane orientations,  $(101)_{\text{SL}}$  and  $(10\bar{1})_{\text{SL}}$  (where the subscript “SL” denotes superlattice). These SL planes are inequivalent and have distinct arrangements of QDs (Figure 2.10b and e), which facilitated the use of SEM imaging to validate and refine the GISAXS fits (see Section 2.7.9). We find excellent agreement between the GISAXS and SEM data, which is strong evidence that the superlattice unit cell presented in

Figure 2.10 is correct. This agreement also indicates that the SL surfaces have little tendency to reconstruct, such that the SL surface and bulk share the same unit cell.

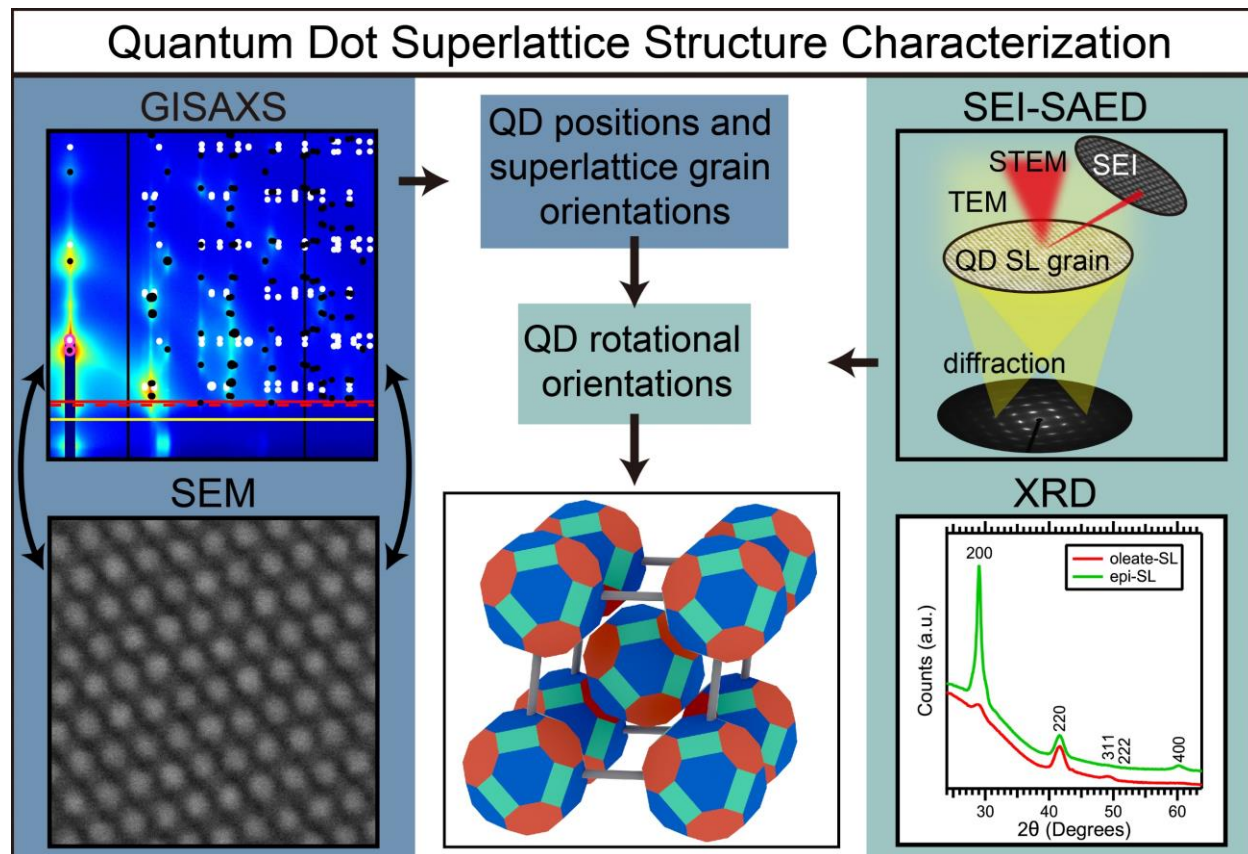


Figure 2.9. Process map for determining the complete unit cell of QD superlattices.<sup>iii</sup> GISAXS and SEM were used to determine the QD positions at the ensemble and single-grain levels. Correlated secondary electron imaging and selected area electron diffraction (SEI-SAED) of single grains was used to determine the QD orientations. Wide-angle XRD was used as a check on the single-grain SEI-SAED results. From Ref 169.

<sup>iii</sup> Alternative methods for determining the full 3D structure of QD SLs are combined transmission small-angle and wide-angle diffraction of individual SL grains using focused X-ray<sup>166,204,205</sup> or electron<sup>206</sup> beams.

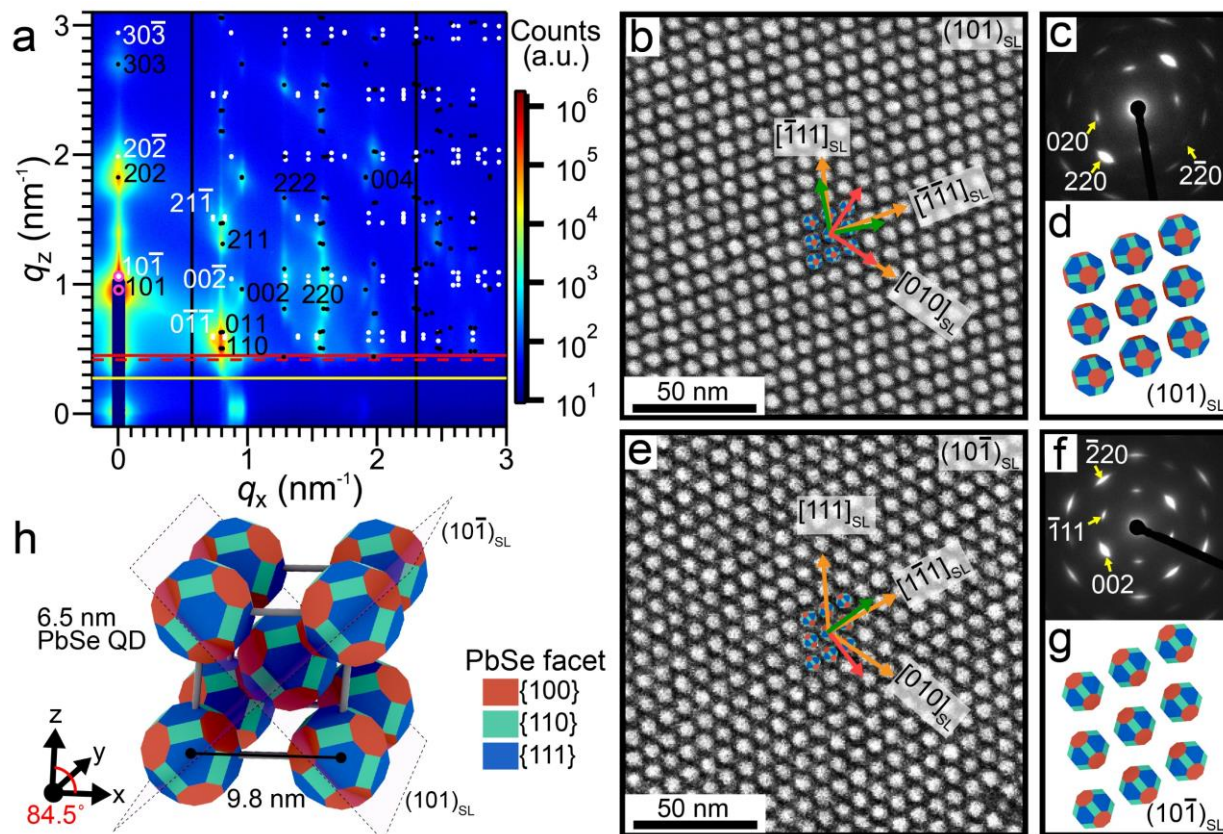


Figure 2.10. Structure of the oleate-capped QD SL films. a) 2D GISAXS pattern of a typical film on a silicon substrate. Overlaid is the calculated spot pattern for a body-centered unit cell ( $a = c = 9.78$  nm,  $b = 9.8$  nm,  $\alpha = 85.5^\circ$ ,  $\beta = 84.5^\circ$ , and  $\gamma = 84^\circ$ ) oriented with a mixture of its  $(101)$  and  $(10\bar{1})$  planes parallel to the substrate surface (black and white dots, respectively). For clarity, only select Miller indices are labelled. The solid and dashed red lines denote the scattering vector  $q_z$  corresponding to the critical angle of the QD film ( $0.195^\circ$ , fit experimentally) and Si substrate ( $0.180^\circ$ ). The yellow line denotes the substrate horizon. b-d, Correlative TEM imaging and electron diffraction of a single  $(101)_{\text{SL}}$ -oriented SL grain. b) Secondary electron image of the grain. Overlaid is a model of the top monolayer of QDs according to the lattice parameters in panel h. Orange arrows denote crystallographic directions of the SL, while green and red arrows indicate two of the  $\langle 100 \rangle_{\text{AL}}$  and  $\langle 110 \rangle_{\text{AL}}$  directions of the PbSe atomic lattice. The scale bar is 50 nm. c) Corresponding SAED pattern of the atomic lattice, with several spots labeled. The zone axis is  $\sim 15^\circ$  from  $[001]_{\text{AL}}$ . d) Model of the first monolayer of QDs on this superlattice plane. Red, cyan, and blue facets correspond to the  $\{100\}$ ,  $\{110\}$ , and  $\{111\}$  planes of PbSe. Slight tilting of the  $[001]_{\text{AL}}$  from the plane normal is visible. e-g) Correlative TEM imaging and diffraction of a  $(10\bar{1})_{\text{SL}}$ -oriented SL grain. e, Secondary electron image with overlaid model and crystallographic axes. f, SAED pattern. The zone axis is  $[110]_{\text{AL}}$ . g) Model of the first monolayer of QDs on this superlattice plane. h) The average rhombohedrally-distorted bcc unit cell of the oleate-capped QD SLs ( $a = 9.8$  nm,  $\alpha = 84.5^\circ$ ). The  $(101)_{\text{SL}}$  and  $(10\bar{1})_{\text{SL}}$  planes are outlined with dashed boxes. See Figure 2.11 for representative images of the oleate-capped SL. From Ref 169. Reprinted with permission from Springer Nature Limited.

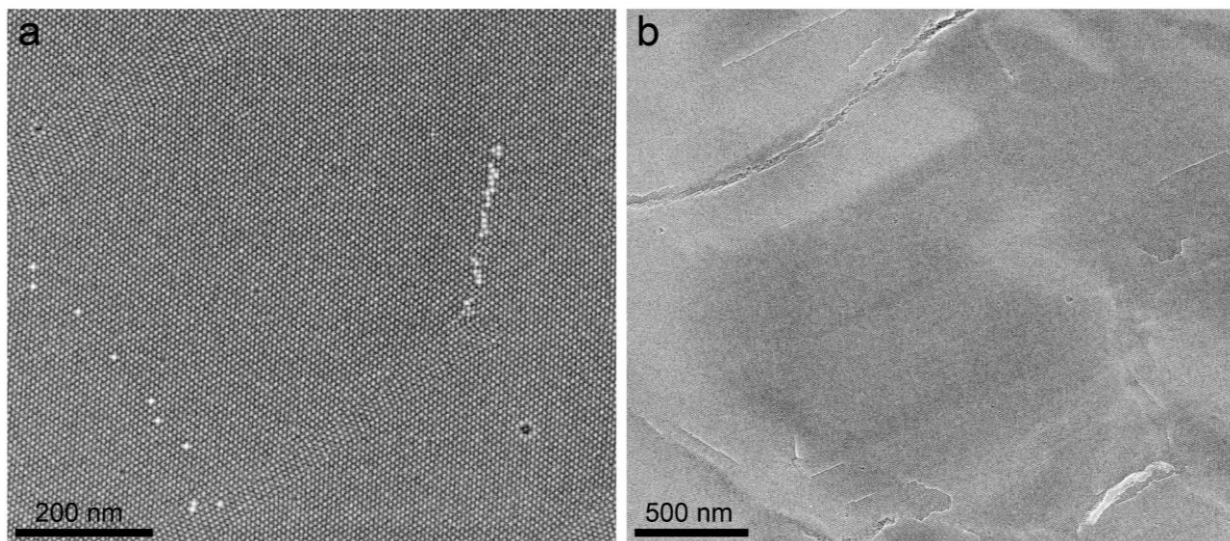


Figure 2.11. Representative SEM images of oleate-capped SLs. a) Medium-magnification image of several grains with a few surface defects (vacancies and adsorbed QDs). b) Lower-magnification image showing some SL step edges and a few nanoscale cracks. From Ref 169.

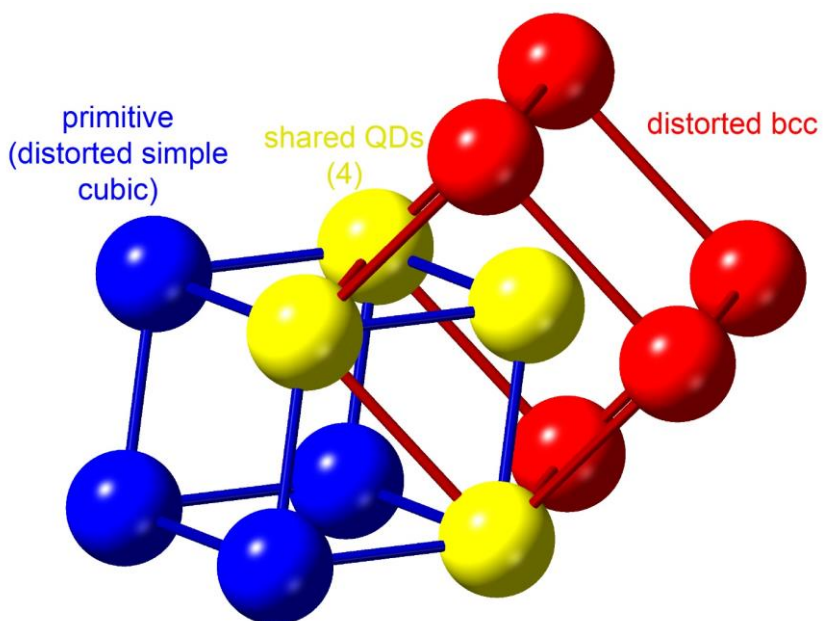


Figure 2.12. SL unit cell description relation. Relationship between the distorted bcc conventional unit cell and rhombohedral primitive unit cell of the average oleate-capped QD SL. The two unit cells have four QDs in common (yellow). Lattice parameters of the conventional cell:  $a = b = c = 9.8 \text{ nm}$  and  $\alpha = \beta = \gamma = 84.5^\circ$ . From Ref 169.

The GISAXS/SEM analysis provides the positions but not the rotational orientation of the QDs needed to fully specify the unit cell of the oleate-capped SL. We used TEM-based secondary electron imaging and selected area electron diffraction (SAED) of individual  $(101)_{\text{SL}}$ - and  $(10\bar{1})_{\text{SL}}$ -oriented grains to determine the orientation of the QDs with respect to the SL. The images (Figure 2.10b and e) provide the local SL orientation, while SAED patterns of the same grains (Figure 2.10c and f) provide the relationship between the PbSe atomic lattice (AL) and QD SL. We find strong single-crystalline SAED spot patterns indicating that the QDs are rotationally aligned in three dimensions, with complete biaxial alignment between the AL and SL. The crystallographic relationship deduced from correlated imaging and diffraction of many  $(101)_{\text{SL}}$ - and  $(10\bar{1})_{\text{SL}}$ -oriented grains is  $(110)_{\text{AL}} \parallel (10\bar{1})_{\text{SL}}$  and  $[100]_{\text{AL}} \parallel \angle 11^\circ [1\bar{1}1]_{\text{SL}}$  (there is an  $11^\circ$  angle between the two directions). We conclude that the two grain orientations are simply two views of the same structure, rather than two different unit cells. The resulting models of the  $(101)_{\text{SL}}$  and  $(10\bar{1})_{\text{SL}}$  surfaces are shown in Figure 2.10d and g, while Figure 2.10h shows the oleate-capped SL unit cell (with ligands omitted for clarity).

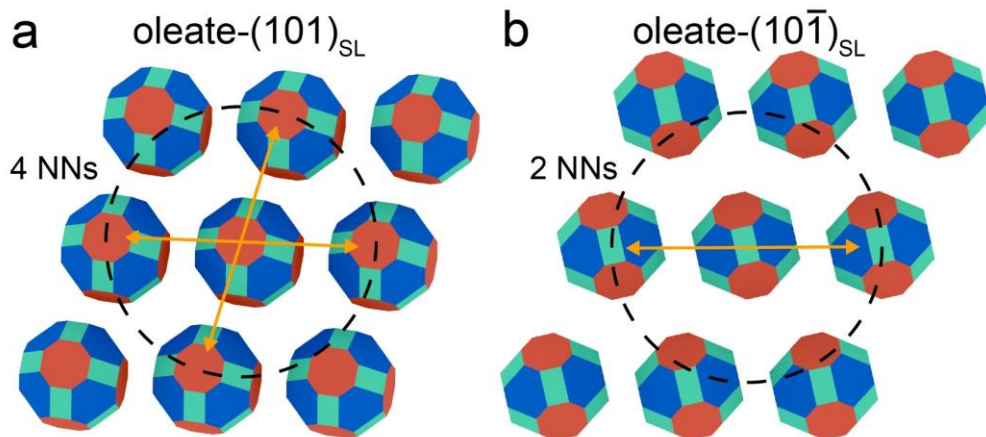


Figure 2.13. Models of the oleate-capped SL surfaces. a) Each QD on the  $(101)_{\text{SL}}$  surface has four close nearest neighbors (NNs) at 8.2 nm and two far NNs at 9.8 nm. b) Each QD on the  $(10\bar{1})_{\text{SL}}$  surface has two close NNs at 8.2 nm and four far NNs (two at 9.3 nm and two at 9.8 nm). The close NNs are denoted with

orange arrows. The dashed black circles are centered on the middle QD and have a radius of 8.2 nm. Red, cyan, and blue facets are  $\{100\}_{AL}$ ,  $\{110\}_{AL}$  and  $\{111\}_{AL}$ , respectively. From Ref 169.

The distorted bcc unit cell of the oleate-capped SL is extraordinary because the QDs are prepositioned to fuse across their  $\{100\}$  facets by simple translational motion. Many papers have reported oleate-capped PbS/Se QD SLs with cubic or tetragonal (bcc, fcc, or bct) unit cells and cofacial  $\{111\}$  facets,<sup>176,189,203–205,207–210</sup> but these structures have eight or twelve nearest neighbors (NNs) and would require significant rotational and translational rearrangement of the QDs to form simple cubic epi-SLs.<sup>163</sup> Many papers have reported oleate-capped PbS/Se QD superlattices with cubic or tetragonal (bcc, fcc, or bct) unit cells with co-facial  $\{111\}$  facets.<sup>189,189,203,207,208</sup> In contrast, each QD in our oleate-capped SL has six NNs with cofacial  $\{100\}$  facets arranged in a rhombohedrally-distorted octahedron (Figure 2.10h and Figure 2.21a). The NNs in our oleate-capped SLs have a center-to-center distance of 8.2 nm and a facet-to-facet distance of 2.1 nm, comparable to the length of the oleate ligands. The QDs are prearranged to fuse to their six NNs via their six  $\{100\}$  facets. On the  $(101)_{SL}$  plane, each QD has four close NNs with cofacial  $\{100\}$  facets at 8.2 nm and two far NNs with cofacial  $\{110\}$  facets at 9.8 nm (Figure 2.10 and Figure 2.13). The QDs on this plane are arranged to fuse with their four close NNs to make a 2D quasi-square epi-SL. In contrast, each QD on the  $(10\bar{1})_{SL}$  plane has two close NNs with cofacial  $\{100\}$  facets at 8.2 nm and four far NNs with cofacial  $\{111\}$  facets (two at 9.3 nm and two at 9.8 nm; Figure 2.10g and Figure 2.13). The QDs on the  $(10\bar{1})_{SL}$  plane are arranged to fuse with their two close NNs to make parallel 1D chains of epi-fused QDs. Therefore, we expected the two grain orientations of the oleate-capped SL to yield two orientations of the epi-SL with very different topography in SEM images.

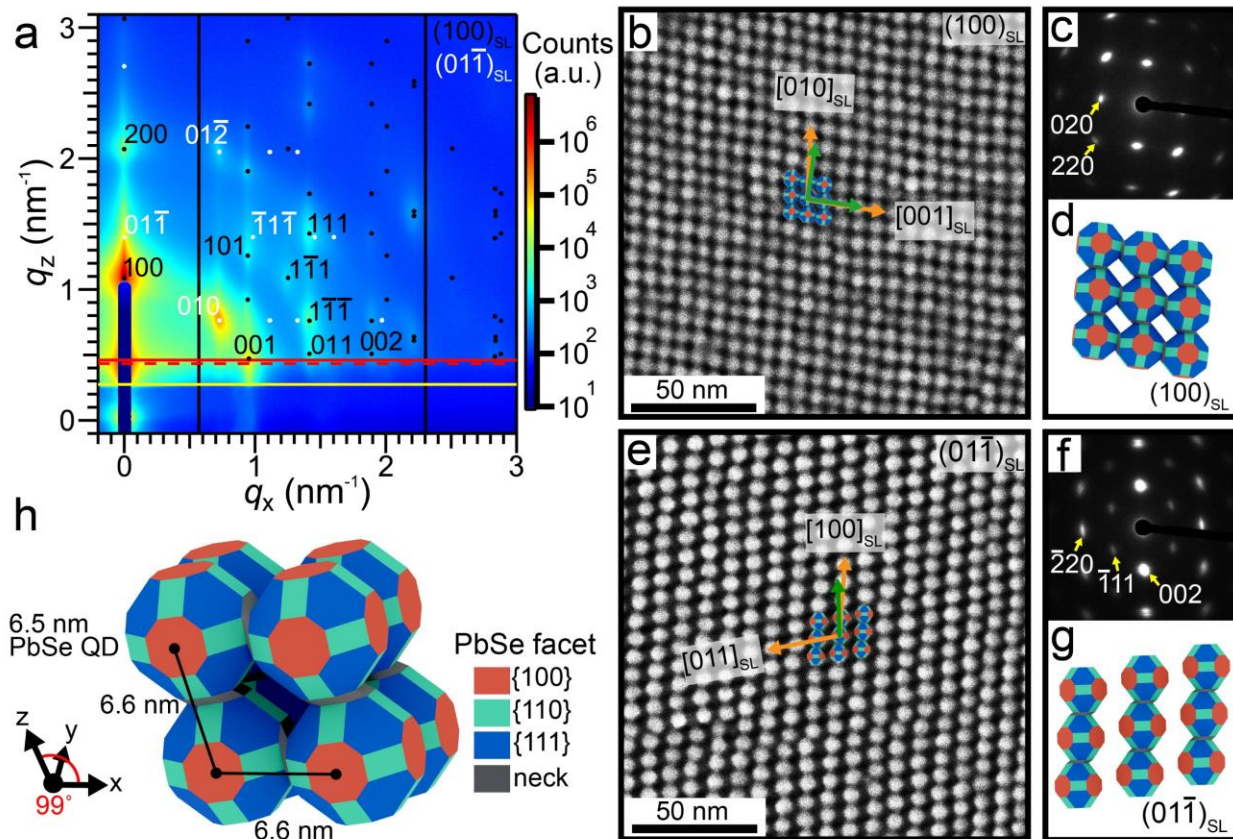


Figure 2.14. Structure of the epi-SL films. a) 2D GISAXS pattern of a typical film on a silicon substrate. Overlaid are the calculated spot patterns for two very similar triclinic unit cells, one (black dots) with  $(100)_{\text{SL}}$  in-plane orientation ( $a = 6.5 \text{ nm}$ ,  $b = c = 6.7 \text{ nm}$ ,  $\alpha = 97^\circ$ ,  $\beta = \gamma = 99^\circ$ ) and the other (white dots) with  $(01\bar{1})_{\text{SL}}$  in-plane orientation ( $a = b = c = 6.5 \text{ nm}$ ,  $\alpha = 95^\circ$ ,  $\beta = \gamma = 97^\circ$ ). We often observed slightly different lattice parameters for the two grain orientations. Only select Miller indices are labelled. The solid and dashed red lines denote the scattering vector  $q_z$  corresponding to the critical angle of the QD film ( $0.21^\circ$ ) and Si substrate ( $0.180^\circ$ ). The yellow line denotes the substrate horizon. b-d) Correlative TEM imaging and electron diffraction for a single  $(100)_{\text{SL}}$ -oriented grain. b) Secondary electron image of the  $(100)_{\text{SL}}$ -oriented SL grain. Overlaid is a model of the top monolayer of QDs according to the lattice parameters in panel h. Orange arrows denote crystallographic directions of the superlattice, while green arrows indicate two of the  $\langle 100 \rangle_{\text{AL}}$  directions of the PbSe atomic lattice. The scale bar is 50 nm. c) Corresponding SAED pattern of the atomic lattice, with several spots labeled. The zone axis is normal to  $(100)_{\text{SL}}$  and  $\sim 5^\circ$  from  $[001]_{\text{AL}}$ . d) Model of the first monolayer of QDs on this superlattice plane. Red, cyan, and blue facets correspond to the  $\{100\}$ ,  $\{110\}$ , and  $\{111\}$  planes of PbSe. e-g) Correlative TEM imaging and diffraction for a  $(01\bar{1})_{\text{SL}}$ -oriented grain. e) Secondary electron image with overlaid model and crystallographic axes. f) SAED pattern. The zone axis is  $[\bar{1}\bar{1}0]_{\text{AL}}$ . g) Model of the first monolayer of QDs on this superlattice plane. h) The distorted simple cubic unit cell of the epi-fused QD SL ( $a = 6.6 \text{ nm}$  and  $\alpha = 99^\circ$ ). See Figure 2.15 for wide-area SEM images of these films and Figure 2.16 for analysis of a twinned epi-SL grain. From Ref 169. Reprinted with permission from Springer Nature Limited.

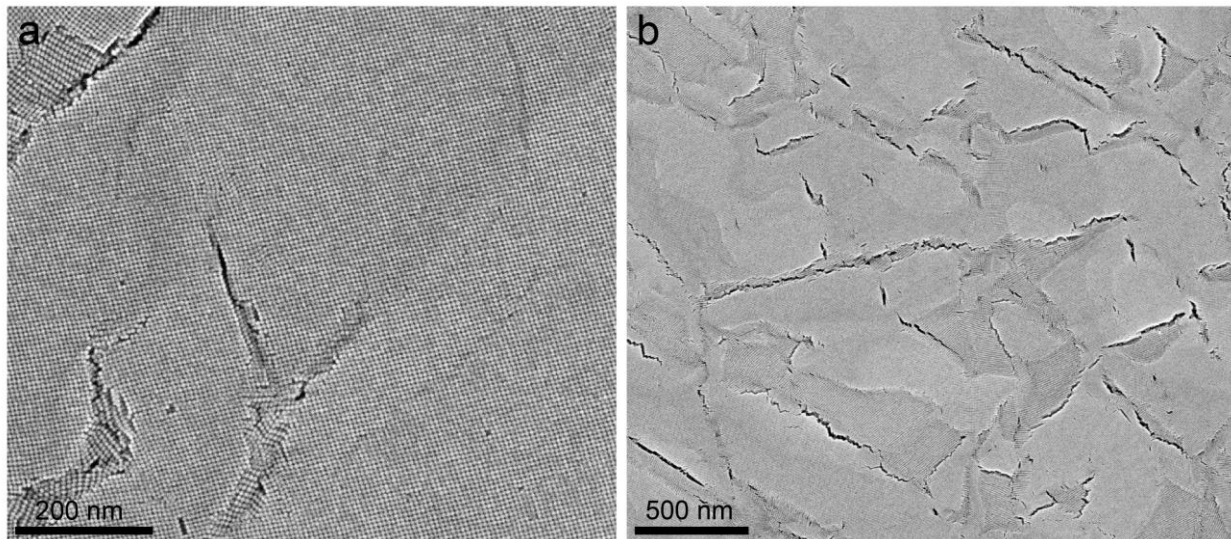


Figure 2.15. Representative SEM images of epi-SLs. a) Medium-magnification image of a single  $(100)_{\text{SL}}$ -oriented grain with some nano-cracks. A few other grains are visible within the cracks and in the upper left corner of the image. b) Lower-magnification image showing a network of nano-cracks. The cracks occur mostly at the SL grain boundaries and are caused by volume loss during oleate removal and QD fusion. Bright regions of the film are  $(100)_{\text{SL}}$ -oriented grains, while darker regions are  $(01\bar{1})_{\text{SL}}$ -oriented grains. Contrast between the grain orientations stems from the different atomic lattice orientations (the in-plane facet is  $(100)_{\text{AL}}$  in  $(100)_{\text{SL}}$ -oriented grains and  $(110)_{\text{AL}}$  in  $(01\bar{1})_{\text{SL}}$ -oriented grains). This epi-SL film was made with EDA and  $\text{PbI}_2$  treatments (no ALD). From Ref 169.

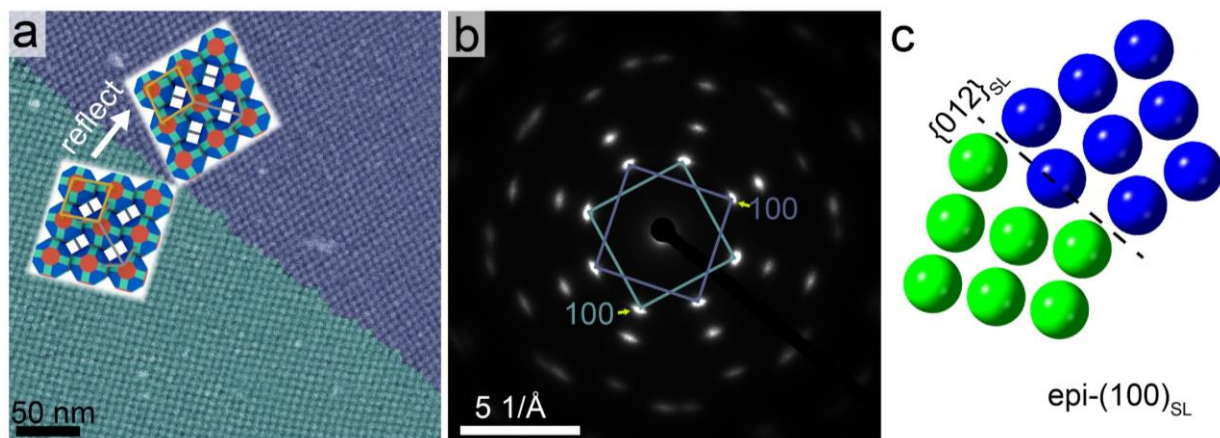


Figure 2.16. Correlated imaging and diffraction of a twinned  $(100)_{\text{SL}}$ -oriented epi-SL grain. a) Secondary electron image of a  $(01\bar{2})_{\text{SL}}/(0\bar{2}1)_{\text{SL}}$  twin boundary. QD models of the twin surfaces are inset. The scale bar is 50 nm. b) SAED pattern of the same area, color coded to match the image. c) Model of the epi-SL twin boundary. The dashed line denotes the twin plane. From Ref 169.



The unit cell of the epi-SL films was determined in the same fashion. GISAXS/SEM analysis shows that the films are polycrystalline SLs with a triclinic primitive unit cell with lattice parameters  $a \approx b \approx c = 6.6 \pm 0.2$  nm and  $\alpha \approx \beta \approx \gamma = 99 \pm 2^\circ$  and a mixture of  $(100)_{\text{SL}}$  and  $(01\bar{1})_{\text{SL}}$  in-plane grain orientations (Figure 2.14a). The average structure can be described as a slightly-distorted simple cubic primitive cell or a highly-distorted bcc conventional cell (see Figure 2.21). We use the distorted simple cubic description because it is easier to visualize. As in the oleate-capped SL, each QD in the epi-SL has six nearest neighbors arranged in a rhombohedrally-distorted octahedron, but with a much smaller center-to-center distance (6.5-6.7 nm vs. 8.2 nm) because the QDs in the epi-SL are fused with epitaxial necks 1-3 atomic layers in length. Our previous TEM studies demonstrated that Pb and Se atoms flow from adjoining facets into the neck regions during epi-fusion of PbSe QDs, thereby distorting the QD shape.<sup>178</sup> Examples of  $(100)_{\text{SL}}$ - and  $(01\bar{1})_{\text{SL}}$ -oriented grains are shown in Figure 2.14b-d and Figure 2.14e-g, respectively. The  $(100)_{\text{SL}}$  grains appear in secondary electron images as quasi-square 2D lattices, while the  $(01\bar{1})_{\text{SL}}$  grains feature parallel chains of fused QDs (Figure 2.14b and e). The latter morphology is expected for a  $\{110\}$  projection of a simple cubic lattice, where the inter-QD distance is  $a$  within the chains and  $a\sqrt{2}$  between the chains. The AL and SL are crystallographically related as  $(110)_{\text{AL}} \parallel (01\bar{1})_{\text{SL}}$  and  $[100]_{\text{AL}} \parallel \angle 5^\circ [100]_{\text{SL}}$ . Figure 2.14h depicts the average epi-SL unit cell (ligands omitted).

We next evaluated necking and epitaxial fusion between QDs, including neck thickness and uniformity, two factors that directly impact the degree and variation of electronic coupling between QDs.<sup>123,135,146</sup> Because our SLs are 3D and non-cubic, direct imaging does not allow for precise analysis of individual necks. We therefore use a variety of techniques to assess epitaxial fusion in our 3D epi-SLs. High-resolution TEM images of 3D epi-SLs (Figure 2.17) show continuous PbSe

lattice along  $[100]_{\text{SL}}$ , which strongly suggests that epitaxial connections extend between QDs in that direction.

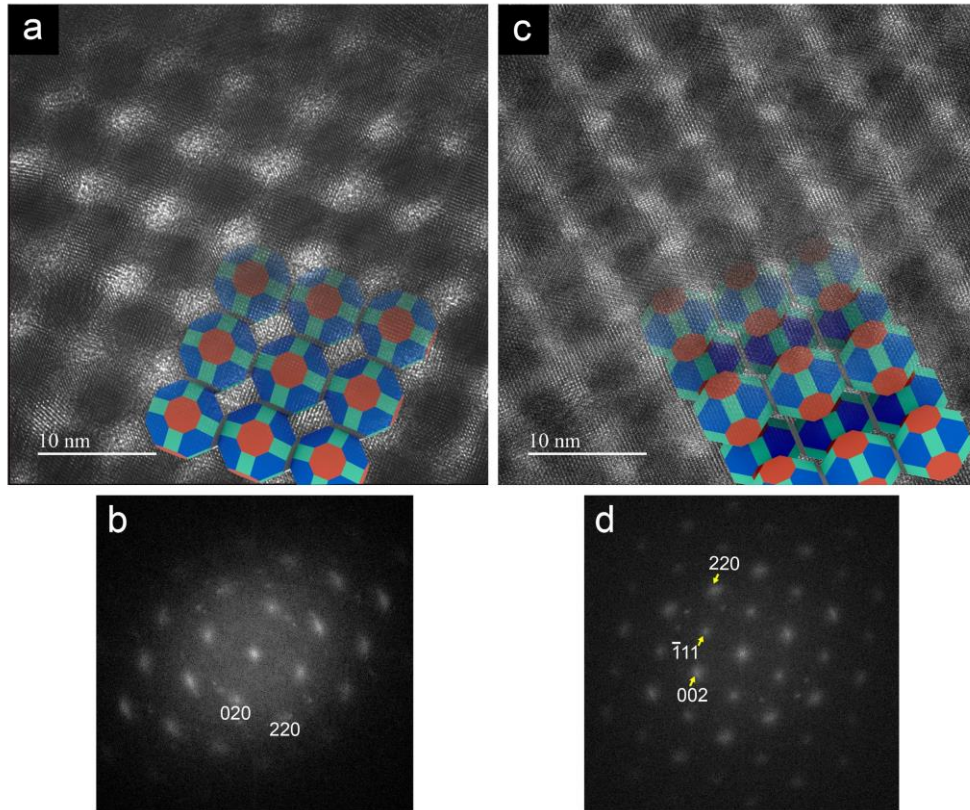


Figure 2.17. TEM images of 3D epi-SLs showing QD fusion along the  $\langle 100 \rangle_{\text{AL}}$  directions. a) High-resolution image of a  $(100)_{\text{SL}}$ -oriented epi-SL grain (EDA/PbI<sub>2</sub> treated), showing clear epitaxial fusion between QDs along the two in-plane  $\langle 100 \rangle_{\text{AL}}$  axes. The SL grain is 40-50 nm thick. A structural model of the first QD monolayer is superimposed on the image. b) 2D fast Fourier transform of the TEM image, with the 020 and 220 spots labeled. c) High-resolution image of a  $(01\bar{1})_{\text{SL}}$ -oriented epi-SL grain (EDA/PbI<sub>2</sub> treated), showing epitaxially-fused chains of QDs running nearly parallel to the single in-plane  $\langle 100 \rangle_{\text{AL}}$  axis. The QD chains result in regularly-spaced bands running from the lower left to the upper right of the image. The SL grain is 40-50 nm thick. A structural model of the first two QD monolayers is superimposed on the image. d) 2D fast Fourier transform of this image, with the 002, 220, and  $\bar{1}11$  spots labeled. From Ref 169.

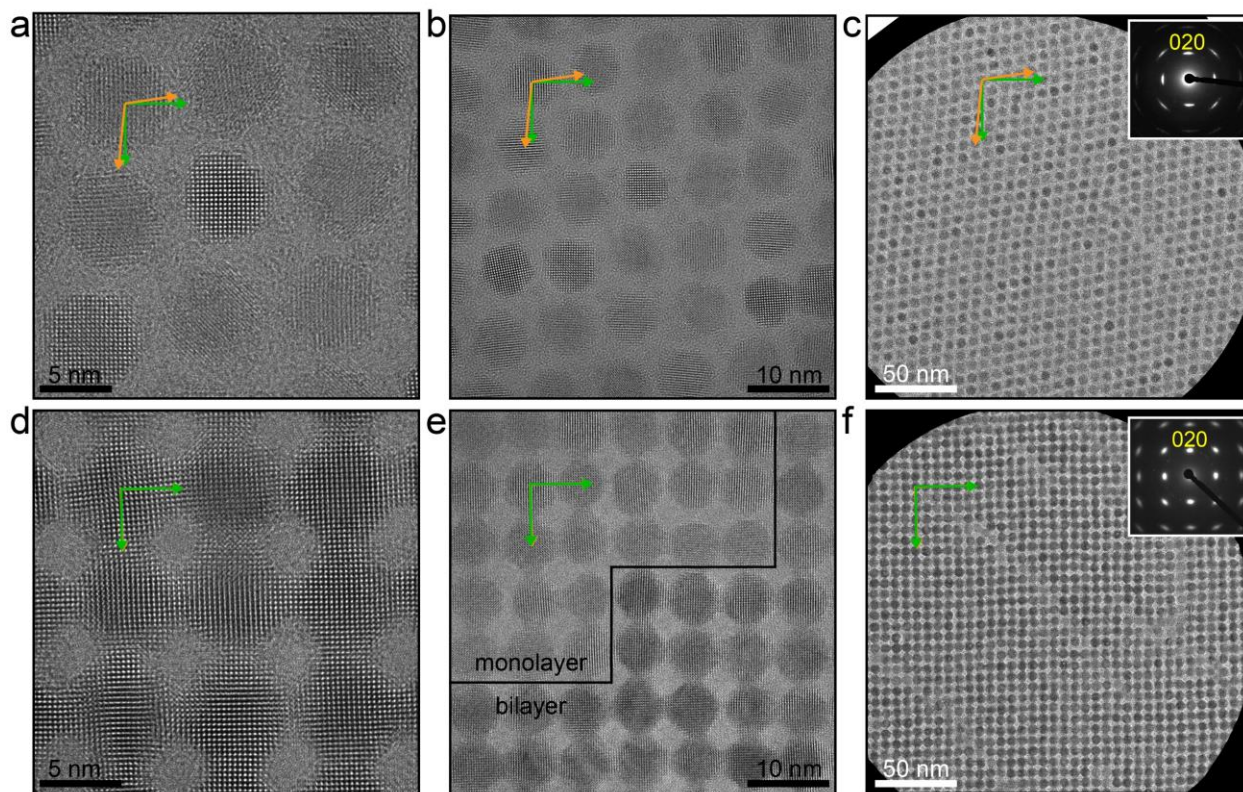


Figure 2.18. TEM images of 2D oleate-capped SL and epi-SLs showing QD fusion along the  $\langle 100 \rangle_{\text{AL}}$  directions. These 2D SLs (QD monolayers and bilayers) were prepared by self-assembly on EG using a low QD concentration. a) TEM image of an oleate-capped 2D SL at high magnification, b) intermediate magnification, and c) low magnification, along with the corresponding SAED pattern (inset). The QDs adopt an oblique 2D lattice nearly identical in structure to the  $(101)_{\text{SL}}$  surface of the 3D oleate-capped SL described in the text. Expressed in terms of a distorted bcc unit cell, the 2D SL has lattice constants  $a = 10.5$  nm and  $\alpha = 84.5^\circ$ , compared to  $a = 9.8$  nm and  $\alpha = 84.5^\circ$  for the 3D oleate-capped SL. The strong SAED spot pattern shows that the QDs are biaxially aligned within the monolayer. The zone axis is  $[100]_{\text{AL}}$ . Each diffraction spot has the shape of a circular arc, indicating some in-plane rotational freedom of the QDs. The 200 spots have an angular width of  $17.3^\circ$  (FWHM). As on the  $(101)_{\text{SL}}$  surface of the 3D SL, each QD in the monolayer has cofacial  $\{100\}$  facets with its four close nearest neighbors. Green and orange arrows denote  $\langle 100 \rangle_{\text{AL}}$  and  $\langle \bar{1}\bar{1}\bar{1} \rangle_{\text{SL}}$ , respectively. Scale bars are labeled. d) TEM image of a 2D epi-SL at high magnification, e) intermediate magnification, and f) low magnification, along with the corresponding SAED pattern (inset). Clear epitaxial fusion along  $\langle 100 \rangle_{\text{AL}}$  is observed. The zone axis is again  $[100]_{\text{AL}}$ . In contrast to the rhombohedrally-distorted 3D epi-SL, the 2D epi-SL is almost perfectly square, even as a bilayer (panels e and f). The diffraction spots are less elongated than in the oleate-capped 2D SL because epi-fusion forces better QD-QD registry and a tighter distribution of QD rotational orientations. The 200 spots have an angular width of only  $13.5^\circ$  (FWHM). Green and orange arrows denote  $\langle 100 \rangle_{\text{AL}}$  and  $\langle 100 \rangle_{\text{SL}}$ , respectively. Scale bars are labeled. From Ref 169.

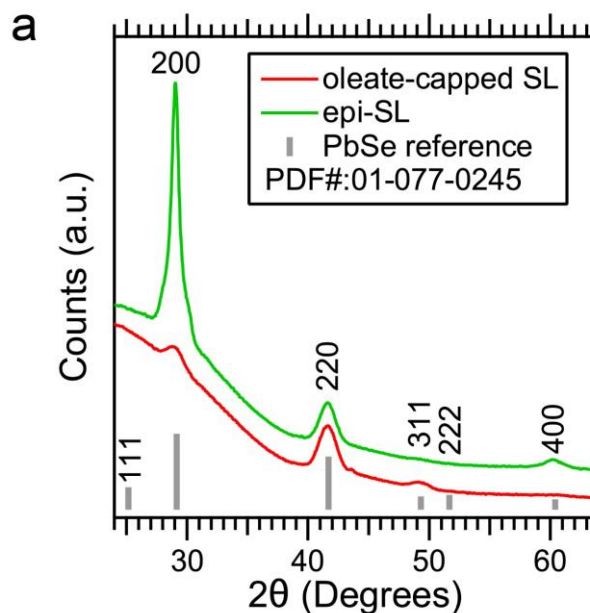


Figure 2.19. Representative wide-angle  $\theta$ - $2\theta$  XRD patterns of oleate-capped and epi-SL films. Films were deposited on glass slides. Relative to the PbSe powder reference pattern (gray bars), the oleate-capped SL (red trace) is highly textured, with only a 220 peak (from the  $(10\bar{1})_{\text{SL}}$ -oriented grains, see Fig. 2g), a small 200 peak (from the  $(101)_{\text{SL}}$ -oriented grains, Fig. 2d), and a proportional 311 peak (from  $(101)_{\text{SL}}$ -oriented SL grains containing QDs with their  $(311)_{\text{AL}}$  planes parallel to the film surface). The epi-SL (green trace) shows a similarly-sized 220 peak (from the  $(01\bar{1})_{\text{SL}}$ -oriented grains) and a very strong 200 peak (from the  $(100)_{\text{SL}}$ -oriented grains), with no other atomic lattice orientations visible. The height of the 220 peak is similar for both films because this plane remains parallel to the film surface when the oleate- $(10\bar{1})_{\text{SL}}$  grains transform to epi- $(01\bar{1})_{\text{SL}}$  grains. The phase transition involves a small ( $10^\circ$ ) rotation of the QDs about their  $[110]_{\text{AL}}$  axes, so the tilt of the  $(110)_{\text{AL}}$  planes does not change. The width of the 220 peak is also similar for both films because the QDs fuse across their  $\{100\}$  facets, not their  $\{110\}$  facets. In contrast, the 200 peak is both taller and narrower after epi-fusion. This peak grows in height because the phase transformation brings the  $(200)_{\text{AL}}$  planes, which are slightly tilted ( $\sim 15^\circ$ ) from the film surface in the oleate- $(101)_{\text{SL}}$  grains, into nearly-perfect parallel alignment with the film surface in the epi- $(100)_{\text{SL}}$  grains, thereby boosting the diffracted intensity. The observed narrowing of the 200 peak is consistent with an increase in crystallite size along the  $\langle 100 \rangle_{\text{AL}}$  directions due to fusion of QDs across their  $\{100\}$  facets. The epi-SL was made using EDA and  $\text{PbI}_2$  treatments, without ALD. From Ref 169.

Table 3. Results of Scherrer XRD crystallite size analysis.

Sample	$\langle 200 \rangle$ Crystallite Size (nm)	$\langle 220 \rangle$ Crystallite Size (nm)
oleate-capped SL	$6.4 \pm 0.06$	$6.6 \pm 0.3$
epi-SL	$9.2 \pm 0.03$	$7.0 \pm 0.2$

To directly observe epitaxial necks, we made and imaged SL monolayers assembled on EG. Our oleate-capped SL monolayers adopt an oblique 2D lattice nearly identical to the  $(101)_{\text{SL}}$  of the 3D

oleate-capped SL, with the same biaxial QD alignment preserved (Figure 2.18). Treatment with EDA produces a square lattice monolayer of QDs with alignment between  $[100]_{\text{SL}}$  and  $\{100\}_{\text{AL}}$  facets and clearly visible epitaxial necks between NNs. X-ray diffraction (XRD) measurements (Figure 2.19) of oleate-capped and epi-SL films support the biaxial QD/SL relationships described above, and provide evidence for epi-fusion of  $\{100\}_{\text{AL}}$  facets throughout the 3D bulk of the SL. Scherrer crystallite size analysis of PbSe  $\langle 200 \rangle$  and  $\langle 220 \rangle$  peaks shows (Table 3) that after EDA treatment the QDs coarsen along  $\langle 200 \rangle$ , as is expected for  $\{100\}_{\text{AL}}$  epi-fusion. Crystallite size along  $\langle 220 \rangle$  does not change significantly because no epi-fusion occurs along that crystallographic direction.

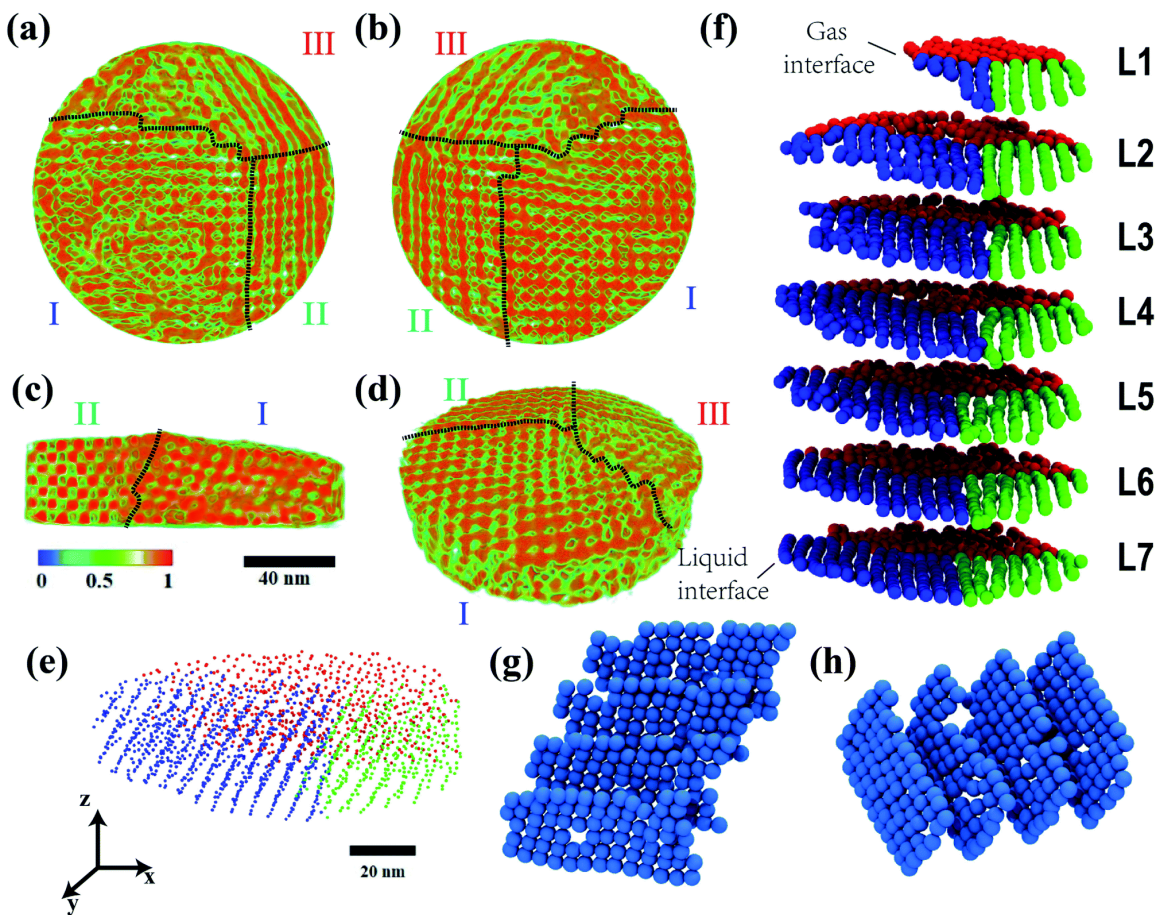


Figure 2.20. The epi-SL tomogram and QD positions. a) Top, b) bottom, c) cross-section, and d) perspective views of the tomogram of the epi-SL film. The color scale denotes the normalized electron density in units

of  $e^-$  per  $\text{nm}^3$ . Dashed lines represent grain boundaries between the three SL grains (labeled grain I, II, and III). The scale bar is 40 nm. e) Perspective image of the center of mass coordinates of all QDs in the sample. Each QD is represented by a sphere with a diameter of 1 nm (for ease of viewing). The QDs are color coded according to their location in grain I (blue), grain II (green), or grain III (red). The scale bar is 20 nm. f) Exploded view of the seven QD layers of the sample to illustrate the internal structure of the epi-SL film. Each QD is represented by a 6 nm diameter sphere. Layer 1 (L1) is the top layer of the originally floating film (at the QD/gas interface), while layer 7 (L7) is the bottom layer of the film (at the liquid/QD interface). The QDs are color coded according to panel (e). g-h) Representative monolayers in grain I separated along direction  $x$  and  $y$ , representing SL lattice planes of (g)  $(100)_{\text{SL}}$  and (h)  $(010)_{\text{SL}}$ . From Ref 170. See that paper for more details on sample preparation, measurement, and analysis methods.

Table 4. Statistics from structural analysis of an epi-SL tomogram.

Parameter	Grain I	Grain II	Grain III	Total
Number of QDs	903	389	554	1846
Space filling fraction	0.53	0.51	0.48	0.51
Possible necks	2343	1028	1494	4865
Observed necks	1760	774	959	3493
Connectivity	75%	75%	64%	72%
Average number of necks	3.8	4.0	3.4	3.7
Average neck diameter (nm)	4.0	3.5	5.0	4.1

We also performed full-tilt HAADF-STEM electron tomography<sup>170</sup> on an epi-SL needle sample prepared using focused ion beam milling.<sup>iv</sup> An example tomogram (Figure 2.20) shows a 7-layer polycrystalline epi-SL composed of 1846 PbSe QDs. With a spatial resolution of 0.65 nm, we were able to quantify neck thickness and other structural parameters of the epi-SL (Table 4). The QDs in the more ordered region of the sample (Grains I and II) have an average of 3.8 to 4.0 necks per QD out of a total of 6 possible necks for the distorted simple cubic epi-SL structure. The average neck diameter ranges between 3.5 to 4.0 nm, which corresponds to 53-61% of the original QD diameter. This degree of epitaxial necking should produce extremely strong electronic coupling. Data from this single tomogram highlights the need for improved structural perfection and control in the self-assembly and epitaxial fusion processes. Future experiments within our group aim to

<sup>iv</sup> This work was performed in collaboration with the Moulé group at UC Davis and is described in Ref 170.

make strong structure/property relationships through iterative feedback and insight from electron tomography measurements. Efforts to control the atomic-scale structure of epi-SLs are underway in other laboratories, for example, through the use of thermal annealing.<sup>160,172</sup>

#### ***2.4. Collective Topo-epitaxy***

How does the oleate-capped SL transform into the epi-SL? Figure 2.21 shows our proposed pathway of the phase transition from the oleate-capped SL to the epi-SL. The phase transition is triggered by the removal of oleate and is driven by the lower surface area and free energy of the epi-SL. Because the QDs in the oleate-capped SL are biaxially aligned with cofacial  $\{100\}$  facets, formation of the epi-SL requires only translation and a  $10^\circ$  rotation of each QD about a common  $[110]_{\text{AL}}$  axis. The coordination polyhedron of the SL (the rhombohedrally-distorted octahedron, Figure 2.21) is conserved during this phase transition and, while we emphasize different unit cells before and after epi-fusion, the topology of the QD array remains fundamentally unchanged. We find that the  $(101)_{\text{SL}}$ - and  $(10\bar{1})_{\text{SL}}$ -oriented grains of the oleate-capped SL convert to  $(100)_{\text{SL}}$ - and  $(01\bar{1})_{\text{SL}}$ -oriented grains of the epi-SL, respectively, as discussed above and shown in Figure 2.21b-c.

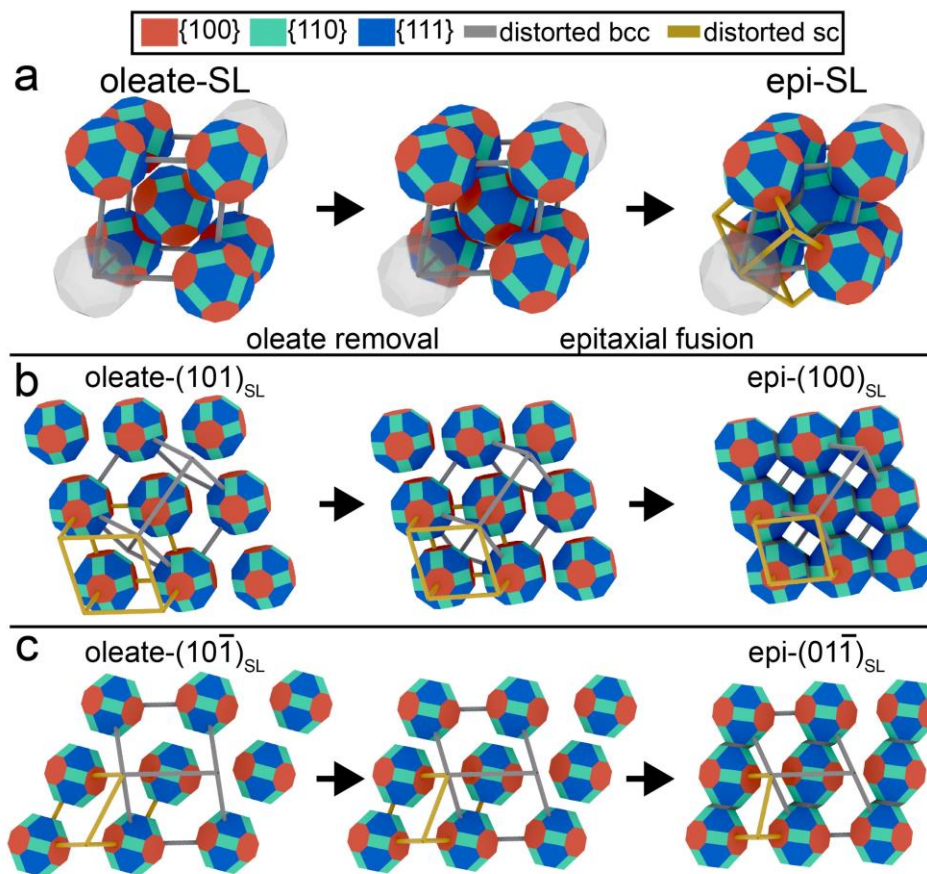


Figure 2.21. The phase transition pathway. Formation of the epi-SL proceeds by nearly-pure translational motion of the QDs. a) Transformation of the unit cell. (left) The distorted bcc unit cell of the oleate-capped SL emphasizing the distorted octahedral, {100}AL-cofacial coordination environment of each QD. As oleate is removed (center), there is a ~1.6 nm translation of the corner QDs toward the center QD and slight rotation ( $10^\circ$ ) of all of the QDs about a common [110]AL axis (in-plane for (100)SL-oriented grains and out-of-plane for (011̄)SL-oriented grains) to form the epi-SL (right). Pb and Se atoms flow into the interfacet regions to form epitaxial necks that are 0.5-1 unit cells long. Gray and yellow unit cells correspond to the distorted bcc conventional cell and distorted simple cubic primitive cell, respectively. Red, cyan, and blue facets correspond to the {100}, {110}, and {111} planes of PbSe. Dark gray shading denotes the epitaxial necks between QDs. b) Transformation of the (101)SL surface of the oleate-capped SL to the (100)SL surface of the epi-SL. c) Transformation of the (101̄)SL surface of the oleate-capped SL to the (011̄)SL surface of the epi-SL. From Ref 169. Reprinted with permission from Springer Nature Limited.

This phase transition is a striking example of collective, multiscale topotaxy and epitaxy in a colloidal nanocrystal solid. Formation of the epi-SL involves 3D epitaxial attachment of the  $10^3$ - $10^5$  QDs in each SL grain. The parent and product SLs are single crystals (in both the AL and SL) related by a specific geometric transformation. Thus, the SLs have a definite 3D crystallographic



relationship and the phase transition is atomically topotactic. The topotactic relationship between the SLs is  $(10\bar{1})_{\text{oleate-SL}} \parallel (01\bar{1})_{\text{epi-SL}}$  and  $[1\bar{1}1]_{\text{oleate-SL}} \parallel \angle 15.5^\circ [100]_{\text{epi-SL}}$ . Knowing that the mechanism is topotactic will help researchers improve the spatial order of these epi-SLs by optimizing the structure of the oleate-capped SLs and controlling the kinetics of the phase transition.

Given the topotactic phase transition, it is especially important to understand why the oleate-capped SLs adopt a distorted bcc unit cell with cofacial  $\{100\}$  QDs. Studies of truncate-cubic PbS/Se QDs and metallic NCs show acute or obtuse rhombohedral structures with partial overlap of  $\{100\}$  crystal facets.<sup>76,78,162,211</sup> While fcc structures are expected in assemblies of hard spheres, the driving force for bcc assembly is attributed primarily to entropy maximization of ligand packing.<sup>73</sup> In QD SLs with  $L/R_{\text{QD}} > 0.6$  (where  $L$  is the nominal ligand length and  $R_{\text{QD}}$  is the QD radius) and weak inter-QD attractive forces ( $< 0.1kT$ ), the bcc structure was found to maximize entropy due to reduced ligand packing frustration.<sup>80</sup> Several studies have emphasized that the SL unit cell is determined by the effective QD shape, which is a convolution of QD faceting and ligand coverage.<sup>81,189,207</sup> Shape anisotropy drives orientational ordering of the QDs that in turn determines the superlattice symmetry. In the present case, we speculate that there is a steric and/or electrostatic driving force for cofacial alignment of the  $\{100\}$  QD facets. If cofacial  $\{100\}$  facet alignment lowers the SL energy, then a rhombohedral distortion from a perfect bcc unit cell is expected because such a distortion increases  $\{100\}$  facet overlap (Figure 2.23). A perfect bcc cell (lattice angle  $\alpha = 90^\circ$ ) provides very poor  $\{100\}$  facet overlap (extremely distorted octahedral coordination with the six nearest neighbors having the best  $\{100\}$  facet alignment). In the opposite limit of extreme rhombohedral distortion ( $\alpha = 60^\circ$ ), the SL has a simple cubic unit cell with perfect octahedral coordination and maximum  $\{100\}$  facet overlap between the QDs (at least seven times

greater overlap area than for bcc). The fact that the oleate-capped SL adopts a structure between simple cubic and body-centered cubic suggests a metastable state due to competing forces: entropic contributions drive the SL towards a bcc structure,<sup>73,79,80</sup> however weak ligand coverage on {100} facets leads (i) a non-spherical effective QD shape and (ii) stronger electrostatic interactions between them. Increasing the oleate coverage should reduce directional inter-QD forces and eventually may result in a loss of QD rotational alignment, although long-range (>5 nm) inter-particle torque has been observed.<sup>83,156</sup> We hypothesized that an increase in overall oleate coverage (and thus, the {100} coverage; see Figure 2.4) would cause the oleate-capped SL to shift towards a more perfect bcc structure. We reasoned that lower oleate coverage should increase the driving force for {100} facet overlap and result in more distorted (less bcc-like) SLs.

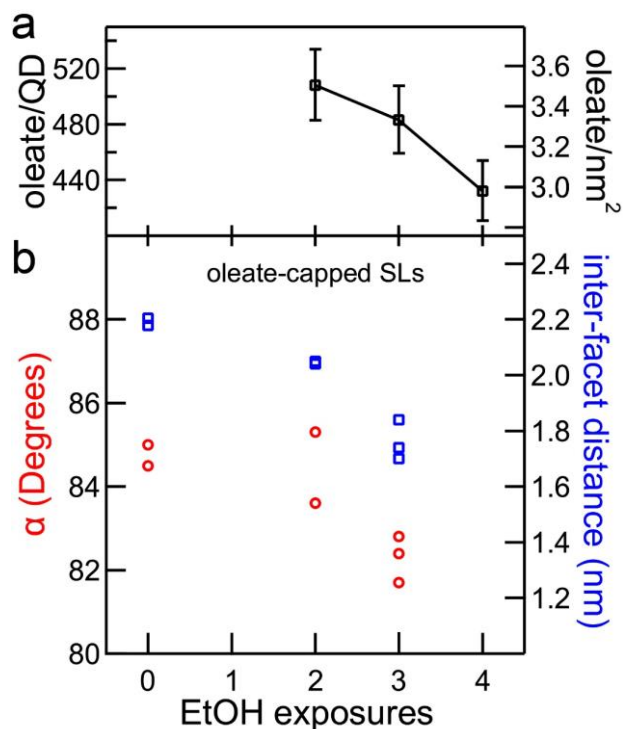


Figure 2.22. Impact of QD cleaning cycles on oleate coverage and the size of the rhombohedral distortion of the oleate-capped SLs. a) The number of oleate ligands per QD versus the number of EtOH cleaning cycles as determined by quantitative NMR (see Table 5). Oleate surface coverage (oleate/nm<sup>2</sup>) is calculated assuming a surface area of 145 nm<sup>2</sup> per QD. b) Measured lattice angle ( $\alpha$ ) of the distorted bcc unit cell (red circles) and distance between the {100} facets of neighboring QDs (blue squares) for oleate-capped SLs made from QDs with zero, two, or three EtOH cleaning cycles. Samples with zero EtOH exposures were

cleaned with three cycles of precipitation in acetonitrile and redispersion in toluene, which should result in QDs with the highest oleate coverage in this series of samples.<sup>94</sup> With decreasing oleate coverage, the rhombohedral distortion becomes more severe (smaller  $\alpha$ ) and the distance between {100} facets decreases (the unit cell shrinks). These data were assembled from seven batches of QDs with first exciton peak energies of 0.668-0.685 eV. We note that the epi-SL can be described as a distorted bcc structure with  $\alpha = 71.66^\circ$  and an inter-facet distance of 0.3-0.4 nm, while a distorted bcc cell with  $\alpha = 60^\circ$  is equivalent to a perfect simple cubic structure. From Ref 169.

Table 5. NMR quantification of oleate ligand coverage.

cleaning cycles	oleate ligands per QD	oleate/nm <sup>2</sup>	oleate removal (% from cycle #2)
2	505 ± 28	3.48 ± 0.19	0
3	478 ± 26	3.30 ± 0.18	5 ± 7
4	430 ± 24	2.97 ± 0.16	15 ± 7

Indeed, we find that the rhombohedral distortion systematically increases from  $\alpha = 85.0^\circ$  to  $\alpha = 82.0^\circ$  with decreasing oleate coverage (Figure 2.22). A preference for cofacial {100} facets explains the observed rhombohedral distortion and the increasing distortion with decreasing ligand coverage. Control of the rhombohedral distortion has practical importance because oleate-capped SLs with more {100} facet overlap are better positioned for fusion and may produce epi-SLs of greater structural perfection. In contrast, reducing the oleate coverage leads to stronger inter-QD attractive forces, smaller SL grains, and premature epi-fusion of {100} facets.

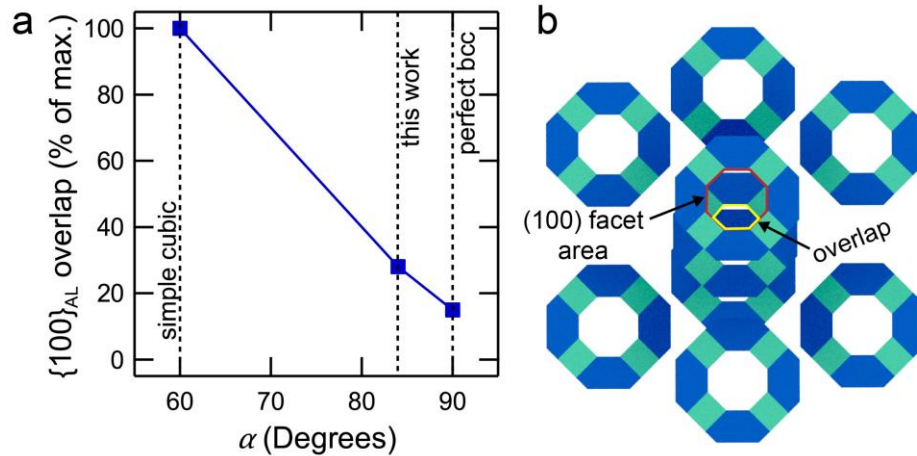


Figure 2.23.  $\{100\}_{AL}$  facet overlap as a function of lattice angle  $\alpha$  for oleate-capped SLs with rhombohedrally-distorted bcc unit cells. a)  $\{100\}$  facet overlap versus  $\alpha$ . The distance between  $\{100\}$  facets was held constant at 2.1 nm. When  $\alpha = 60^\circ$ , the unit cell is simple cubic and each QD has ideal octahedral coordination with the possibility of perfect overlap of its six  $\{100\}$  facets with its six nearest neighbors. The maximum overlap area is then the entire  $\{100\}$  facet (100%). When  $\alpha = 90^\circ$ , the unit cell is bcc and each QD has cubic (8-fold) coordination with a maximum  $\{100\}$  facet overlap area almost seven times smaller (15%). The unit cell with  $\alpha \sim 84.5^\circ$  shown in Figure 2.10h has an overlap area of 28%. The overlap increases as  $\alpha$  is further reduced. We note that decreasing the inter-facet distance will also increase facet overlap for a fixed  $\alpha$ . b) A model of the oleate-capped SL with  $\{100\}$  facets rendered transparent. To determine the areal overlap, the view direction was aligned with  $\langle 100 \rangle_{AL}$  and the entire facet area (red lines) and overlap area (yellow lines) were measured. The percent overlap of each of the three orthogonal pairs of  $\{100\}$  facets was averaged and plotted in panel a. From Ref 169.

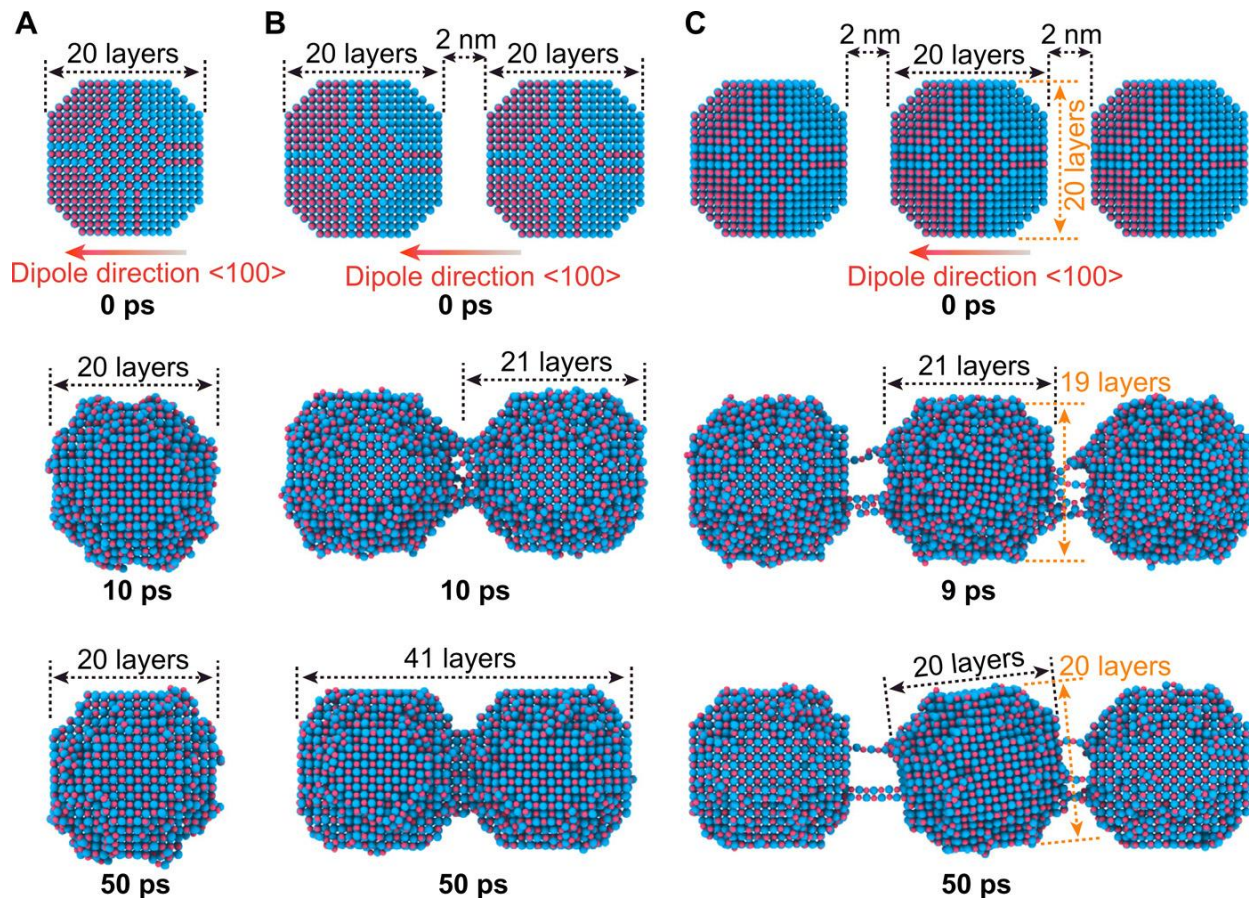


Figure 2.24. Molecular dynamics simulation on the deformability of polar PbSe QDs. Atom color code: blue, Pb; pink, Se. a) Snapshots of the trajectory of single-dipolar nanocrystal at 300 K, starting with a dipole moment caused by fast ligand removal. Polar nanocrystal monomer exhibits the tendency to become symmetrized through surface atom diffusion; nevertheless, this does not lead to formation of extra lattice fringes along  $\langle 100 \rangle$  directions. b) Snapshots of the trajectory of two dipolar nanocrystals initially aligned along the dipole direction with a gap distance of 2 nm at 300 K. Translation and rotation of the two nanocrystals centers are not restricted, allowing them to move toward each other and get attached. Although the two nanocrystals move toward each other, their deformation happens before they touch each other, and the resulting edge-to-edge distance is 12.3 nm (41 layers) larger than the distance shown by two nanocrystals rigidly touch with each other (12.0 nm, 40 layers). c) Snapshots of the trajectory of three dipolar nanocrystals aligned with the same dipole direction with gap distances of 2 nm at 300 K. Translation and rotation of the two outside nanocrystal centers are eliminated, whereas the middle one is free to translate and rotate, imitating the situation of the boundary of two superlattice matrices. From Ref 178. Reprinted with permission from AAAS.

In-situ TEM experiments and molecular dynamics simulations show that, following oleate exchange and the concomitant reduction in inter-QD distance, the QDs can deform prior to epitaxial fusion (Figure 2.24). In this model of oriented attachment, molecular filaments form

bridges between neighboring QDs which can then either grow to irreversibly form necks, or detach. The contribution of specific inter-QD forces (osmotic, Coulomb, van der Waals, entropic) that lead to QD orientation and attachment are not completely understood, however these experiments and MD simulations show the dynamic nature of the epitaxial fusion process.<sup>83</sup>

### ***2.5. Effects of Atomic Layer Deposition***

We assessed the structural and electronic impact of infilling and overcoating the epi-SLs with amorphous alumina by ALD. Previous work has shown that ALD infilling can greatly improve the electrical properties and environmental stability of QD solids.<sup>9,114</sup> We expected this approach to also be useful for tuning the surface chemistry and doping of the epi-SLs. XRD and GISAXS data prove that ALD infilling leaves the QD size, unit cell, and spatial order of the epi-SLs unchanged (Figure 2.25 and Figure 2.26). Cross-sectional elemental mapping of single SL grains by STEM-based energy dispersive spectroscopy shows that the alumina infilling is uniform (Figure 2.27a-b). However, infilling also causes a nearly-complete bleach of the first exciton peak and the appearance of a 1S-1P intraband transition in optical absorption spectra, consistent with very strong doping of the epi-SLs by the ALD coating (Figure 2.27c).<sup>47,48</sup> Field-effect transistor electrical measurements corroborate these changes in the optical spectra. Before ALD, the epi-SLs act as ambipolar transistors with dominant p-channels and free carrier concentrations low enough to be readily modulated with an applied gate bias (Figure 2.27d and Figure 2.29).

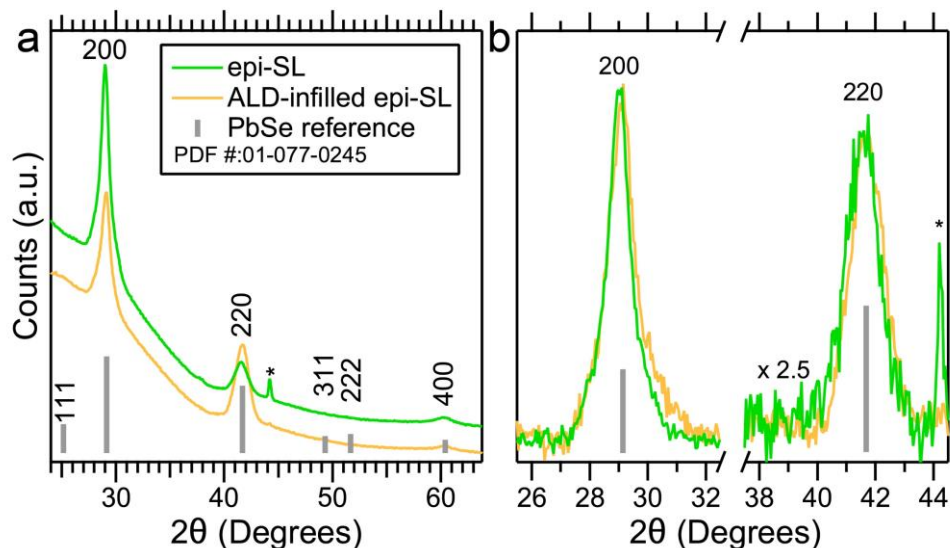


Figure 2.25. Wide-angle  $\theta$ - $2\theta$  XRD patterns of an epi-SL showing no change in QD size after ALD infilling. a) XRD patterns of epi-SLs with and without ALD infilling. The two samples have different 220 and 200 peak intensities because the parent oleate-capped SLs had different percentages of the two SL grain orientations, not because ALD infilling changes the grain orientations. The small peak at  $44.2^\circ$  (\*) is an artifact from the instrument. b) Magnified views of the normalized 200 and 220 peaks, showing no significant change in peak width (QD size) after ALD infilling. From Ref 169.

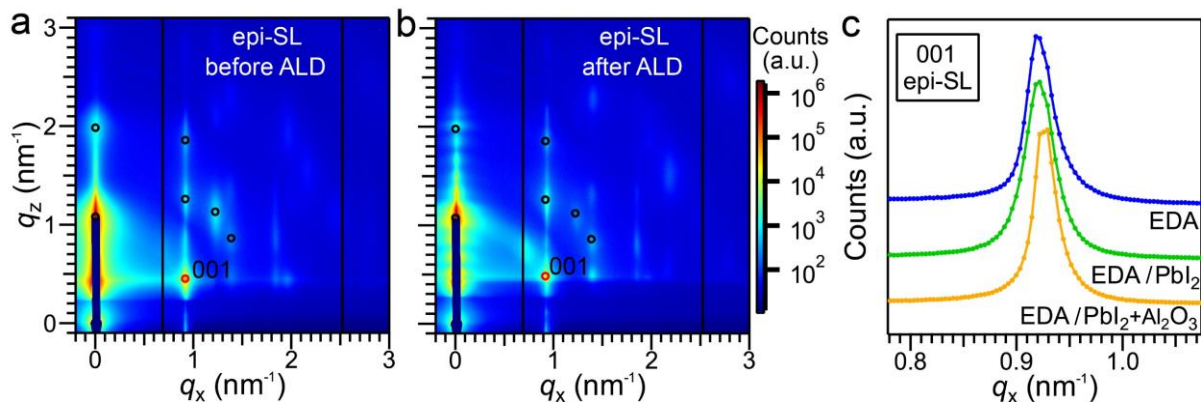


Figure 2.26. Effect of ALD alumina infilling on the epi-SL structure. a-b) GISAXS patterns of  $\text{PbI}_2$ -treated epi-SLs before and after alumina infilling. There is no discernable change in SL structure or spatial order. Open black circles mark several diffraction spots of the pre-ALD film to illustrate the negligible shift in peak positions. Intensity oscillations along  $q_z$  in the post-ALD film result from interference of X-rays within the 30 nm thick alumina overlayer. c) Vertically-integrated line profiles of the  $001_{\text{AL}}$  diffraction spot (labeled with red circles in panels a and b). Data for an epi-SL prior to  $\text{PbI}_2$  treatment are also shown (blue). The variation in peak positions corresponds to a real space scatter of  $\sim 1 \text{ \AA}$ . Together, these data show that the epi-SL is quite rigid, such that subsequent treatments ( $\text{PbI}_2$  and ALD infilling) have little effect on its structure.

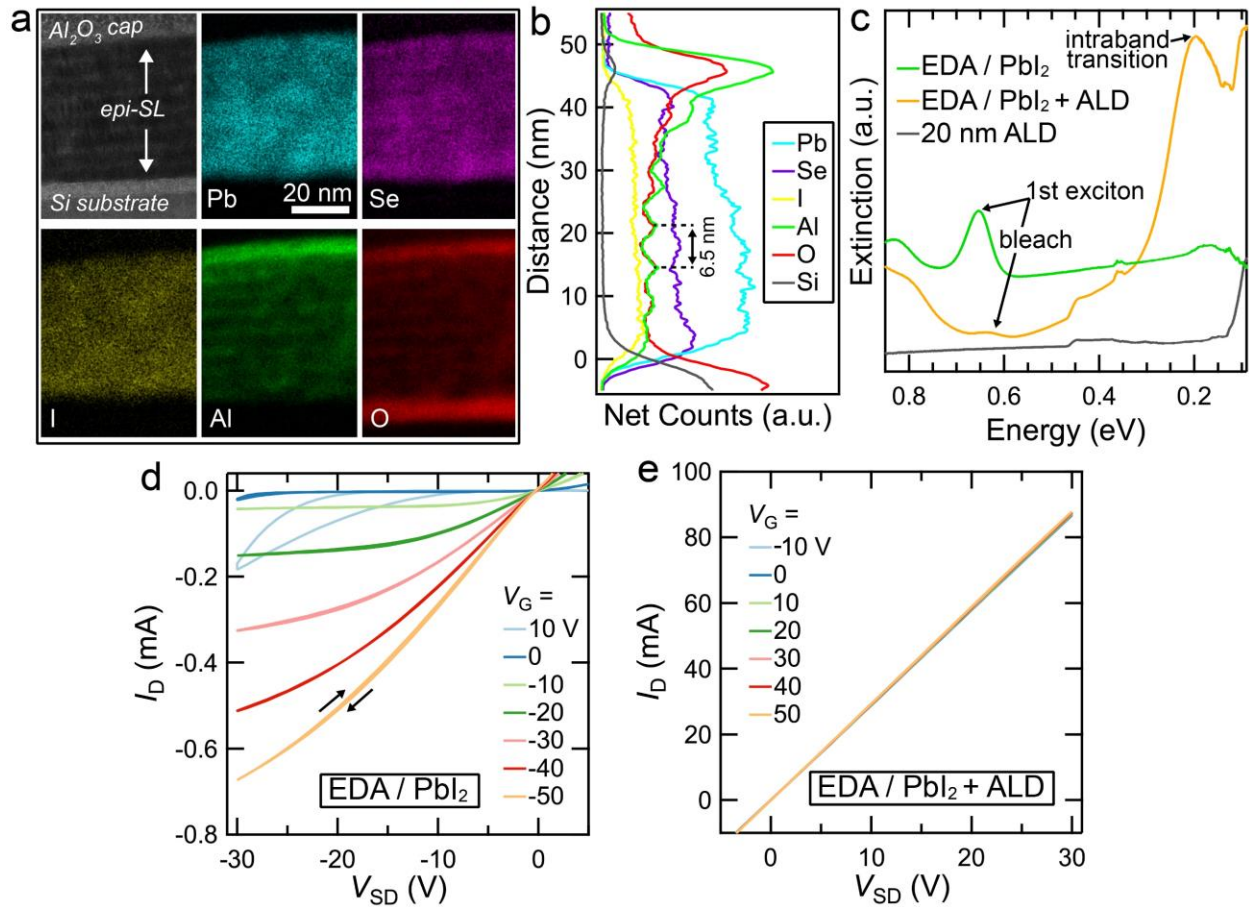


Figure 2.27. Effect of ALD alumina infilling on the epi-SL chemical, optical, and electronic properties. a) Bright-field STEM image and EDS elemental maps of a cross-section of a 51 nm (8 QD layer) thick, (100)<sub>SL</sub>-oriented, alumina infilled epi-SL prepared on a Si substrate by focused ion beam. b) The integrated line profiles of each element along the film normal. Aluminum and oxygen are present throughout the film, indicating complete ALD infilling. The aluminum and oxygen signals oscillate with a period of ~6.5 nm because the infilled void space is arranged in interconnected channels running along the <100><sub>SL</sub> directions, parallel to the substrate surface (Figure 2.28). An SiO<sub>2</sub> interlayer (6 nm thick) and Al<sub>2</sub>O<sub>3</sub> capping layer (8 nm thick) are also evident. Lead, selenium, and iodine are distributed homogeneously throughout the film. c) FTIR spectra of an epi-SL before and after alumina infilling and overcoating (20 nm of alumina). Infilling results in a strong bleach of the first exciton peak and appearance of a 1S-1P intraband peak at ~0.2 eV. The spectrum of a 20 nm thick ALD alumina film (no QDs) is shown for reference. d) Output characteristics of a PbI<sub>2</sub>-treated epi-SL field-effect transistor (FET) before ALD infilling, showing substantial modulation of the source-drain current ( $I_D$ ) by the gate bias ( $V_G$ ). e) Output characteristics of an epi-SL transistor after infilling with amorphous alumina, showing loss of gate modulation due to high doping. From Ref 169. Reprinted with permission from Springer Nature Limited.



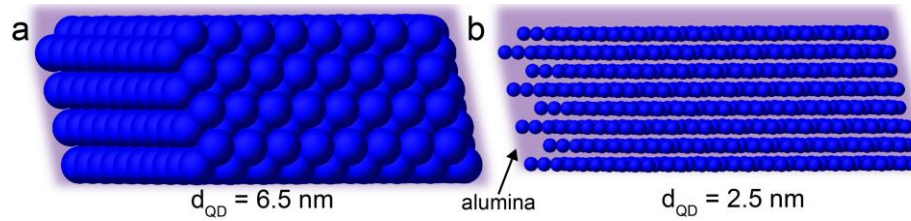


Figure 2.28. Model of the ALD-infilled epi-SL sample shown in Figure 2.27a-b. a) Cross-sectional view of the (100)SL-oriented epi-SL grain with the QDs drawn to scale (6.5 nm diameter). The zone axis is not a high-symmetry direction of the SL (*i.e.*, not a low-index Miller plane). b) Identical view but with artificially small QDs (2.5 nm diameter) to reveal the horizontal void channels within the SL that are infilled by alumina. These horizontal channels generate the Al and O signal oscillations observed in Figure 2.27b. The channels also run vertically, but these are obscured by the skew of the sample relative to the electron beam. From Ref 169.

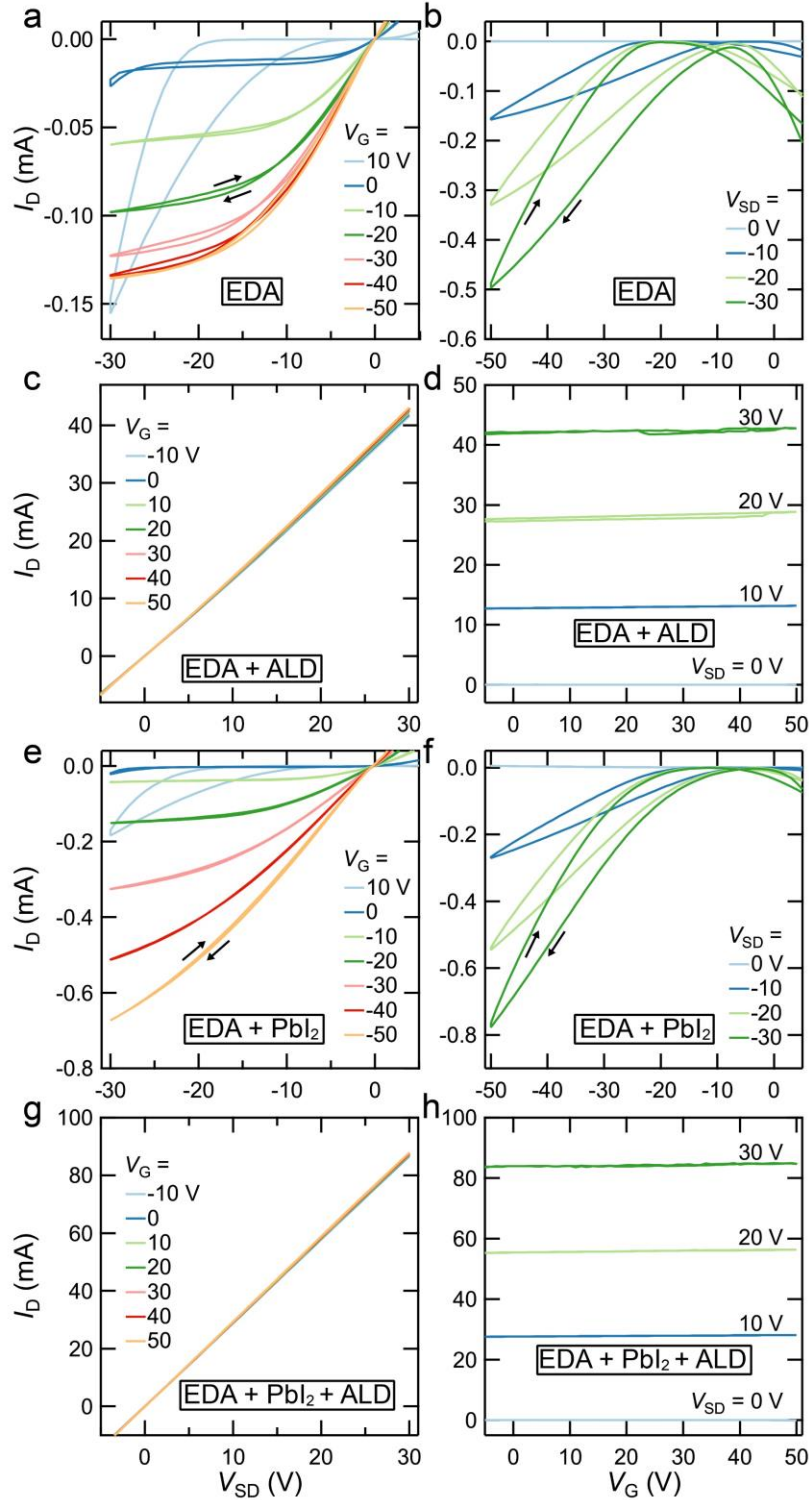


Figure 2.29. Epi-SL field-effect transistor results. a) Output and b) transfer characteristics of an epi-SL FET without  $\text{PbI}_2$  treatment or ALD infilling. c) Output and d) transfer characteristics of an alumina-infilled epi-SL FET (no  $\text{PbI}_2$  treatment). e) Output and f) transfer characteristics of a  $\text{PbI}_2$ -treated epi-SL FET (no ALD). g) Output and h) transfer characteristics of a  $\text{PbI}_2$ -treated, alumina-infilled epi-SL FET. All measurements were performed at 298 K in a glove box with a sweep rate of 40 V/s. The transistors were fabricated in a

bottom contact (5 nm Ti, 35 nm Au), global back gate ( $p^{++}$  Si, 200 nm SiO<sub>2</sub>,  $C_{\text{ox}} = 17.5$  nF/cm<sup>2</sup>) geometry with a channel length and width of 25  $\mu\text{m}$  and 1000  $\mu\text{m}$ , respectively. The linear field-effect mobilities in Table 6 were determined at  $|V_{\text{SD}}| = 10$  V and  $|V_{\text{G}}| = 40$  V using the standard gradual-channel approximation equation for electron and hole mobility.

Table 6. Linear field-effect mobilities for the epi-SL FETs.

epi-SL type	FET polarity	$\mu_{\text{p,forward}}/\mu_{\text{p,reverse}}^*$ (cm <sup>2</sup> /Vs)	$\mu_{\text{n,forward}}/\mu_{\text{n,reverse}}^*$ (cm <sup>2</sup> /Vs)
EDA	ambipolar	0.91/0.50	0.74/0.34
EDA + ALD	$n$	-	0.84/0.84
EDA/PbI <sub>2</sub>	ambipolar	1.07/1.32	0.79/0.44
EDA/PbI <sub>2</sub> + ALD	$n$	-	2.13/2.13

\*Since some of the FETs exhibited  $I$ - $V$  hysteresis, we report mobility for both forward and reverse voltage sweeps.

However, after ALD, the transistors become highly conductive and exhibit quasi-linear current-voltage curves with almost no modulation by the gate bias, due to a very high (nearly degenerate) free electron concentration (Figure 2.27e and Figure 2.29). We note that before ALD infilling, both the EDA- and EDA/PbI<sub>2</sub>-treated FETs behave as ambipolar transistors with a dominant p-channel and weaker n-channel (Figure 2.29b and f). The channel polarity of a quantum dot FET can depend on many factors, including the quantum dot synthesis chemistry, film stoichiometry, ligand coverage, oxidation, contacts, and gate dielectric. Our FTIR data show that the EDA-treated devices are covered in glycoxide and oleate, not EDA. Similarly, the PbI<sub>2</sub>-treated devices have a mixture of glycoxide, oleate, and iodide on the surface. We believe that the adsorbed glycoxide may be the reason that the  $p$ -channel is stronger than the  $n$ -channel in these devices, but further work is required to fully establish the factors that determine the polarity of these FETs.

The carrier mobility of the epi-SLs is artificially low due to grain boundaries in the polycrystalline superlattices, significant cracking/tearing of the films, and incomplete coverage of the FET

channel by the stamped films. The epi-SLs are polycrystalline films with an average lateral grain size of 0.25  $\mu\text{m}$ . The channel length is much larger (25  $\mu\text{m}$ ), so carriers must transit many grain boundaries to move between the source and drain contacts. Also, the epi-SLs are laced with cracks and tears, sometimes extensively, and mechanical contact with the electrodes and dielectric tends to be mediocre. All of this can greatly reduce the measured mobility. Because the epi-SLs are polycrystalline and cracked, grain boundaries and cracks dominate the FET measurements, and the reported mobility (Table 6) can be considered a lower limit. The Law group measured higher mobilities ( $\sim 10 \text{ cm}^2 \text{ V}^{-1} \text{ s}^{-1}$ ) in ALD-infilled amorphous QD films made with different surface chemistries from the chemistry studied here.<sup>114</sup> One reason for the higher mobility is the better mechanical quality of the amorphous films, which are made by layer-by-layer dip coating and therefore are completely free of cracks and have excellent interfaces with the dielectric and contact metals, all of which boosts mobility. A second reason for the higher mobility may be the completely different surface chemistry employed to make the two types of QD films (*e.g.*,  $\text{Na}_2\text{S}$  for the amorphous films versus EDA/EG for the epi-SLs). We also measured the sign of the thermopower by the hot-wire method and found that the films have positive Seebeck coefficients (*p*-type) before ALD and negative Seebeck coefficients (*n*-type) after ALD, in agreement with the FET results.

Strong doping by alumina infilling is remarkable because it has not been observed for amorphous PbSe QD films made using thiol, sulfide, thiocyanate, or carboxylic acid ligands.<sup>9,114,129</sup> Following the work described above, we found that thermal annealing eliminated the high doping level of the ALD-infilled films—this is described in Chapter 4. Another group has reported high doping and the emergence of an intraband transition after infilling PbS QD films with alumina ALD.<sup>116</sup> Additionally, we have observed intermittent periods of high *n*-type doping of films that, in the

past, have produced FETs with well-behaved  $n$ -channel characteristics. It is unknown what aspect(s) of the QD/alumina interface determine the overall doping profile and what causes strong  $n$ -type doping in alumina-infilled QD films, or why thermal annealing can eliminate the doping. Apparently, specific aspects of the structure or surface chemistry of these EDA- and EDA/PbI<sub>2</sub>-treated epi-SLs results in the formation of a high concentration of donor defects upon alumina deposition. While the origin of the excessive doping upon ALD infilling is unclear at this time, our results underscore the critical role of surface chemistry in determining the doping and electrical properties of QD epi-SLs.

## **2.6. Conclusions**

We used dual-space structural analysis at the ensemble and single-grain levels to determine the complete unit cell of oleate-capped and epitaxially-fused PbSe QD SLs and the pathway of the oleate- to epi-SL transformation. We find that attraction between nearly ligand-free PbSe{100} facets produces a rhombohedrally-distorted bcc oleate-capped SL in which each QD has six nearest neighbors with cofacial {100} facets. This remarkable structure enables epitaxial fusion of the {100} facets without the need for QD rotation, yielding a highly-ordered epi-SL with a distorted simple cubic unit cell. We show that the phase transition combines 3D, collective epitaxy with atomic topotaxy of the QDs. To our knowledge, this is the first demonstration of a topotactic transformation involving oriented attachment of an ensemble of crystals. This topo-epitaxial phase transition illustrates the multiscale spatial order that is possible with self-assembled QD solids. Knowledge of the formation mechanism provides a foundation for the rational fabrication of QD epi-SLs with improved spatial order and electrical properties, which we exploit later in this thesis. However, surface chemistry, not spatial order, may ultimately determine the electrical properties of epi-SLs. The dual role of surface ligands as determinants of electronic behavior and arbiters of

SL structure creates exciting opportunities and challenges for making high-quality epi-SLs. We show that the carrier type and concentration change dramatically after infilling the films with alumina by ALD. Infilling has no effect on the superlattice structure but results in very high carrier densities. The development of well-defined, tunable, and robust surface chemistries that minimize spatial and energetic disorder will be essential for making QD epi-SLs that exhibit the emergent mesoscale property of delocalized band transport.

There are several basic pathways forward for improving the quality of epi-SLs. One is to improve the quality of the oleate-capped SLs. We have qualitative (but robust) evidence that QDs with higher oleate coverage result in better QD SLs. These observations are supported by a recent report that points towards the importance of *unbound* ligand in the QD suspension.<sup>212</sup> In principle, three factors determine the size of SL grains: (i) strength of inter-QD attractive forces; (ii) the density of SL nucleation sites, perhaps associated with impurities in the QD suspension or on the EG surface; (iii) time that QDs can rearrange to their lowest energy configuration. In principle, one might want to extend the self-assembly time (solvent evaporation time) by using a different carrier solvent or using a pressurize vessel. However, ethylene glycol—the subphase on which the films are assembled—seems to slowly strip oleate from the QD surface. Extended exposure of oleate-capped PbSe QDs to EG leads to oleate stripping and eventually to QD fusion. The exact chemistry of this process is not well understood, but empirically we see the result. If the oleate desorption process is thermally activated,<sup>181</sup> perhaps reducing the temperature of film formation can allow the evaporation and self-assembly process to be extended, thereby improving the quality of the SLs. If the chemical mechanism for oleate desorption can be discovered, perhaps it can be prevented through chemical or other means. The size of SL grains may also be increased using ultra-clean solutions. The larger the oleate-capped SLs, the larger the epi-SLs can be. One lesson from looking

at the literature on MBE-grown QD SLs is that the spatial order of those systems was relatively poor. What they lacked in SL translational order they made up for in terms of the atomic lattice crystallinity. Researchers may find that the translational order of the epi-SL is less important for mini-bands than crystalline defects and epi-SL surface states. The combination of thermal annealing to remove dislocations followed by the growth of an epitaxial shell<sup>15,173,177</sup> may achieve results closer to those in the old MBE QD literature.<sup>213</sup>

## **2.7. Methods**

### *2.7.1. PbSe QD Synthesis*

PbSe QDs were synthesized and purified using standard air-free techniques. PbO (1.50 g), OA (5.00 g), and ODE (10.00 g) were mixed and degassed in a three-neck round-bottom flask at room temperature. Then the mixture was heated at 110°C under vacuum to form Pb(OA)<sub>2</sub> and dry the solution. After 1.5 hours, the Pb(OA)<sub>2</sub> solution was heated to 180°C under argon flow and 9.5 mL of a 1 M solution of TOP-Se containing 200 μL of DPP was rapidly injected into this hot solution. An immediate darkening of the solution was observed, and the QDs were grown for 105 seconds at ~160°C. The reaction was quenched with a liquid nitrogen bath and injection of 10 mL of anhydrous hexanes. The QDs were purified in an N<sub>2</sub>-filled glovebox (<0.5 ppm O<sub>2</sub>) by adding 10 mL of hexanes and 20 mL of ethanol to the reaction solution, collecting the QDs by centrifugation, performing one cycle of redispersion/precipitation using hexanes/ethanol (10 mL/20 mL), and then drying and storing the QDs as a powder in the glovebox.

### *2.7.2. Epi-SL film fabrication*

SL fabrication was performed in N<sub>2</sub>-filled gloveboxes with <0.5 ppm O<sub>2</sub>. Oleate-capped PbSe QD superlattices were prepared by carefully drop-casting 60-70 μL of a 6-10 mg/mL solution of PbSe QDs dispersed in hexanes onto 7 mL of ethylene glycol in a Teflon well (3.5 cm wide × 5 cm long × 1 cm deep) that was cleaned by soaking overnight in 5 M nitric acid and then soaking and rinsing in Millipore water at least ten times. After depositing the QD solution, the well was immediately covered with a glass slide and the hexane allowed to slowly evaporate in 6-8 minutes, resulting in a smooth, dry QD film floating on the EG surface. The slide was then removed and 100 μL of a 7.5 M solution of ethylenediamine in acetonitrile was slowly (5-10 s) injected into the EG directly underneath the film. As the EDA solution spread throughout the well, the film visibly darkened, indicating film densification and epi-SL formation. After 30 seconds, the darkened SL film nearest to the EDA injection point was transferred to a solid substrate (Si, glass, or TEM grid) by manual stamping using a vacuum wand. All substrates (except TEM grids) were cleaned by 15 minutes of sonication in acetone, water, and isopropanol, dried under flowing air, soaked in a 100 mM solution of 3-MPTMS in toluene for 1 hour to functionalize the surface for improved QD

adhesion, then rinsed with neat toluene and dried under flowing air. The stamped film was rinsed vigorously with neat acetonitrile and dried under flowing  $N_2$ . Next, the SL film was immediately soaked in a 10 mM solution of  $PbI_2$  in DMSO for 5 minutes, rinsed with copious amounts of DMSO and acetonitrile, and dried under flowing  $N_2$ . Amorphous alumina deposition was performed in a homemade cold-wall traveling wave ALD system within a glovebox using trimethylaluminum and water at a substrate temperature of  $60^\circ C$  and a base pressure of 0.08 Torr. Precursors were introduced to the ALD chamber using computer-controlled diaphragm valves in-line with a 130 sccm stream of nitrogen carrier gas. Pulse and purge times were 20 ms and 75 s for both precursors.

### *2.7.3. Basic optical and chemical characterization*

Optical absorbance measurements of QDs dispersed in TCE were performed with a Perkin-Elmer Lambda 950 spectrophotometer. Neat TCE served as the background for the solution measurements. Fourier transform infrared (FTIR) transmission spectra of SL films on double-side polished intrinsic Si substrates were acquired in dry air on a Nicolet 6700 spectrometer at a resolution of  $4\text{ cm}^{-1}$  with a blank Si substrate as the background. Scanning electron microscopy was performed on an FEI Magellan 400L XHR SEM operating at 10 kV and 25-50 pA. Samples for TEM-based energy dispersive spectroscopy (EDS) mapping were prepared on a Tescan GAIA3 SEM-FIB. X-ray photoelectron spectra were acquired with a Kratos AXIS Supra spectrometer using monochromatic Al  $K\alpha$  radiation at an X-ray power of 225 W. XPS samples were prepared on clean Si substrates soaked in a 1% vol. hydrofluoric acid solution for 10 minutes, rinsed with water and immediately ( $<2\text{ min}$ ) transferred to a glovebox ( $<0.5\text{ ppm O}_2$ ). SL films deposited onto these substrates were transferred to the XPS system completely air-free via an integrated glovebox. Oleate-capped SL spectra were charge corrected to place the aliphatic carbon of oleate at 284.6 eV, while the other spectra were charge corrected to align the Pb 4f<sub>5/2</sub> peak of PbSe with that of the oleate-capped SL spectrum at 137.3 eV. Inductively coupled plasma mass spectrometry (ICP-MS) measurements were carried out using the standard additions method on a Nu AttoM ES HR-ICP-MS spectrometer using 10 cycles of 500 sweeps with 500  $\mu\text{s}$  dwells per peak. Samples were prepared by forming epi-SL films on the surface of EG inside a centrifuge tube, then vigorously mixing the entire solution and collecting the liquid by centrifugation through an Amicon Ultra-15 centrifugal filter unit (10 kDa molecular weight cut-off). The solutions were then diluted with 2% nitric acid before standards addition and measurement. A second set of ICP-MS experiments was completed by Huffman-Hazen Laboratories. For these experiments, samples were prepared by extracting the EG subphase from beneath epi-SL films after a typical treatment time (30-45 seconds), then filtering out any residual QDs using an Amicon Ultra-15 filter. Additional details about the ICP-MS experiments are provided in Method S2.

### *2.7.4. Small-angle X-ray scattering*

GISAXS and solution transmission SAXS measurements were performed on Beamline 7.3.3 of the Advanced Light source (ALS) at Lawrence Berkeley National Laboratory using 10 keV monochromatic X-rays ( $\lambda = 1.24\text{ \AA}$ ) with an energy bandwidth of 1%. For GISAXS measurements, SL films were prepared on Si substrates and transported with the QD suspensions to the ALS under nitrogen to minimize air exposure prior to measurement. However, measurements were performed in air. A Dectris Pilatus 2M detector with a pixel size of  $0.172 \times 0.172\text{ mm}$  and  $1475 \times 1679$  pixels was used to record the 2D scattering



patterns. A silver behenate standard was used to determine the sample-to-detector distance and beam center. Exposure times ranged from 0.2 to 30 s. The grazing angle of incidence was varied from 0.2° to 0.3°. Manual pattern fitting was performed using the IndexGIXS software package provided by Detlef Smilgies of the Cornell High Energy Synchrotron Source. The critical angles of the films were fit empirically (0.195° for the oleate-capped SLs and 0.21° for the epi-SLs) to capture the breadth of the Yoneda band. A 30 mg/mL octane suspension of QDs was drawn into a 2 mm × 0.2 mm glass capillary with a 0.150 mm wall thickness (Electron Microscopy Sciences). The solution was exposed to air briefly before and during measurement. The sample-to-detector distance was 2994.78 mm as calibrated by the silver behenate standard. Signal was collected for 120 s, and an octane-filled blank capillary was used for background subtraction. The Nika software package<sup>187</sup> in Igor Pro was used to azimuthally integrate (25-75°) the SAXS pattern and correct for the background using the octane-filled blank. Particle distribution fitting was performed using a spherical form factor with a Gaussian spread of QD diameters in the NIST SANS Analysis package in Igor Pro.<sup>188</sup> No instrumental broadening was included in the fitting procedure, which indicates the reported polydispersity is likely an overestimation.

### 2.7.5. Oleate coverage in FTIR experiments

We estimated the amount of oleate removal by EDA and PbI<sub>2</sub> treatments by integrating the area of C-H peaks at ~3000 cm<sup>-1</sup>. The spectra were baseline corrected and fit with a multi-peak fitting routine. Peaks from adsorbed ethylene glycol were ignored and the oleate peaks were integrated, giving peak areas  $A_{\text{oleate}}$ ,  $A_{\text{EDA}}$ , and  $A_{\text{EDA/PbI}_2}$  for the oleate-capped SL, the epi-SL before PbI<sub>2</sub> treatment, and the epi-SL after PbI<sub>2</sub> treatment, respectively. After density correction<sup>v</sup>, the percent removal of oleate can be estimated as:

$$\% \text{ oleate removed} = \left( 1 - \frac{A_{\text{EDA or EDA/PbI}_2} \times \sigma_{\text{oleate}}}{A_{\text{oleate}} \times \sigma_{\text{epi}}} \right) \times 100\% \quad (2.3)$$

### 2.7.6. Isotope labelling experiments

For tests with ethylene glycol-*d*<sub>4</sub>, superlattice films were prepared as described above on the surface of EG-*d*<sub>4</sub> in smaller, circular Teflon wells (~1 mL of EG-*d*<sub>4</sub>). 20 μL of 7.5 M 1,2-ethylenediamine in acetonitrile was injected to achieve the same overall concentration as in the larger wells (~105 mM) and allowed to react for 30 seconds. Films were stamped onto double-side polished (DSP) Si and measured by FTIR spectroscopy. For tests with 1,2-ethylenediamine-*d*<sub>4</sub>, a 1:1 volume mixture of EDA-*d*<sub>4</sub> and acetonitrile was injected into the EG subphase of the normal wells and allowed to react for 3-8 minutes before stamping the films onto DSP Si for FTIR measurements. Attenuated total reflectance FTIR spectra of neat EG, EG-*d*<sub>4</sub>, EDA and EDA-*d*<sub>4</sub> were collected as references.

---

<sup>v</sup> After accounting for the increased areal density of QDs in the epi-SLs ( $\sigma_{\text{oleate}} = 0.0155$  QDs/nm<sup>2</sup> on the (101)<sub>SL</sub> plane of the oleate-capped SL versus  $\sigma_{\text{epi}} = 0.0232$  QDs/nm<sup>2</sup> on the (100)<sub>SL</sub> plane of both types of epi-SLs, which are the two dominant grain orientations for the samples discussed in Chapters 2 and 3. Later attempts at oleate quantification incorporated a film coverage correction factor.

### 2.7.7. Determination of surface oleate coverage

The oleate/QD ratio and oleate surface coverage (oleate/nm<sup>2</sup>) were determined using nuclear magnetic resonance (NMR) spectroscopy and optical absorbance spectroscopy following a modified version of a published procedure. Known masses of dried QDs from syntheses with two, three, or four cleaning cycles (one cycle consists of redispersion with 20 mL of hexane followed by precipitation with 10 mL of ethanol) were dispersed in anhydrous toluene-*d*<sub>8</sub> (dried over molecular sieves) and injected into precision NMR tubes (Wilmad, 528-PP-7). <sup>1</sup>H NMR spectra were acquired at 296 K with a Bruker DRX 500 spectrometer (500 MHz, BBO probe) using sixteen scans at a delay time of 100 seconds to accommodate the long T<sub>1</sub> relaxation times of surface-bound oleate. The absolute concentration of oleate ligands was determined with an internal reference (6.45 mM of ferrocene). The QD number concentration was determined from optical absorption spectra of QD suspensions using the size-dependent molar extinction coefficient of Ref 47. 51 μL of the QD suspension used for NMR was removed prior to ferrocene addition, dried under nitrogen flow and vacuum, and redispersed in a known volume of tetrachloroethylene (TCE). The absorbance of this suspension at  $h\nu = 3.1$  eV was measured, background corrected against neat TCE, and used to calculate the QD number concentration using  $c = \frac{A_{3.1\text{eV}}}{0.0277(ld^3)}$ , where  $c$  is the QD concentration (in μM),  $A_{3.1\text{eV}}$  is the absorbance at a photon energy of 3.1 eV,  $l$  is the path length in centimeters, and  $d$  is the QD diameter in nanometers.<sup>47</sup> We note that although this equation was derived specifically for PbSe QDs suspended in CCl<sub>4</sub>, the use of TCE as solvent gave the same absorbance values to within ±1%. The oleate/QD ratio was then calculated from the measured oleate and QD concentrations. The average oleate coverage (oleate/nm<sup>2</sup>) was calculated by dividing the oleate/QD ratio by the surface area per QD (145 nm<sup>2</sup>) from our STEM-derived structural model of these QDs.<sup>178</sup>

### 2.7.8. Inductively coupled plasma mass spectrometry

We performed two rounds of ICP-MS measurements.

*First round of experiments.* In the first round of ICP-MS experiments, SL films were self-assembled on the surface of ethylene glycol (EG) from a known mass of QDs and treated with 1,2-ethylenediamine (EDA), NH<sub>4</sub>SCN, or 1,2-ethanedithiol (EDT) for ~130 minutes. The QDs were then separated from the EG by centrifuge filtration and the Pb content of the EG was measured by ICP-MS. Note that this treatment time is approximately 250 times longer than we used for the SL films discussed in the text, so this first round of ICP-MS measurements provides information about the chemistry in the limit of long treatment times. The results are presented in Table 7.

Table 7. ICP-MS results for Pb removal by prolonged in-situ ligand treatments.

Sample	[Pb] in EG (ppbm)	Pb atoms removed per QD
neat EG (no QDs)	< 1	n/a
OA-capped QDs ( <i>control</i> )	159 ± 48	n/a
EDA-treated QDs	8858 ± 272	602 ± 84
EDT-treated QDs	118 ± 5.4	~0
SCN-treated QDs	409 ± 26	17 ± 5

ppbm = parts per billion by mass

Treatment of the films with EDA resulted in a 55-fold increase in the concentration of Pb in EG compared to the control (no ligand treatment), indicating that EDA removes a significant amount of Pb from the QDs. In contrast, EDT shows no tendency to remove Pb, while SCN<sup>-</sup> may remove a small amount of Pb (~3% of the amount removed by EDA). We estimated the average number of Pb atoms removed per QD from the known number and initial stoichiometry of the QDs in these samples (see Method S1 and Figure S2). Our results clearly show that prolonged EDA treatment strips Pb from the QDs, whereas EDT and SCN<sup>-</sup> remove very little to no Pb.

*Experimental details.* The inductively coupled plasma mass spectrometry (ICP-MS) measurements of the EG sub-phase were carried out on a Nu AttoM ES HR-ICP-MS spectrometer using 10 cycles of 500 sweeps with 500 μs dwells per peak. Samples were prepared in a glove box by depositing 60 μL of a QD suspension in hexane (6.0 mg/mL) onto the surface of 5.0 mL of EG in a centrifuge tube. The hexane was allowed to evaporate over the course of ~15 min, leaving a dried SL film on the EG surface. An appropriate volume of an acetonitrile solution of EDA, NH<sub>4</sub>SCN, or EDT was then injected into the EG sub-phase under the QD film to yield total concentrations of 1.0 M EDA, 1.0 mM NH<sub>4</sub>SCN, or 2.0 mM EDT. These concentrations were selected because they yield QD films with similar oleate coverage while avoiding extreme QD fusion. The centrifuge tube was then capped and shaken vigorously for 30 seconds to ensure maximum possible exposure of the QDs to the treatment molecules. The entire sample was poured into a centrifuge filter unit (Amicon Ultra-15, 10 kDa), sealed with Parafilm, and centrifuged outside of the glove box at 5000 rcf (~6682 rpm) for 120 min to remove all of the QDs from the EG solution. The EG solution therefore remained in contact with the QDs for a total of ~130 minutes. The filtered EG solution was diluted with double-distilled nitric acid (TraceMetal grade, Fisher Scientific) and injected into the ICP-MS. A single-element Pb standard was used to create an external calibration curve for Pb quantification.

To verify the efficacy of QD removal by centrifuge filtration, the EDA treatment solution was drop-cast on a TEM grid and dried under vacuum. No QDs were found after extensive searching by TEM, proving that the filters are extremely effective at capturing the QDs. We conclude that any Pb measured in the EG is present as dissolved Pb (in the control experiment, probably residual precursor or byproducts from the QD synthesis), rather than QDs that escape into the filtrate.

*Second round of experiments.* In the second round of experiments, oleate-capped SLs were fabricated on the surface of ethylene glycol from a known mass of quantum dots and treated with EDA (105 mM total concentration) for 30-45 seconds, at which point the ethylene glycol was extracted from underneath the

film using a syringe, centrifuge filtered, and analyzed by ICP-MS for both Pb and Se content. In addition to three of these films and a control sample (a floating oleate-capped SL without EDA treatment), we measured EG from (i) a prolonged EDA treatment (615 seconds) of a film floating on ethylene glycol and (ii) a film prepared by spin-coating a known mass of QDs onto a Si substrate, then immersing the film into a bath of 105 mM EDA in EG for 45 seconds while stirring the solution with the substrate to aid mixing. The results are compiled in Table S3.

Table 8. ICP-MS results for Pb and Se removal by normal in-situ ligand treatments.

Sample	[Pb] in EG (ppbm)	Pb atoms removed per QD	[Se] in EG (ppbm)	Se atoms removed per QD
OA-capped QDs ( <i>control</i> )	5	n/a	4	n/a
EDA #1	239	14 ± 2	6	<1
EDA #2	131	8 ± 2	6	<1
EDA #3	252	15 ± 2	4	<1
long EDA	635	37 ± 6	5	<1
spin-cast	411*	24 ± 4	4	<1

\* The mass of the spin-cast film was 13% of the epi-SLs. The value listed is corrected for this difference in film mass.

The three normal epi-SL films show 8-15 Pb atoms removed per dot, which is a lower bound on the actual Pb removal due to undersampling of Pb-containing species diffusing from the film into the unstirred EG sub-phase. The improved mixing possible with the spin-cast film increased Pb removal to 24 atoms/QD, while more prolonged EDA treatment resulted in greater Pb removal (37 atoms/QD). These findings suggest that (i) removal of Pb(OA)<sub>x</sub> by EDA accounts for only a small fraction of the ~404 oleate ligands removed per QD (80% of 505 ligands/QD) during the normal EDA treatment, and (ii) epitaxial fusion occurs despite the minimal loss of surface Pb atoms. These data also confirm that Se is not removed by EDA.

*Experimental details.* The floating films were prepared by depositing 60 μL of a QD suspension in hexane (10.0 mg/mL) onto the surface of 7.0 mL of EG in a Teflon well. The hexane was allowed to evaporate over the course of ~7 min, leaving a dried SL film on the EG surface. The control film was allowed to sit on the EG for ~1 minute before the EG was extracted. For the three normal epi-SLs, 100 μL of a 7.5 M EDA solution in acetonitrile was injected into the EG and allowed to react for 30-45 seconds before the EG was collected. The long EDA sample was prepared in the same way, except that the film was allowed to react with EDA for ~615 seconds before EG collection. The spin-cast film was prepared by spin coating a 30 mg/mL QD suspension in octane onto a cleaned Si substrate and immersing it in a 105 mM solution of EDA in 7.0 mL of EG and 50 μL of acetonitrile (identical to the epi-SLs). The substrate was waved back and forth for 45 seconds and then removed from the solution. The mass of an identical oleate-capped film was measured to be 78.75 μg. For all samples, the entire volume of collected EG was poured into a centrifuge filter unit (Amicon Ultra-15, 10 kDa), sealed with Parafilm, and centrifuged outside of the glove box at 5000 rcf (~6682 rpm) for 120 min to remove any stowaway QDs from the EG solution. ICP-MS elemental quantification of Pb and Se in the filtrates was performed by Huffman Hazen Laboratories.

### 2.7.9. GISAXS fitting refinement

The section below describes the image analysis and least-squares fitting procedure used to constrain the GISAXS fits.

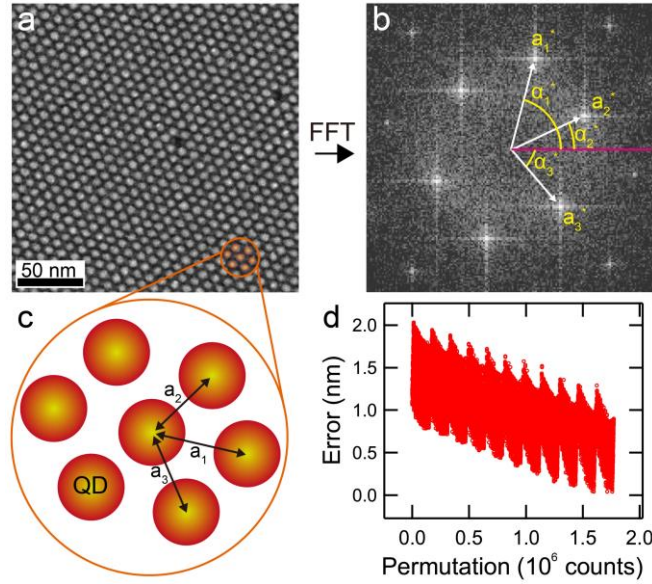


Figure 2.30. SEM image analysis used to constrain the GISAXS fits of the SL unit cell. a) Typical SEM image of a (101)SL-oriented oleate-capped SL used for determining inter-QD distances. Scale bar = 50 nm. b) Corresponding FFT image. The vectors  $\mathbf{a}_n^*$  are the three shortest reciprocal lattice vectors. The reciprocal lattice angles  $\alpha_n^*$  are measured relative to the pink horizontal line (with clockwise rotation negative). c) Model of the surface of this oleate-capped SL grain. d) An example of graphical output from the Python-based least-squares fitting program used to guide the GISAXS fits.

The in-plane inter-QD distances ( $a_n$ ) are calculated from  $\mathbf{a}_n^*$  and  $\alpha_n^*$  according to Equations 1-3:

$$|a_1| = \frac{|a_2^*|}{|\cos(\alpha_3^* - \alpha_2^* + 90^\circ)|} = \frac{|a_1^*|}{|\cos(\alpha_1^* - \alpha_3^* + 90^\circ)|} \quad (1)$$

$$|a_2| = \frac{|a_2^*|}{|\cos(\alpha_2^* - \alpha_1^* - 90^\circ)|} = \frac{|a_3^*|}{|\cos(\alpha_1^* - \alpha_3^* - 90^\circ)|} \quad (2)$$

$$|a_3| = \frac{|a_3^*|}{|\cos(\alpha_3^* - \alpha_2^* - 90^\circ)|} = \frac{|a_1^*|}{|\cos(\alpha_2^* - \alpha_1^* + 90^\circ)|} \quad (3)$$

To determine if any 3D SL unit cell was consistent with both the GISAXS patterns and the inter-QD distances measured by SEM, the 2D lattice observed in SEM was compared to low-order Miller planes of bcc, fcc, and hcp crystals. bcc(110) gave the closest match and was therefore used as a starting point for the

SL model. To precisely fit the SEM and GISAXS data, we relaxed the bcc symmetry and calculated the inter-QD distances ( $a_n$ ) for  $>10^6$  unique sets of lattice parameters spanning the range of  $9.2 \text{ nm} < a, b, c < 10.2 \text{ nm}$  and  $75^\circ < \alpha, \beta, \gamma < 90^\circ$ . Local best fits were determined by minimizing the error function,  $\epsilon$ , defined as:

$$\epsilon = \sqrt{(a_1 - d_{1f})^2 + (a_2 - d_{2f})^2 + (a_3 - d_{3f})^2}$$

where  $a_n$  and  $d_{nf}$  are the measured and calculated inter-dot distances, respectively. The SEM fitting procedure was used iteratively to optimize manual GISAXS fitting and generate agreement with SEM image analysis. The program generates  $\epsilon$  for each set of unique lattice parameters, then reports the ten best fits to use as a starting point for manual GISAXS fitting. These lattice parameters were then used in the IndexGIXS software for GISAXS fitting.<sup>214</sup> This SEM fitting procedure helped to iteratively optimize manual GISAXS fits and reveal that the two SL grains observed in experiments were actually two different orientations of the same SL unit cell.

### 2.7.10. Transmission electron microscopy

A JEOL JEM-2100F TEM operating at 200 kV was used to image isolated QDs prepared by drop-casting  $\sim 2 \mu\text{L}$  of a dilute ( $<1 \text{ mg/mL}$ ) hexane suspension onto a lacey carbon grid (with a carbon film). SL samples for TEM analysis were prepared by stamping QD films from the EG surface onto holey carbon TEM grids (without a carbon film coating). The use of TEM grids free of a carbon film was critical for high-quality secondary electron imaging in the TEM. Imaging, diffraction, and energy dispersive spectroscopy (EDS) elemental mapping were performed on a JEOL JEM-2800 TEM. Scanning TEM experiments (secondary electron imaging and EDS mapping) employed a probe size of 1.0 nm. Hyperspectral EDS images were collected using a 30-minute acquisition time. Electron diffraction patterns were acquired at a parallel beam condition. Sample holder tilt was  $0^\circ$  unless otherwise noted. Correlated secondary electron imaging (SEI) and selected area electron diffraction (SAED) experiments were carried out by first imaging a SL grain in STEM mode with the secondary electron detector, then switching to TEM mode to collect the SAED pattern of the same location. Image rotation between STEM, diffraction, and imaging modes was corrected for in our correlated S/TEM experiments, yielding a rotational alignment error of  $<5^\circ$ .

### 2.7.11. Electrical measurements

All field-effect transistor measurements were performed at room temperature in a glove box at a sweep rate of  $\sim 40 \text{ V/s}$  using a Keithley 2636B source measure unit run by custom LabView software. The transistors were fabricated in a bottom contact (5 nm Ti, 35 nm Au), global back gate ( $p^{++} \text{ Si}$ , 200 nm  $\text{SiO}_2$ ,  $C_{\text{ox}} = 17.5 \text{ nF/cm}^2$ ) geometry with a channel length and width of  $L = 25 \mu\text{m}$  and  $W = 1000 \mu\text{m}$ , respectively. Linear field-effect mobilities ( $\mu_{\text{lin}}$ ) were determined at  $|V_{\text{SD}}| = 10 \text{ V}$  and  $|V_{\text{G}}| = 40 \text{ V}$  using the gradual channel approximation equation for electron and hole mobility:

$$\left. \frac{dI_{\text{D}}}{dV_{\text{G}}} \right|_{V_{\text{SD}}} = \frac{WC_{\text{ox}}V_{\text{SD}}}{L} \mu_{\text{lin}}$$

## CHAPTER 3

### PHOTOINITIATED EPI-SL FORMATION

Here we demonstrate photo-initiated formation of epitaxially-fused SLs (epi-SLs). In the previous chapter we discussed epi-SLs formed via assembly on a liquid subphase through manual injection of a chemical trigger into that subphase. However, this process results in radial ligand exchange gradients and mechanical disturbances that cause partial SL film destruction and chemical/structural inhomogeneity. These imperfections make it difficult to reproducibly synthesize and study high quality epi-SLs. Furthermore, these films exhibit cracks at multiple length scales, some of which may be due to the destructive injection process. We hypothesized that higher quality epi-SLs are possible using a contact-free approach whereby light—rather than manual injection—initiates epi-SL formation.

The most popular chemical trigger for epi-SL formation is 1,2-ethylenediamine (EDA). It was proposed to displace  $\text{Pb}(\text{oleate})_2$  from the QD surface via a Lewis acid-base reaction, resulting in deprotection and epitaxial fusion of the QDs.<sup>40,133,146,165,169,192</sup> Our findings presented in Section 3.3 disprove this Lewis acid-base mechanism as the primary cause of oleate removal and epi-SL formation. In this chapter, we build on prior work to definitively demonstrate that EDA acts as a Brønsted base (proton acceptor) that deprotonates EG, leading to the formation of ethylene glycoxide which then exchanges with surface oleate. Deprotection of the QD surface facilitates epitaxial fusion of the QDs. We form high-quality epi-SLs using several different Brønsted bases—both amines and simple bases—at concentrations that produce glycoxide concentrations similar to typical EDA treatment conditions. We use FTIR and structural analysis of SEM images

to relate chemical trigger basicity with the extent of oleate removal and epi-SL formation. We use these mechanistic insights to form epi-SLs using UV illumination in combination with a photo base generator dissolved in the EG. This basic demonstration of light-triggered epi-SL assembly should enable finer control of epi-SL structure and direct photopatterning of QD-based optoelectronic circuitry.

Light-initiated ligand exchange of QDs on solid substrates<sup>215–220</sup> and liquid EG surfaces<sup>221</sup> has been used to alter the solubility and/or surface chemistry of QDs. A major focus has been placed on direct optical/UV/e-beam patterning, which enables on-chip design of QD-based light-emitting or electronic devices. In the course of our experiments on this topic, Gao *et al.* showed that they could trigger oleate removal by photoactivation of a photoacid generator dissolved in the EG, resulting in SL densification and QD fusion within regions of the SL illuminated by UV light.<sup>221</sup>

Photo-initiation of epi-SLs offers several key advantages over films made with manual point injection of a chemical trigger. First, photo-initiation eliminates the mechanically disruptive and inhomogeneous liquid currents associated with injection of the chemical trigger. The point injection method leads to radial ligand exchange/SL structure gradients and causes significant mechanical disturbance of the film. Second, it allows for arbitrary photopatterning of the epi-SL. Third, it allows fabrication of arbitrarily large epi-SL films since the process is unconstrained by diffusion of a chemical trigger from the injection point. Fourth, it facilitates more precise control of the concentration-time profile of glycoxide. Finally, it should enable more precise control and uniformity during epi-SL assembly, thus boosting the likelihood of mini-band formation in these materials. These five potential advantages should lead to reproducible and scalable epi-SL synthesis, applicable to basic research efforts and future integration into optoelectronic devices.



### 3.1. Epi-SL Formation with Brønsted Bases

Oleate-capped SL films<sup>vi</sup> were self-assembled on a liquid EG subphase (see Section 2.7.2) and treated with amines of varying basicity. We hypothesized that increasing the basicity of the amine would result in more glycoxide formation, more oleate removal, and more complete epi-SL conversion. FTIR was used to evaluate the relationship between amine basicity and oleate removal (Figure 3.1b) and shows that stronger bases (lower  $pK_b$ ) result in greater oleate removal. Piperidine ( $pK_b = 3.7$ ) and trimethylamine ( $pK_b = 4.5$ ) removed >95% of the oleate and caused severe epi-fusion of the QDs, while EDA ( $pK_b \sim 5$ ), triethanolamine ( $pK_b = 6.3$ ), aniline ( $pK_b = 9.5$ ), and quinoline ( $pK_b = 10.3$ ) removed 85%, 50%, ~5% and ~0% of the oleate, respectively, and caused progressively less epi-fusion in SEM images. Films treated with either of the two weakest bases (aniline and quinoline) showed no oleate loss or epi-fusion at all. The corresponding FTIR spectra (Figure 3.1b) show the presence of adsorbed glycoxide for all treatments with measurable oleate removal. Furthermore, we did not observe any peaks in any sample corresponding to adsorbed amine, consistent with the glycoxide-oleate exchange hypothesis. SEM images qualitatively agree with the results from FTIR measurements: more oleate removal results in more complete epi-SL conversion. Quantitative structural analysis of the films is described below.

---

<sup>vi</sup> In these studies, we used PbSe QDs nearly identical to those presented in Chapter 2. For reasons that are not understood, the SLs discussed here tended to adopt the  $(10\bar{1})_{SL}$  oleate-capped SL orientation, which converts into the  $(01\bar{1})_{SL}$  epi-SL orientation.

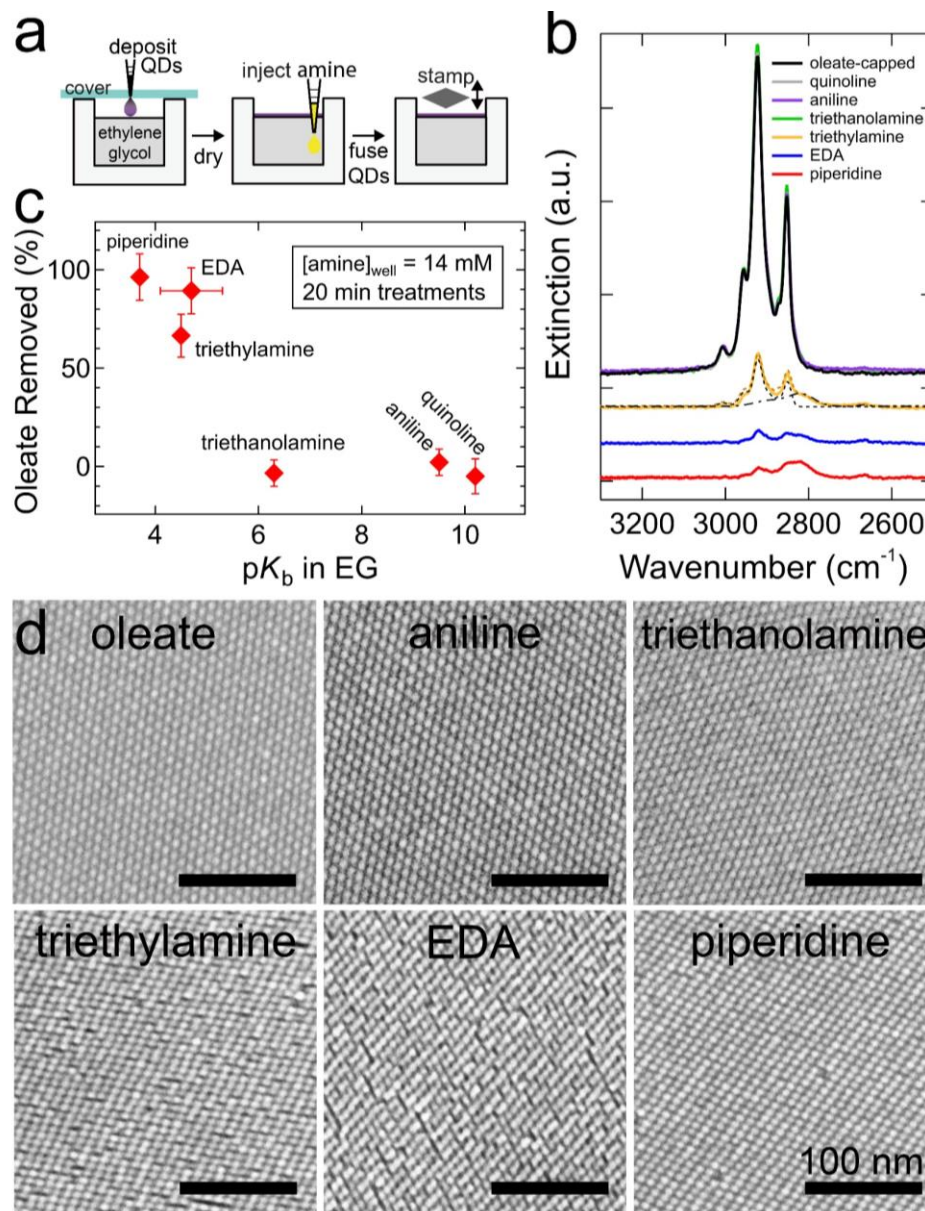


Figure 3.1. Amine-triggered conversion of oleate-capped PbSe QD SLs to epi-SLs. (a) A cartoon of the fabrication process. Amine dissolved in EG was injected by syringe under an oleate-capped QD SL floating on EG in a 5-cm diameter quartz petri dish. The QD films were then stamp transferred to double-side polished silicon substrates. (b) Typical FTIR spectra of an as-made oleate-capped SL (black) and SLs treated by one of six different amines (piperidine, ethylenediamine, triethylamine, triethanolamine, aniline, and quinolone) using an amine concentration of 14 mM and a 20 minute treatment time. The oleate-capped film was aged on the EG surface for 20 min to control for the time spent on EG. The spectrum of the triethylamine-treated film is deconvolved into its oleate-capped component (black dashed line) and glycoxide-capped component (black dash-dotted line). The total fit for this sample is also shown (dashed brown line). The spectra are offset for clarity. (c) Plot of the percent oleate removed (as determined from the FTIR spectral fits) versus the  $pK_b$  for each amine in EG. Experimental  $pK_b$  values were taken from literature.<sup>222–226</sup> (d) SEM images of an oleate-capped SL and SLs treated with different amines.

We next explored whether epi-SLs could be formed using tetrabutylammonium hydroxide (TBAOH) as a chemical trigger.  $\text{OH}^-$  is a strong base in EG that deprotonates EG to form ethylene glycoxide and water. Based on our findings of basicity-driven oleate removal, we hypothesized that a simple Brønsted base would lead to oleate removal (and ultimately, the epi-SL) through the formation of a glycoxide intermediate. To test this hypothesis, TBAOH was dissolved in EG, injected into the SL subphase, and allowed to react with the SL film. The SL films were evaluated using the same FTIR/SEM approach described for the amines. FTIR and SEM data (Figure 3.2) show that increasing the concentration of TBAOH leads to a monotonic increase in oleate removal, consistent with our hypothesis that basicity drives oleate removal. Additionally, for all SL films with significant oleate removal we see characteristic glycoxide peaks by FTIR (see Section 2.2).

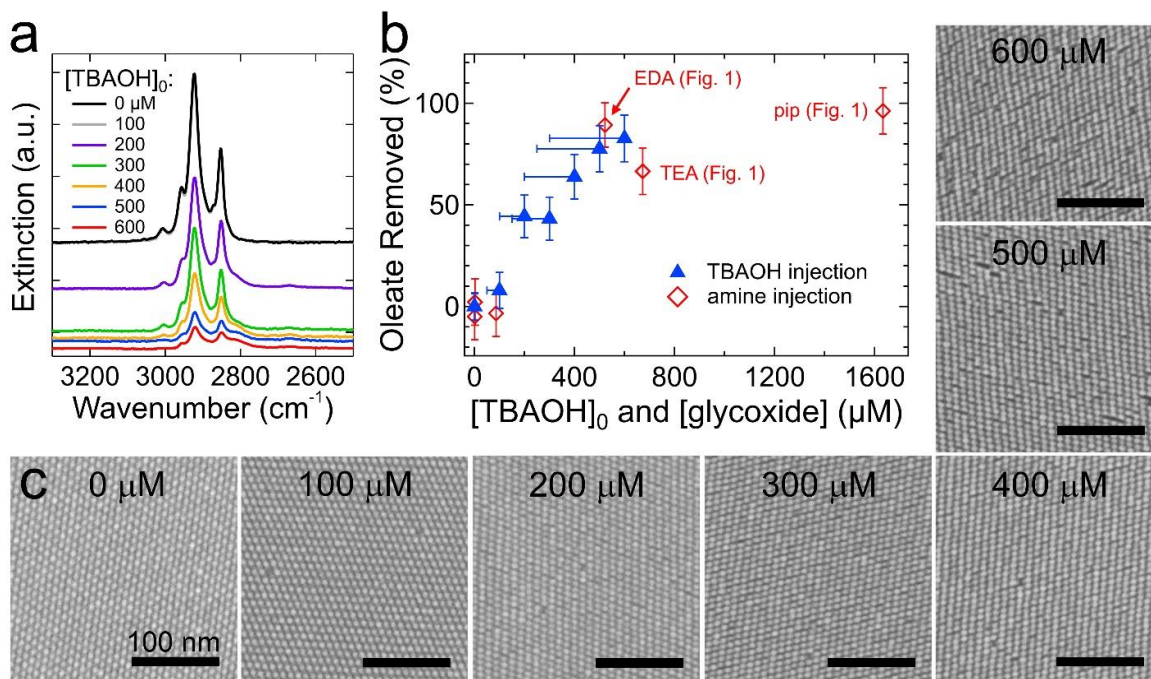


Figure 3.2. Hydroxide-triggered conversion of oleate-capped SLs to epi-SLs. (a) Typical FTIR spectra of an as-made oleate-capped SL and SLs treated in different concentrations of TBAOH. The spectra are corrected for differences in film thickness at each location. The treatment time was 20 minutes. (b) Plot of the percent oleate removal versus hydroxide concentration. (b) Plan-view SEM images of the as-made film and the full range of hydroxide-treated films.

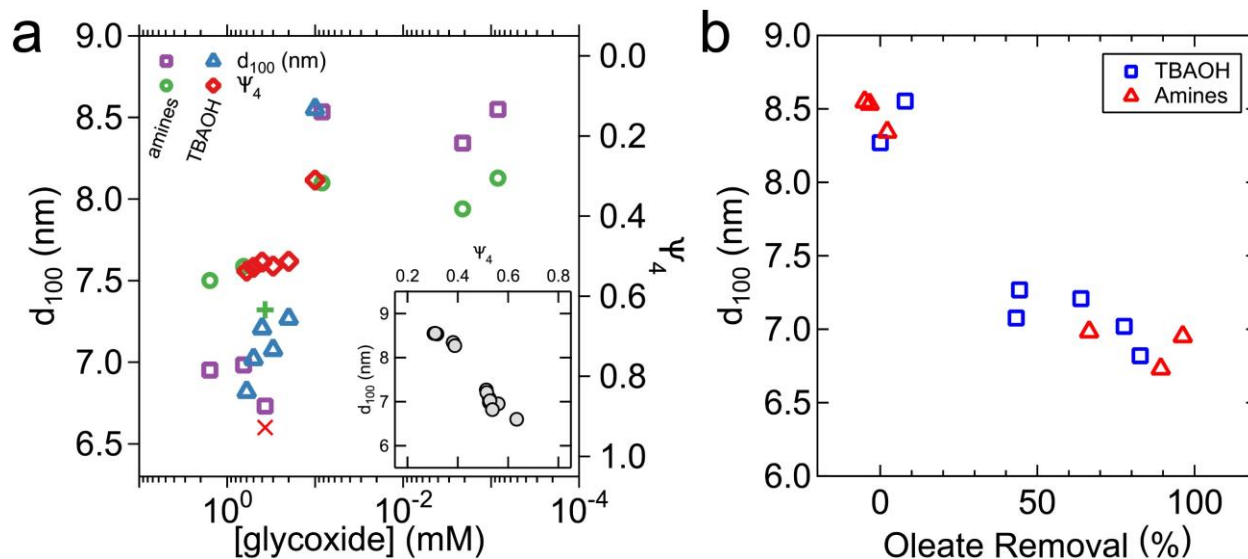


Figure 3.3. Structural analysis of SLs treated with amines and TBAOH. SEM images were analyzed using the method described in Section 3.5.3. a) Compilation of  $d_{100}$  and  $\Psi_4$  values for TBAOH- and amine-treated films. For the amines,  $pK_b$  values were used to estimate the resultant concentration of glycoxide. For TBAOH we assumed total dissociation in EG. Glycoxide is assumed to be singly deprotonated in solution. The red X and green cross represent the epi-SL  $d_{100}$  distance (6.6 nm) and  $\Psi_4$  value, respectively, determined from the epi-SL structure in Chapter 2. The figure inset shows strong correlation between changes in  $d_{100}$  and  $\Psi_4$ . b) Comparison of oleate removal and  $d_{100}$ .

We also evaluated the structure of each SL treatment condition using semi-automated real- and reciprocal-space analysis of SEM images (see Section 3.5.3). Two structural metrics were extracted from the SEM data sets: (i)  $\Psi_4$ , the 4<sup>th</sup>-order bond parameter, a quantity valued between 0-1 that measures the degree of four-fold lattice symmetry as observed *via* plan-view SEM;<sup>159</sup> (ii)  $d_{100}$ , the nearest-neighbor (NN) distance, which in the epi-SL corresponds to the nearest-neighbor center-to-center distance (*i.e.*, the length of  $[100]_{SL}$ ).  $\Psi_4$  approaches 0 as the unit cell of the SL deviates from a perfect square net and becomes more oblique. For the  $(10\bar{1})_{SL}$  oleate-capped/ $(01\bar{1})_{SL}$  epi-SL orientation,  $\Psi_4$  spans between  $\sim 0.29$  for a pristine oleate-capped SL to  $\sim 0.56$  for a fully-formed epi-SL.  $d_{100}$  spans between  $\sim 8.6$  nm in pristine oleate-capped SLs to  $\sim 6.7$  nm in epi-fused SLs. Taken together, these values provide a holistic view of the changing SL symmetry and

densification that occur during the oleate-to-epi-SL conversion. Figure 3.3a shows  $\Psi_4$  and  $d_{100}$  plotted against glycoxide concentration, which was calculated based on either complete dissociation of TBAOH or using the  $pK_b$  of the amine (see Section 3.5.4). As the concentration of glycoxide increases, the SL structure tends towards the final epi-SL structure; the inter-dot distances decrease, and the SL symmetry shifts. Interestingly, the change in both structural parameters is switch-like, with no SL structures in between those of the oleate-capped and epi-SLs. The full datasets are provided in Table 9 and Table 10. Figure 3.3b demonstrates the relationship between oleate removal and contraction of  $d_{100}$ —the SL densifies and the NN distances decrease as more oleate is removed. The concomitant change in  $d_{100}$  and  $\Psi_4$  shows how deprotection of the QDs leads to strong interaction of  $\{100\}$  PbSe facets, which drives the structure away from the quasi-8-fold coordinate distorted bcc lattice (oleate-capped SL) towards a 6-fold coordinate distorted cubic structure (epi-SL).

Based on our findings with amines and TBAOH, we conclude that oleate removal and epi-SL formation is unambiguously driven by exchange of oleate by glycoxide. The formation of glycoxide is initiated through reaction of a Brønsted base with the EG subphase. Thus, the use of amines is not required. Furthermore, we note that factors other than the ability of an amine to deprotonate EG – such as amine type (primary, secondary, or tertiary), denticity, and size – were uncorrelated with oleate removal and epi-fusion. However, solubility of the oleate/ammonium ion-pair likely impacts the degree of oleate exchange.<sup>40</sup>

Table 9. Structural parameters of SL films treated using various amines.

Amine	[100] (nm)	$\Psi_4$
oleate-capped	$8.61 \pm 0.15$	$0.331 \pm 0.078$
ethylenediamine	$6.73 \pm 0.11$	NR*
piperidine	$6.95 \pm 0.08$	$0.561 \pm 0.087$
triethylamine	$6.98 \pm 0.05$	$0.526 \pm 0.101$
aniline	$8.34 \pm 0.08$	$0.382 \pm 0.075$
quinoline	$8.55 \pm 0.04$	$0.305 \pm 0.068$
triethanolamine	$8.53 \pm 0.10$	$0.305 \pm 0.095$

Table 10. Structural parameters of SL films treated using tetrabutylammonium hydroxide (TBAOH).

[TBAOH] ( $\mu$ M)	[100] (nm)	$\Psi_4$
[100]	$8.55 \pm 0.11$	$0.310 \pm 0.076$
[200]	$7.27 \pm 0.12$	$0.513 \pm 0.097$
[300]	$7.08 \pm 0.06$	$0.525 \pm 0.074$
[400]	$7.21 \pm 0.15$	$0.515 \pm 0.074$
[500]	$7.02 \pm 0.09$	$0.528 \pm 0.080$
[600]	$6.82 \pm 0.12$	$0.537 \pm 0.096$

### 3.2. Photo-initiated Epi-SLs

We then reasoned that SL structural quality, ligand exchange homogeneity, and scalability could be improved by triggering epi-SL formation using uniform, *in-situ* illumination of a photobase dissolved in the EG subphase. We tested this concept using the photobase generator (PBG) (*E*)-1-piperidino-3-(2-hydroxyphenyl)-2-propen-1-one (see inset of Figure 3.4), which is a commercially available compound with moderate solubility in ethylene glycol that irreversibly liberates piperidine ( $pK_b = 3.7$ ) upon irradiation with UV light. Figure 3.4 shows basic chemical and optical characterization of the PBG molecule we used for epi-SL fabrication. The strongest absorption peak is at  $\sim 290$  nm, however we used a UV-C lamp with peak emission intensity at 254 nm, as

denoted on Figure 3.4b. Epi-SL films were made by first fabricating an oleate-capped SL on EG containing pre-dissolved PBG. Once the oleate-capped SL was formed, the UV light was switched on, illuminating from below the EG/SL.<sup>vii</sup> We used a quartz dish for epi-SL fabrication because glass and Teflon are opaque to UV light. SL densification was visible after the UV light was turned on, and after an empirically determined interval, the SL films were stamped for further characterization.

---

<sup>vii</sup> The concentration-time profile for an optimal epi-SL structure is currently under study; here we provide a proof-of-concept.

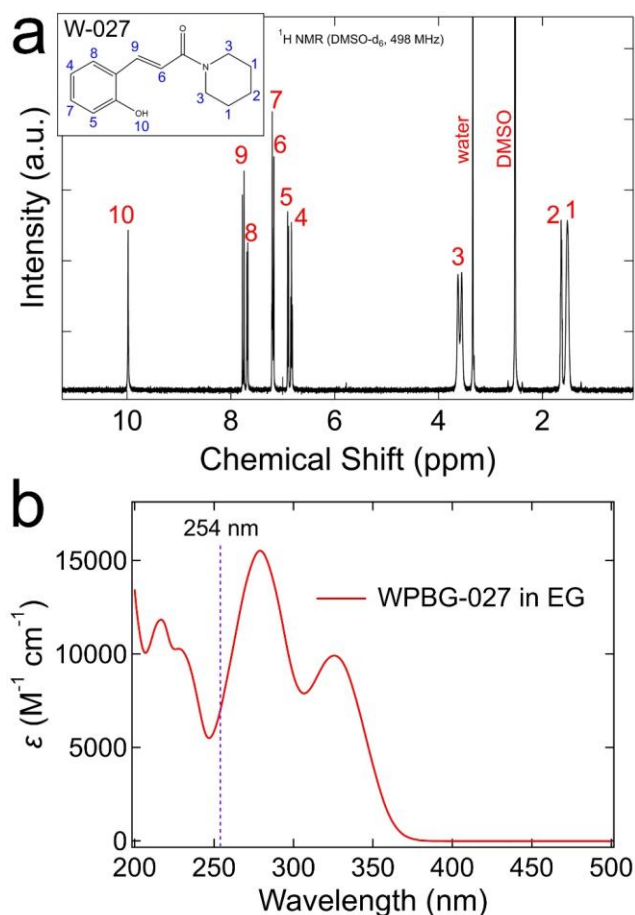


Figure 3.4. Structural and optical characterization of the photobase generator (E)-1-piperidino-3-(2-hydroxyphenyl)-2-propen-1-one (WPBG-027). (a) Proton nuclear magnetic resonance ( $^1\text{H}$ -NMR) spectrum of the molecule in DMSO, with all peaks assigned on the molecular structure. (b) UV-vis spectrum of the PBG dissolved in EG. The absorption coefficient at the excitation wavelength (254 nm) is  $7030 \text{ M}^{-1} \text{ cm}^{-1}$ .

**(E)-1-Piperidino-3-(2-hydroxyphenyl)-2-propen-1-one (PBG W-027):**  $^1\text{H}$  NMR (DMSO- $d_6$ , 498 MHz):  $\delta$  (ppm) - 9.98 (peak 10, 1H, s), 7.76 (peak 9, 1H, d,  $J = 15.51$  Hz), 7.68 (peak 8, 1H, dd), 7.20 (peak 7, 1H, t,  $J = 7.4$  Hz), 7.19 (peak 6, 1H, d,  $J = 15.5$  Hz), 6.90 (peak 5, 1H, d,  $J = 8.1$  Hz), 6.83 (peak 4, 1H, t,  $J = 7.4$  Hz), 3.59 (peak 3, 4H, d,  $J = 35.5$  Hz), 1.64 (peak 2, 2H, m), 1.52 (peak 1, 4H, br).

Table 11. NMR peak analysis of W-027 photobase molecule.

Peak (Chemical Shift)	Norm. Integrated Area	Norm. Expected Area
10 (9.98)	1.00	1
9 (7.76)	0.91	1
8 (7.68)	1.00	1
7 (7.20)	1.13	1
6 (7.19)	0.94	1
5 (6.90)	0.97	1
4 (6.83)	0.97	1
3 (3.59)	4.34	4
2 (1.64)	1.99	2
1 (1.52)	4.04	4



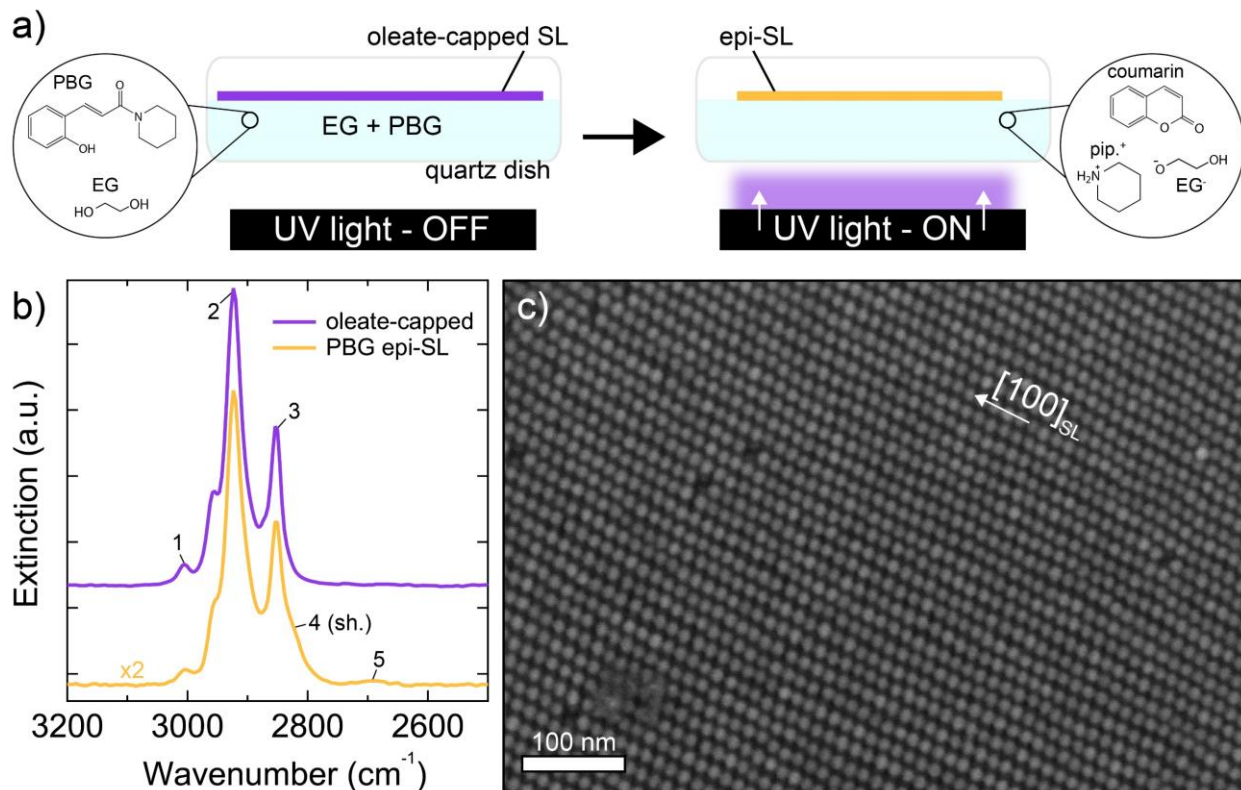


Figure 3.5. Characterization of epi-SLs made using a photobase generator. (a) Cartoon depiction of the photo-initiated formation of epi-SLs using a photobase. First, an oleate-capped SL is formed on the surface of EG spiked with photobase generator (PBG). UV illumination liberates piperidine from the PBG. The piperidine deprotonates EG, and the deprotonated EG exchanges with surface-bound oleate. (b) FTIR spectra of oleate-capped (purple) and PBG epi-SL (yellow) films. The epi-SL spectrum is multiplied by 2x. Labeled peaks are assigned as follows: peaks 1-3 are adsorbed oleate (1:  $\nu(\text{HC}=\text{CH})$ , 2:  $\nu_{\text{as}}(\text{CH}_2)$ , 3:  $\nu_{\text{s}}(\text{CH}_2)$ ), and peaks 4-5 are adsorbed ethylene glycoxide (4:  $\nu_{\text{as}}(\text{CH}_2)$ , 5:  $\nu_{\text{s}}(\text{CH}_2)$ ). (c) SEM image of an  $(01\bar{1})$ -oriented epi-SL formed by photo-initiation of a PBG. Fabrication conditions for the PBG epi-SL film:  $[\text{PBG}] = 1 \text{ mM}$ , 4 hours of  $10 \text{ mW cm}^{-2}$  illumination with a  $\lambda = 254 \text{ nm}$  Hg lamp.

Figure 3.5a shows the basic scheme of epi-SL formation *via* illumination of a photobase generator. Upon illumination of the PBG with UV light, the PBG is converted into equimolar amounts of piperidine and coumarin. Piperidine is a reasonably strong base and can deprotonate EG to form glycoxide. The newly-formed glycoxide exchanges for surface-bound oleate, leading to epi-SL formation. FTIR of the PBG-treated SL film (Figure 3.5b) reveals oleate loss comparable to piperidine-treated films, as well as the emergence of the expected glycoxide peaks. Control experiments show that SL films assembled on a PBG/EG solution but *without* UV exposure do not

experience the same amount of oleate loss or the emergence of glycoxide peaks by FTIR. SEM images (Figure 3.5c) show that the epi-SL has been formed following a four hour exposure to the photo-exposed PBG. Together, these observations confirm the scheme laid out in Figure 3.5a: liberation of piperidine from the PBG upon photo-exposure, formation of glycoxide, and exchange with surface-bound oleate. A four hour treatment is required for complete epi-SL conversion because the solubility limit of the PBG in EG is limited to  $\sim 1$  mM. Assuming 100% conversion of PBG into piperidine ( $pK_b = 3.6$ ), 1 mM solution of PBG should result in a glycoxide concentration of  $\sim 460$   $\mu\text{M}$ . For reference, the piperidine films in Figure 3.1 were treated for 20 min with an approximate glycoxide concentration of 1.7 mM.

Experiments are underway to optimize the concentration-time profile of the PBG and UV light exposure. To ensure that the combination of UV exposure of the photobase leads to epi-SL formation, we performed a series of control experiments, analyzing the resultant SL films using the SEM analysis method described in Section 3.5.3.

UV-illuminated PBG leads to significantly more densification of the SL film (*i.e.*, conversion to epi-SL) than does any combination of heating, dwell time on the EG surface, PBG-free UV exposure, or dark PBG exposure. Fabrication of the epi-SLs *via* UV illumination resulted in slight heating of the EG (to  $< 38$   $^{\circ}\text{C}$ ) and required  $< 5$  hours of total exposure time of the SL to EG. We therefore tested the effects of heating, PBG, and UV exposure on the SL structure. Structural analysis of these SL films shows (Figure 3.6) that indeed the photo-exposed PBG solution results in significantly more epi-SL conversion than any of the controls. These control experiments highlight that efforts to control heating and that reduce time-on-EG should enable finer control over the chemistry driving epi-SL formation. We note that increased time on EG leads to significant SL densification and when possible should be avoided. This observation agrees with

the findings of Van Maekelbergh and coworkers, who fabricated 2D epi-SLs without any chemical trigger, relying instead upon the apparent (but not well understood) ability of neat EG to strip oleate and cause epitaxial fusion.<sup>88</sup>

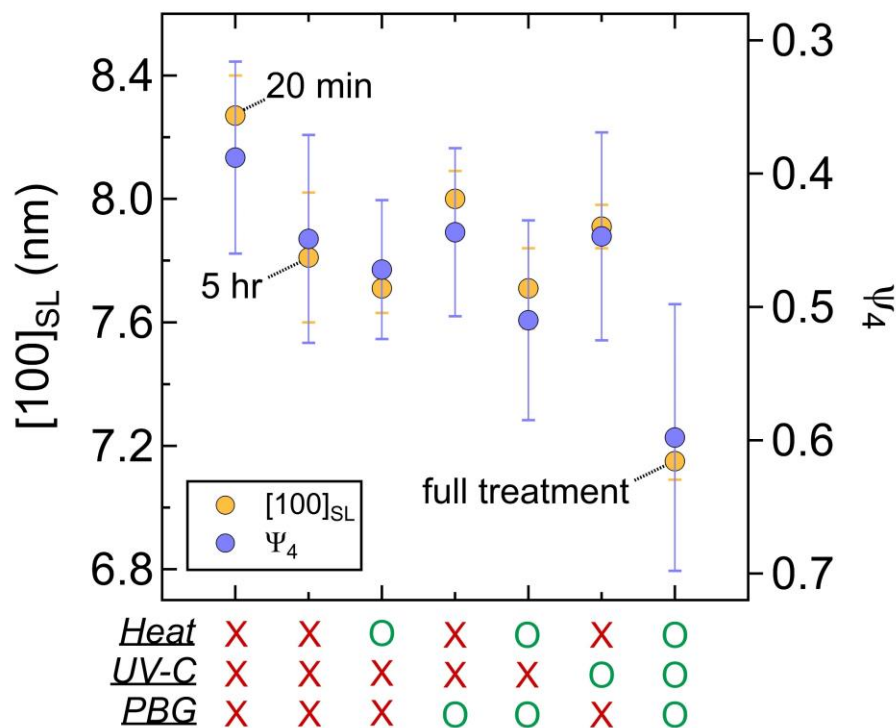


Figure 3.6. Structural analysis of photobase epi-SL film controls. These experiments evaluate how the SL structure is affected by heating, UV light exposure, and the presence of PBG in the subphase, as well as combinations of these conditions. Films were analyzed according to Section 3.5.3. All films were left to dwell on the EG for five hours (unless noted otherwise). For film heating, the entire EG bath was placed on a hot-plate and heated to 38 °C, the approximate temperature of the petri dish under constant UV irradiation.

### 3.3. Proposed Mechanism of Ligand Exchange

The chemical mechanism by which EDA leads to oleate removal from the oleate-capped SL was previously attributed to chelation of Pb by EDA, followed by desorption of the Pb(oleate)<sub>2</sub>-EDA adduct (Figure 3.7a).<sup>40,146,192</sup> We showed in Section 2.2 that this mechanism does not cause epi-SL formation. Figure 3.7b shows our proposed mechanism of oleate exchange by glycoxide. In

this scheme, a Brønsted base (*e.g.*, EDA) deprotonates EG, producing a glycoxide anion. This glycoxide anion exchanges for oleate on the QD surface, resulting in a layer of short glycoxide anions bound to the QD surface. These short ligands enable intimate QD-QD contact and eventual epitaxial fusion. Below, we test this hypothesis and show that it is indeed correct.

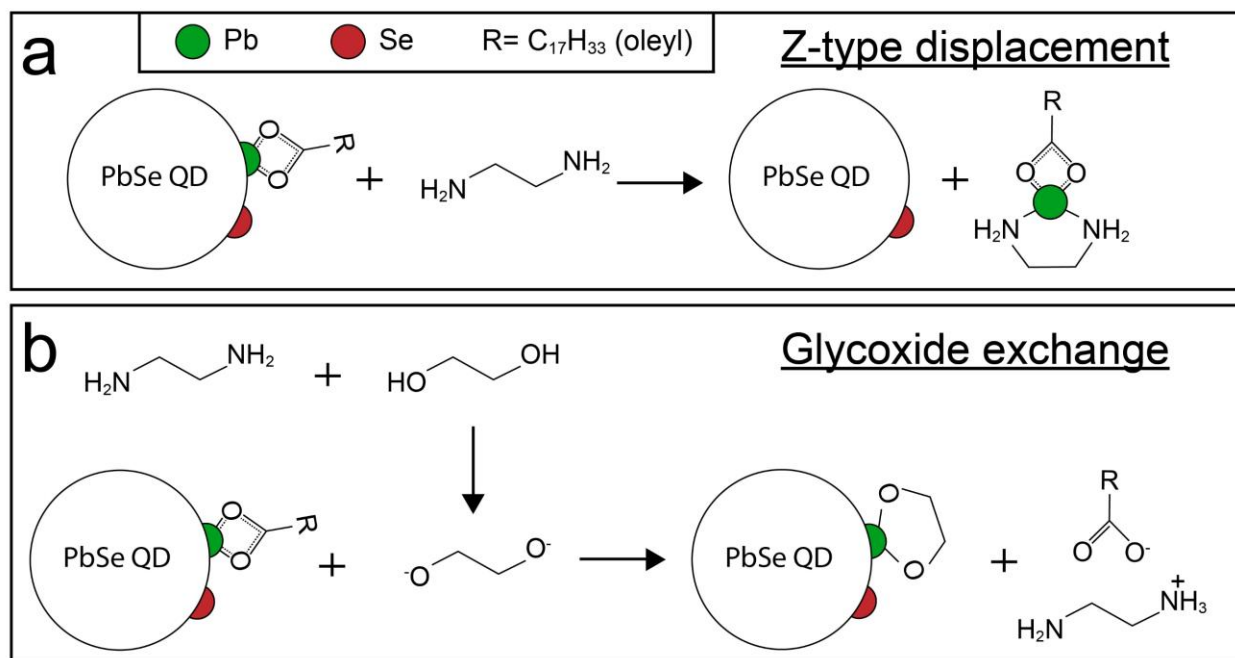


Figure 3.7. Proposed chemical pathways for epi-SL formation. a) Adapted from Anderson *et al.*, L-promoted Z-type displacement mediated by EDA.<sup>192</sup> This process requires binding of EDA to Pb(oleate)<sub>2</sub> on the QD surface, followed by the desorption of (κ<sup>2</sup>-EDA)Pb(oleate)<sub>2</sub> from the QD. For simplicity, Pb is drawn having only one bound oleate, but in principle there are two per Pb atom. b) Glycoxide-mediated oleate exchange: in this process, EDA deprotonates ethylene glycol, which then exchanges for surface-bound oleate. This results in adsorption of ethylene glycoxide to Pb on the QD surface and dissolution of an oleate/protonated EDA ion-pair into EG. Green and red semi-spheres represent Pb and Se, respectively. Not drawn to scale; for illustrative purposes only.

Based on literature values we estimated the pK<sub>b</sub> of EDA in EG to be 4.68, which at an overall EDA concentration of 100 mM yields a glycoxide concentration of 1.1 mM. This is similar to or larger than concentrations used for other anionic ligand exchanges (such as SCN<sup>-</sup>).<sup>114,129</sup> In the original epi-SL report by Hanrath *et al.*, they use an EDA concentration of 250 mM, yielding a

glycoxide concentration of 2.2 mM. We therefore believe that glycoxide/oleate exchange explains all the previously reported epi-SL films made with amines.

Why is glycoxide important? In other words, why not use any X-type ligand? We hypothesize that amines have yielded the best results because their mild basicity leads to a diluted concentration of glycoxide. Our experiments using TBAOH show SL structural evolution that is more binary than continuous. In other words, at a [TBAOH] = 0.1 mM there is very little structural change, but at 0.2 mM the epi-SL has almost fully formed. This small difference in concentration represents a very small region of the parameter space a researcher may be exploring. Thus, we expect many more X-type ligands to be capable of producing epi-SLs, however care must be taken to identify the correct concentration-time profile. On the other hand, there may be some unique aspect of glycoxide (binding strength, denticity, size, solubility) that enable synthesis of high quality epi-SL.

### ***3.4. Conclusion***

We built upon insight into the surface chemistry of epi-SLs to design and demonstrate photo-initiated epi-SL assembly using a photobase generator dissolved in the EG subphase. This simple demonstration paves the way for careful study of processing/structure relationships in photo-triggered epi-SLs. Efforts are ongoing to understand whether the gentler and more uniform ligand exchange offered by photo-triggering will yield epi-SLs with better nano-, micro-, and milli-meter scale morphology than the injection-made films. An exciting aspect of this process is that photo-triggered epi-SLs should be significantly more reproducible. More reproducible films mean studies can be carried out more quickly and with clearer outcomes. Also, our demonstration of epi-SL formation using arbitrary Brønsted bases may allow finer control of epi-SL structure.

There are a few obvious areas where the simple process we presented here can be improved and built upon. The current PBG molecule has limited solubility in EG and so the resultant piperidine concentration following illumination yields a sub-optimal concentration of glycoxide. Increasing PBG solubility or the basicity of the photobase will allow the reaction time to be reduced, which should improve structural quality of the resulting epi-SL. It may turn out that completely uniform glycoxide exchange results in isotropic stresses within the SL film that generate more nano-tearing. This sort of issue could be solved by exposing the PBG-containing solution *via* a progressive front of UV light that sweeps across the SL, from one end to the other. More complex cocktails of photo-reactive molecules could be used for a two-part reaction: the first to initiate epi-SL formation, and the second step (using a different excitation wavelength) to quench the reaction. For example, we know that iodide capping stabilizes the SL structure and prevents further epi-fusion. A variation on this theme is to mix a PBG and a photoacid generator (PAG), each with different excitation wavelengths. Excitation of the PBG initiates epi-SL formation, and excitation of the PAG produces neutralizing acid for the photobase, effectively quenching the reaction.

### **3.5. Methods**

#### *3.5.1. Film fabrication and basic characterization.*

Epi-SLs were synthesized using ~6.5 nm PbSe QDs following the procedures outlined in Section 2.7. All FTIR measurements were performed in air and were corrected to account for film coverage and thickness variation (see Figure 3.8).

### 3.5.2. Analysis of FTIR spectra

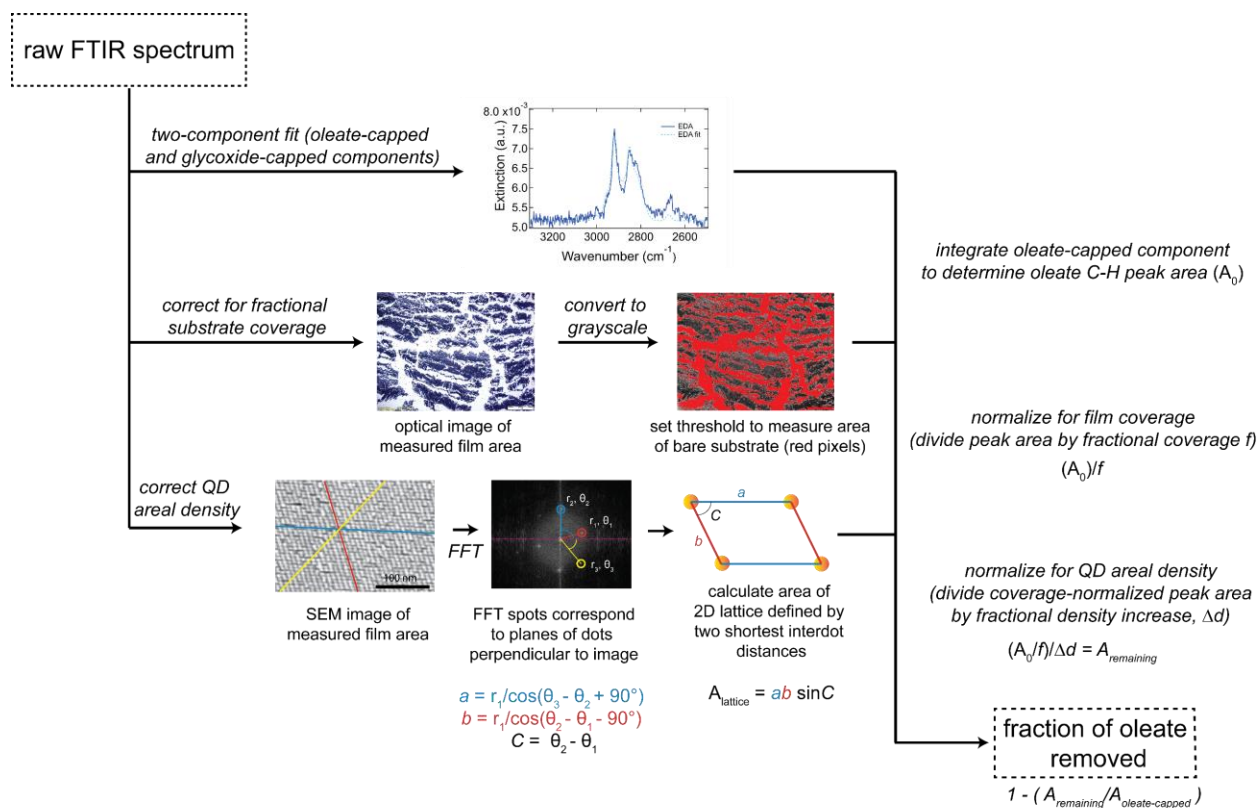


Figure 3.8. Method for quantifying oleate removal from QD SL films using FTIR. The peak area of oleate C-H stretching is quantified on a per-QD basis and compared between film-types. Three sample-dependent factors modulate the raw peak area: (i) glycoxide peaks are deconvoluted using peak fitting and subtraction; (ii) variability in coverage of the substrate by SL film is accounted for using optical microscope images of FTIR samples (iii) changes in QD SL density are determined through analysis of SEM images. The fraction of oleate removed ( $F$ ) is given as:

$$F = 1 - \left( \frac{A_0}{f \Delta d} \right) / A_{OA}$$

where  $A_0$  is the integrated C-H stretching area after glycoxide peak subtraction,  $f$  is the fraction of film coverage,  $\Delta d$  is the change in areal density of the SL (relative to the oleate-capped SL reference sample), and  $A_{OA}$  is the peak area of the oleate-capped reference sample.

### 3.5.3. Image analysis

High-throughput, quantitative analysis of SL images enables insight into important structure/processing relationships. To these ends, we developed a Python-based image analysis tool that generates quantitative information about SL ordering, unit cell parameters, para-crystallinity, and grain size. Using a machine

learning-based clustering algorithm, the software also classifies point, linear, and 2D SL defects. Figure 3.9a delineates the image analysis process flow.

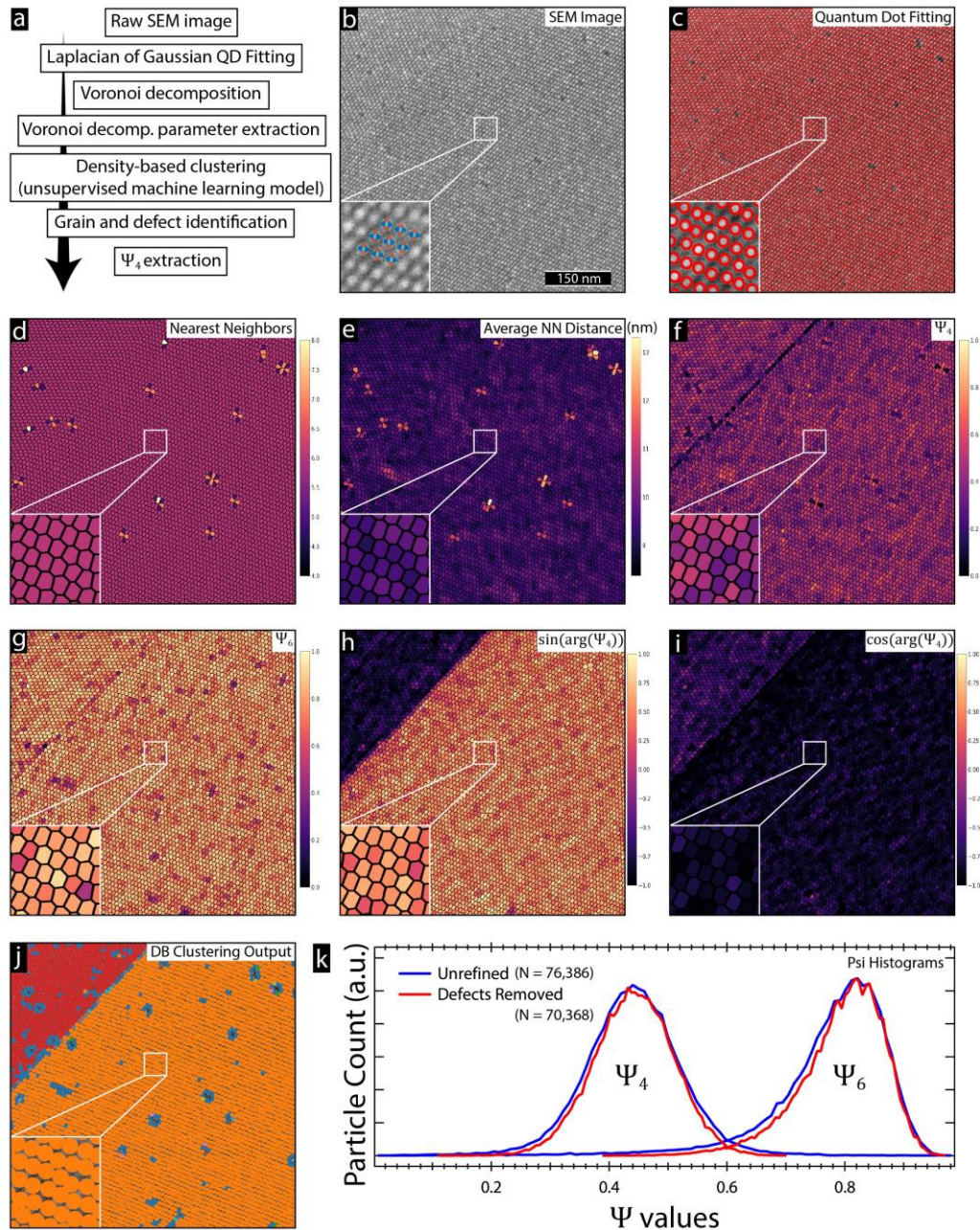


Figure 3.9 Semi-automated superlattice image analysis. a) Flow chart of the full analysis process, b) raw SEM image of an epi-SL with a high-mag inset. c) The same SEM image with results of QD fitting; red circles outline the region where QDs were identified. d-i) Color-coded Voronoi decompositions of the SL image. Each image is labelled with the SL parameter mapped onto the image. j) SEM image of the SL overlaid with QDs colored according to results of density-based clustering using the features shown in (d-i). k) Histogram of 4<sup>th</sup> and 6<sup>th</sup> order bond parameters acquired from 10 SEM images. The red curves are



histograms are generated after removal of defective QDs. The blue curves are from all QDs identified in the image. 76,386 QDs were analyzed for the blue curves.

For each film processing condition or sample-type, we acquired and analyzed ~10 high-resolution (1.5 pixels/nm) images (Figure 3.9b). First, QDs within the image were identified using a blob detection algorithm (Figure 3.9c). The Laplacian of Gaussian approach yielded the most reliable output. We note that using this method, the QD position is limited to single pixel values, meaning our spatial resolution is limited to the image resolution (0.66 nm). More advanced iterations of this software should include sub-pixel fitting of the QD center-of-mass.<sup>159</sup> We next calculated the Voronoi decomposition (VD) of the QD array (Figure 3.9d-i). The VD provides information about local SL symmetry (*i.e.*, a QD and its nearest neighbors (NNs)) which we used to extract quantitative information about the SL and perform the ML-based clustering. Several key structural parameters were extracted from the VD: 6 parameters: 1) number of NNs; 2) average NN distance; 3) standard deviation of NN distance; 4) distance of each NN; 5) area of each Voronoi cell; 6) angle of each NN relative to a reference.

These values can be collected and analyzed to determine various average structural parameters of the SL. For example, the distance between each QD and its two NNs gives the close-packed distance of the SL. In the epi-SL this corresponds to  $\langle 100 \rangle_{\text{SL}}$ . One possible issue arises in films with a high density of structural defects, or in films with multiple SL grain orientations. The ML-based clustering algorithm provides a method to classify QDs within the image based on unique aspects of their local SL environment. It also allows us to eliminate certain particles from the analysis, or to analyze separate grains individually. The first step for clustering analysis involves creation of a design matrix that contains relevant structural information for each QD. The design matrix is an  $n \times p$  array, where each row corresponds to the  $n^{\text{th}}$  QD in the image, and has six feature columns, as follows: (i) number of nearest neighbors in the Voronoi cell, (ii) average nearest neighbor distance; (iii)  $\Psi_4$ , (iv)  $\Psi_6$ , (v)  $\arg(\sin(\Psi_4))$ , and (vi)  $\arg(\cos(\Psi_4))$ .

$$\Psi_a = \frac{1}{P} \sum p_q^{ia\phi_q},$$

where  $P$  is the perimeter of a Voronoi cell,  $p_q$  is the edge length of the Voronoi cell corresponding to the  $q^{\text{th}}$  NN,  $i$  is the imaginary number,  $a$  is the bond-order parameter (*e.g.*, 4 or 6) and  $\phi_q$  is the angle of the  $q^{\text{th}}$  NN. Features with small or noisy variance can be removed at will. Optional features such as standard deviation in NN distance and Voronoi cell area can be added. Color-coded Voronoi decompositions of each of the above features are shown in Figure 3.9d-i. Density-based spatial clustering (DBSCAN) was performed on the design matrix, resulting in an arbitrary number of particle classes, which were then color-coded on the SEM image (Figure 3.9j). The DBSCAN algorithm contains only one fitting parameter ( $\epsilon$ ) which was set empirically to generate the most visually sensible outputs. Segregating the QDs by their clustered classes, we can eliminate contributions from QDs at defect sites. For example, Figure 3.9k shows  $\Psi$  values from all QDs (unrefined) and those colored orange (defects removed) in Figure 3.9j.

Interdot distance values ( $d_{100}$ ) were extracted from simple FFTs of SEM images. We compared these values to those derived from the image analysis software and find good agreement. We opted to use values from FFT analysis because those values are not subject to limitations in the resolution of the blob detection algorithm.

### 3.5.4. $pK_b$ of amines

The  $pK_b$  of amines were determined using literature values (see figure caption). Values were compared between water and ethylene glycol, and a linear regression was applied to account for missing data points, including the  $pK_b$  of EDA in EG. We find close agreement between the  $pK_b$  in water and EG.

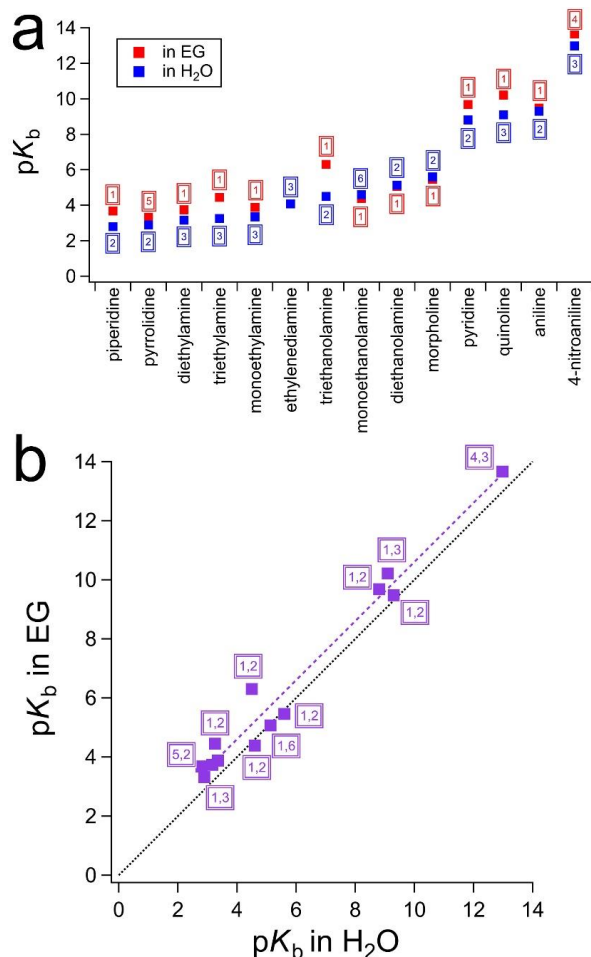


Figure 3.10.  $pK_b$  values of amines in water and ethylene glycol. (a) Plot of the  $pK_b$  values of a series of amines in water (blue) and ethylene glycol (red), as reported in literature and arranged in order of decreasing base strength. (b) Plot of the  $pK_b$  value of each amine in water versus EG.<sup>222–226</sup> The black dotted line is the equivalence line ( $pK_{b,water} = pK_{b,EG}$ ). The purple dashed line is a linear fit of the data, which yields  $pK_{b,EG} = 0.6061 \times pK_{b,water} + 0.9996$  ( $r^2 = 0.97$ ). Using this relationship and the known  $pK_{b,water}$  value of EDA, the  $pK_{b,EG}$  of EDA is estimated to be 4.68.

## CHAPTER 4

### SINGLE-GRAIN EPI-SL ELECTRONICS

This chapter discusses intrinsic charge transport phenomena within individual grains of PbSe QD epi-SLs. The epi-SLs discussed in this chapter have  $\sim 10\times$  larger grain sizes than those presented in Chapter 2, enabling single-grain epi-SL field-effect transistors (SG FETs) with multi- $\mu\text{m}$  lateral dimensions. Charge transport in epi-SLs has been explored using a variety of contact/non-contact DC/AC methods, but no clear signatures of mini-band transport have been presented. The goal of our work is to develop key SL structure/processing/transport relationships that leads to epi-SLs with sufficient coupling and order to generate mini-band transport. A more complete discussion of charge transport in QD solids and epi-SLs is presented in Chapter 1.

First, we develop a nanofabrication process for deterministically integrating large, pristine epi-SL single-grains into FETs. Next, we assess the structure and morphology of individual SG FETs. The electrical properties of numerous SG FETs are characterized using field-effect transistor measurements. These room temperature measurements are complemented by variable-temperature SG FET studies, which provide insight into charge transport phenomena within our epi-SLs. Our SG epi-SL FETs have room temperature hole mobilities between  $0.5\text{-}5\text{ cm}^2\text{V}^{-1}\text{s}^{-1}$ . Cooling the devices to 12 K shows that weakly activated ( $E_a = 3.6\text{ meV}$ ) nearest-neighbor hopping dominates down to  $\sim 50\text{ K}$ . Below 50 K the mobility is nearly independent of temperature. We observe peaks in the drain current at low temperature, which we attribute to sequential filling of the discrete epi-SL (*i.e.*, QD) valence band states.

#### ***4.1. Single-grain Field-effect Transistors***

Single-grain epi-SL FETs (SG FETs) were fabricated according to a microelectronics fabrication process that consists of three major components: 1) fabrication of pre-patterned substrates, 2)

deposition of epi-SL film and encapsulation by atomic layer deposition (ALD) alumina, 3) lithographic patterning of electrical leads and electrodes defining the SG FET. Details of the fabrication procedure are provided in Section 4.4.

Figure 4.1 shows basic characterization of a SG FET (Figure 4.1a). Single epi-SL grains were identified using SEM, then incorporated into the SG FETs following the procedure outlined in Section 4.4.3. Two sets of gold electrodes are visible in Figure 4.1c: Au-1, which span from pre-patterned contact pads (out of the image) to within  $\sim 5 \mu\text{m}$  of the grain, and Au-2, which connect Au-1 to the edge of the epi-SL grain. Au-1 are deposited on top of an electrically insulating  $\sim 30 \text{ nm}$  alumina layer (see Section 4.4.8) and Au-2 are deposited into vias etched into the alumina layer that enable good electrical contact to the epi-SL (see Section 4.4.9). The active device region—typically  $2\text{-}9 \mu\text{m}$  in width and  $3\text{-}9 \mu\text{m}$  in length—is defined by the “fingertip” electrodes (Au-2; Figure 4.1b) Not all devices were single-grain; SL crystallinity was evaluated by taking FFTs of high-resolution SEM images (Figure 4.1b inset).<sup>viii</sup> To prevent oxidation, all fabrication prior to ALD encapsulation of the device was performed in a nitrogen glovebox; the epi-SL was never exposed to ambient air during device fabrication.

---

<sup>viii</sup> We refer to all devices in this section as SG devices (single-grain devices) to differentiate them from large polycrystalline epi-SL FETs.

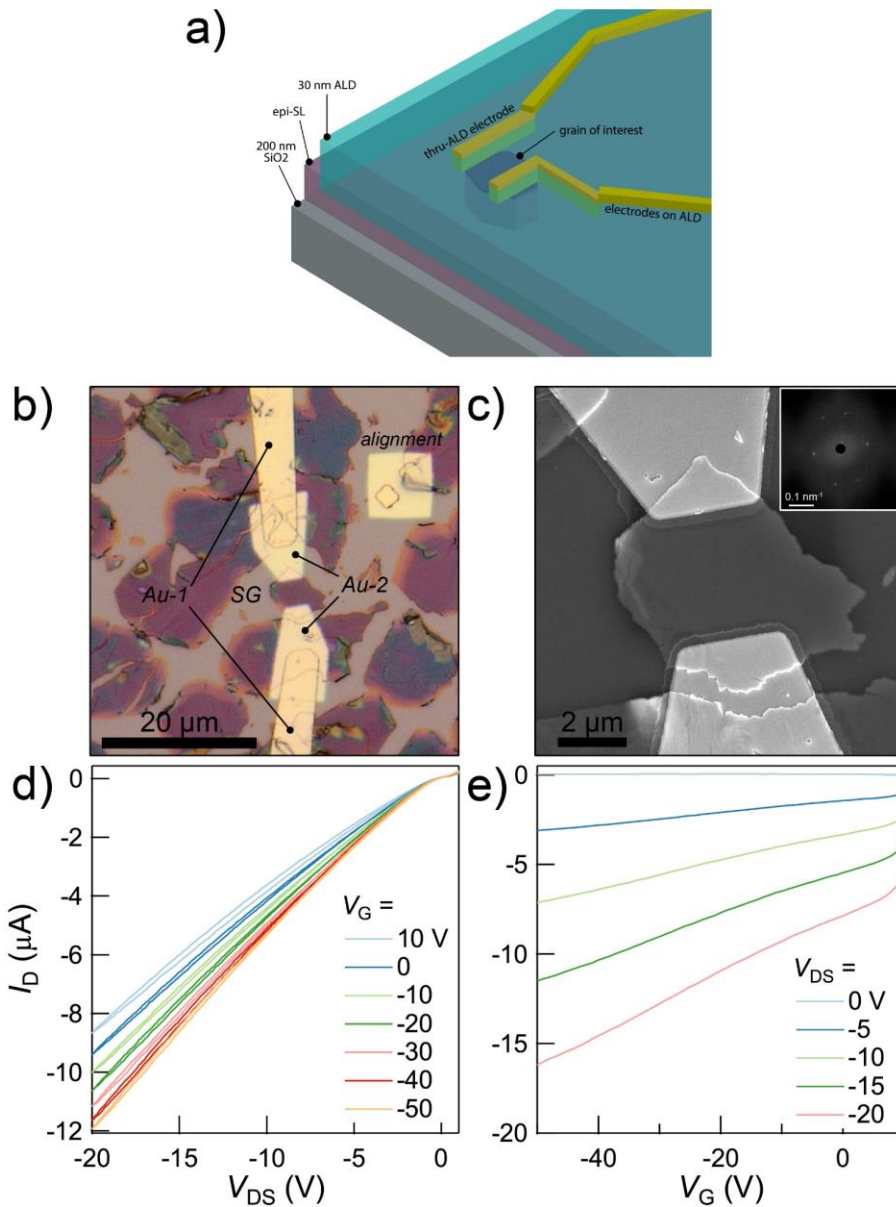


Figure 4.1. Single-grain epi-SL field-effect transistors. a) Cartoon showing a perspective view of a SG FET. b) Optical image of a SG FET. Au-1 are electrodes deposited on top of the epi-SL/alumina stack. Au-2 are electrodes deposited into vias etched into the alumina layer. Both are patterned using electron beam lithography. Au-2 electrodes connect the edge of the epi-SL SG and Au-1 electrodes. Alignment markers used for EBL can be seen in the upper-right corner of the image. Scale bar is 20  $\mu\text{m}$ . c) High-magnification SEM image of the device shown in (b). The electrodes (Au-2) form the active area of the SG FET. This particular device is 3  $\mu\text{m}$  in width and 4  $\mu\text{m}$  in length. The halo around the edge of both electrodes is due to undercut of the alumina etch that occurs prior to metallization. Scale bar is 2  $\mu\text{m}$ . The flake is single-crystalline, as shown in the FFT (inset), as indicated by the presence of a single set of well-defined reciprocal space spots. Analysis of the FFT shows that the SL grain has a  $[100]_{\text{SL}}$  length of 6.95 nm. Scale bar of the FFT is 0.1  $\text{nm}^{-1}$ . d) Output characteristics of the SG FET shown in (a,b). Measurements were

acquired at room temperature in the dark at a sweep rate of 50 V/s. e) Transfer characteristics, acquired at the same conditions as (d).

Charge transport in SG FETs was first evaluated using room temperature FET measurements. Output ( $I_D$  vs.  $V_{DS}$ ) and transfer ( $I_D$  vs.  $V_G$ ) curves of an SG FET (Figure 4.1c,d) show that they are  $p$ -dominant transistors with poor  $I_{on}/I_{off}$  and a positive threshold voltage. Hole mobilities were extracted from transfer curves at  $V_{SD} = -15$  V and  $V_{GS} = -45$  V using the gradual channel approximation. In our champion SG chip, we find an average room temperature (RT) hole mobility of  $1.98$   $\text{cm}^2/\text{Vs}$ , which to our knowledge is the highest reported hole mobility for any PbX QD FET,<sup>114,227,228</sup> and is slightly higher than our previously reported record for polycrystalline epi-SLs ( $1.1$   $\text{cm}^2/\text{Vs}$ ).<sup>169</sup> The RT mobility of our champion device is  $4.8$   $\text{cm}^2/\text{Vs}$ .

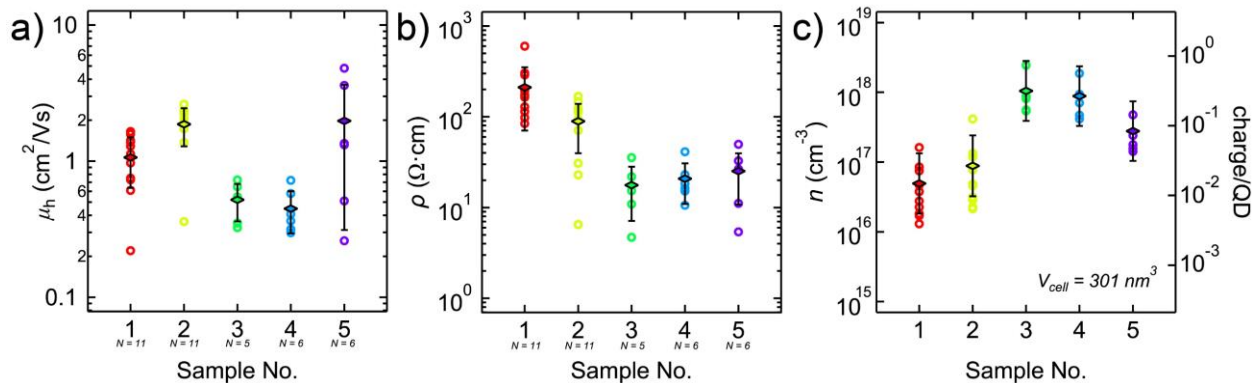


Figure 4.2. Single-grain field-effect transistor electronic properties. (a-c) The figures show data taken from five separate chips (Sample No.) with each chip containing between 5 to 11 devices. Full details of the analysis are provided in Table 12. a) Mobility values extracted from forward-sweep transfer curves at  $V_{DS} = -15$  V and  $V_G = -45$  V. Transfer curves were acquired at a sweep rate of 50 V/s. Mobilities were not corrected to account for the bias-stress effect. b) Resistivity values taken at  $V_G = 0$  V. c) Carrier concentration estimates were made using the mobility and resistivity values in (a,b). All measurements were performed at room temperature.

Figure 4.2 shows the compiled RT electronic properties of 39 SG FETs distributed across five different substrates. Chip-averaged hole mobilities (Figure 4.2a) vary between  $0.45$ - $1.98$   $\text{cm}^2/\text{Vs}$ . We note that these mobility values are likely underestimates due to the bias-stress effect, which is

prominent in these devices at room temperature.<sup>229</sup> The resistivity of each SG FET was extracted at  $V_G = 0$  and is plotted in Figure 4.2b. Using resistivity and mobility values, we estimate the carrier concentration and QD occupation. We note that field-effect mobility may be an overestimate of the *equilibrium* mobility and may lead to artificially high carrier concentration results. Taking these carrier concentration values as approximately correct, we can calculate the free carrier density on a per-QD basis. The epi-SL has approximate lattice parameters of  $a = 6.8$  nm (from SEM image analysis) and  $\alpha = 99^\circ$  and therefore an epi-SL unit cell volume  $V_{\text{cell}} = 3.01 * 10^{-19}$  cm<sup>3</sup>. In our distorted cubic epi-SLs there is 1 QD per unit cell. Therefore, charge occupation ranges from 0.32 charges/QD in the most heavily doped chip to 0.015 charges/QD in the least doped chip. The origin of these doping differences is not known; there are numerous possible sources (*e.g.*, variations in ligand composition, QD fusion, and thermal annealing) within the epi-SL and at the semiconductor/dielectric interface that may cause this variation. We note that chip-to-chip variation likely results from inhomogeneous ligand exchange (a shortcoming of the point-injection method), QD batch differences, and differences in the degree of epi-fusion. Inhomogeneity of the point-injection was part of the motivation for the work in Chapter 3. Table 12 shows the complete room temperature SG FET data set for all five chips (including analysis of epi-SL structure).

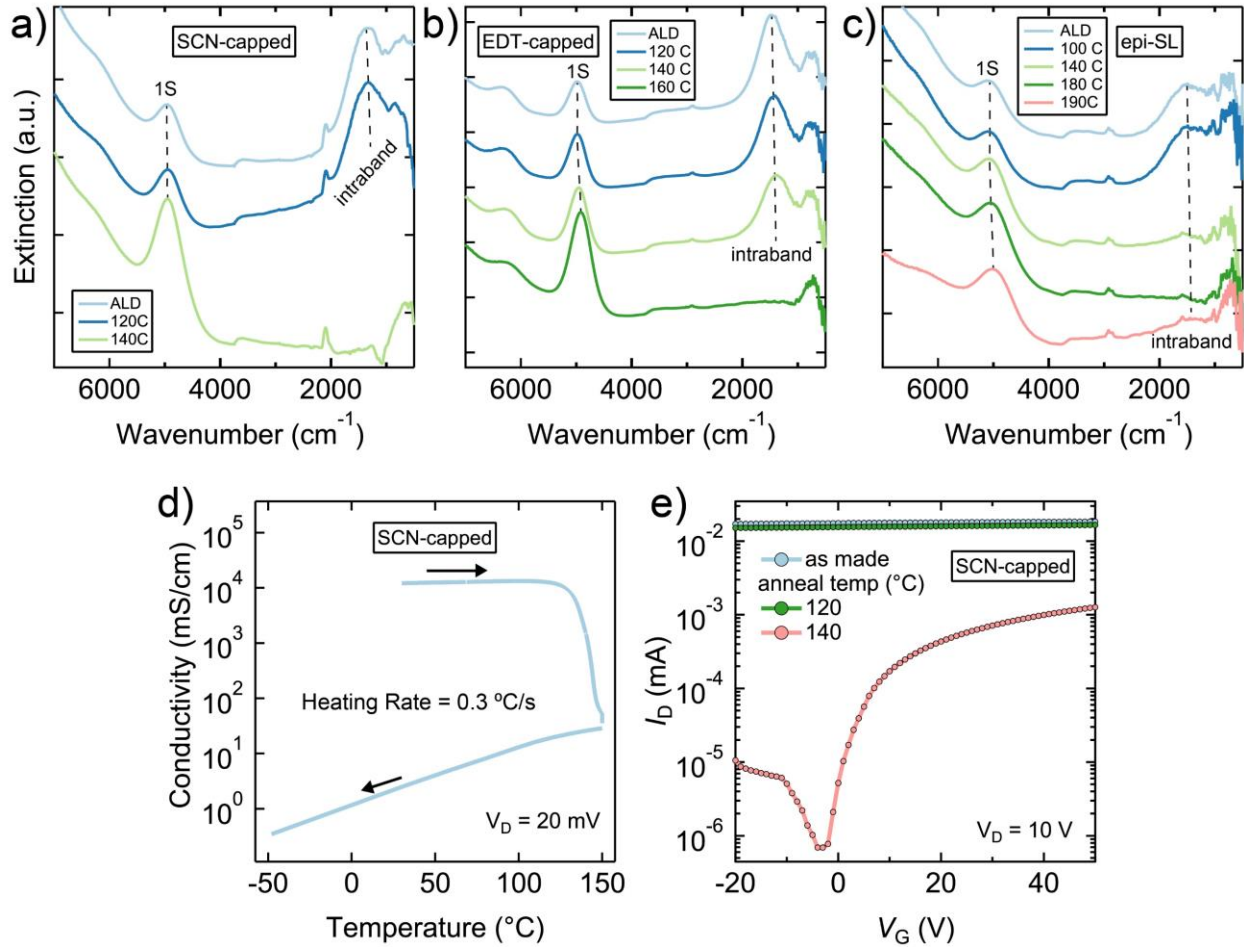


Figure 4.3. Impact of annealing on the doping profile of ALD-infilled PbSe QD films. All films were infilled and capped with 20 nm of alumina ALD deposited at 60 °C. FTIR spectra of (a) amorphous (no long-range order) SCN-capped QD film, (b) amorphous EDT-capped QD film, and (c) EDA-treated epi-SL film show 1<sup>st</sup> exciton bleaching in as-made film (“ALD”) and associated appearance of an intraband transition at ~1000 cm<sup>-1</sup>. This is due to filling of the 1S QD state (8 e<sup>-</sup>/QD) by an unknown doping source associated with the alumina. The intraband transition is an optical transition between the 1S<sub>e</sub> and 1P<sub>e</sub> states.<sup>48</sup> After annealing for three minutes at the temperatures specified in the graphs, the intensity of the intraband transition is reduced (or eliminated) and the strength of the first exciton transition (1S) is increased, indicating a significant reduction in doping. d) In-situ conductivity of an SCN-capped amorphous QD FET as a function of temperature. The heating rate was 0.3 °C/second. At ~140 °C the conductivity drops precipitously, indicating elimination of the *n*-type donor. The conductivity drops at the same temperature as the elimination of the intraband transition in (a). e) Transfer curves of the FET in (d) show that the off current of the FET drops after annealing at 140 °C. This is associated with a sharp reduction in the free carrier concentration. All annealing steps were performed for five minutes, except for in (d) which underwent continuous heating from room temperature to 150 °C.

These SG FETs have different electronic properties than our previously reported ALD-infilled epi-SL FETs, which were strongly doped *n*-type.<sup>169</sup> The difference in doping profiles is because—



in contrast to those reported in Chapter 2—the epi-SLs reported here underwent post-ALD thermal annealing. Figure 4.3 shows the effects of brief thermal annealing treatments on three types of ALD-infilled PbSe QD films. We found that brief (~3-5 minute) annealing at ~150 °C causes a precipitous reduction in free carrier concentration, and even switching from *n*- to *p*-dominant FETs. The effect appears to be consistent across QD film chemistries and SL structures (*i.e.*, epi-SLs and amorphous QD solids), indicating that the proximate cause lies in the alumina layer rather than surface ligands or the QDs themselves. The mechanism for this thermally-induced change in doping is currently unknown, but we suspect it is due to either (*i*) a thermally-activated chemical reaction occurring at the alumina/QD interface, or (*ii*) elimination of fixed charge/charge trap states within the alumina layer. Importantly, the width of the 1<sup>st</sup>-exciton transition is unaffected by annealing, indicating that there is no additional sintering of the QDs.<sup>172</sup>

We briefly sought to understand the relationship between the structure and electronic properties of epi-SLs. Chips 1 and 2 were continuous, polycrystalline (poly) epi-SL films. Chips 3-5 were nearly all single-grain, and all but two devices were composed of epi-SL grains with  $(01\bar{1})_{\text{SL}}$  orientation (see Table 12). Chips 3 and 4 were ~70 nm thick, whereas the others were 50 nm thick. Chips 1 and 2 were made with Batch 1 QDs, and Chips 3-5 were made with Batch 2 QDs (see Section 4.4.10). We observe no obvious correlation between epi-SL crystallinity and mobility, at least in room temperature FET measurements. To gain a deeper understanding of charge transport mechanism(s) in our SG FETs, we performed temperature-dependent FET measurements down to 80 K. One device was cooled to 12 K.

Table 12. Summary of electronic and structural properties of epi-SL single-grain devices.

Chip	Device	Mobility <sup>i</sup>	Resistivity	Carrier Conc.	Channel Length	Channel Width	Approx. Thickness <sup>ii</sup>	[100] <sub>SL</sub> <sup>iii</sup>	Area/QD <sup>iv</sup>
		(cm <sup>2</sup> V <sup>-1</sup> s <sup>-1</sup> )	(Ω·cm)	(cm <sup>-3</sup> )	(μm)	(μm)	(nm)	(nm)	(nm <sup>2</sup> )
1 <sup>v</sup>	1	0.73	114.2	7.5E+16	2.5	3	50	6.98	59.07
	2	1.29	128.6	3.8E+16	2.5	3	50	7.21	60.87
	3	1.38	164.1	2.8E+16	3	3	50	7.25	62.28
	4	1.13	304.0	1.8E+16	2	3	50	7.01	60.16
	5	0.22	174.8	1.6E+17	2	2	50	6.89	59.85
	6	0.97	170.0	3.8E+16	3	3	50	--	--
	7	1.42	194.3	2.3E+16	3	3	50	7.16	58.77
	8	1.65	290.1	1.3E+16	3	3	50	--	--
	9	--	--	--	3	4	50	7.11	59.90
	10	0.75	97.7	8.5E+16	3	3	50	--	--
	11	1.58	84.2	4.7E+16	3	3	50	7.17	60.60
	12	0.61	600.6	1.7E+16	3	3	50	7.17	58.83
2 <sup>v</sup>	1	1.74	113.8	3.2E+16	3	6	50	--	--
	2	0.36	146.4	1.2E+17	3	6	50	--	--
	3	1.37	93.9	4.8E+16	3	6	50	--	--
	4	1.87	116.1	2.9E+16	3	6	50	--	--
	5	2.04	22.9	1.3E+17	3	6	50	--	--
	6	2.62	30.7	7.8E+16	3	6	50	--	--
	7	2.24	123.9	2.2E+16	1.2	33	50	--	--
	8	1.92	71.0	4.6E+16	3	9	50	--	--
	9	2.31	6.5	4.1E+17	3	9	50	--	--
	10	--	--	--	3	9	50	--	--

<sup>i</sup> Calculated from forward sweep transfer curves at V<sub>G</sub> = -45 V and V<sub>DS</sub> = -15 V, acquired between 50-250 V/s.

<sup>ii</sup> Estimated from the empirical relationship between epi-SL color and thickness measurements made using SEM.

<sup>iii</sup> Distance of close-packed direction (epi-fusion direction) extracted from SEM images of the epi-SL grain(s).

<sup>iv</sup> Areal density of QDs in the epi-SL grain(s).

<sup>v</sup> Polycrystalline and made with Batch 1 QDs.

Chip	Device	Mobility <sup>i</sup>	Resistivity	Carrier Conc.	Channel Length	Channel Width	Approx. Thickness <sup>ii</sup>	[100] <sub>SL</sub> <sup>iii</sup>	Area/QD <sup>iv</sup>
		(cm <sup>2</sup> V <sup>-1</sup> s <sup>-1</sup> )	(Ω·cm)	(cm <sup>-3</sup> )	(μm)	(μm)	(nm)	(nm)	(nm <sup>2</sup> )
	11	2.34	89.4	3.0E+16	3	9	50	--	--
	12	1.73	168.0	2.1E+16	3	9	50	--	--
3 <sup>vi</sup>	1	--	--	--	3	6	70	6.88	61.29
	2	0.351	21.9	8.1E+17	6	6	70	6.97	61.57
	3	--	--	--	4	6	70	6.94	61.88
	4	--	--	--	3	6	70	7.02	61.27
	5	0.65	10.9	8.8E+17	3	6	70	6.98	62.60
	6	--	--	--	3	9	70	7.00	61.43
	7	--	--	--	3	6	70	7.02	62.44
	8	--	--	--	3	6	70	7.04	62.81
	9	--	--	--	3	6	70	--	--
	10	0.325	35.5	5.4E+17	3	6	70	6.96	61.42
	11	0.728	15.3	5.6E+17	4	4	70	6.98	62.03
	12	0.547	4.7	2.4E+18	5	4	70	6.98	62.86
4 <sup>vi</sup>	1	0.316	10.6	1.9E+18	3	6	70	6.99	61.05
	4	0.579	15.2	7.1E+17	4	3	70	6.94	59.87
	5	0.723	18.4	4.7E+17	3	6	70	6.92	60.89
	6	0.298	23.0	9.1E+17	2	5	70	7.10	60.99
	7	0.408	16.3	9.4E+17	3	6	70	7.09	61.93
	8	--	--	--	4	4	70	6.88	59.75
5 <sup>vi</sup>	9	0.364	41.2	4.2E+17	3	6	70	7.07	61.38
	4	1.32	26.5	1.8E+17	3	4.5	50	6.97	59.98
	5	1.35	32.7	1.4E+17	3.3	5.3	50	6.97	48.03 <sup>vii</sup>
	6	0.26	49.7	4.8E+17	3.6	4.4	50	--	--
	7	3.60	11.1	1.6E+17	7	7	50	7.11	60.99

<sup>vi</sup> Single-crystalline and made with Batch 2 QDs.

<sup>vii</sup> These epi-SL grains were oriented with their (100) plane parallel to the substrate surface, which results in a higher areal density of QDs.

Chip	Device	Mobility <sup>i</sup>	Resistivity	Carrier Conc.	Channel Length	Channel Width	Approx. Thickness <sup>ii</sup>	[100] <sub>SL</sub> <sup>iii</sup>	Area/QD <sup>iv</sup>
		(cm <sup>2</sup> V <sup>-1</sup> s <sup>-1</sup> )	(Ω·cm)	(cm <sup>-3</sup> )	(μm)	(μm)	(nm)	(nm)	(nm <sup>2</sup> )
	8	0.51	25.7	4.8E+17	3	3	50	6.77	57.62
	9	4.82	5.4	2.4E+17	6.5	5.5	50	7.00	50.00 <sup>vii</sup>

## 4.2. Variable-temperature FET Measurements

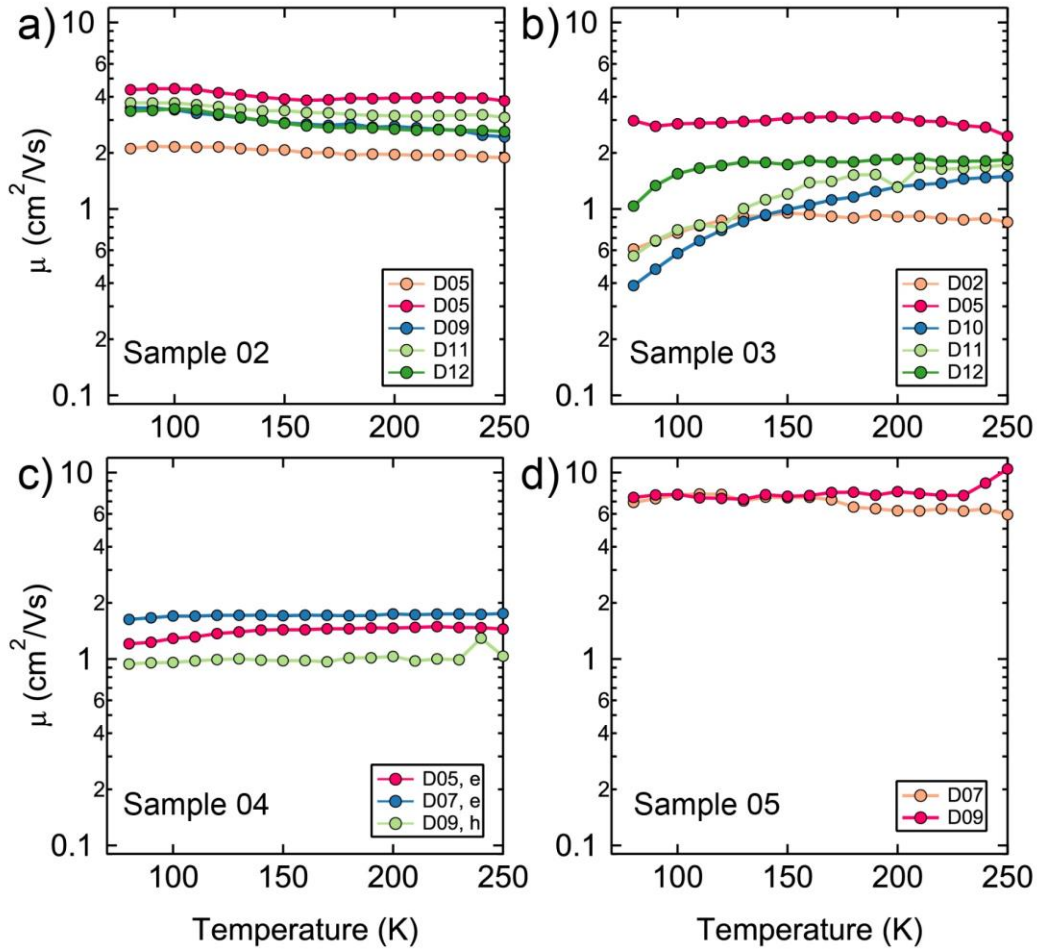


Figure 4.4. Temperature-dependent mobility of single-grain epi-SL field-effect transistors. Chips 3,4, and 5 were corrected to account for bias-stress induced losses (see Section 4.4.11). The temperature range was truncated at 250 K because higher temperatures produced significant hysteresis in transfer curves. All mobilities were calculated at  $V_{DS} = -15$  V,  $V_G = -45$  V using the gradual-channel approximation (see Section 2.7.11). Note that Chip 2 mobility was not corrected for current transients related to the bias-stress effect.

We performed variable-temperature electrical measurements of 15 SG FETs distributed across four chips. By reducing the measurement temperature, we can reduce or eliminate the bias-stress effect, which manifests as a transient decay in the drain current ( $I_{DS}$ ) upon application of a gate bias (see Section 4.4.11). Additionally, temperature dependence of the mobility gives insight into

charge transport processes within the epi-SL. Hole mobility values<sup>i</sup> extracted from these 15 SG FETs are presented in Figure 4.4. The mobility values are remarkably consistent within and across the four chips, validating that the fabrication process is robust and reproducible.

Almost all the SG FETs show mobilities from 80 to 250 K that are nearly independent of temperature. These findings agree with a previous report of ALD-infilled *amorphous* PbSe QD solids that showed temperature-independent electron mobility over the same temperature range.<sup>114</sup> In that report, the hole mobility decreases with increasing temperature, however this is likely due to the bias-stress effect.<sup>114</sup> These findings contrast with the thermally activated transport reported by Hanrath and coworkers,<sup>146</sup> indicating that carriers in our epi-SLs may be partially delocalized. This temperature-independent transport is not understood, but appears to be prominent in ALD-infilled PbSe QD solids. Because the bias-stress effect is active at temperatures as low as 150 K, we performed FET measurements down to 12 K to glean further insight into epi-SL charge transport.

Figure 4.5a shows transfer curves acquired between 12 and 250 K. The FET behavior shifts with increasing temperature from ambipolar conduction to primarily unipolar hole conduction. The threshold voltage of the FET shifts to higher positive gate bias as the temperature increases, presumably due to temperature-dependent changes in the free carrier concentration. Figure 4.5b shows mobility values calculated at each point along the transfer curves. At low temperature, a significant mobility gap appears near the threshold voltage, but at higher temperature the mobility remains relatively constant throughout the applied gate bias range.

---

<sup>i</sup> Chip 4, Devices 5 and 7 were converted to *n*-channel dominant FETs through post-fabrication exposure to an electron beam (imaging). Thus, the mobilities reported are electron mobilities.

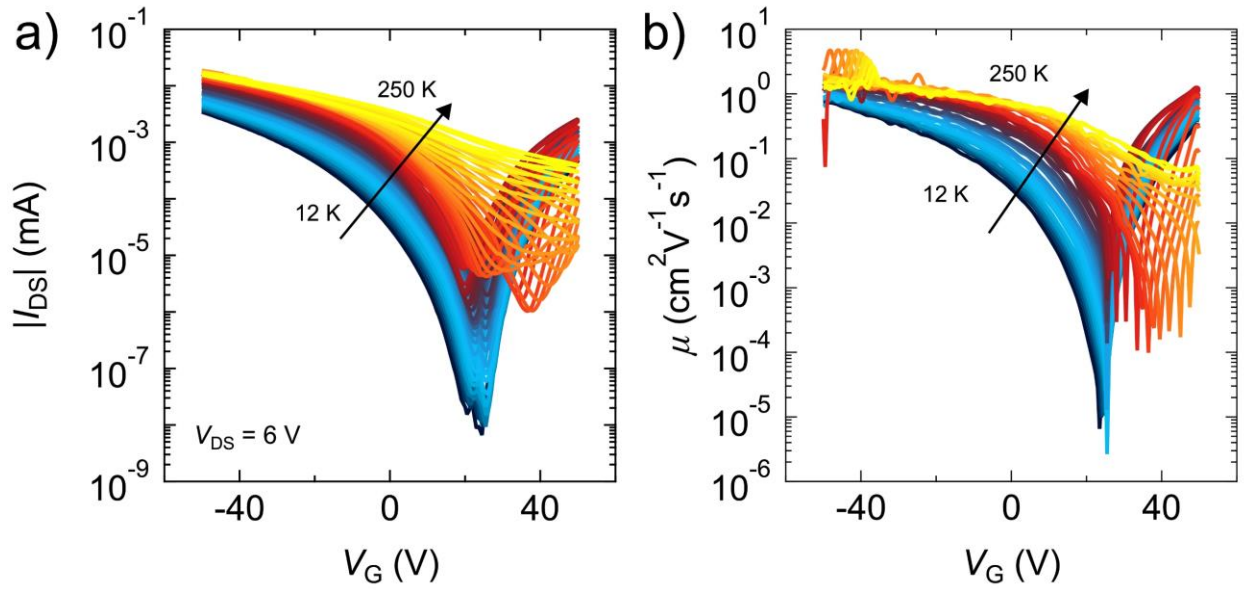


Figure 4.5. Variable-temperature transfer curves and mobility single-grain transistor. a) Transfer curves acquired between  $V_G = -50$  to  $50$  V and  $V_{DS} = 6$  V. b) Mobility acquired at all points of the transfer curves shown in (a). From Chip 5, Device 9.

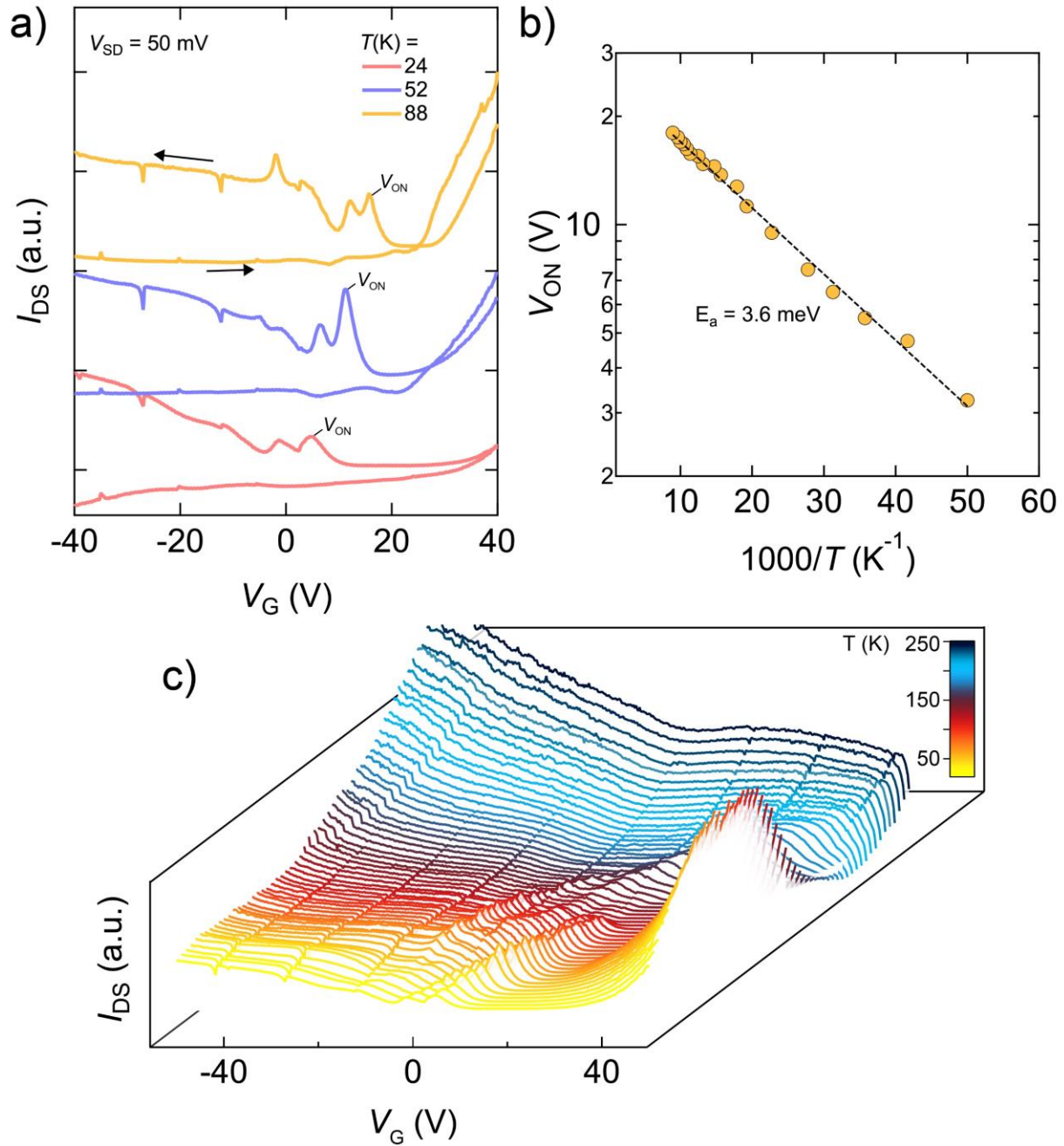


Figure 4.6. Gate-induced state-filling of a single-grain epi-SL field-effect transistor. a) Variable-temperature transfer curves measured at  $V_{DS} = 50$  mV. Visible are local maxima ( $V_{ON}$ ) in  $I_{DS}$  which correspond to the turn-on gate bias of the p-channel. These local maxima shift with temperature. b)  $V_{ON}$  as a function of temperature, fit with  $\ln(V_{ON}) = -E_a/k_B T$ , where  $E_a = 3.6$  meV. c) Full temperature series of the data shown in (a). From Chip 5, Device 9.

Gate bias sweeps with  $V_{DS} < 1$  V produced peaks in the drain current (Figure 4.6). Between  $V_G = +40$  to  $-40$  we observed four peaks in  $I_D$  which shift together as the temperature is varied. Transfer



curves acquired with larger  $V_{DS}$  show that  $V_{ON}$  (see Figure 4.6a) corresponds to the onset of  $p$ -channel conduction, but with apparent loss of the peaks. This relation between  $V_{ON}$  and the onset of  $p$ -channel conduction suggests that the current peaks are due to hole injection into valence band states within the epi-SL. One possible explanation is that they are Coulomb oscillations from the sequential filling of eight  $1S_h$  states. In PbSe QDs there are four degenerate valence band states (eight including spin degeneracy) and—while these  $1S_h$  states are degenerate—there is a charging energy (Coulomb blockade) associated with subsequent addition of electrons or holes to an individual QD or region of epi-SL film.<sup>144</sup> However, the spacing between peaks (several volts) is much larger than anticipated for these samples.<sup>114</sup> An alternate explanation is that each peak corresponds to the discrete electronic states of the QDs. In this scheme, the four peaks would represent the  $1S_h$ ,  $1P_h$ ,  $1D_h$ ,  $1F_h$ . This possibility is also highly unlikely because of the extremely high carrier concentration that would produce.

Figure 4.6b shows that  $V_{ON}$  has a temperature dependence that is well-fit by an Arrhenius model with  $E_a = 3.6$  meV. The charging energy of an epi-SL of similar composition was calculated to be  $\sim 3.4$  meV,<sup>146</sup> however it is unclear why  $V_{ON}$  should have an activation energy of 3.6 meV. Perhaps holes in a shallow acceptor state  $\sim 3.6$  meV below the valence band are ionized, causing a shift in the carrier concentration at the dielectric interface. The loss of current peaks with higher  $V_{DS}$  is possibly because the potential drop across each QD ( $\sim 1.2$  meV/ $V_{DS}$ ) approaches and exceeds the charging energy, resulting in large tunneling rates that smear out charging effects.<sup>144</sup> Current traces in Figure 4.6a were acquired with  $\sim 60$   $\mu$ V dropped across each QD. The current peaks are similarly lost at  $T > 120$  K. Further study is required to fully understand the origin of these peaks and the significance of their temperature and bias dependence.

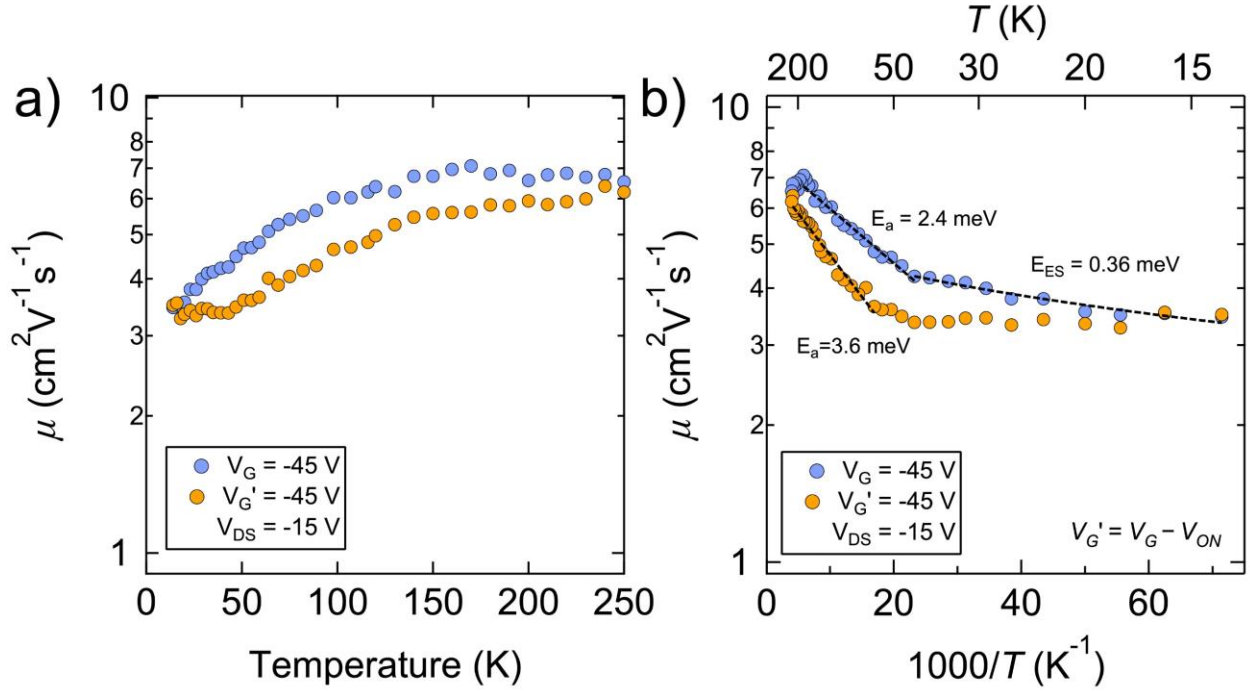


Figure 4.7. Variable-temperature mobility of a single-grain field-effect transistor between 14 to 250 K. a) Plot of mobility vs. temperature. The two curves correspond to mobility values extracted using  $V_G = -45$  V (blue) or  $V_G' = V_G - V_{ON}$  (orange) based on the temperature-dependence of  $V_{ON}$  shown in Figure 4.5. a) Log plot of the mobility shown in (a). Overlaid on the data are fits using  $\mu \propto e^{-\left(\frac{E}{kT}\right)^\beta}$  where  $\beta = 1$  for nearest-neighbor hopping and  $\beta = 0.5$  for Efros-Shklovskii variable-range hopping (VRH). Activation energies are annotated on the graph ( $E_a$  for nearest neighbor hopping,  $E_{ES}$  for E-S VRH).

Figure 4.7 shows the mobility of a SG FET from 14 to 250 K. Below 80 K the device shows more clearly the thermally-activated behavior expected for hopping transport. We calculated the mobility using both a static and threshold-voltage dependent  $V_G$ . The latter is denoted as  $V_G'$  and follows  $V_G' = V_G - V_{ON}$ , where  $V_{ON}$  is the gate bias extracted from the fit in Figure 4.6b. Because these devices show considerable sub-threshold swing, extracting a precise threshold voltage is not possible and therefore we use  $V_G'$ . The plot in Figure 4.7b shows two distinct regions of temperature dependence. At higher temperatures, we find good agreement with a nearest-neighbor hopping model  $\mu \propto e^{-\left(\frac{E_a}{kT}\right)}$  with  $E_a = 2.4$  and  $3.6$  meV for  $V_G = -45$  V and  $V_G' = -45$  V, respectively. The difference between these two values may be due to differences in QD charge occupation. At

$T < 50$  K, the mobility becomes nearly independent of temperature. We are not sure how to explain these results, although it is possible that this temperature range is dominated by Efros-Shklovskii variable-range hopping. However, that yields an activation energy ( $E_{ES}$ ) of  $<1$  meV which may be unphysical. While variable-temperature SG FET measurements provide stimulating and interesting results, further studies are required to better understand transport phenomena in these epi-SLs.

### **4.3. Conclusion**

Charge carrier mobility in our current state-of-the-art epi-SLs is within the range anticipated for QD solids with emergent mini-band transport.<sup>180</sup> Furthermore, nearly temperature-independent mobility at low temperature may be indicative of carrier delocalization, but it is not conclusive. Further analysis and modelling of these results should provide additional insight into the transport physics. The emergence of structure in the drain current of our single-grain transistors at reduced temperature potentially gives insight into carrier occupation of epi-SL states and other electronic properties. Development of a robust single-grain epi-SL device platform is an important achievement and provides fertile ground for future study of epi-SL charge transport.

### **4.4. Methods**

#### *4.4.1. Epi-SL device fabrication*

This section describes the fabrication of single-grain epi-SL devices. I begin with a brief overview of the process, followed below by a comprehensive description.

The fabrication process begins by patterning Si/SiO<sub>2</sub> chips (1.5 cm x 1.5 cm) with metallic electrode pads and a series of alignment markers. These patterns were generated with a custom photomask and traditional photolithography. Epi-SL film was selectively deposited onto a portion of the substrate and then overcoated and infilled with alumina to prevent oxidation and to thermally stabilize the film. High-quality single-grains were identified using scanning electron microscopy and metal electrodes were formed between the grains and pre-patterned electrodes. Vias were etched into the alumina layer so that the metal contacts were in intimate contact with the epi-SL.

A cartoon of the single-grain device construct is shown in Figure 4.8 and highlights several key features, including the two sets of metal electrodes that connect the epi-SL grain (grain of interest) and large pre-patterned electrode pads (not shown). The “electrodes on ALD” contact the pre-patterned electrode pads and approach near the grain of interest, without touching it. They sit on top of a ~30 nm layer of alumina film, meaning they are electrically isolated from the epi-SL film. The “thru-ALD electrodes” connect the tips of the “electrodes on ALD” with the edge of the epi-SL grain through vias in the alumina layer.

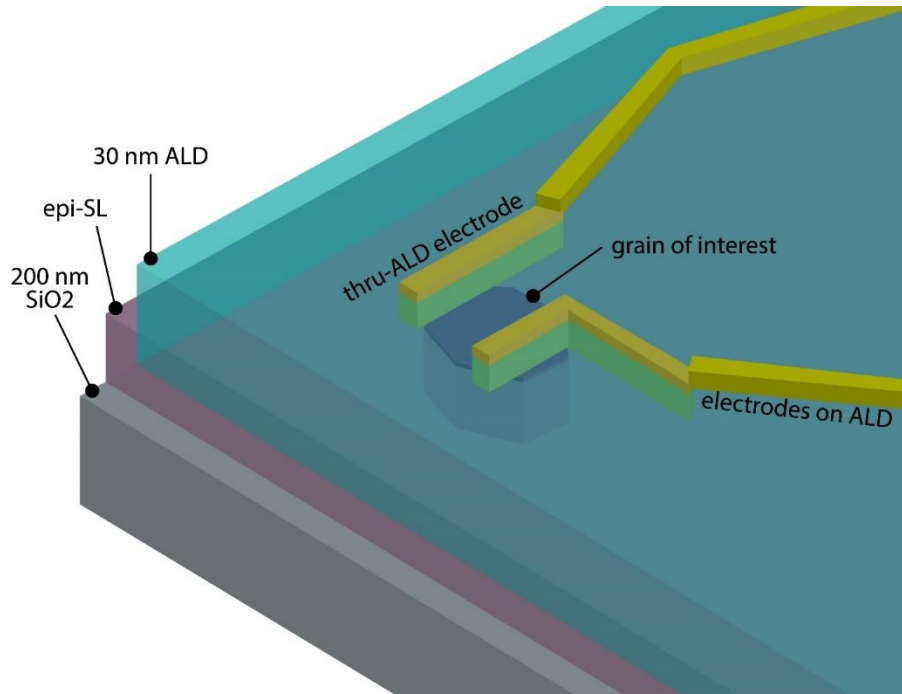


Figure 4.8. Schematic of single-grain epi-SL field-effect transistor. Epi-SL films were deposited onto a degenerately doped silicon substrate with a 200 nm dielectric layer. The epi-SL films were overcoated with ~30 nm of alumina via atomic layer deposition. Electrical contacts were formed to the individual epi-SL grains in two steps: one part of the electrode sits atop the ALD layer, and one part of the electrode goes through a via in the ALD layer and contacts the edge of the epi-SL grain.

#### 4.4.2. Process design criteria

-- *Small fraction of epi-SL film that consists of large ( $> 3 \mu\text{m} \times 3 \mu\text{m}$ ) single-grains.* This requires a deterministic approach where large epi-SL grains can be identified and incorporated into a device construct.

-- *Current epi-SL films are semi-continuous* — neither isolated flakes nor perfectly smooth thin films. Because they are semi-continuous it is non-trivial to isolate charge transport to a single grain.

-- *PbSe QDs are extremely air-sensitive.* Atomic layer deposition infilling and overcoating of the epi-SL using alumina provides good air-stability. This is a consideration because many of the microfabrication and measurement tools required to produce or measure FETs are outside the glovebox.

--PbSe QDs are temperature-sensitive. Heating of non-ALD-infilled QD films above  $\sim 60^\circ\text{C}$  causes some degree of structuro-chemical evolution. This is a consideration because photoresist and e-beam resist—both of which are required in device fabrication—require heating above  $100^\circ\text{C}$ .

--PbSe QDs are chemically reactive. Exposure of PbSe QDs to various solvents or reagents may lead to changes in surface chemistry and structural integrity. The QDs must therefore be protected from chemical exposure during FET fabrication.

#### 4.4.3. Device fabrication recipe

All devices were fabricated on 4-inch  $p^{++}$  [100]-oriented Si wafers with a 200 nm thick dry thermal oxide (Addison Engineering).

1. Wafers were cleaned using 15 minute rounds of sonication in acetone, water, and isopropanol, followed by blow drying with compressed dry air (CDA) and a 15 minute bake at  $110^\circ\text{C}$ .
2. Wafers were patterned using the photomask shown in Figure 4.16a, according to Section 4.4.4.
3. Wafers were descummed using a 5 minute  $\text{O}_2$  plasma clean.
4. 5 nm of Cr and 45 nm of Au were deposited according to Section 4.4.5.
5. Excess metal and photoresist were lifted off according to Section 4.4.4.

At this point, the wafers were diced. Individual chips were used in subsequent processing steps. After dicing, the chips were cleaned following step 1 above.

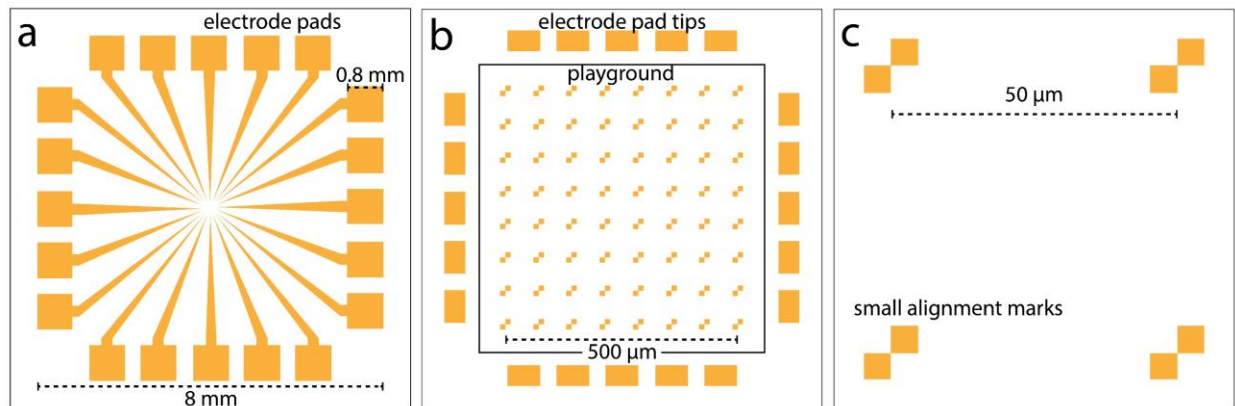


Figure 4.9. Epi-SL device chips following Step 5. All yellow areas consist of 5 nm Cr/45 nm Au. a) Full chip view, including 0.8 mm electrode pads. The full width of the metallized area is 8 mm and the chips are typically diced to be  $\sim 12$  mm on a side. b) Zoomed-in view of the chip-center. Only the tips of the electrode pads are shown. Epi-SL film was stamped into the playground area, which spans  $500\ \mu\text{m}$  and consists of a  $10 \times 10$  array of square alignment markers. c) Zoomed-in view of a single quadrant of small alignment markers. These markers were used for fine alignment in electron beam lithography.

Epi-SL film was deposited solely in the playground region of the substrate using a photolithographic patterning step. This was done to eliminate parasitic current pathways between electrodes on the pre-patterned substrates. Figure 4.9 shows the photoresist image prior to epi-SL deposition.

6. The chips were patterned using *Die C* according to Section 4.4.4. Care was taken to align the photomask such that none of the electrode tips were exposed.

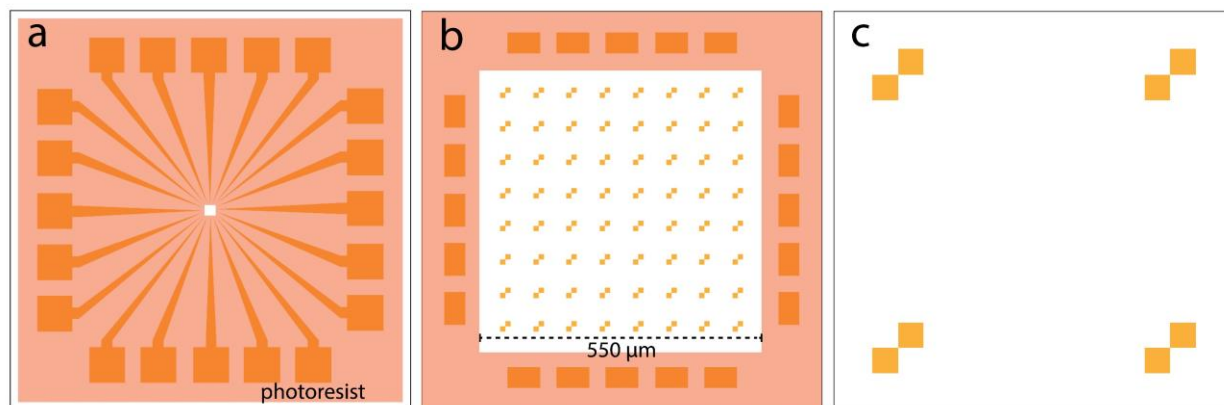


Figure 4.10. Epi-SL device chips following Step 6. Schematic of single-grain device after the second photolithography patterning and development. A 550  $\mu\text{m}$  square trench allows the epi-SL to be deposited in the “playground” area without creating electrical shorts between the finger electrodes.

7. Prior to deposition of the epi-SL, substrates were cleaned using a 5 minute  $\text{O}_2$  plasma cleaning (descum) at 50% power step followed by soaking in a 100 mM 3-MPTMS toluene solution for 1 hour to functionalize the substrate for improved epi-SL adhesion. Substrates were then rinsed with neat toluene and blown dry with  $\text{N}_2$ .

8. Epi-SL films were fabricated and stamped onto the patterned substrates. The substrates were rinsed in acetone, causing the photoresist underlayer and attached film to dissolve. Acetonitrile rinsing resulted in incomplete photoresist removal and partial epi-SL re-deposition.

9.  $\sim 10$  nm of alumina was grown *via* ALD according to Section 4.4.6.

10. The substrate was then imaged in the SEM (10 kV accelerating voltage and 100 pA of filament current) to generate a map of suitably large, pristine epi-SL grains. Care was taken to limit air-exposure during chip transfer to and from the SEM. 10-12 nm thick ALD films were found to provide good air-stability of epi-SLs for several hours. The specified regions of interest (ROIs) were indexed, and a complete map of the playground area was generated.

11. Following ROI identification and mapping, an additional 20 nm of alumina was deposited, resulting in a  $\sim 30$  nm thick alumina overcoat on the entire substrate.

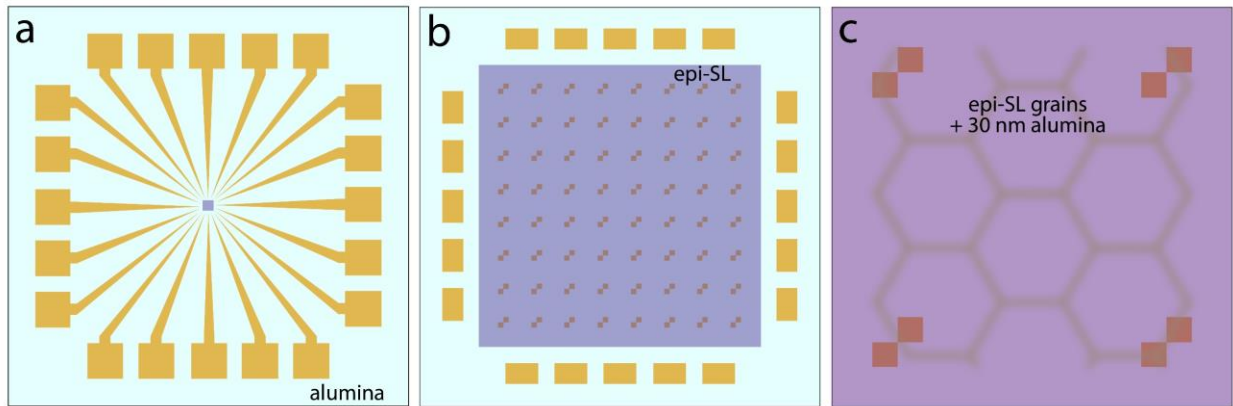


Figure 4.11. Epi-SL device chips following Step 11. The epi-SL film is selectively deposited in the playground area and 30 nm of alumina overcoats the entire substrate. a) Full view of the substrate showing that alumina covers every part of the substrate. b) Zoom in of the playground area. Epi-SL sits within the playground area and does not bridge any of the pre-patterned electrodes. Alumina covers both the substrate and epi-SL film. c) Zoomed view of a single quadrant of small alignment markers. Hexagonal markings represent epi-SL grains.

12. The chips were patterned using *Die B*. Care was taken to align the photomask such that the mask area covered the epi-SL film, but not the electrode tips.

13. Alumina on the exposed areas of the substrate was etched for 55 minutes according to Section 4.4.9.

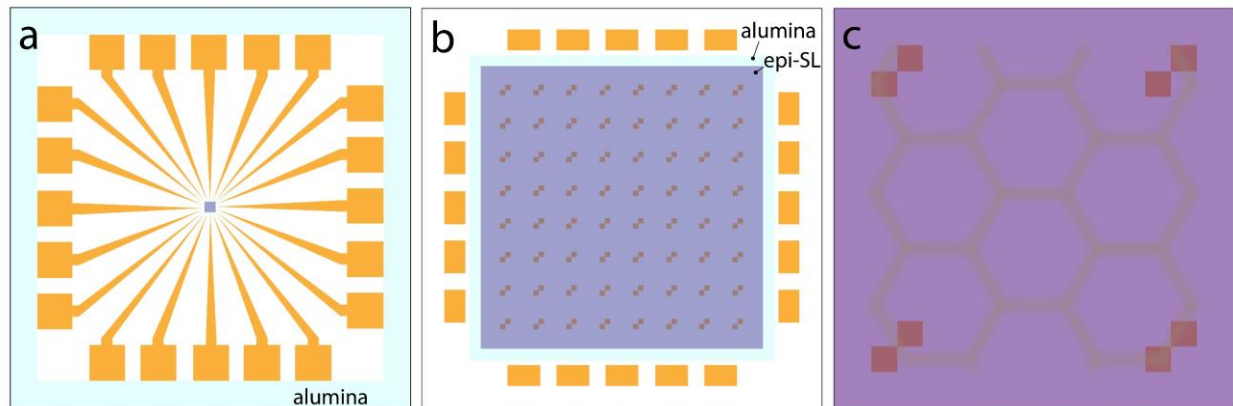


Figure 4.12. Epi-SL device chips following Step 13. Alumina was etched from the electrode pads, but remains on the epi-SL film. a) Full view of the substrate showing that alumina covers only the playground area and the area outside the electrode pads. b) Zoomed-in view of the playground area. Epi-SL sits within the playground area and does not bridge any of the pre-patterned electrodes. Alumina covers only the epi-SL film and has been removed from the electrode tips. c) Zoomed view of a single quadrant of small alignment markers.

Two rounds of electron beam lithography and metallization were used to generate electrical leads that connect the pre-patterned finger electrodes with individual epi-SL grains. The first step involved the deposition of coarse electrical leads that extend from the large finger electrodes to within several  $\mu\text{m}$  of the single-grain of interest. The second step involved connecting the tips of the coarse electrical leads to the edge of the epi-SL grain. These steps were separated because the latter requires that vias be etched in the alumina at the tips of the epi-SL grain.

14. Coarse electrodes that span from pre-patterned electrode tips to within several  $\mu\text{m}$  of the epi-SL grain were designed and patterned according to Section 4.4.7. The beam voltage and current were 30 kV and  $\sim 1.6$  nA, respectively. The total dose was specified at  $550 \mu\text{C}/\text{cm}^2$ .

15. 5 nm of Cr and 45 nm of Au were deposited.

16. Metal lift-off was then performed according to Section 4.4.7. Because alumina still caps the epi-SL film, this processing was carried out in air.

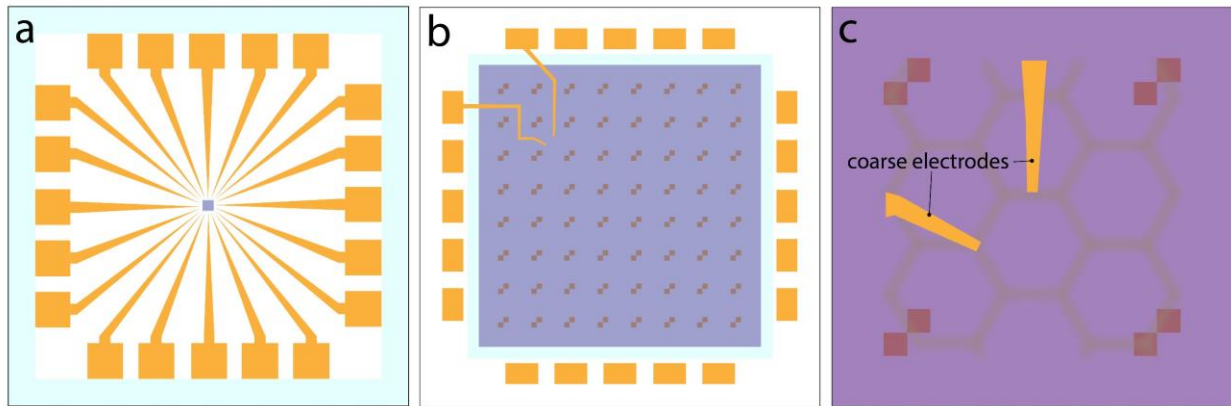


Figure 4.13. Epi-SL device chips following Step 16. Coarse electrodes are deposited on top of the  $\sim 30$  nm ALD alumina layer. a) Full view of the substrate showing that alumina covers only the playground area and the area outside the electrode pads. b) Zoomed-in of the playground area. Epi-SL sits within the playground area and does not bridge any of the pre-patterned electrodes. Alumina covers only the epi-SL film and has been removed from the electrode tips. Coarse electrodes span from the pre-patterned electrodes to near the epi-SL grain of interest. c) Zoomed-in view of a single quadrant of small alignment markers. Hexagonal markings represent epi-SL grains. Coarse electrodes approach within several  $\mu\text{m}$  of the epi-SL grain of interest.

The second electron beam process was used to bridge the electrical leads generated in Steps 14-16 through vias to the individual epi-SL grains.

17. Fine electrodes that span from the coarse electrode tips to the edge of the epi-SL grain were designed and patterned. A beam current of 50 pA and voltage of 30 kV were used. A dose of  $520 \mu\text{C}/\text{cm}^2$  was used.

18. The substrate was transferred into the glovebox and vias were etched for 55 minutes. For this step, de-oxygenated water (freeze-pump-thaw) was used.



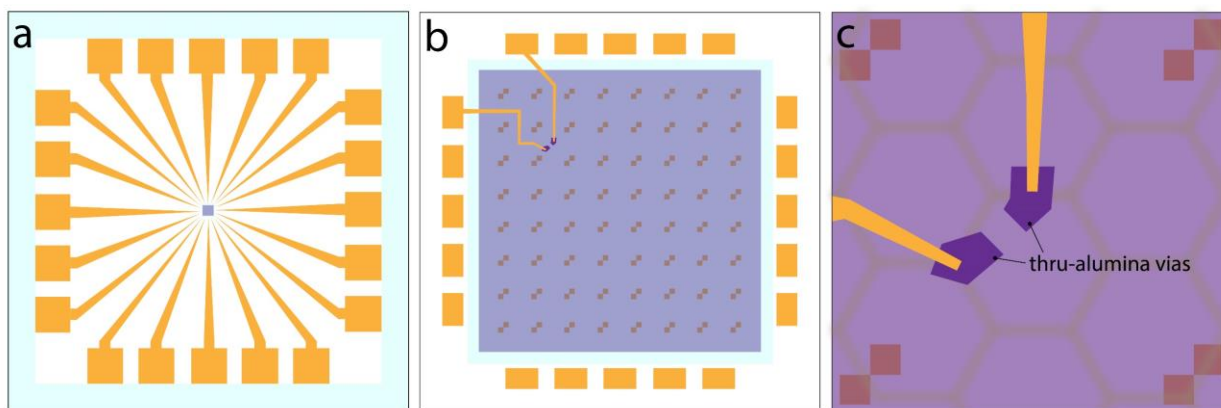


Figure 4.14. Epi-SL device chips following Step 18. Thru-alumina vias formed at the tips of the coarse electrodes define the shape of the fine electrodes. The epi-SL film is exposed at the base of the vias. a) Full view of the substrate. b) Zoomed-in view of the playground area. Epi-SL sits within the playground area and does not bridge any of the pre-patterned electrodes. Alumina covers only the epi-SL film and has been removed from the electrode tips. Coarse electrodes span from the pre-patterned electrodes to near the epi-SL grain of interest. The fine electrode vias are visible. c) Zoomed-in view of a single quadrant of small alignment markers. Hexagonal markings represent epi-SL grains. Coarse electrodes approach within several  $\mu\text{m}$  of the epi-SL grain of interest. Thru-alumina vias span from the coarse electrode tips to the edge of the epi-SL grain of interest.

19. 5 nm of Cr and 45 nm of Au were deposited.

20. Lift-off was carried out by soaking the substrate in acetone for 2 hours followed by agitation of the solution with a glass pipette. This process was performed in the glovebox.

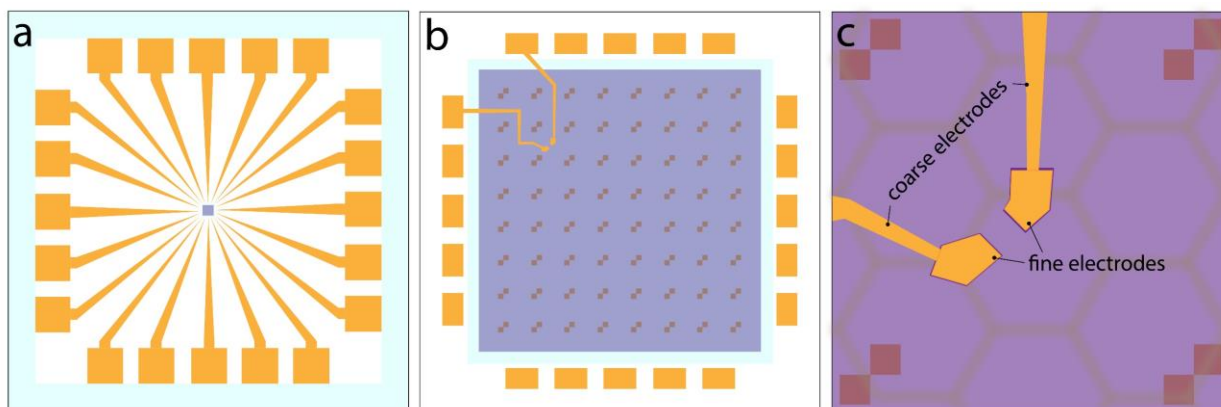


Figure 4.15. Completed epi-SL device chip. Fine electrodes were deposited in the thru-alumina vias, enabling intimate contact with the epi-SL surface. The active device area is defined by the region between the fine electrodes. a) Full view of the substrate. b) Zoomed-in view of the playground area. Epi-SL sits within the playground area and does not bridge any of the pre-patterned electrodes. Alumina covers only the epi-SL film and has been removed from the electrode tips. Coarse electrodes span from the pre-patterned electrodes to near the epi-SL grain of interest. The fine electrodes are visible. c) Zoomed-in view of a single

quadrant of small alignment markers. Hexagonal markings represent epi-SL grains. Coarse electrodes approach within several  $\mu\text{m}$  of the epi-SL grain of interest. Fine electrodes are formed at the tip of the coarse electrodes.

21. Finally, 10-20 nm of ALD was deposited to further stabilize the device.

#### 4.4.4. Photolithography

A photomask (Photosciences Inc.) was used for the three photolithography steps used during device fabrication. There are three unique die patterns (Die A-C) which correspond to these three steps. Figure 4.16a shows the full 5" x 5" photomask design which consists of a 4" diameter array of single-grain device die (Die A; Figure 4.16b) such that a full wafer of pre-patterned substrates can be fabricated at a time. Die A consists of 20 large contact pads that extend into the central "playground" area (Figure 4.16c). There are two sets of registration marks: one set at the edge of the playground area and another set within the playground area. These markers are used for aligning the electron beam lithography patterns. Die B and Die C (Figure 4.16d and Figure 4.16e, respectively) are used on a per-substrate basis (as opposed to wafer scale) for other parts of the fabrication process (*vide infra*).

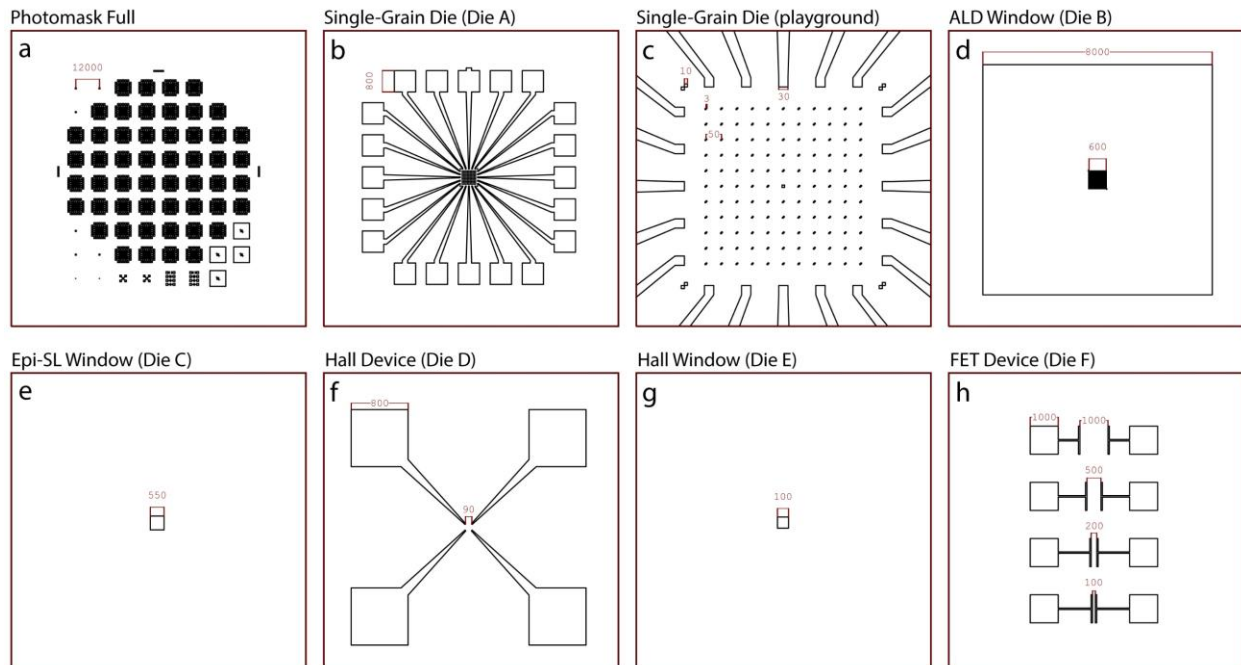


Figure 4.16. Overview of single-grain device photomask and associated die patterns. (Note: All dimensional annotations are in microns.) a) Full view of 5" photomask. The die pitch is 1.2 cm. b) Zoomed in view of single-grain device die. The chip size after dicing is 1.2 cm x 1.2 cm. The device consists of 20 contact pads arranged with a pitch of 1.2 mm and lateral dimensions of 0.8 x 0.8 mm. These contact pads have finger electrodes that extend towards the center of the chip and border the "playground" area shown in (c). c) The central "playground" region of the single-grain device die. The playground area contains 3 x 3  $\mu\text{m}$  registration marks with a 50  $\mu\text{m}$  pitch. d) A 0.6 mm x 0.6 mm dark square used to expose the finger electrodes and contact pads for ALD etching. e) A clear 0.55 mm x 0.55 mm square used to photopattern the single-grain substrate for epi-SL stamping onto the playground area. f) Hall effect device die consisting of four 800  $\mu\text{m}$  x 800  $\mu\text{m}$  contact pads with finger electrodes that end with a spacing of 90  $\mu\text{m}$ . g) A clear 0.55 mm x 0.55 mm square used to photopattern van der Pauw geometry Hall effect device substrates for epi-SL stamping onto the desired active area. h) Field-effect transistor (FET) die consisting of four FETs with electrode spacings of 100, 200, 500, and 1000  $\mu\text{m}$ . The patterns in (d-h) were used to prepare individual die, not wafer-scale patterns.

First, a photoresist primer layer was applied by spin-casting a 20% volume solution of HMDS (hexamethyldisilazane) in *para*-xylene for 140 seconds at 3500 rpm (Program H on Penner spin-coater). A layer of Shipley S1808 photoresist was spin-cast on the HMDS-treated substrate for 3500 rpm for 100 seconds. The photoresist layer was soft-baked at 90 °C for 30 minutes. A photomask was aligned over the substrate and exposed to a Ushio USH-508SA UV lamp for a duration of 2.6 seconds. The wafer or substrate was then soaked in photoresist developer (MF-319) for a duration of 60 seconds, followed by immersion in and gentle rinsing with water. Inspect by optical microscope. Continue development if necessary.

#### 4.4.5. Thermal evaporation of metals

Electrodes were deposited using the in-glovebox MBraun thermal evaporator system. All depositions were performed at a base pressure of < 5E-06 mbar. Deposition rates were monitored using a quartz crystal

microbalance. Gold was deposited at a rate of 0.7 Å/s from gold shot in a Mo boat. Cr was deposited at a rate of 0.1-0.2 Å/s using chromium-plated W rods. A shutter was placed over the chips during the ramp phase of Cr deposition. Once a steady deposition rate was achieved, the shutter was removed. All depositions were performed with the chips mounted to a rotation stage—this was necessary to generate continuous electrodes at various metal-metal interfaces. The rotation speed was set at 50% of the maximum value allowed by the evaporator.

#### *4.4.6. Atomic layer deposition of alumina*

Alumina was deposited in a constant-flow, cold-wall atomic layer deposition system. The platen temperature for all depositions was 60 °C unless otherwise stated. Trimethylaluminum and de-oxygenated water were used as precursors for alumina. The system base pressure was 80 mTorr. A constant flow of ~ 100 sccm of N<sub>2</sub> carrier gas was used throughout each run. Precursors were delivered in 20 ms pulses with purge times of 55 s.

#### *4.4.7. Electron beam lithography*

Electron beam lithography was performed using the NPGS package installed on the FEI Magellan SEM located in the Irvine Materials Research Institute. All write patterns were designed using DesignCAD Express 16 with the NPGS plug-in. Positive PMMA positive resist (MicroChem; 950 A5) was used for all electron beam lithography. Two primary electron beam lithography steps were required for single-grain device fabrication: one coarse electrode and one fine electrode step.

1. PMMA resist was spun onto the chip at 2750 RPM for 1 minute, followed by a brief 4000 RPM flick step. The resist was baked at 150 °C (set temp of hotplate, towards edge) for 3 minutes.
2. Development was performed in a 1:3 solution of MIBK in IPA. The substrate was submerged for 40 seconds with gentle swirling to carry developed resist away from the substrate. The resist image was inspected under an optical microscope to evaluate the completion/quality of the development.
3. Lift-off was performed by soaking the substrate in acetone for 2-3 hours. After this period of soaking, a glass pipette was used to vigorously douse the substrate with acetone. The quality and completion of lift-off was evaluated using an optical microscope. Sonication was not used because it caused epi-SL film delamination.
4. Proper exposure conditions were determined using a dose array. Fine electrodes were written at a magnification of 1200x and coarse electrodes were written at a magnification of 120x. The line and point spacings were set to their minimum achievable value, subject to keeping the dwell time above 0.2 μs.
5. Follow the process outlined above to deposit e-beam resist onto the substrate you wish to pattern.
6. Close the Magellan software. Stop the GUI (exit), then Stop the SEM server. It takes a couple of minutes to fully shut down. Once it is shut down, Start the SEM software.
7. Log in to the EBL computer (user: supervisor, password: supervisor). Restart the computer. Wait until the SEM software has fully come back on-line and you have logged in before you log back in to the

EBL computer after restart. When the EBL computer comes back up it will begin a DAC calibration of the NPGS hardware. There are two parts to this. Hit “Enter” after the first part. If the DAC calibration doesn’t automatically start (never happened to me) then it will when you open the NPGS software.

8. Place the substrate onto the SEM stub with two copper clips. Carefully place the copper clips onto the edges of the substrate. Ensure that you do not scratch off any of the e-beam resist, otherwise metal will deposit in those regions and may potentially short various electrodes. You must leave some corners of the substrate exposed and not covered by the copper clips. This is for doing the substrate tilt correction in the SEM.

9. On the exposed corners of the substrate make small scratches using a SiC scribe. These scratches are used for focusing the SEM beam on the surface. You need 3-4 scratches. The further apart they are on the substrate, the better.

10. Load the chip into the SEM. Align the substrate so that the notch on top of the central electrode pad is facing away from the transfer arm, directly into the SEM. This ensures that the substrate is aligned correctly in the SEM.

11. Take NavCam photo.

12. With the beam condition at 30 kV and the write current, focus on one of the corners of the substrate.

13. Link z-height. Bring the stage height to 7 mm.

14. Turn the beam off – move the stage such that you are sitting over the playground area. Set the mag around 200x.

15. Take a single scan of the playground area.

16. Use the XT Alignment feature to make the substrate sit perfectly horizontal.

17. Zoom in to around 1200x.

18. Take a single scan make fine adjustments of the stage rotation (may need to use compucentric rotation feature). If your beam current is 1.6 nA or higher you must be very careful to limit total beam exposure.

19. You may retake the NavCam photo if you made a significant rotation, otherwise it does not make a big difference.

20. Once the stage rotation is set, move the stage back to the corner.

21. Focus again (high mag). Do normal alignments. Link stage height. Move to 7 mm. Repeat this 3 times.

22. Unlink stage height.
23. In the NPGS software, click “Set WD to 7 mm”. The beam focus will click around, but hopefully return to a good focus condition.
24. In the NPGS software, select “Direct Stage Control” to begin the chip tilt correction program. Press “Enter” twice on the NPGS keyboard to begin collecting a new dataset. Press the space bar to acquire the first data point. Move to the other scratches you made on the substrate. Focus on each one, followed by pressing the space bar on the EBL computer. After 3 or 4 scratches have been focused on, exit the process by pressing “Enter” twice, then “Esc”.
25. In the NPGS software, select the Run File that you created. You can simulate the pattern to ensure that it will work.
26. Move the stage to the center of the pattern. You can take one scan and make fine adjustments of the stage position to ensure you are very close to the ideal pattern center.
27. On the NPGS software, click “NPGS mode”. The SEM computer should now say “External” in the upper-left quadrant.
28. Right-click the Run File on the NPGS software, then click “Process Run File”.
29. If there is an alignment step, the alignment part of the process will begin.
30. During pattern writing, double-check the picoammeter to make sure there is a current flowing. There can sometimes be an issue when you switch from NPGS mode to SEM mode (or *vice versa*) where the crossover of the beam shifts behind the aperture and the current will drop to 0.
31. After pattern writing, move the stage to off the writing area. Turn the beam off. Then switch back from NPGS mode to SEM mode.
32. Unload the chip.

*Tips for pattern design.*

- Start with a template pattern which has the features of the pre-patterned substrate. They are included below in Figure 4.17 (red and lime green).
- Load images into Layer 1. If the images are rotated you are best served rotating the image in an external program, then loading the rotated image into DCE16.
- Draw the coarse electrodes to approach the ROI (the single grain).

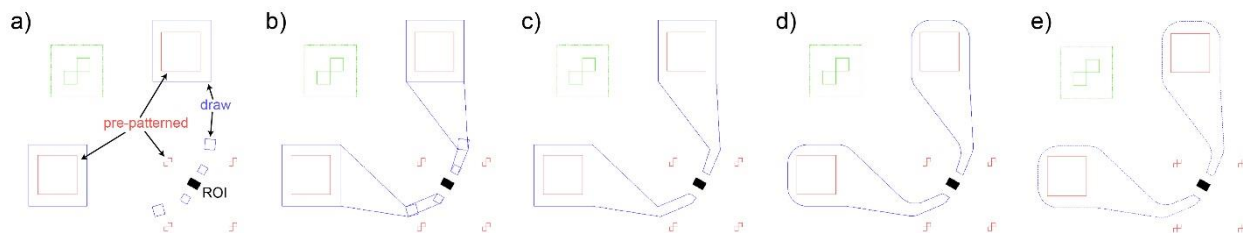


Figure 4.17. Steps for drawing coarse electrodes in Design CAD Express 16. a) Identify the region of interest (black rectangle). Draw a series of squares in Layer 2 that will bridge the tips of the pre-patterned electrodes to near the ROI. b) Connect the squares using the Line tool in DCE16. Form a closed polygon. c) Delete the squares. d) Filet the edges of the polygon such that you have rounded edges on the electrodes. e) Convert the line from a solid line to a dashed line. NPGS will not fill lines that are solid (vs. dashed).

Learn the keyboard shortcuts in DCE16. Here are some useful ones:

Key	Description
“	Brings up a window to query for dimensions of a rectangle that you are drawing. Select the rectangle option, click somewhere on the drawing, then hit “ to bring up a window the queries for rectangle dimensions.
<b>b</b>	Combine several lines into a single line. For example, after you filet the corner of a polygon, you need to recombine the lines back into a closed polygon.
,	Snaps the cursor to the nearest point on the drawing.
<b>f</b>	Brings up a window to filet the corner of a polygon. Set the filet radius, then select the two sides of the object you want to filet.
<b>v</b>	Draw line.
<b>m</b>	Move object.

#### 4.4.8. Electrical properties of ALD alumina

We evaluated the through-plane electrical resistivity of ALD alumina films. Since the epi-SL films are semi-continuous, the alumina layer deposited in Step 11 must make the coarse electrodes (Steps 14-17) electrically isolated from the QD film (and therefore, each other). Although idealized ALD generates conformal thin films (even in highly-anisotropic structures), the formation of islands and pinholes is well documented.<sup>230</sup> These pinholes may serve as shunts for current to flow between regions of the epi-SL film away from the desired single-grain region.

Alumina thin films with different thicknesses were deposited at 60 °C onto pre-patterned conductive ITO/glass substrates. Next, 5 nm of Cr and 45 nm of Au were thermally evaporated onto the substrate using a shadow mask such that the overlap of the ITO and Cr/Au metal layers was confined to a known area. The electrical resistance of the devices was measured by sweeping the voltage between  $\pm 20$  mV. The differential resistance ( $dI/dV$ ) was extracted, and the electrical resistivity was calculated using the known alumina thickness and device geometry. Figure 4.18 shows the electrical resistivity as a function of alumina thickness.

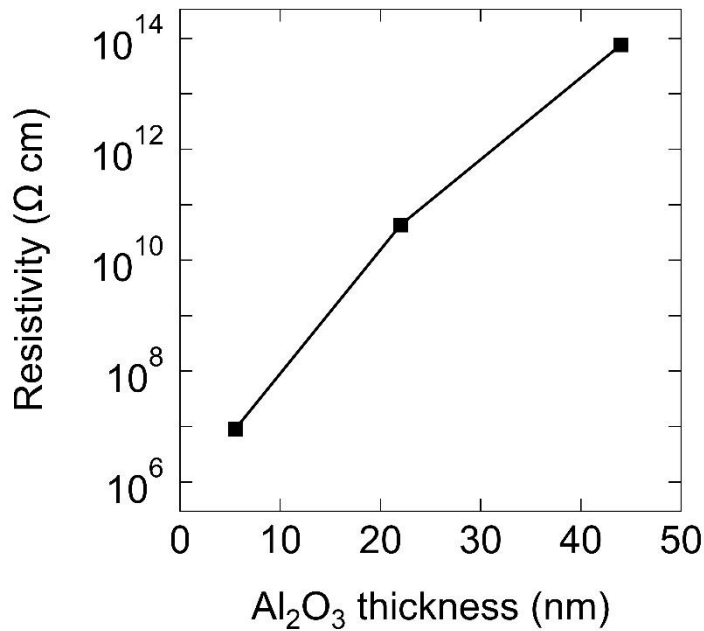


Figure 4.18. Electrical resistivity of ALD alumina thin films deposited at 60 °C as a function of film thickness.

Based on the geometry of the coarse electrodes used in the SG epi-SL devices, an ALD film thickness of 30 nm was deemed sufficiently thick to provide good electrical insulation. The thickness-dependent resistivity highlights the presence of shunts in thinner alumina films.

#### 4.4.9. Alumina wet etch

Two steps of the epi-SL device fabrication process require precise etching of ALD alumina. The quality of electrical contacts requires complete removal of alumina. Alumina deposited by atomic layer deposition was etched using a glycine-buffered (40.7 mM) sodium hydroxide (32.0 mM) with an approximate pH of 10. Glycine was selected as a buffer because it has a  $pK_a \sim 9.7$ . The alumina etch rate of this solution was probed using X-ray reflectivity, a diffractometry technique used for high-precision analysis of thin films. For these experiments, ~15 nm thick alumina films were grown on bare Si substrates. The substrates were then immersed in etchant solutions for different durations and the thicknesses of the films were measured by XRR. The XRR data were fit using a 3-layer model, including: 1) the Si substrate; 2) a thin (~1.5 nm) low-density interfacial layer; 3) the alumina film. The thickness of the alumina films was extracted and plotted as a function of etch time (Figure 4.19).



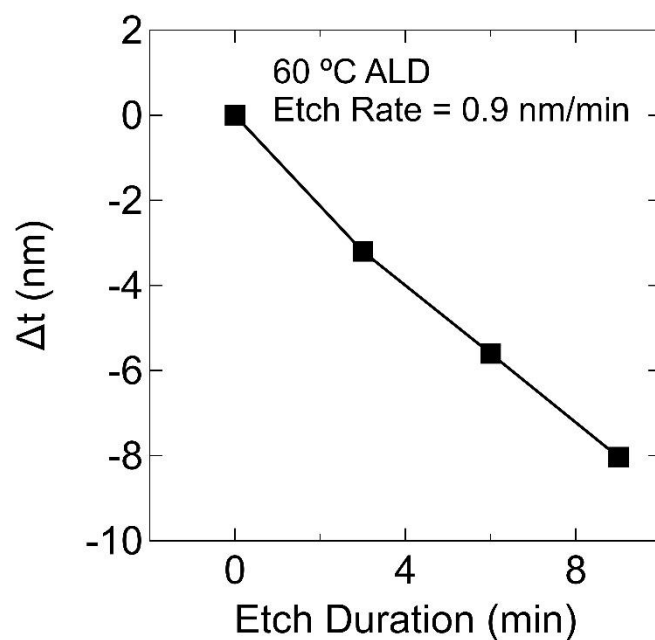


Figure 4.19. Etch rate of alumina using X-ray reflectivity. Alumina films grown at 60 °C were deposited on bare Si substrates and etched for different durations using an aqueous solution of glycine-buffered sodium hydroxide (pH = 10). Film thicknesses were extracted from XRR data, yielding an etch rate of 0.9 nm/min.

It was found that the deposition temperature of the alumina led to differences in alumina etch rate. For example, alumina deposited at 150 °C etched at a rate of ~0.4 nm/min. This decrease in etch rate is likely due to densification of the alumina film which occurs as the platen temperature increases.<sup>231</sup>

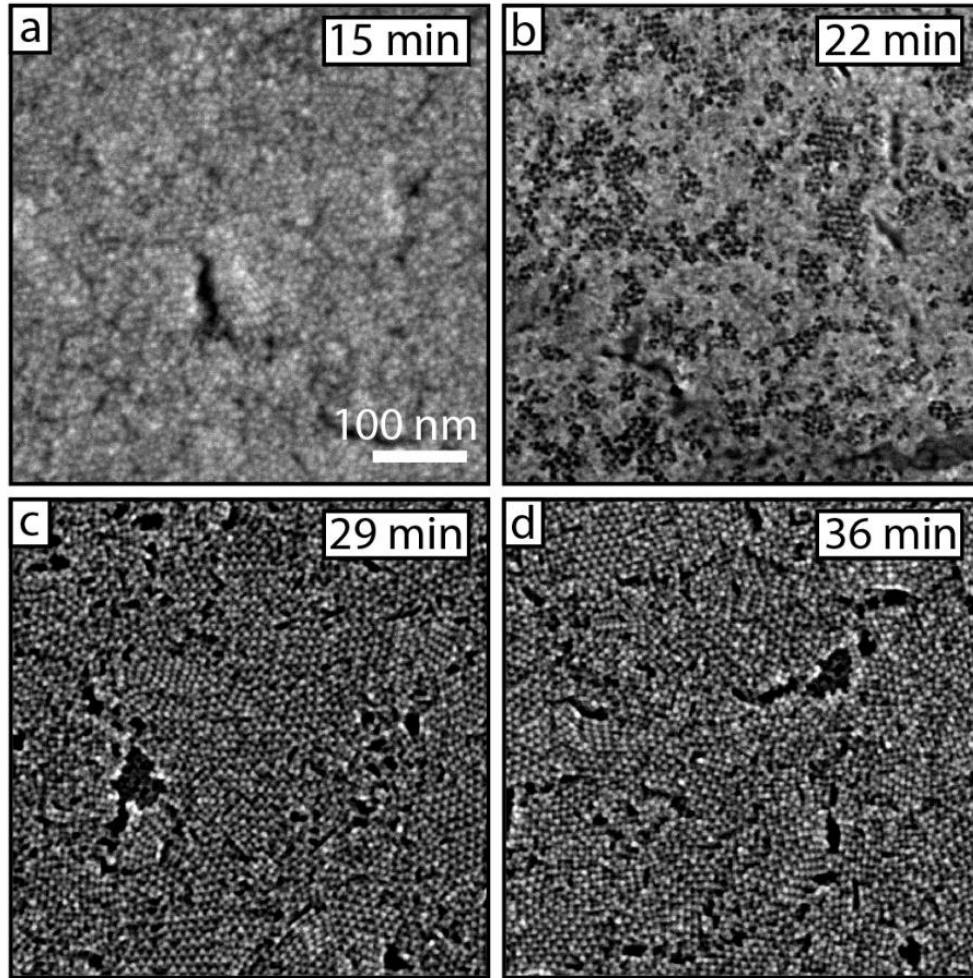


Figure 4.20. Evaluating the etch rate of ALD alumina deposited on a QD thin film. ~15 nm of ALD alumina was deposited onto spin-cast QD films, then etched according to the durations specified in the insets: a) 15 minute etch; b) 22 minute etch; c) 29 minute etch; d) 36 minute etch. A nearly continuous alumina film remains after 15 minutes. After 22 minutes, the alumina film is patchy and some parts of the QD film are exposed. After 29 minutes the alumina is completely etched. After an additional 17 minutes of etching (29 to 36 minutes) the QD film morphology does not change significantly, indicating that slight over-etching is not likely to be problematic for making electrical contacts to the QD film.

To further evaluate the alumina etch process, spin-cast QD films capped with a 15 nm alumina layer were etched for different durations. The extent, quality, and impact of the etch process were evaluated using SEM, as shown in Figure 4.20. To completely etch the 15 nm alumina film required 29 minutes, nearly twice what was expected based on the XRR results in Figure 4.19. This disparity is likely due to details of the ALD growth process on a QD film *versus* a pristine Si surface and/or limitations of XRR to generate meaningful data from a nanoporous film such as that shown in Figure 4.20b. For SG epi-SL device fabrication, an etch rate of ~0.6 nm/min was used to ensure complete alumina removal.

#### 4.4.10. Quantum dot synthesis and purification

Quantum dots were synthesized according to the process described in 2.7.1. Purification was performed using toluene/acetonitrile (tol/MeCN) as the solvent/anti-solvent, rather than hexane/ethanol. NMR experiments show that purification with the former mixture results in residual oleate/lead oleate in the QD mixture. We found empirically that QDs washed using tol/MeCN yield larger oleate-capped SL grains. These findings are in agreement with literature reports.<sup>212</sup> For the SG FETs presented here, two batches of QDs were used. Batch 1 had eight rounds of tol/MeCN purification, whereas Batch 2 had only two rounds. In a typical round, 3 mL of toluene were mixed with the QDs followed by addition of 24 mL of MeCN. The mixture was centrifuged for five minutes at 3000 rpm. Following purification the QDs were dried under dynamic vacuum.

#### 4.4.11. Bias-stress effect

We investigated the impact of the bias-stress effect on mobility values extracted from FET measurements. The bias-stress effect occurs in organic and QD-based FETs and is characterized by a steady decrease in drain-source current (and therefore, the apparent mobility) at fixed source-drain and gate biases.<sup>229</sup> The effect is attributed to gate bias-induced trapped charges or mobile ions at the semiconductor-dielectric interface that screen the gate-induced electric field. The bias-stress effect has been shown in some cases to diminish with decreasing temperature. We therefore evaluated the magnitude and temperature-dependence of the bias stress effect.

Figure 4.21 shows  $I_D$  transients of a FET at three different temperatures. The gate bias ( $V_G$ ) was initially held at 0 V, then after 30 seconds  $V_G$  was switched to + 50 V (for electron transport) or -50 V (for hole transport). To quantify the impact of these transients on the electron/hole mobilities, we measured the fraction of  $I_D$  loss according to the equation:

$$I_{loss} = 1 - \frac{I_{max} - I(t)}{I_{max} - I_{min}}$$

To correct the mobility values extracted from transfer curves, we calculated  $I_{loss}$  with a delay time equal to the amount of time it took to perform a single transfer curve measurement.

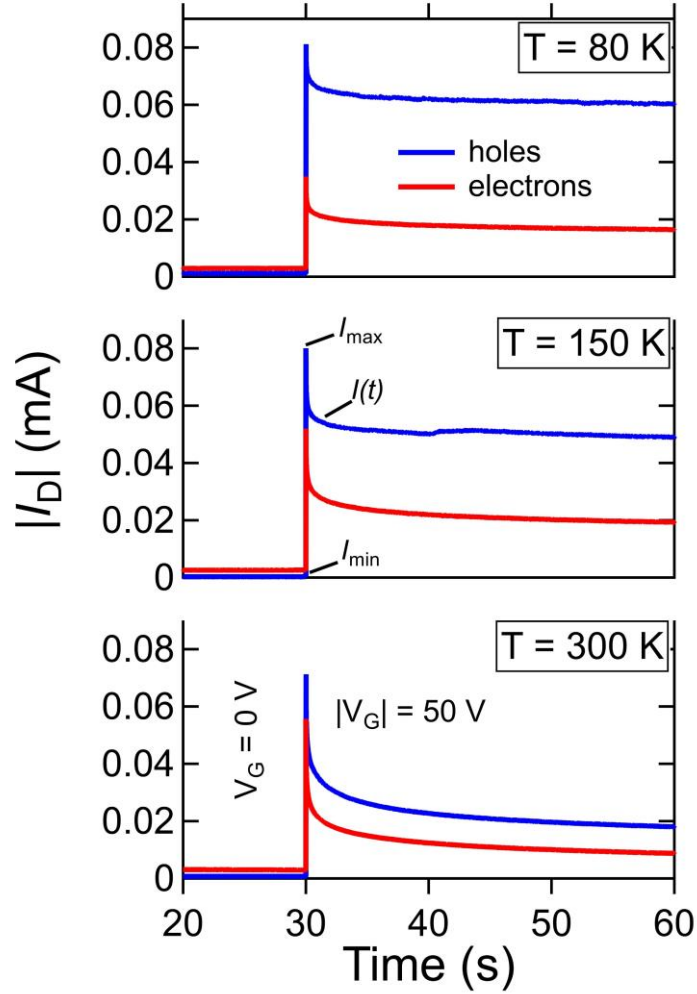


Figure 4.21. Impact of the bias-stress effect on charge mobility calculations. Transient curves acquired at three different temperatures (see annotation).  $I_{max}$  is the peak current achieved after switching of the gate bias.  $I(t)$  is the current after some decay time  $t$ .  $I_{min}$  is the average current value prior to application of the gate bias.

## CHAPTER 5

### CONCLUSION

#### *5.1. Summary*

We have investigated in detail the formation and chemical, optical, and electronic properties of epitaxially-fused PbSe quantum dot superlattices. We also showed that individual epi-SL grains can be successfully integrated into devices and reliability characterized using traditional microelectronics techniques.

We first elucidated how a batch of colloidal QDs is converted into a 3-D epi-SL. We first determined the composition, shape, and surface ligand coverage of the PbSe QDs used throughout this work. Next, the oleate-capped SL and epi-SL structures were established using a powerful combination of X-ray scattering, X-ray diffraction, and correlative electron microscopy/diffraction. By knowing the SL structures, we unraveled the full 3-D phase transformation. Tunability of the oleate-capped SL unit cell and grain size was demonstrated through careful control of oleate coverage. The phase transformation between the SL structures was shown to be the first known example of a collective topo-epitaxial transition. These structural insights will allow researchers to rationally improve the structural quality of epi-SLs.

The oleate-capped SL is converted into the epi-SL through a chemical mechanism revealed using a combination of chemical analysis techniques. We showed that ethylene glycol is made an active participant in the assembly process *via* deprotonation by a Brønsted base. Using this insight, we developed a novel photo-initiated epi-SL fabrication process using a photobase to deprotonate the

ethylene glycol, thereby initiating epi-SL formation. This novel photo-initiated synthesis process should enable epi-SLs of higher quality and uniformity.

Finally, single-grains of the epi-SL were integrated deterministically into field-effect transistors. The fabrication process developed here accommodates the sensitivity of PbSe QDs to a variety of environmental, chemical, and thermal factors. We measured numerous single-grain field-effect transistors, with some devices outperforming the previous record PbX QD hole mobilities 10-fold. Variable-temperature transistor studies showed that charge transport in our epi-SLs is weakly thermally activated, suggesting that hopping transport still dominates within individual epi-SL grains. The fabrication methodology and measurement results provide exciting opportunities for future researchers to understand epi-SL transport physics.

## **5.2. Outlook**

There are many exciting avenues for the development and characterization of epi-SLs.

Improvements in the epi-SL structure can be achieved in three ways. First, the process should be partially automated to eliminate vibrations and other mechanical disturbances. Along these lines, the cleanliness of the reagents and QD solutions should be maximized. Second, increasing the size of the oleate-capped SL is critically important, because their size and perfection limit the ultimate quality of the final epi-SL. Increasing oleate coverage has proven to be our best weapon for increasing oleate-capped SL grain size, but increased sophistication in the self-assembly process (*e.g.*, solvent annealing) should help as well. High-throughput experimentation would be helpful in assessing whether major gains in oleate-capped SL grain size can be found across a broader region of phase space: for example, trying different solvents, ligands, subphases, temperatures, and so on. Finally, the conversion of the oleate-capped SL to the epi-SL can be improved through

finer control over the chemical-triggering process. Replacing amines with other bases may allow for finer control of the epi-SL structure. More dramatic gains can be achieved using photo-triggering, which will improve uniformity and should allow for better control over assembly and fusion processes.

We also need to better understand how processing changes affect the structural and optical/electronic properties of epi-SLs. Unravelling the forms of structural/energetic disorder that prevent mini-band formation will require electrical and structural characterization of individual epi-SL grains. Developing a pipeline for rapid analysis of individual epi-SL grains using, for example, Hall effect, reflectance spectroscopy, and electron tomography, will greatly decrease the time until mini-band transport can be conclusively demonstrated. Finally, experimentalists must work with theorists to devise a concrete method of demonstrating mini-band transport.

## REFERENCES

1. Ekimov, A. Growth and optical properties of semiconductor nanocrystals in a glass matrix. *Journal of Luminescence* **70**, 1–20 (1996).
2. Ekimov, A. I. & Onushchenko, A. A. Quantum size effect in three-dimensional microscopic semiconductor crystals. *Journal of Experimental and Theoretical Physics Letters* **34**, 363–366 (1981).
3. Steigerwald, M. L. *et al.* Surface derivatization and isolation of semiconductor cluster molecules. *J. Am. Chem. Soc.* **110**, 3046–3050 (1988).
4. Murray, C. B., Norris, D. J. & Bawendi, M. G. Synthesis and characterization of nearly monodisperse CdE (E = sulfur, selenium, tellurium) semiconductor nanocrystallites. *J. Am. Chem. Soc.* **115**, 8706–8715 (1993).
5. Murray, C. B., Kagan, C. R. & Bawendi, M. G. Self-Organization of CdSe nanocrystallites into three-dimensional quantum dot superlattices. *Science* **270**, 1335–1338 (1995).
6. Kagan, C. R., Murray, C. B., Nirmal, M. & Bawendi, M. G. Electronic energy transfer in CdSe quantum dot solids. *Phys. Rev. Lett.* **76**, 1517–1520 (1996).
7. Yu, D., Wang, C. & Guyot-Sionnest, P. n-Type conducting CdSe nanocrystal solids. *Science* **300**, 1277–1280 (2003).
8. Luther, J. M. *et al.* Schottky solar cells based on colloidal nanocrystal films. *Nano Lett.* **8**, 3488–3492 (2008).
9. Liu, Y. *et al.* Robust, functional nanocrystal solids by infilling with atomic layer deposition. *Nano Lett.* **11**, 5349–5355 (2011).
10. Barmparis, G. D., Lodziana, Z., Lopez, N. & Remediakis, I. N. Nanoparticle shapes by using Wulff constructions and first-principles calculations. *Beilstein J. Nanotechnol.* **6**, 361–368 (2015).
11. Nair, P. S., Fritz, K. P. & Scholes, G. D. Evolutionary shape control during colloidal quantum-dot growth. *Small* **3**, 481–487 (2007).
12. Peng, X. *et al.* Shape control of CdSe nanocrystals. *Nature* **404**, 59–61 (2000).
13. Peters, J. L. *et al.* Ligand-induced shape transformation of PbSe nanocrystals. *Chem. Mater.* **29**, 4122–4128 (2017).
14. Baumgardner, W., Quan, Z., Fang, J. & Hanrath, T. Timing matters: the underappreciated role of temperature ramp rate for shape control and reproducibility of quantum dot synthesis. *Nanoscale* **4**, 3625–3628 (2012).
15. Reiss, P., Protière, M. & Li, L. Core/shell semiconductor nanocrystals. *Small* **5**, 154–168 (2009).
16. Hanifi, D. A. *et al.* Redefining near-unity luminescence in quantum dots with photothermal threshold quantum yield. *Science* **363**, 1199–1202 (2019).
17. Reimann, S. M. & Manninen, M. Electronic structure of quantum dots. *Rev. Mod. Phys.* **74**, 1283–1342 (2002).
18. Pietryga, J. M. *et al.* Spectroscopic and device aspects of nanocrystal quantum dots. *Chem. Rev.* **116**, 10513–10622 (2016).
19. McKittrick, J. & Shea-Rohwer, L. E. Review: Down conversion materials for solid-state lighting. *Journal of the American Ceramic Society* **97**, 1327–1352 (2014).
20. Bourzac, K. Quantum dots go on display. *Nature News* **493**, 283 (2013).
21. Kumar, P., Singh, S. & Kumar Gupta, B. Future prospects of luminescent nanomaterial based security inks: from synthesis to anti-counterfeiting applications. *Nanoscale* **8**, 14297–14340 (2016).
22. Fan, F. *et al.* Continuous-wave lasing in colloidal quantum dot solids enabled by facet-selective epitaxy. *Nature* **544**, 75–79 (2017).



23. Bergren, M. R. *et al.* High-performance CuInS<sub>2</sub> quantum dot laminated glass luminescent solar concentrators for windows. *ACS Energy Lett.* **3**, 520–525 (2018).
24. Michalet, X. *et al.* Quantum dots for live cells, in vivo imaging, and diagnostics. *Science* **307**, 538–544 (2005).
25. Aharonovich, I., Englund, D. & Toth, M. Solid-state single-photon emitters. *Nature Photonics* **10**, 631–641 (2016).
26. Dai, X. *et al.* Solution-processed, high-performance light-emitting diodes based on quantum dots. *Nature* **515**, 96–99 (2014).
27. Pu, Y., Cai, F., Wang, D., Wang, J.-X. & Chen, J.-F. Colloidal synthesis of semiconductor quantum dots toward large-scale production: A Review. *Ind. Eng. Chem. Res.* **57**, 1790–1802 (2018).
28. Wanger, D. D., Correa, R. E., Dauler, E. A. & Bawendi, M. G. The dominant role of exciton quenching in PbS quantum-dot-based photovoltaic devices. *Nano Lett.* **13**, 5907–5912 (2013).
29. Chen, O. *et al.* Compact high-quality CdSe–CdS core–shell nanocrystals with narrow emission linewidths and suppressed blinking. *Nature Materials* **12**, 445–451 (2013).
30. Galland, C. *et al.* Two types of luminescence blinking revealed by spectroelectrochemistry of single quantum dots. *Nature* **479**, 203–207 (2011).
31. Yuan, G., Gómez, D. E., Kirkwood, N., Boldt, K. & Mulvaney, P. Two mechanisms determine quantum dot blinking. *ACS Nano* **12**, 3397–3405 (2018).
32. Yazdani, N., Volk, S., Yarema, O., Yarema, M. & Wood, V. Size, ligand, and defect-dependent electron–phonon coupling in chalcogenide and perovskite nanocrystals and its impact on luminescence line widths. *ACS Photonics* (2020).
33. Law, M. *et al.* Determining the internal quantum efficiency of PbSe nanocrystal solar cells with the aid of an optical model. *Nano Lett.* **8**, 3904–3910 (2008).
34. Hens, Z. & Moreels, I. Light absorption by colloidal semiconductor quantum dots. *Journal of Materials Chemistry* **22**, 10406–10415 (2012).
35. Moreels, I. *et al.* Size-dependent optical properties of colloidal PbS quantum dots. *ACS Nano* **3**, 3023–3030 (2009).
36. Moreels, I. *et al.* Composition and size-dependent extinction coefficient of colloidal PbSe quantum dots. *Chem. Mater.* **19**, 6101–6106 (2007).
37. Dement, D. B., Puri, M. & Ferry, V. E. Determining the complex refractive index of neat CdSe/CdS quantum dot films. *J. Phys. Chem. C* **122**, 21557–21568 (2018).
38. Diroll, B. T., Gaulding, E. A., Kagan, C. R. & Murray, C. B. Spectrally-resolved dielectric functions of solution-cast quantum dot thin films. *Chem. Mater.* **27**, 6463–6469 (2015).
39. Grinolds, D. D. W., Brown, P. R., Harris, D. K., Bulovic, V. & Bawendi, M. G. Quantum-dot size and thin-film dielectric constant: precision measurement and disparity with simple models. *Nano Lett.* **15**, 21–26 (2015).
40. Walravens, W. *et al.* Chemically triggered formation of two-dimensional epitaxial quantum dot superlattices. *ACS Nano* **10**, 6861–6870 (2016).
41. An, J. M., Franceschetti, A., Dudiy, S. V. & Zunger, A. The peculiar electronic structure of PbSe quantum dots. *Nano Lett.* **6**, 2728–2735 (2006).
42. Wehrenberg, B. L., Wang, C. & Guyot-Sionnest, P. Interband and intraband optical studies of PbSe colloidal quantum dots. *J. Phys. Chem. B* **106**, 10634–10640 (2002).
43. Semonin, O. E. *et al.* Absolute photoluminescence quantum yields of ir-26 dye, PbS, and PbSe Quantum Dots. *J. Phys. Chem. Lett.* **1**, 2445–2450 (2010).
44. Pietryga, J. M. *et al.* Pushing the band gap envelope: mid-infrared emitting colloidal PbSe quantum dots. *J. Am. Chem. Soc.* **126**, 11752–11753 (2004).

45. Hughes, B. K. *et al.* Control of PbSe quantum dot surface chemistry and photophysics using an alkylselenide ligand. *ACS Nano* **6**, 5498–5506 (2012).
46. Joo, J. *et al.* A reduction pathway in the synthesis of PbSe nanocrystal quantum dots. *J. Am. Chem. Soc.* **131**, 10620–10628 (2009).
47. Koh, W. *et al.* Heavily doped n-type PbSe and PbS nanocrystals using ground-state charge transfer from cobaltocene. *Scientific Reports* **3**, 2004 (2013).
48. Araujo, J. J., Brozek, C. K., Kroupa, D. M. & Gamelin, D. R. Degenerately n-doped colloidal PbSe quantum dots: band assignments and electrostatic effects. *Nano Lett.* **18**, 3893–3900 (2018).
49. Beard, M. C. & Ellingson, R. J. Multiple exciton generation in semiconductor nanocrystals: Toward efficient solar energy conversion. *Laser & Photonics Reviews* **2**, 377–399 (2008).
50. Hanna, M. C. & Nozik, A. J. Solar conversion efficiency of photovoltaic and photoelectrolysis cells with carrier multiplication absorbers. *Journal of Applied Physics* **100**, 074510 (2006).
51. ten Cate, S. *et al.* Activating carrier multiplication in PbSe quantum dot solids by infilling with atomic layer deposition. *J. Phys. Chem. Lett.* **4**, 1766–1770 (2013).
52. Spoor, F. C. M., Tomić, S., Houtepen, A. J. & Siebbeles, L. D. A. Broadband cooling spectra of hot electrons and holes in PbSe quantum dots. *ACS Nano* **11**, 6286–6294 (2017).
53. Schaller, R. D., Sykora, M., Pietryga, J. M. & Klimov, V. I. Seven excitons at a cost of one: redefining the limits for conversion efficiency of photons into charge carriers. *Nano Lett.* **6**, 424–429 (2006).
54. Semonin, O. E. *et al.* Peak external photocurrent quantum efficiency exceeding 100% via MEG in a quantum dot solar cell. *Science* **334**, 1530–1533 (2011).
55. LaMer, V. K. & Dinegar, R. H. Theory, production and mechanism of formation of monodispersed hydrosols. *J. Am. Chem. Soc.* **72**, 4847–4854 (1950).
56. Wang, F., Richards, V. N., Shields, S. P. & Buhro, W. E. Kinetics and mechanisms of aggregative nanocrystal growth. *Chem. Mater.* **26**, 5–21 (2014).
57. Johnson, C. A. Generalization of the Gibbs-Thomson equation. *Surface Science* **3**, 429–444 (1965).
58. Park, J., Joo, J., Kwon, S. G., Jang, Y. & Hyeon, T. Synthesis of monodisperse spherical nanocrystals. *Angewandte Chemie International Edition* **46**, 4630–4660 (2007).
59. De Nolf, K. *et al.* Controlling the size of hot injection made nanocrystals by manipulating the diffusion coefficient of the solute. *J. Am. Chem. Soc.* **137**, 2495–2505 (2015).
60. Murray, C. B. *et al.* Colloidal synthesis of nanocrystals and nanocrystal superlattices. *IBM Journal of Research and Development* **45**, 47–56 (2001).
61. Houtepen, A. J., Koole, R., Vanmaekelbergh, D., Meeldijk, J. & Hickey, S. G. The hidden role of acetate in the PbSe nanocrystal synthesis. *J. Am. Chem. Soc.* **128**, 6792–6793 (2006).
62. Evans, C. M., Evans, M. E. & Krauss, T. D. Mysteries of TOPSe revealed: insights into quantum dot nucleation. *J. Am. Chem. Soc.* **132**, 10973–10975 (2010).
63. Frenette, L. C. & Krauss, T. D. Uncovering active precursors in colloidal quantum dot synthesis. *Nature Communications* **8**, 1–8 (2017).
64. Zhang, J., Gao, J., Miller, E. M., Luther, J. M. & Beard, M. C. Diffusion-controlled synthesis of PbS and PbSe quantum dots with in-situ halide passivation for quantum dot solar cells. *ACS Nano* **8**, 614–622 (2014).
65. Yarema, M. *et al.* Upscaling colloidal nanocrystal hot-injection syntheses via reactor underpressure. *Chem. Mater.* **29**, 796–803 (2017).
66. Williamson, C. B., Nevers, D. R., Hanrath, T. & Robinson, R. D. Prodigious effects of concentration intensification on nanoparticle synthesis: a high-quality, scalable approach. *J. Am. Chem. Soc.* **137**, 15843–15851 (2015).

67. Hendricks, M. P., Campos, M. P., Cleveland, G. T., Plante, I. J.-L. & Owen, J. S. A tunable library of substituted thiourea precursors to metal sulfide nanocrystals. *Science* **348**, 1226–1230 (2015).
68. Campos, M. P. *et al.* A library of selenourea precursors to PbSe nanocrystals with size distributions near the homogeneous limit. *J. Am. Chem. Soc.* **139**, 2296–2305 (2017).
69. van Embden, J., Chesman, A. S. R. & Jasieniak, J. J. The heat-up synthesis of colloidal nanocrystals. *Chem. Mater.* **27**, 2246–2285 (2015).
70. Casavola, M. *et al.* Anisotropic cation exchange in PbSe/CdSe core/shell nanocrystals of different geometry. *Chem. Mater.* **24**, 294–302 (2012).
71. Kim, S. *et al.* Air-stable and efficient PbSe quantum-dot solar cells based upon ZnSe to PbSe cation-exchanged quantum dots. *ACS Nano* **9**, 8157–8164 (2015).
72. Zhang, J. *et al.* Preparation of Cd/Pb chalcogenide heterostructured janus particles via controllable cation exchange. *ACS Nano* **9**, 7151–7163 (2015).
73. Boles, M. A., Engel, M. & Talapin, D. V. Self-assembly of colloidal nanocrystals: from intricate structures to functional materials. *Chem. Rev.* **116**, 11220–11289 (2016).
74. Frenkel, D. Entropy-driven phase transitions. *Physica A: Statistical Mechanics and its Applications* **263**, 26–38 (1999).
75. Bealing, C. R., Baumgardner, W. J., Choi, J. J., Hanrath, T. & Hennig, R. G. Predicting nanocrystal shape through consideration of surface-ligand interactions. *ACS Nano* **6**, 2118–2127 (2012).
76. Damasceno, P. F., Engel, M. & Glotzer, S. C. Predictive self-assembly of polyhedra into complex structures. *Science* **337**, 453–457 (2012).
77. Anders, G. van, Klotsa, D., Ahmed, N. K., Engel, M. & Glotzer, S. C. Understanding shape entropy through local dense packing. *PNAS* **111**, E4812–E4821 (2014).
78. Zhang, Y., Lu, F., van der Lelie, D. & Gang, O. Continuous phase transformation in nanocube assemblies. *Phys. Rev. Lett.* **107**, 135701 (2011).
79. Zihlerl, P. & Kamien, R. D. Maximizing entropy by minimizing area: towards a new principle of self-organization. *J. Phys. Chem. B* **105**, 10147–10158 (2001).
80. Goodfellow, B. W., Yu, Y., Bosoy, C. A., Smilgies, D.-M. & Korgel, B. A. The role of ligand packing frustration in body-centered cubic (bcc) superlattices of colloidal nanocrystals. *J. Phys. Chem. Lett.* **6**, 2406–2412 (2015).
81. Fan, Z. & Grünwald, M. Orientational order in self-assembled nanocrystal superlattices. *J. Am. Chem. Soc.* **141**, 1980–1988 (2019).
82. Dong, A., Jiao, Y. & Milliron, D. J. Electronically coupled nanocrystal superlattice films by *in-situ* ligand exchange at the liquid–air interface. *ACS Nano* **7**, 10978–10984 (2013).
83. Li, D. *et al.* Direction-specific interactions control crystal growth by oriented attachment. *Science* **336**, 1014–1018 (2012).
84. Xia, Y. *et al.* Facet control for trap-state suppression in colloidal quantum dot solids. *Advanced Functional Materials* **30**, 2000594 (2020).
85. Morris-Cohen, A. J., Malicki, M., Peterson, M. D., Slavin, J. W. J. & Weiss, E. A. Chemical, structural, and quantitative analysis of the ligand shells of colloidal quantum dots. *Chem. Mater.* **25**, 1155–1165 (2013).
86. Zherebetskyy, D. *et al.* Hydroxylation of the surface of PbS nanocrystals passivated with oleic acid. *Science* **344**, 1380–1384 (2014).
87. Moreels, I., Fritzing, B., Martins, J. C. & Hens, Z. Surface chemistry of colloidal PbSe nanocrystals. *J. Am. Chem. Soc.* **130**, 15081–15086 (2008).
88. Peters, J. L., van der Bok, J. C., Hofmann, J. P. & Vanmaekelbergh, D. Hybrid oleate–iodide ligand shell for air-stable PbSe nanocrystals and superstructures. *Chem. Mater.* **31**, 5808–5815 (2019).

89. Sykora, M. *et al.* Effect of air exposure on surface properties, electronic structure, and carrier relaxation in PbSe nanocrystals. *ACS Nano* **4**, 2021–2034 (2010).
90. Zhang, J. *et al.* PbSe quantum dot solar cells with more than 6% efficiency fabricated in ambient atmosphere. *Nano Lett.* **14**, 6010–6015 (2014).
91. Woo, J. Y. *et al.* Ultrastable PbSe nanocrystal quantum dots via in situ formation of atomically thin halide adlayers on PbSe(100). *J. Am. Chem. Soc.* **136**, 8883–8886 (2014).
92. Bae, W. K. *et al.* Highly effective surface passivation of PbSe quantum dots through reaction with molecular chlorine. *J. Am. Chem. Soc.* **134**, 20160–20168 (2012).
93. Shen, Y., Y. Gee, M. & B. Greytak, A. Purification technologies for colloidal nanocrystals. *Chemical Communications* **53**, 827–841 (2017).
94. Hassinen, A. *et al.* Short-chain alcohols strip X-type ligands and quench the luminescence of PbSe and CdSe quantum dots, Acetonitrile Does Not. *J. Am. Chem. Soc.* **134**, 20705–20712 (2012).
95. Kagan, C. R. & Murray, C. B. Charge transport in strongly coupled quantum dot solids. *Nat Nano* **10**, 1013–1026 (2015).
96. Kroupa, D. M. *et al.* Tuning colloidal quantum dot band edge positions through solution-phase surface chemistry modification. *Nature Communications* **8**, 1–8 (2017).
97. Lin, Q. *et al.* Phase-transfer ligand exchange of lead chalcogenide quantum dots for direct deposition of thick, highly conductive films. *J. Am. Chem. Soc.* **139**, 6644–6653 (2017).
98. Zhang, Y. *et al.* Lead selenide colloidal quantum dot solar cells achieving high open-circuit voltage with one-step deposition strategy. *J. Phys. Chem. Lett.* **9**, 3598–3603 (2018).
99. Liu, M. *et al.* Hybrid organic–inorganic inks flatten the energy landscape in colloidal quantum dot solids. *Nature Materials* **16**, 258–263 (2017).
100. Balazs, D. M., Dunbar, T. A., Smilgies, D.-M. & Hanrath, T. The coupled dynamics of colloidal nanoparticle spreading and self-assembly at a fluid–fluid interface. *Langmuir* (2020).
101. Voznyy, O. *et al.* A charge-orbital balance picture of doping in colloidal quantum dot solids. *ACS Nano* **6**, 8448–8455 (2012).
102. Oh, S. J. *et al.* Stoichiometric control of lead chalcogenide nanocrystal solids to enhance their electronic and optoelectronic device performance. *ACS Nano* **7**, 2413–2421 (2013).
103. Luther, J. M. & Pietryga, J. M. Stoichiometry Control in Quantum Dots: A Viable Analog to Impurity Doping of Bulk Materials. *ACS Nano* **7**, 1845–1849 (2013).
104. Allgaier, R. S. & Scanlon, W. W. Mobility of electrons and holes in PbS, PbSe, and PbTe between room temperature and 4.2 K. *Phys. Rev.* **111**, 1029–1037 (1958).
105. Crisp, R. W. *et al.* Metal halide solid-state surface treatment for high efficiency PbS and PbSe qd solar cells. *Scientific Reports* **5**, 9945 (2015).
106. Law, M. *et al.* Structural, optical, and electrical properties of PbSe nanocrystal solids treated thermally or with simple amines. *J. Am. Chem. Soc.* **130**, 5974–5985 (2008).
107. Talapin, D. V. & Murray, C. B. PbSe Nanocrystal Solids for n- and p-Channel Thin Film Field-Effect Transistors. *Science* **310**, 86–89 (2005).
108. Brown, P. R. *et al.* Energy Level Modification in Lead Sulfide Quantum Dot Thin Films through Ligand Exchange. *ACS Nano* **8**, 5863–5872 (2014).
109. George, S. M. Atomic Layer Deposition: An Overview. *Chem. Rev.* **110**, 111–131 (2010).
110. Choi, J. J. *et al.* PbSe nanocrystal excitonic solar cells. *Nano Lett.* **9**, 3749–3755 (2009).
111. Oh, S. J. *et al.* Designing high-performance PbS and PbSe nanocrystal electronic devices through stepwise, post-synthesis, colloidal atomic layer deposition. *Nano Lett.* **14**, 1559–1566 (2014).

112. Ithurria, S. & Talapin, D. V. Colloidal atomic layer deposition (c-ALD) using self-limiting reactions at nanocrystal surface coupled to phase transfer between polar and nonpolar media. *J. Am. Chem. Soc.* **134**, 18585–18590 (2012).
113. Ihly, R., Tolentino, J., Liu, Y., Gibbs, M. & Law, M. The photothermal stability of PbS quantum dot solids. *ACS Nano* **5**, 8175–8186 (2011).
114. Liu, Y. *et al.* PbSe quantum dot field-effect transistors with air-stable electron mobilities above  $7 \text{ cm}^2\text{V}^{-1}\text{s}^{-1}$ . *Nano Lett.* **13**, 1578–1587 (2013).
115. Yun, H. J. *et al.* Charge-transport mechanisms in  $\text{CuInSe}_x\text{S}_{2-x}$  quantum-dot films. *ACS Nano* **12**, 12587–12596 (2018).
116. Ramiro, I. *et al.* Mid- and long-wave infrared optoelectronics via intraband transitions in PbS colloidal quantum dots. *Nano Lett.* **20**, 1003–1008 (2020).
117. Zhao, Q. *et al.* The effect of dielectric environment on doping efficiency in colloidal PbSe nanostructures. *ACS Nano* **12**, 1313–1320 (2018).
118. Liu, Y. *et al.* Dependence of carrier mobility on nanocrystal size and ligand length in PbSe nanocrystal solids. *Nano Lett.* **10**, 1960–1969 (2010).
119. Lan, X. *et al.* Quantum dot solids showing state-resolved band-like transport. *Nature Materials* **19**, 323–329 (2020).
120. Lee, J.-S., Kovalenko, M. V., Huang, J., Chung, D. S. & Talapin, D. V. Band-like transport, high electron mobility and high photoconductivity in all-inorganic nanocrystal arrays. *Nat Nano* **6**, 348–352 (2011).
121. Jiang, C.-W. & Green, M. A. Silicon quantum dot superlattices: Modeling of energy bands, densities of states, and mobilities for silicon tandem solar cell applications. *Journal of Applied Physics* **99**, 114902 (2006).
122. Lazarenkova, O. L. & Balandin, A. A. Miniband formation in a quantum dot crystal. *Journal of Applied Physics* **89**, 5509–5515 (2001).
123. Kalesaki, E., Evers, W. H., Allan, G., Vanmaekelbergh, D. & Delerue, C. Electronic structure of atomically coherent square semiconductor superlattices with dimensionality below two. *Phys. Rev. B* **88**, 115431 (2013).
124. Shklovskii, B. I. & Efros, A. L. *Electronic Properties of Doped Semiconductors*. (Springer Science & Business Media, 2013).
125. Guyot-Sionnest, P. Electrical transport in colloidal quantum dot films. *J. Phys. Chem. Lett.* **3**, 1169–1175 (2012).
126. Yu, D., Wang, C., Wehrenberg, B. L. & Guyot-Sionnest, P. Variable range hopping conduction in semiconductor nanocrystal solids. *Phys. Rev. Lett.* **92**, 216802 (2004).
127. Chu, I.-H., Radulaski, M., Vukmirovic, N., Cheng, H.-P. & Wang, L.-W. Charge transport in a quantum dot supercrystal. *J. Phys. Chem. C* **115**, 21409–21415 (2011).
128. Prodanović, N., Vukmirović, N., Ikonić, Z., Harrison, P. & Indjin, D. Importance of Polaronic Effects for Charge Transport in CdSe Quantum Dot Solids. *J. Phys. Chem. Lett.* **5**, 1335–1340 (2014).
129. Tolentino, J. Designing quantum dot solids for optoelectronic devices through matrix engineering. (UC Irvine Doctoral Dissertation, 2015).
130. Scheele, M. *et al.* PbS Nanoparticles capped with Tetrathiafulvalenetetracarboxylate: Utilizing energy level alignment for efficient carrier transport. *ACS Nano* **8**, 2532–2540 (2014).
131. Scheele, M., Brütting, W. & Schreiber, F. Coupled organic–inorganic nanostructures (COIN). *Physical Chemistry Chemical Physics* **17**, 97–111 (2015).
132. André, A. *et al.* Toward conductive mesocrystalline assemblies: PbS nanocrystals cross-linked with tetrathiafulvalene dicarboxylate. *Chem. Mater.* **27**, 8105–8115 (2015).
133. Balazs, D. M. *et al.* Electron mobility of  $24 \text{ cm}^2\text{V}^{-1}\text{s}^{-1}$  in PbSe colloidal-quantum-dot superlattices. *Adv. Mater.* **30**, 1802265 (2018).

134. Scheele, M. To be or not to be: band-like transport in quantum dot solids. *Zeitschrift für Physikalische Chemie* **229**, 167–178 (2014).
135. Chen, T. *et al.* Metal-insulator transition in films of doped semiconductor nanocrystals. *Nat Mater* **15**, 299–303 (2016).
136. Talgorn, E. *et al.* Unity quantum yield of photogenerated charges and band-like transport in quantum-dot solids. *Nat Nanotechnol* **6**, 733–739 (2011).
137. Choi, J.-H. *et al.* Bandlike transport in strongly coupled and doped quantum dot solids: a route to high-performance thin-film electronics. *Nano Lett.* **12**, 2631–2638 (2012).
138. Liu, Y., Peard, N. & Grossman, J. C. Bandlike transport in PbS quantum dot superlattices with quantum confinement. *J. Phys. Chem. Lett.* **10**, 3756–3762 (2019).
139. Gilmore, R. H. *et al.* Inverse temperature dependence of charge carrier hopping in quantum dot solids. *ACS Nano* **12**, 7741–7749 (2018).
140. Deveaud, B., Shah, J., Damen, T. C., Lambert, B. & Regreny, A. Bloch transport of electrons and holes in superlattice minibands: Direct measurement by subpicosecond luminescence spectroscopy. *Phys. Rev. Lett.* **58**, 2582–2585 (1987).
141. Leo, K., Bolivar, P. H., Brüggemann, F., Schwedler, R. & Köhler, K. Observation of Bloch oscillations in a semiconductor superlattice. *Solid State Communications* **84**, 943–946 (1992).
142. Waschke, C. *et al.* Coherent submillimeter-wave emission from Bloch oscillations in a semiconductor superlattice. *Phys. Rev. Lett.* **70**, 3319–3322 (1993).
143. Greenberg, B. L. *et al.* ZnO Nanocrystal networks near the insulator–metal transition: tuning contact radius and electron density with intense pulsed light. *Nano Lett.* **17**, 4634–4642 (2017).
144. Kittel, C. *Introduction to Solid State Physics*. (Wiley, 2004).
145. Nika, D. L., Pokatilov, E. P., Shao, Q. & Balandin, A. A. Charge-carrier states and light absorption in ordered quantum dot superlattices. *Phys. Rev. B* **76**, 125417 (2007).
146. Whitham, K. *et al.* Charge transport and localization in atomically coherent quantum dot solids. *Nat Mater* **15**, 557–563 (2016).
147. Gómez-Campos, F. M., Rodríguez-Bolívar, S. & Califano, M. High-mobility toolkit for quantum dot films. *ACS Photonics* **3**, 2059–2067 (2016).
148. Remacle, F. & Levine, R. D. Quantum dots as chemical building blocks: elementary theoretical considerations. *ChemPhysChem* **2**, 20–36 (2001).
149. Esaki, L. & Tsu, R. Superlattice and negative differential conductivity in semiconductors. *IBM Journal of Research and Development* **14**, 61–65 (1970).
150. Lei, X. L., Horing, N. J. M. & Cui, H. L. Theory of negative differential conductivity in a superlattice miniband. *Phys. Rev. Lett.* **66**, 3277–3280 (1991).
151. Chen, F., Stokes, K. L., Zhou, W., Fang, J. & Murray, C. B. Synthesis and properties of lead selenide nanocrystal solids. *MRS Online Proceedings Library Archive* **691**, (2001).
152. Evers, W. H. *et al.* Low-dimensional semiconductor superlattices formed by geometric control over nanocrystal attachment. *Nano Lett.* **13**, 2317–2323 (2013).
153. Penn, R. L. & Banfield, J. F. Morphology development and crystal growth in nanocrystalline aggregates under hydrothermal conditions: insights from titania. *Geochimica et Cosmochimica Acta* **63**, 1549–1557 (1999).
154. Chen, J. D., Wang, Y. J., Wei, K., Zhang, S. H. & Shi, X. T. Self-organization of hydroxyapatite nanorods through oriented attachment. *Biomaterials* **28**, 2275–2280 (2007).
155. Penn, R. L. & Banfield, J. F. Imperfect oriented attachment: dislocation generation in defect-free nanocrystals. *Science* **281**, 969–971 (1998).

156. Liu, L. *et al.* Connecting energetics to dynamics in particle growth by oriented attachment using real-time observations. *Nat Commun* **11**, 1045 (2020).
157. Cho, K. S., Talapin, D. V., Gaschler, W. & Murray, C. B. Designing PbSe nanowires and nanorings through oriented attachment of nanoparticles. *J. Am. Chem. Soc.* **127**, 7140–7147 (2005).
158. Savitzky, B. H. *et al.* Propagation of structural disorder in epitaxially connected quantum dot solids from atomic to micron scale. *Nano Lett.* **16**, 5714–5718 (2016).
159. McCray, A. R. C., Savitzky, B. H., Whitham, K., Hanrath, T. & Kourkoutis, L. F. Orientational disorder in epitaxially connected quantum dot solids. *ACS Nano* **13**, 11460–11468 (2019).
160. Smeaton, M. A., El Baggari, I., Balazs, D. M., Hanrath, T. & Kourkoutis, L. F. Mapping defect relaxation in quantum dot solids upon *in-situ* heating. *ACS Nano* **15**, 719–726 (2021).
161. daSilva, J. C. *et al.* Mechanistic insights into superlattice transformation at a single nanocrystal level using nanobeam electron diffraction. *Nano Lett.* **20**, 5267–5274 (2020).
162. Choi, J. J., Bian, K., Baumgardner, W. J., Smilgies, D.-M. & Hanrath, T. Interface-induced nucleation, orientational alignment and symmetry transformations in nanocube superlattices. *Nano Lett.* **12**, 4791–4798 (2012).
163. Whitham, K. & Hanrath, T. Formation of epitaxially connected quantum dot solids: nucleation and coherent phase transition. *J. Phys. Chem. Lett.* **8**, 2623–2628 (2017).
164. Geuchies, J. J. *et al.* *In-situ* study of the formation mechanism of two-dimensional superlattices from PbSe nanocrystals. *Nature Materials* **15**, 1248–1254 (2016).
165. Sandeep, C. S. S. *et al.* Epitaxially connected PbSe quantum-dot films: controlled neck formation and optoelectronic properties. *ACS Nano* **8**, 11499–11511 (2014).
166. Zaluzhnyy, I. A. *et al.* Quantifying angular correlations between the atomic lattice and the superlattice of nanocrystals assembled with directional linking. *Nano Lett.* **17**, 3511–3517 (2017).
167. Boneschanscher, M. P. *et al.* Long-range orientation and atomic attachment of nanocrystals in 2D honeycomb superlattices. *Science* **344**, 1377–1380 (2014).
168. Maiti, S. *et al.* Revealing structure and crystallographic orientation of soft epitaxial assembly of nanocrystals by grazing incidence X-ray scattering. *J. Phys. Chem. Lett.* **10**, 6324–6330 (2019).
169. Abelson, A. *et al.* Collective topo-epitaxy in the self-assembly of a 3D quantum dot superlattice. *Nature Materials* (2020).
170. Chu, X. *et al.* Structural characterization of a polycrystalline epitaxially-fused colloidal quantum dot superlattice by electron tomography. *J. Mater. Chem. A* **8**, 18254–18265 (2020).
171. Reich, K. V. & Shklovskii, B. I. Dielectric constant and charging energy in array of touching nanocrystals. *Appl. Phys. Lett.* **108**, 113104 (2016).
172. Walravens, W. *et al.* Setting carriers free: healing faulty interfaces promotes delocalization and transport in nanocrystal solids. *ACS Nano* **13**, 12774–12786 (2019).
173. Ondry, J. C., Philbin, J. P., Lostica, M., Rabani, E. & Alivisatos, A. P. Colloidal synthesis path to 2D crystalline quantum dot superlattices. *ACS Nano* **15**, 2251–2262 (2021).
174. Ondry, J. C., Hauwiller, M. R. & Alivisatos, A. P. Dynamics and removal pathway of edge dislocations in imperfectly attached PbTe nanocrystal pairs: toward design rules for oriented attachment. *ACS Nano* **12**, 3178–3189 (2018).
175. Ondry, J. C. & Alivisatos, A. P. Application of dislocation theory to minimize defects in artificial solids built with nanocrystal building blocks. *Acc. Chem. Res.* **54**, 1419–1429 (2021).
176. Baumgardner, W. J., Whitham, K. & Hanrath, T. Confined-but-connected quantum solids via controlled ligand displacement. *Nano Lett.* **13**, 3225–3231 (2013).

177. Treml, B. E. *et al.* Successive ionic layer absorption and reaction for postassembly control over inorganic interdot bonds in long-range ordered nanocrystal films. *ACS Appl. Mater. Interfaces* **9**, 13500–13507 (2017).
178. Wang, Y. *et al.* Dynamic deformability of individual PbSe nanocrystals during superlattice phase transitions. *Science Advances* **5**, eaaw5623 (2019).
179. Wang, Y. *et al.* In situ TEM observation of neck formation during oriented attachment of PbSe nanocrystals. *Nano Res.* **12**, 2549–2553 (2019).
180. Li, H., Zhitomirsky, D., Dave, S. & Grossman, J. C. Toward the ultimate limit of connectivity in quantum dots with high mobility and clean gaps. *ACS Nano* **10**, 606–614 (2016).
181. Evers, W. H. *et al.* High charge mobility in two-dimensional percolative networks of PbSe quantum dots connected by atomic bonds. *Nat Commun* **6**, 8195 (2015).
182. Alimoradi Jazi, M. *et al.* Transport properties of a two-dimensional PbSe square superstructure in an electrolyte-gated transistor. *Nano Lett.* **17**, 5238–5243 (2017).
183. Dong, A., Chen, J., Vora, P. M., Kikkawa, J. M. & Murray, C. B. Binary nanocrystal superlattice membranes self-assembled at the liquid–air interface. *Nature* **466**, 474–477 (2010).
184. Zhao, M. *et al.* High hole mobility in long-range ordered 2D lead sulfide nanocrystal monolayer films. *Advanced Functional Materials* **26**, 5182–5188 (2016).
185. Peters, J. L. *et al.* Mono- and Multilayer Silicene-Type Honeycomb lattices by oriented attachment of PbSe nanocrystals: synthesis, structural characterization, and analysis of the disorder. *Chem. Mat.* **30**, 4831–4837 (2018).
186. Shannon, R. D. & Rossi, R. C. Definition of topotaxy. *Nature* **202**, 1000–1001 (1964).
187. Ilavsky, J. Nika: software for two-dimensional data reduction. *J Appl Cryst* **45**, 324–328 (2012).
188. Kline, S. R. Reduction and analysis of SANS and USANS data using IGOR Pro. *J Appl Cryst* **39**, 895–900 (2006).
189. Choi, J. J. *et al.* Controlling nanocrystal superlattice symmetry and shape-anisotropic interactions through variable ligand surface coverage. *J. Am. Chem. Soc.* **133**, 3131–3138 (2011).
190. Hens, Z. & Martins, J. C. A Solution NMR toolbox for characterizing the surface chemistry of colloidal nanocrystals. *Chem. Mater.* **25**, 1211–1221 (2013).
191. Moreels, I., Fritzing, B., Martins, J. C. & Hens, Z. Surface chemistry of colloidal PbSe nanocrystals. *J. Am. Chem. Soc.* **130**, 15081–15086 (2008).
192. Anderson, N. C., Hendricks, M. P., Choi, J. J. & Owen, J. S. Ligand exchange and the stoichiometry of metal chalcogenide nanocrystals: spectroscopic observation of facile metal-carboxylate displacement and binding. *J. Am. Chem. Soc.* **135**, 18536–18548 (2013).
193. Cass, L. C., Malicki, M. & Weiss, E. A. The chemical environments of oleate species within samples of oleate-coated PbS quantum dots. *Anal. Chem.* **85**, 6974–6979 (2013).
194. De Roo, J. *et al.* Probing solvent–ligand interactions in colloidal nanocrystals by the NMR line broadening. *Chem. Mater.* **30**, 5485–5492 (2018).
195. Karel Čapek, R., Yanover, D. & Lifshitz, E. Size control by rate control in colloidal PbSe quantum dot synthesis. *Nanoscale* **7**, 5299–5310 (2015).
196. Liu, C. *et al.* Unpublished results.
197. Grisorio, R., Debellis, D., Suranna, G. P., Gigli, G. & Giansante, C. The dynamic organic/inorganic interface of colloidal PbS quantum dots. *Angewandte Chemie International Edition* **55**, 6628–6633 (2016).
198. Harris, R. D. *et al.* Electronic processes within quantum dot–molecule complexes. *Chem. Rev.* **116**, 12865–12919 (2016).
199. Ning, Z. *et al.* Air-stable n-type colloidal quantum dot solids. *Nature Materials* **13**, 822–828 (2014).



200. Lynch, C. T., Mazdiyasi, K. S., Smith, J. S. & Crawford, W. J. Infrared spectra of transition metal alkoxides. *Anal. Chem.* **36**, 2332–2337 (1964).
201. Tangboriboon, N., Pakdeewanishukho, K., Jamieson, A., Sirivat, A. & Wongkasemjit, S. Electrical properties of a novel lead alkoxide precursor: Lead glycolate. *Materials Chemistry and Physics* **98**, 138–143 (2006).
202. Buckley, P. & Giguère, P. A. Infrared studies on rotational isomerism. I. Ethylene glycol. *Can. J. Chem.* **45**, 397–407 (1967).
203. Weidman, M. C., Smilgies, D.-M. & Tisdale, W. A. Kinetics of the self-assembly of nanocrystal superlattices measured by real-time *in situ* X-ray scattering. *Nature Materials* **15**, 775–781 (2016).
204. Li, R., Bian, K., Hanrath, T., Bassett, W. A. & Wang, Z. Decoding the Superlattice and Interface Structure of Truncate PbS Nanocrystal-Assembled Supercrystal and Associated Interaction Forces. *J. Am. Chem. Soc.* **136**, 12047–12055 (2014).
205. Bian, K., Li, R. & Fan, H. Controlled self-assembly and tuning of large PbS nanoparticle supercrystals. *Chem. Mater.* **30**, 6788–6793 (2018).
206. Nagaoka, Y. *et al.* Superstructures generated from truncated tetrahedral quantum dots. *Nature* **561**, 378–382 (2018).
207. Bian, K. *et al.* Shape-anisotropy driven symmetry transformations in nanocrystal superlattice polymorphs. *ACS Nano* **5**, 2815–2823 (2011).
208. Simon, P. *et al.* PbS–Organic Mesocrystals: The relationship between nanocrystal orientation and superlattice array. *Angewandte Chemie International Edition* **51**, 10776–10781 (2012).
209. Santra, P. K., Palmstrom, A. F., Tassone, C. J. & Bent, S. F. Molecular ligands control superlattice structure and crystallite orientation in colloidal quantum dot solids. *Chem. Mater.* **28**, 7072–7081 (2016).
210. Novák, J. *et al.* Site-specific ligand interactions favor the tetragonal distortion of PbS nanocrystal superlattices. *ACS Appl. Mater. Interfaces* **8**, 22526–22533 (2016).
211. Li, R. *et al.* An obtuse rhombohedral superlattice assembled by Pt nanocubes. *Nano Lett.* **15**, 6254–6260 (2015).
212. Winslow, S. W., Swan, J. W. & Tisdale, W. A. The importance of unbound ligand in nanocrystal superlattice formation. *J. Am. Chem. Soc.* **142**, 9675–9685 (2020).
213. Chomette, A., Deveaud, B., Regreny, A. & Bastard, G. Observation of carrier localization in intentionally disordered GaAs/GaAlAs superlattices. *Phys. Rev. Lett.* **57**, 1464–1467 (1986).
214. Smilgies, D.-M. & Blasini, D. R. Indexation scheme for oriented molecular thin films studied with grazing-incidence reciprocal-space mapping. *J Appl. Cryst.* **40**, 716–718 (2007).
215. Dieleman, C. D. *et al.* Universal direct patterning of colloidal quantum dots by (extreme) ultraviolet and electron beam lithography. *Nanoscale* **12**, 11306–11316 (2020).
216. Wang, Y., Fedin, I., Zhang, H. & Talapin, D. V. Direct optical lithography of functional inorganic nanomaterials. *Science* **357**, 385–388 (2017).
217. Wang, Y., Pan, J.-A., Wu, H. & Talapin, D. V. Direct wavelength-selective optical and electron-beam lithography of functional inorganic nanomaterials. *ACS Nano* **13**, 13917–13931 (2019).
218. Cho, H. *et al.* Direct optical patterning of quantum dot light-emitting diodes via *in-situ* ligand exchange. *Advanced Materials* **32**, 2003805 (2020).
219. Gheshlaghi, N. *et al.* Self-resonant microlasers of colloidal quantum wells constructed by direct deep patterning. *Nano Lett.* **21**, 4598–4605 (2021).
220. Yang, J. *et al.* High-resolution patterning of colloidal quantum dots via non-destructive, light-driven ligand crosslinking. *Nat Commun* **11**, 2874 (2020).
221. Gao, Y., Huang, J.-Y., Balazs, D. M., Xu, Y. & Hanrath, T. Photoinitiated transformation of nanocrystal superlattice polymorphs assembled at a fluid interface. *Advanced Materials Interfaces* **7**, 2001064 (2020).

222. Kundu, K. K. & Das, M. N. Autoprotolysis constants of ethylene glycol and propylene glycol and dissociation constants of some acids and bases in the solvents at 30° C. *J. Chem. Eng. Data* **9**, 82–86 (1964).
223. *Handbook of Chemistry and Physics 100th Edition*. (CRC Press, 2019).
224. Bates, R. G. Solute-solvent interactions and acid-base dissociation in mixed solvent systems. *Journal of Electroanalytical Chemistry and Interfacial Electrochemistry* **29**, 1–19 (1971).
225. Breant, M., Arnaud, N. & Desmetre, S. Spectrophotometric determination of the pH scale in ethane-1,2-diol. *Analytica Chimica Acta* **104**, 181–183 (1979).
226. Hulanicki, A. & Głab, S. Coulometric titrations in microscale study of ionic equilibria. *Fresenius J Anal Chem* **337**, 512–517 (1990).
227. Scheele, M. *et al.* Nonmonotonic size dependence in the hole mobility of methoxide-stabilized PbSe quantum dot solids. *ACS Nano* **7**, 6774–6781 (2013).
228. Jo, C. H. *et al.* Low-temperature annealed PbS quantum dot films for scalable and flexible ambipolar thin-film-transistors and circuits. *J. Mater. Chem. C* **2**, 10305–10311 (2014).
229. Osedach, T. P. *et al.* Bias-stress effect in 1,2-ethanedithiol-treated PbS quantum dot field-effect transistors. *ACS Nano* **6**, 3121–3127 (2012).
230. Zhang, Y. *et al.* Investigation of the defect density in ultra-thin Al<sub>2</sub>O<sub>3</sub> films grown using atomic layer deposition. *Surface and Coatings Technology* **205**, 3334–3339 (2011).
231. Groner, M. D., Fabreguette, F. H., Elam, J. W. & George, S. M. Low-temperature Al<sub>2</sub>O<sub>3</sub> atomic layer deposition. *Chem. Mater.* **16**, 639–645 (2004).